Development of spectral domain techniques for the analysis of printed transmission lines with nonzero conductor thickness

by

Erik Speksnijder

Thesis committee:	Prof. dr. A. Neto,	TU Delft, supervisor
	Dr. D. Cavallo,	TU Delft,
	Dr. ir. M. Spirito,	TU Delft, external member

Contents

1
Introduction

Sub-millimetre wave applications have been receiving an increasing attention from the antenna engineering community. Such attention has been driven by their potential for designing front ends of diminished dimensions, together with the possibility of providing wide band channels. Potential applications include wireless communication and radar systems [1],[2],[3], astronomical instrumentation [4],[5],[6], and security imaging [7],[8],[9]. The analysis and design of the antennas, embedded in sub-millimetre wave front ends, require the accurate modelling of relevant parameters, such as the input impedance, the radiation patterns and the mutual coupling. Most often, the design of these structures resorts to commercial full-wave solvers, which allow for the necessary flexibility to investigate substantially different geometries. However, generic commercial software tools often suffer from computation overhead and correspondingly long simulation times. At times, high-frequency techniques, such as the Physical Optics (PO) have been utilized to facilitate the analysis of quasi optical systems. For instance, in the analysis of lens antennas [10], these techniques have been applied somewhat successfully [11],[12].

Nevertheless, high frequency techniques remain limited in their scope. In particular, if the lens antennas are small in terms of the wavelength, the approximations implicit in the asymptotic analysis can render them severely inaccurate. Recently, for instance, small-size lens antennas have been used as elements for coherent arrays [2], as shown in Fig 1.1a, or as the core lens in core shell lens structures [3], as shown in Fig 1.1b. In these cases, the ray propagations via Geometrical Optics (GO) or the PO integrations become inaccurate when the curvatures of the surfaces are small with respect to the wavelength. These inherent limitations are calling for the development of simulation tools that can model these specific structures efficiently, but without compromising the accuracy.

To achieve this goal, the THz Sensing Group [13],[14] has recently started with the development of a dedicated 3-dimensional Method of Moments tool that is suitable for the analysis of dielectric lenses. To be able to analyse structures with dimensions in the order of a few wavelengths, it is necessary to maintain a volumetric sub-gridding which is fairly large in terms of the wavelength inside the dielectric, $\lambda_d = \lambda_0/\sqrt{\varepsilon_r}$, where λ_0 denotes the free space wavelength and ε_r denotes the relative dielectric permittivity. Assuming that $\lambda_d/10$ is the required sub-gridding, a lens with a leading dimension of $2\lambda_0 \approx 3\lambda_d$ requires roughly $N_{\text{MoM}} \approx 10^5$ unknowns, which is a large, but manageable number, even with regular laptops. The tool developed in the THz Sensing Group provides the solution to such a problem in a run time of about 1 minute. However, the majority of the lens feeds that could reasonably be expected within such a lens system, are characterized by dimensions that are much smaller than $\lambda_d/10$. Specifically, if the feeds are to be realized in integrated technology, the characteristic dimensions of dipoles and transmission lines will be those permitted by the technology: i.e. micrometric or even nanometric. As a case in point, the thickness of standard Printed Circuit Board (PCB) technology is in the order of $w_z \approx 20\mu$m and the minimal width of PCB lines is typically $w_y \approx 100\mu$m. However, in integrated technology $w_z \approx 0.2-2\mu$m, while $w_y \approx 1-10\mu$m. Consequently, if one had to use a 10μm resolution for a lens with a leading dimension of 2mm, the number of unknowns would be $N_{\text{MoM}} \approx 24 \cdot 10^9$. Problems of such scale cannot be expected to be solved anywhere in the near future.

To circumvent this problem, the strategy, adopted in the THz Sensing group, has been to hybridize the lens feed analysis [15], [16]. The feed would be studied with a full wave technique, i.e. MoM or similar, in which the reaction integral via the lens would be approximated using the PO approximations. This technique is certainly valid, as long as the dimensions of the lens are large enough in terms of the wavelength.

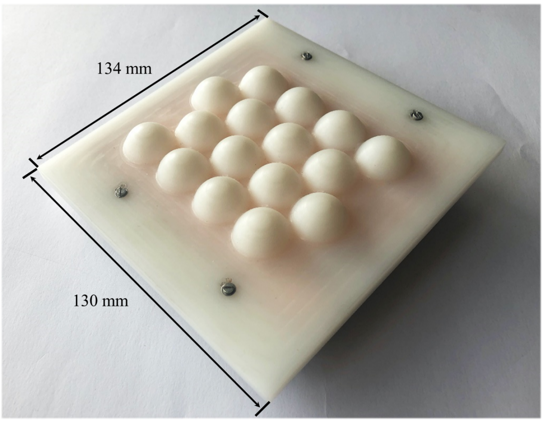

(a)

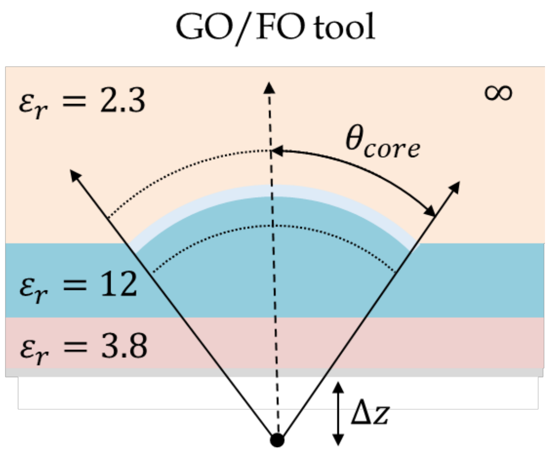

(b)

Figure 1.1: Applications of small lenses (a) as elements for coherent arrays [2] and (b) as the core-shell lens for fly eyes applications [3]

1.0.1. Auxiliary feed strategy

In a parallel effort, the broader goal of the MoM development in the THz Sensing group is now to develop a strategy to separate the characterization of the feeding structure and the lens antennas, while trying to maintain a higher simulation accuracy than a PO hybridization would permit: i.e. being able to study smaller lenses for which the use of the PO would be entirely inappropriate. To reach this goal, the original feed structure, with fine details, can be replaced by an auxiliary feed structure, that has the same dynamic (i.e. radiating) equivalent currents, but much coarser dimensions. The analysis of the auxiliary feed can then be performed together with the analysis of the already coarsely discretized lens structure. Since the interaction between the lens and the auxiliary feed only occurs via the dynamic components of the spectrum, one can isolate such interaction from the numerical results. This can be achieved by expressing the result, obtained by simulating the lens with the auxiliary feed, as the superposition of a contribution due to the auxiliary feed, operating in the presence of an infinite dielectric and the contribution due to the reflections inside the lens. Once this latter interaction term is found, the analysis of the original finely discretized feed can simply be complemented with the contribution from the lens, which will be the same for the original and the auxiliary feed.

1.0.2. Towards the synthesis of the auxiliary feeds

The synthesis of such an auxiliary feed structure, in the presence of an infinite dielectric, rather than a finite lens, can be obtained in many alternative ways. For instance, the analysis of both the original feed and the auxiliary feed could be performed, resorting to a purely numerical MoM procedure, iterating the analysis of trial auxiliary geometries until a certain geometry satisfies the requirements. However, in order to converge faster to a useful geometry, one first needs to acquire a better understanding of the characterizing features of the proposed feeds. Specifically, in integrated technology with thicknesses of the metal in the order of $w_z \approx 0.2 - 2\mu$m and $w_y \approx 1 - 10\mu$m, the dimensions are much closer to the penetration depth, which, for metals, is in the order of 0.3μm at 300GHz. The small dimensions in terms of the penetration depth imply that for the guided waves that propagate along the metallic lines, the Ohmic losses are high and the wave velocity itself is very different from the one in absence of losses.

For these reasons, it has been decided to develop a dedicated tool to investigate the properties of planar transmission lines, that are typically used in the millimetre and sub-millimetre waves regimes, accounting for the thickness of the material explicitly. The chosen tool is the typical transmission line Green's function [15],[17],[18],[19], which was shown to be a powerful tool to investigate planar open guiding structures. The method is typically used, assuming that the open guiding structure is infinitely extended along the x-direction and infinitesimally thin. A surface boundary condition is then imposed to derive the equivalent current, flowing along the longitudinal direction. Typically, the propagation constant, the (complex) characteristic impedance and the losses are derived from the polar contributions in the spectrum of the longitudinal current.

In microstrips, however, the inclusion of the thickness becomes significant in the evaluation of the characteristic impedance, when this thickness is comparable to the distance between the main conductor and the

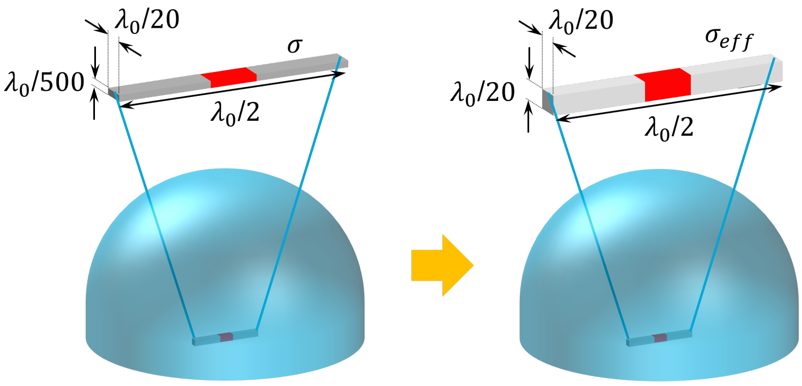

Figure 1.2: Equivalent procedure to simulate a feed with realistic dimensions by simulating a feed with convenient dimensions together with an adjusted conductivity σ_{eff}

ground plane [20],[21]. Moreover, if the finite thickness of the conductor is not embedded into the formulation, the influence of the thickness of the conductor on the losses of the transmission line, has to be introduced in an alternative way. The software tool, proposed in [19], estimates the influence of the conductor thickness by using the modified surface impedance, given by [22]. However, this approach fails to take into account the asymmetric current distribution inside the main conductor of the microstrip.

Due to the new desire to accurately take into account the dispersion properties of the lines, associated to the metal thickness, the assumption of infinitesimal thickness is not satisfactory. To account for the actual thickness, a different volumetric integral equation has been set up that guarantees the verification of the appropriate volumetric constitutive relations of a conductor with finite conductivity. The procedure has been developed in the frequency domain, starting from a 3D integral representation of the stratified media Green's function for the case of dipoles in generic stratifications, including those that support leaky wave propagation. In all cases, one of the 3 integrals can be closed analytically, which leads to a quasi analytical tool to obtain the electric currents inside the metals. Thanks to the availability of this tool, a parametric analysis has been performed on a family of important transmission lines. This family includes microstrips, as well as dipoles in free space and in the presence of a semi-infinite dielectric region. This last case is particularly relevant, as it represents a widely used type of leaky wave radiator, adopted in THz Sensing group.

1.1. Contribution of the thesis

The core content of this thesis is concerned with the development of a spectral domain formulation to characterize printed transmission lines, in the presence of an arbitrary stratification, taking into account the finite thickness of the conductors. In particular, the applicability of this formulation will be demonstrated by studying one of the most common transmission line topologies: the microstrip. As explained in the previous section, within the scope of the overall project, carried out in the THz Sensing Group, the purpose of the spectral domain formulation is to characterize the thin metallic feed of the integrated lens antennas. Therefore, the spectral formulation will also be used to study dipoles in the presence of a semi-infinite dielectric stratification, which support leaky wave propagation.

In order to validate the newly developed spectral domain formulation, the Volumetric Method of Moments (V-MoM), available from the group, has been taken as a starting point. In [14], the use of the V-MoM was proposed, for the analysis of integrated lens antennas, due to its suitability for simulating geometries of resonant size, and its ease in handling material inhomogeneity's. The V-MoM, developed in [14], uses a structured grid, which provides the possibility of reducing the memory requirements and the computational complexity by means of the Conjugate Gradient Fast Fourier Transform (CG-FFT). Moreover, the use of a structured grid allows one to pre-compute and reuse the reaction integrals, associated to the employed integral equation, when simulating multiple different geometries.

However, the tool developed in [14] had not been optimized in terms of its computation time. Additionally, the numerical calculation of the reaction integrals, that was implemented in [14], was relatively inaccurate, compared to alternative computation schemes, such as the method, introduced in [23]. Furthermore, the V-MoM has inherent difficulties when simulating geometries that are not well-represented by the structured grid.

The thesis thus presents a second important part, which is somewhat separated from the original task: the optimization of the MATLAB tool, developed in [14]. To this extent, the numerical procedure, used to solve the matrix equation of the V-MoM, is optimized in terms of its computation time. Moreover, a more accurate procedure for the numerical calculation of the reaction integrals has been implemented, based on the method, proposed in [23]. Additionally, a solution is presented to improve the accuracy of the V-MoM, when simulating geometries that are not well-represented by the structured grid.

1.2. Thesis Outline

Since this thesis work was embedded in the main research line of the THz Sensing group on the development of a MoM tool, dedicated to the analysis of antenna excited dielectric lenses, Chapter 2, provides an overview of the V-MoM, developed in [14]. The V-MoM solves the Electric Field Integral Equation (EFIE), obtained by invoking the volume equivalence theorem [24]. The EFIE is then discretized using a structured grid, consisting of piece-wise constant basis functions, which converts the integral equation to a matrix equation that is solved using an iterative technique called the Conjugate Gradient Fast Fourier Transform (CG-FFT).

Next, Chapter 3 describes the work on the optimization of the V-MoM in terms of accuracy and computation time that was performed during the thesis project. To this extent, the computation time of the V-MoM has been improved by optimizing the memory allocation during the simulation as well as the implementation of the FFT based matrix-vector products. Moreover, a solution is presented to enhance the accuracy of the V-MoM when simulating geometries that are not well-represented by the structured grid. This procedure refines the representation of the scatterer by averaging the permittivity of the voxels that are located at the boundary of the scatterer. Finally, a more accurate procedure for the numerical calculation of the reaction integrals is implemented, based on a reduction from volume to surface integrals [23].

The core of the thesis work starts in Chapter 4. This chapter introduces the spectral domain formulation that allows us to study infinitely long printed transmission lines, taking into account the non-zero thickness of the conductors. This formulation is based on the local form of Ohm's law and will be introduced by studying an infinitely long dipole located in free space. By approximating the exponential decay inside the dipole with the Leontovich boundary condition [25], an expression is obtained for the spectrum of the longitudinal current distribution. The relevant parameters of the transmission line are then extracted from the polar singularities in the spectrum. In particular, the residue contribution of the input admittance is interpreted as the contribution from two infinitely long transmission lines. This interpretation is then substantiated by demonstrating its resemblance with the characteristic impedance obtained by defining the voltage along the transmission line as the line integral of the transverse electric field.

In Chapter 5, the formulation developed in Chapter 4 is extended to allow the characterization of printed transmission lines in the presence of an arbitrary stratification, using the spectral domain Green's function for stratified media. Since the spectral domain Green's function for stratified media has a spectral dependence along the transverse dimensions and a spatial dependence on z and z', the projection in the y-direction is performed in the spectral domain, while the projection in the z-direction is performed in the spatial domain. To represent the asymmetric geometry of the microstrip, the transverse current distribution is expanded into two basis function, each with an exponential decay starting from the bottom or the top of the metal strip.

Next, Chapter 6 introduces an equivalent circuit representation to model the input impedance of a microstrip, printed on an electrically thin dielectric substrate. This circuit representation is based on the extraction of two dominant parts of the current spectrum: the dynamic part and the quasi-static part. The dynamic part of the spectrum refers to the portion of the spectrum that is related to small values of k_x and can be approximated by a Taylor approximation around the pole. On the other hand, the asymptotic part of the spectrum refers to the limit for k_x tending to infinity and can be approximated by only retaining the $k_y = 0$ component of the spectrum. By interpreting the quasi-TEM wave launched along the microstrip as the current along two infinitely long transmission lines, connected to a transformer, we can define a gap impedance that is almost purely imaginary. This gap impedance can then be approximated using the two dominant parts of the current spectrum.

Finally, in Chapter 7, the formulation, developed in Chapters 4 and 5 is used to study a leaky structure containing a dipole in the presence of a semi-infinite dielectric region. This geometry is particularly relevant with respect to the overall research line carried out in the THz Sensing Group, as it allows us to obtain a better understanding of the properties of the dynamic (i.e. radiating) components of the metallic feed, in an effort to isolate the contributions due to the reflections inside the lens. Since the leaky wave pole is located on the bottom Riemann Sheet with, the appropriate transverse integration path has been chosen to obtain the physically significant leaky wave pole. A parametric analysis is then performed to gain insight into the properties of the dynamic (i.e. radiating) currents along the dipole.

2

Overview of the Volumetric Method of Moments

This chapter provides an overview of the Volumetric Method of Moments (V-MoM), developed in [14]. The objective of the V-MoM is to solve the Electric Field InteIgral Equation (EFIE) that is obtained by invoking the volume equivalence theorem [24]. To this extent, the EFIE is discretized using a structured grid, consisting of piece-wise constant basis functions. This procedure converts the integral equation to a matrix equation that is solved using an iterative technique called the Conjugate Gradient Fast Fourier Transform (CG-FFT).

The V-MoM has three distinct advantages. First of all, by using the same grid, the reaction integrals can be pre-computed and reused to simulate multiple different geometries. Second, as a consequence of the use of a structured grid, the system matrix has a Toeplitz structure, which allows for a reduction of the memory requirements by storing only $2N_t$ entries, instead of $9N_t^2$ entries, where N_t denotes the total number of voxels within the grid. Finally, the Toeplitz structure of the system matrix allows us to use the CG-FFT, which results in a significant reduction of the total computation time, when dealing with large-scale problems.

This chapter is structured as follows. First, Section 2.1 formulates the Electric Field Integral Equation (EFIE) by invoking the volume equivalence theorem [24]. In Section 2.2, the EFIE is discretized by employing the Method of Moments [26]. Subsequently, Section 2.3 defines the grid and describes the computation of the reaction integrals. Next, Section 2.4 describes the inversion of the system matrix by means of an iterative technique called the Conjugate Gradient (CG). Finally, Section 2.5 describes how FFTs can be utilized to accelerate the matrix-vector products, performed by the CG.

2.1. Integral equation

The objective of the Volumetric Method of Moments (V-MoM) is to solve a forward problem in which an incident electric field $\vec{E}^i(\vec{r})$ illuminates an arbitrary scatterer, constituted of a material with a relative permittivity $\varepsilon_r(\vec{r})$, which occupies a volume V. The object is assumed to be embedded in a homogeneous background medium with relative permittivity $\varepsilon_{r,bg}$. The total electric field inside the scatterer can be written as the superposition of the incident field $\vec{E}^i(\vec{r})$ and the scattered field $\vec{E}^s(\vec{r})$, as shown in the following expression

$$\vec{E}(\vec{r}) = \vec{E}^i(\vec{r}) + \vec{E}^s(\vec{r}) \tag{2.1}$$

By invoking the volume equivalence theorem [24], the scatterer can be replaced by an equivalent current distribution $\vec{J}_{\text{eq}}(\vec{r})$, radiating in free space, as shown in Fig. 2.1. $\vec{J}_{\text{eq}}(\vec{r})$ is related to the total electric field inside the scatterer through an effective conductivity $\sigma_{\text{eff}}(\vec{r})$ as follows

$$\vec{J}_{\text{eq}}(\vec{r}) = \sigma_{\text{eff}}(\vec{r})\vec{E}(\vec{r}), \tag{2.2}$$

where $\sigma_{\text{eff}}(\vec{r})$ is defined as follows

$$\sigma_{\text{eff}} = j\omega\varepsilon_0(\varepsilon_r(\vec{r}) - \varepsilon_{r,bg}). \tag{2.3}$$

Since the equivalent currents radiate in free space, $\vec{E}^s(\vec{r})$ can be expressed as the convolution between the free space Green's function $G_{fs}^{EJ}(\vec{r}-\vec{r}')$ and $\vec{J}_{\text{eq}}(\vec{r})$, as shown in the following expression

$$\vec{E}^s(\vec{r}) = \iiint_V G_{fs}^{EJ}(\vec{r}-\vec{r}')\vec{J}_{\text{eq}}(\vec{r}')\,d\vec{r}'. \tag{2.4}$$

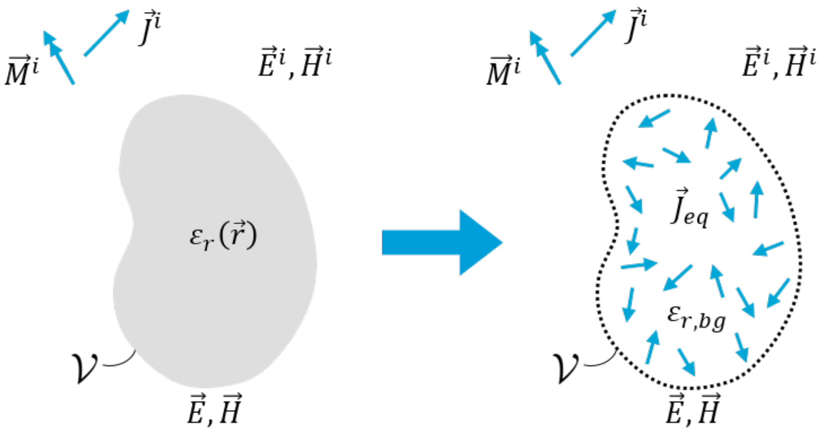

Figure 2.1: Replacement of the scatterer with an equivalent current distribution $\vec{J}_{\text{eq}}(\vec{r})$, radiating in free space, by invoking the volume equivalence theorem [24]

By substituting (2.3) and (2.4) into (2.1), we obtain the following expression

$$\vec{E}^i(\vec{r}) = \frac{\vec{J}_{\text{eq}}(\vec{r})}{\sigma_{\text{eff}}(\vec{r})} - \iiint_V G_{fs}^{EJ}(\vec{r}-\vec{r}')\vec{J}_{\text{eq}}(\vec{r}')\,d\vec{r}'. \tag{2.5}$$

The integral equation, given by (2.5), is called the Electric Field Integral Equation (EFIE) and will be discretized and solved with the Method of Moments (MoM), as described in the following section.

2.2. Discretization integral equation

The first step in the Method of Moments [26] is to expand the unknown in the integral equation as the summation of a number of basis functions, as shown in the following expression

$$\vec{J}_{\text{eq}}(\vec{r}) = \sum_{n=1}^{N_t} i_n \vec{b}_n(\vec{r}). \tag{2.6}$$

By substituting (2.6) into (2.5), we obtain the following expression

$$\vec{E}^i(\vec{r}) = \sum_{n=1}^{N_t} i_n \left(\frac{\vec{b}_n(\vec{r})}{\sigma_{\text{eff}}(\vec{r})} - \iiint_V G_{fs}^{EJ}(\vec{r}-\vec{r}')\vec{b}_n(\vec{r})\,d\vec{r}' \right). \tag{2.7}$$

To convert (2.7) to a matrix equation, we will first define the following projection operator

$$\langle f(\vec{r}), g(\vec{r})\rangle_V = \iiint_V f(\vec{r})g(\vec{r})\,d\vec{r}. \tag{2.8}$$

Since the integral operator in (2.5), defines a mapping from the function space $L^2(\mathbb{R}^3)$ to $L^2(\mathbb{R}^3)$ [23], adopting the Galerkin method guarantees convergence in the norm when the set of basis functions spans the aforementioned function space [27],[28]. By applying a Galerkin projection to (2.7), we obtain the following expression

$$\underbrace{\langle \vec{E}^i, \vec{b}_m(\vec{r})\rangle_V}_{①} = \sum_{n=1}^{N_t} i_n \left(\underbrace{\frac{\langle \vec{b}_n(\vec{r}), \vec{b}_m(\vec{r})\rangle_V}{\sigma_{\text{eff}}(\vec{r})}}_{②} - \underbrace{\langle \iiint_V G_{fs}^{EJ}(\vec{r}-\vec{r}')\vec{b}_n(\vec{r}')\,d\vec{r}', \vec{b}_m(\vec{r})\rangle_V}_{③} \right). \tag{2.9}$$

As explained in [29], it is necessary that the set of basis functions spans the aforementioned function space. Since the equivalent currents defined in (2.3) are fictitious, they do not satisfy any continuity condition [29]. Hence, it is not necessary that the set of basis function enforces any continuity condition either. The simplest choice is to use piece-wise constant basis functions, as shown in the following expression

$$\vec{b}_n(\vec{r}) = \frac{1}{\Delta^2}\text{rect}\left(\frac{\vec{r}-\vec{r}_n'}{\Delta}\right)\hat{p}_n, \tag{2.10}$$

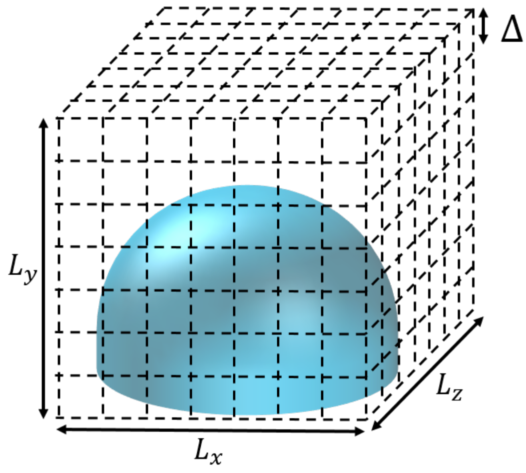

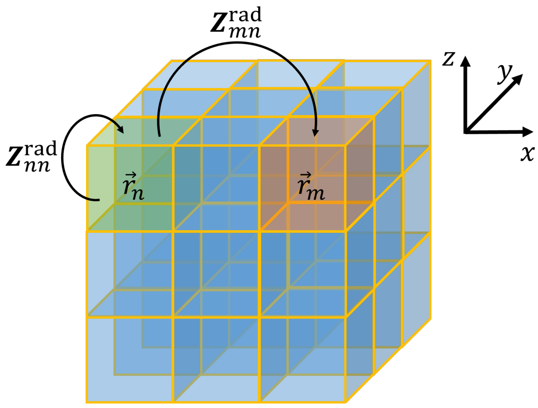

Figure 2.2: (a) Structured grid having dimensions L_x, L_y and L_z, and discretized with voxels of size Δ and (b) distinction between the self-integrals and the mutual integrals of the coupling matrix $\mathbf{Z}^{\text{rad}}$

where $\hat{p}_n \in \{\hat{x}, \hat{y}, \hat{z}\}$, depending on the polarization of the basis function. The chosen set of basis functions allows for an analytical evaluation of the forcing term ① as well as the term ② in (2.9). The forcing term becomes as follows

$$\langle \vec{E}^i, \vec{b}_m(\vec{r})\rangle_V = \vec{E}^i \cdot \hat{p}_m \Delta = v_m, \tag{2.11}$$

where v_m denotes the voltage, impressed on the m^{th} basis function. The term ② in (2.9) becomes as follows

$$\frac{\langle \vec{b}_n(\vec{r}), \vec{b}_m(\vec{r})\rangle_V}{\sigma_{\text{eff}}(\vec{r})} = \frac{\delta_{mn}}{\sigma_{\text{eff},n}\Delta}, \tag{2.12}$$

where δ_{mn} denotes the Kronecker delta. By defining the diagonal matrix $\mathbf{Z}^{\text{mat}}$ as follows

$$\mathbf{Z}^{\text{mat}} = \text{diag}\left(\frac{1}{\sigma_{\text{eff},1}\Delta}, \frac{1}{\sigma_{\text{eff},2}\Delta}, \ldots, \frac{1}{\sigma_{\text{eff},N_t}\Delta}\right), \tag{2.13}$$

and by defining the coupling matrix $\mathbf{Z}^{\text{rad}}$ as follows

$$\mathbf{Z}^{\text{rad}}_{mn} = -\langle \iiint_V G^{EJ}_{fs}(\vec{r} - \vec{r}\,')\vec{b}_n(\vec{r}\,')\, d\vec{r}\,', \vec{b}_m(\vec{r})\rangle_V, \tag{2.14}$$

(2.9) can be written as the following matrix equation,

$$\mathbf{v} = (\mathbf{Z}^{\text{mat}} + \mathbf{Z}^{\text{rad}})\mathbf{i}, \tag{2.15}$$

where $\mathbf{v}$ denotes the excitation vector and $\mathbf{i}$ denotes the unknown current vector.

2.3. Definition of the grid and computation of the integrals

To discretize the integral equation in (2.5), a rectangular volume is defined, containing the scatterer, and having dimensions L_x, L_y and L_z, as shown in Fig 2.2a. Subsequently, a structured mesh is defined, which divides the rectangular volume into cubic subdomains having a length Δ in the x-, y- and z-directions.

Once the grid is defined, we can obtain the coupling matrix $\mathbf{Z}^{\text{rad}}$. Evaluating the entries of the coupling matrix $\mathbf{Z}^{\text{rad}}$ requires the numerical evaluation of the 6D reaction integrals given by (2.14). When the source and observation point coincide, the singularity in the Green's function $G^{EJ}_{fs}(\vec{r} - \vec{r}\,')$ requires appropriate treatment. Therefore, the integrals in (2.14) are divided into two categories, as shown in Fig. 2.2b: the self-integrals, i.e. the integrals with $m = n$, and the mutual integrals, i.e. the integrals with $m \neq n$. The mutual reaction integrals have been calculated by discretizing the source and observation regions into a uniform submesh, as shown in Fig 2.3. The reaction integrals can then be calculated as follows

$$\mathbf{Z}^{\text{rad}}_{mn} = -\frac{\ell^6}{\Delta^4} \sum_{l,p,q} \sum_{l',p',q'} G^{EJ}_{fs}(\vec{r}_{l,p,q} - \vec{r}_{l',p',q'}), \tag{2.16}$$

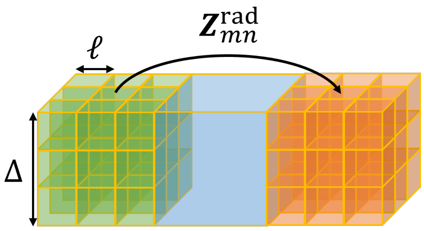

Figure 2.3: Uniform submesh to calculate the reaction integrals

where ℓ denotes the size of the submesh. The self-reaction integrals cannot be calculated directly from (2.14), due to the singularity of the Green's function, when the source and observation point coincide. However, as shown in [30] and [31], the electric field inside the source region can be rigorously derived, which leads to the following expression

$$\mathbf{Z}_{mn}^{\mathrm{rad}} = -\langle \iiint_{V-V_\delta} G_{fs}^{EJ}(\vec{r}-\vec{r}')\vec{b}_n(\vec{r}')\,d\vec{r}', \vec{b}_m(\vec{r})\rangle_V - \frac{1}{j\omega\varepsilon_0\Delta}\left(\frac{2}{3}e^{-jka}(1+jka)-1\right), \tag{2.17}$$

where V_δ denotes a spherical volume, used to exclude the singularity of $G_{fs}^{EJ}(\vec{r}-\vec{r}')$, and a denotes the radius of V_δ. Similar to before, (2.17) has been calculated by discretizing the source and observation regions into a uniform submesh, which leads to the following expression.

$$\mathbf{Z}_{nn}^{\mathrm{rad}} = -\frac{\ell^6}{\Delta^4}\sum_{l,p,q}\sum_{l',p',q'\neq l,p,q} G_{fs}^{EJ}(\vec{r}_{l,p,q}-\vec{r}_{l',p',q'}) - \frac{1}{j\omega\varepsilon_0\Delta}\left(\frac{2}{3}e^{-jk\ell(\frac{3}{4\pi})^{\frac{1}{3}}}\left(1+jk\ell\left(\frac{3}{4\pi}\right)^{\frac{1}{3}}\right)-1\right), \tag{2.18}$$

where the radius $a = \ell(\frac{3}{4\pi})^{\frac{1}{3}}$ has been chosen such that the spherical volume V_δ is equal the volume of the cubic submesh.

2.4. Iterative solver

Solving the matrix equation in (2.15), requires the inversion of the impedance matrix $\mathbf{Z}^{\mathrm{mat}} + \mathbf{Z}^{\mathrm{rad}}$. To alleviate the memory requirements and to decrease the computational complexity, the tool utilizes the Conjugate Gradient Fast Fourier Transform (CG-FFT) [32]. The Conjugate Gradient (CG) is an iterative technique that approximates the solution to a linear system. To understand the procedure, let us consider the following matrix equation

$$\mathbf{Zi} = \mathbf{v}. \tag{2.19}$$

Instead of solving (2.19) directly, the Conjugate Gradient first defines the following functional

$$f(\mathbf{i}) = \frac{1}{2}\mathbf{i}^{\mathrm{T}}\mathbf{Zi} - \mathbf{i}^{\mathrm{T}}\mathbf{v}, \tag{2.20}$$

whose minimum coincides with the solution of (2.19). The minimum of (2.20) is then obtained in an iterative manner, using successive approximations.

The overall algorithm is shown in Fig. 2.4. The CG starts with an initial guess $\mathbf{i}^{(0)}$. Subsequently, at each iteration, a residual error $\mathbf{r}^{(k)}$ is calculated, associated with the approximation $\mathbf{i}^{(k)}$. Based on the residual error $\mathbf{r}^{(k)}$, the CG computes a new approximation $\mathbf{i}^{(k+1)}$. This procedure continues until a predetermined tolerance ϵ is reached. Unfortunately, the procedure shown in Fig. 2.4 is still unfeasible in terms of memory requirements and computational complexity, when performed in a traditional manner. To understand the reason, let us consider the computation of the residual error

$$\mathbf{r}^{(k)} = \mathbf{v} - \underbrace{\mathbf{Z}^{\mathrm{mat}}\cdot\mathbf{i}^{(k)}}_{①} + \underbrace{\mathbf{Z}^{\mathrm{rad}}\cdot\mathbf{i}^{(k)}}_{②}. \tag{2.21}$$

$\mathbf{Z}^{\mathrm{mat}}$ denotes the diagonal matrix defined in (2.12). Hence, product ① only requires us to store N_t entries and to perform N_t operations, where N_t denotes the number of unknowns. However, the coupling matrix $\mathbf{Z}^{\mathrm{rad}}$ is a full matrix. Therefore, product ② requires us to store N_t^2 entries and to perform N_t^2 operations. Fortunately,

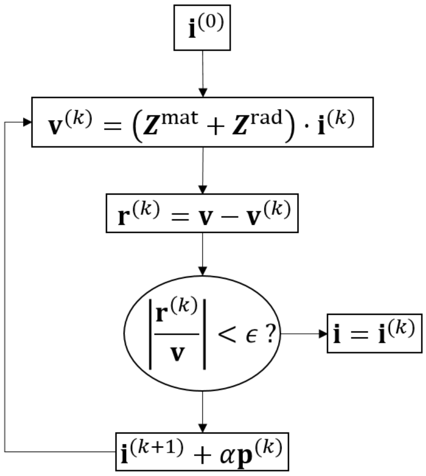

Figure 2.4: Iterative method to solve the matrix equation

the choice of the structured grid and the translational invariance of the free space Green's function $G_{fs}^{EJ}(\vec{r}-\vec{r}')$, result in a coupling matrix with a Toeplitz structure. The Toeplitz structure of $\mathbf{Z}^{\text{rad}}$ allows us to reduce the memory requirements and to accelerate the matrix-vector products by utilizing FFTs. This procedure will be explained in the following section.

2.5. FFT-based solver

As mentioned in Section 2.4, the Toeplitz structure of the coupling matrix $\mathbf{Z}^{\text{mat}}$ allows us to reduce the memory requirements and to accelerate the matrix-vector products in (2.21). To understand the underlying principles, we will first consider the case of a one-dimensional grid and subsequently, extend the procedure to two- and three-dimensional geometries.

2.5.1. One-dimensional geometry

Let us consider a one-dimensional grid consisting of N_x equispaced basis functions, as shown in Fig 2.5. The coupling matrix $\mathbf{Z}^{\text{rad}}$ can be expressed explicitly as follows

$$\mathbf{Z}^{\text{rad}} = \begin{bmatrix} Z_{11} & Z_{12} & Z_{13} & \cdots & Z_{1N_x} \\ Z_{21} & Z_{22} & Z_{23} & \cdots & Z_{2N_x} \\ Z_{31} & Z_{32} & Z_{33} & \cdots & Z_{3N_x} \\ \vdots & \vdots & \vdots & \ddots & \vdots \\ Z_{N_x1} & Z_{N_x2} & Z_{N_x3} & \cdots & Z_{N_xN_x} \end{bmatrix}, \tag{2.22}$$

where Z_{ij} represents the projection of the scattered field, produced by the j^{th} basis function, onto the i^{th} test function. Due to the translational invariance of the free space Green's function $G_{fs}^{EJ}(\vec{r}-\vec{r}')$, the mutual coupling only depends on the relative distance between the basis functions. Hence, by defining $Z_{ij} = Z_{i-j}$, we obtain the following Toeplitz matrix

$$\mathbf{Z}^{\text{rad}} = \begin{bmatrix} Z_0 & Z_{-1} & Z_{-2} & \cdots & Z_{1-N_x} \\ Z_1 & Z_0 & Z_{-1} & \cdots & Z_{2-N_x} \\ Z_2 & Z_1 & Z_0 & \cdots & Z_{3-N_x} \\ \vdots & \vdots & \vdots & \ddots & \vdots \\ Z_{N_x-1} & Z_{N_x-2} & Z_{N_x-3} & \cdots & Z_0 \end{bmatrix}. \tag{2.23}$$

The Toeplitz structure in (2.23) allows us to characterize the entire coupling matrix $\mathbf{Z}^{\text{rad}}$ by storing only the first row and column of (2.23) into the following $(2N_x-1)$-by-1 vector

$$\dot{\mathbf{z}}^{\text{rad}} = \begin{bmatrix} Z_{N_x-1} & Z_{N_x-2} & \cdots & Z_1 & Z_0 & Z_{-1} & \cdots & Z_{2-N_x} & Z_{1-N_x} \end{bmatrix}^T, \tag{2.24}$$

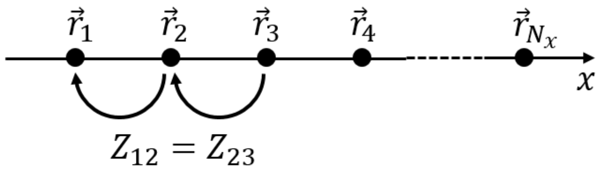

Figure 2.5: One-dimensional grid consisting of N_x equispaced basis functions

which reduces the memory requirements from N_x^2 to $2N_x - 1$. To understand how FFTs can be utilized to accelerate the matrix-vector product in (2.21), let us consider the product between $\mathbf{Z}^{\text{rad}}$ and $\mathbf{i}$, which can be expressed explicitly, as follows

$$\mathbf{v}^{\text{rad}} = \mathbf{Z}^{\text{rad}} \cdot \mathbf{i} = \begin{bmatrix} Z_0 & Z_{-1} & \cdots & Z_{1-N_x} \\ Z_1 & Z_0 & \cdots & Z_{2-N_x} \\ \vdots & \vdots & \ddots & \vdots \\ Z_{N_x-1} & Z_{N_x-2} & \cdots & Z_0 \end{bmatrix} \cdot \begin{bmatrix} i_1 \\ i_2 \\ \vdots \\ i_{N_x} \end{bmatrix} = \begin{bmatrix} Z_0 \cdot i_1 + Z_{-1} \cdot i_2 + \cdots + Z_{1-N_x} \cdot i_{N_x} \\ Z_1 \cdot i_1 + Z_0 \cdot i_2 + \cdots + Z_{2-N_x} \cdot i_{N_x} \\ \vdots \\ Z_{N_x-1} \cdot i_1 + Z_{N_x-2} \cdot i_2 + \cdots + Z_0 \cdot i_{N_x} \end{bmatrix}. \tag{2.25}$$

By examining (2.25), we can see that the first entry of the resulting vector $\mathbf{v}^{\text{rad}}$ can be represented as the multiplication of the vector $\mathbf{i}$ with the last N_x entries of $\dot{\mathbf{z}}^{\text{rad}}$, as shown below

$$\begin{array}{cccccccc} Z_{N_x-1} & Z_{N_x-2} & \cdots & Z_1 & Z_0 & Z_{-1} & \cdots & Z_{2-N_x} & Z_{1-N_x} \\ & & & & i_1 & i_2 & \cdots & i_{N_x-1} & i_{N_x} \end{array}$$

Similarly, the second entry of $\mathbf{v}^{\text{rad}}$ can be represented as the multiplication of the vector $\mathbf{i}$ with element Z_1 till element Z_{2-N_x}, as shown below

$$\begin{array}{cccccccc} Z_{N_x-1} & Z_{N_x-2} & \cdots & Z_1 & Z_0 & Z_{-1} & \cdots & Z_{2-N_x} & Z_{1-N_x} \\ & & & i_1 & i_2 & i_3 & \cdots & i_{N_x} & \end{array}$$

By repeating the above procedure N_x times, it becomes apparent that the matrix-vector product in (2.25) can be represented as an element-wise multiplication of the vector $\mathbf{i}$ with a backsliding window that selects the appropriate elements of the vector $\dot{\mathbf{z}}^{\text{rad}}$. This procedure can be represented as follows

$$\mathbf{v}^{\text{rad}} = [\text{flip}(\dot{\mathbf{z}}^{\text{rad}} * \text{flip}(\mathbf{i}^{\text{p}}))]_{1:N_x} \tag{2.26}$$

where $*$ denotes the circular convolution and $\mathbf{i}^{\text{p}}$ is the following $(2N_x - 1)$-by-1 vector

$$\mathbf{i}^{\text{p}} = \begin{bmatrix} 0 & \cdots & 0 & i_1 & i_2 & i_3 & \cdots & i_{N_x}, \end{bmatrix}^T. \tag{2.27}$$

which contains the vector $\mathbf{i}$, padded by $N_x - 1$ zeros. The subscript $1 : N_x$ in (2.26) indicates the selection of the first N_x elements of the resulting vector. Note that $\mathbf{i}^{\text{p}}$, as well as the resulting vector, have to be flipped before and after the circular convolution, due to the fact that we are using a backsliding window, instead of a forward sliding window, as in the usual definition of the circular convolution. Finally, the circular convolution in (2.26) can be equivalently calculated as an element-wise multiplication in the frequency domain, which results in the following expression

$$\mathbf{v} = \left[\text{flip}\left(\text{IFFT}\left(\text{FFT}(\dot{\mathbf{z}}^{\text{rad}}) \odot \text{FFT}(\text{flip}(\mathbf{i}^{\text{p}}))\right)\right)\right]_{1:N_x}, \tag{2.28}$$

where $\odot$ denotes the Hadamard product. This procedure reduces the computational complexity of the matrix-vector product in (2.21) from $\mathcal{O}(N_t^2)$ to $\mathcal{O}(N_t \log N_t)$. The overall procedure is depicted schematically in Fig 2.6.

2.5.2. Two dimensional geometry

In a two-dimensional geometry, the translational invariance of $G_{fs}^{EJ}(\vec{r} - \vec{r}')$ leads to the following block Toeplitz structure

$$\mathbf{Z}^{\text{rad}} = \begin{bmatrix} \mathbf{Z}_0 & \mathbf{Z}_{-1} & \mathbf{Z}_{-2} & \cdots & \mathbf{Z}_{1-N_y} \\ \mathbf{Z}_1 & \mathbf{Z}_0 & \mathbf{Z}_{-1} & \cdots & \mathbf{Z}_{2-N_y} \\ \mathbf{Z}_2 & \mathbf{Z}_1 & \mathbf{Z}_0 & \cdots & \mathbf{Z}_{3-N_y} \\ \vdots & \vdots & \vdots & \ddots & \vdots \\ \mathbf{Z}_{N_y-1} & \mathbf{Z}_{N_y-2} & \mathbf{Z}_{N_y-3} & \cdots & \mathbf{Z}_0 \end{bmatrix}, \tag{2.29}$$

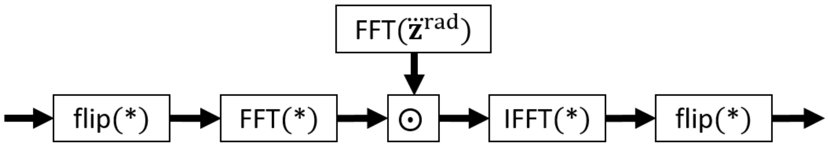

Figure 2.6: Equivalent procedure to calculate the matrix-vector product in (2.25)

where each block $\mathbf{Z}_i$ has a Toeplitz structure as in (2.23). Analogous to the one-dimensional case, the matrix in (2.29) can be characterized by the following $(2N_x-1)$-by-$(2N_y-1)$ matrix

$$\ddot{\mathbf{z}}^{\mathrm{rad}} = \begin{bmatrix} Z_{N_x-1,N_y-1} & \cdots & Z_{N_x-1,1} & Z_{N_x-1,0} & Z_{N_x-1,-1} & \cdots & Z_{1-N_x,1-N_y} \\ \vdots & \ddots & \vdots & \vdots & \vdots & \ddots & \vdots \\ Z_{1,N_y-1} & \cdots & Z_{1,1} & Z_{1,0} & Z_{-1,0} & \cdots & Z_{1,1-N_y} \\ Z_{0,N_y-1} & \cdots & Z_{1,1} & Z_{1,1} & Z_{1,1} & \cdots & Z_{0,1-N_y} \\ Z_{-1,N_y-1} & \cdots & Z_{1,1} & Z_{1,1} & Z_{1,1} & \cdots & Z_{-1,1-N_y} \\ \vdots & \ddots & \vdots & \vdots & \vdots & \ddots & \vdots \\ Z_{1-N_x,N_y-1} & \cdots & Z_{1-N_x,1} & Z_{1-N_x,0} & Z_{1-N_x,-1} & \cdots & Z_{1-N_x,1-N_y} \end{bmatrix}, \tag{2.30}$$

where the subscripts i and j of each entry Z_{ij}, refer to the difference in location in the x- and y-direction, between the source and observation point. Similarly, the vector $\mathbf{i}$ has to be rearranged into the following $(2N_x-1)$-by-$(2N_y-1)$ matrix, that is again appropriately zero-padded

$$\mathbf{i}^{\mathrm{p}} = \begin{bmatrix} 0 & 0 & \cdots & 0 & 0 & \cdots & 0 \\ 0 & 0 & \cdots & 0 & 0 & \cdots & 0 \\ \vdots & \vdots & \ddots & \vdots & \vdots & \ddots & \vdots \\ 0 & 0 & \cdots & i_{1,1} & i_{1,2} & \cdots & i_{1,N_y} \\ 0 & 0 & \cdots & i_{2,1} & i_{2,2} & \cdots & i_{2,N_y} \\ \vdots & \vdots & \ddots & \vdots & \vdots & \ddots & \vdots \\ 0 & 0 & \cdots & i_{N_x,1} & i_{N_x,2} & \cdots & i_{N_x,N_y} \end{bmatrix}. \tag{2.31}$$

The procedure for computing the matrix-vector products, remains essentially the same as in the 1-dimensional case. This time, however, the one-dimensional FFTs are replaced by 2-dimensional FFTs and the flips are performed over the rows and columns of the matrices. The overall procedure is still depicted in Fig. 2.6

2.5.3. Three dimensional geometry

In the 3-dimensional case, the translational invariance of the free space Green's function $G_{fs}^{EJ}(\vec{r}-\vec{r}\,')$ results in a coupling matrix $\mathbf{Z}^{\mathrm{rad}}$ with the same block-Toeplitz structure, shown in (2.29). This time, however, each block $\mathbf{Z}_i$ has itself a block-Toeplitz structure. In this case, $\mathbf{Z}^{\mathrm{rad}}$ can be be characterized by the $(2N_x-1)$-by-$(2N_y-1)$-by-$(2N_z-1)$ tensor $\dddot{\mathbf{z}}^{\mathrm{rad}}$, where the subscripts i, j and k of each entry $\dddot{z}^{\mathrm{rad}}_{i,j,k}$ represent the difference in location in the x-, y- and z-direction, between the source and observation point. The vector $\mathbf{i}$ has to be rearranged into the $(2N_x-1)$-by-$(2N_y-1)$-by-$(2N_z-1)$ tensor $\mathbf{i}^{\mathrm{p}}$, where the entries $i^{\mathrm{p}}_{i,j,k}$ contain the entries of $\mathbf{i}$, whenever $N_x \le i \le 2N_x-1$, $N_y \le j \le 2N_y-1$ and $N_z \le k \le 2N_z-1$, and are filled with zeros everywhere else. In the 3-dimensional case, the procedure to compute the matrix-vector products remains essentially the same as in the 1-dimensional case, apart from the fact that the 1-dimensional FFTs are replaced by 3-dimensional FFTs and the fact that the flips are now performed over all 3 dimensions of the corresponding tensors. Hence, the overall procedure is still depicted in Fig. 2.6.

Finally, we have to consider the polarizations of the basis and test functions. By taking into account all possible polarizations, the matrix-vector product in (2.21) can be expressed as follows

$$\mathbf{Z}^{\mathrm{rad}}\cdot\mathbf{i} = \begin{bmatrix} \mathbf{Z}_{xx} & \mathbf{Z}_{xy} & \mathbf{Z}_{xz} \\ \mathbf{Z}_{yx} & \mathbf{Z}_{yy} & \mathbf{Z}_{yz} \\ \mathbf{Z}_{zx} & \mathbf{Z}_{zy} & \mathbf{Z}_{zz} \end{bmatrix} \cdot \begin{bmatrix} \mathbf{i}_x \\ \mathbf{i}_y \\ \mathbf{i}_z \end{bmatrix} = \begin{bmatrix} \mathbf{Z}_{xx} \\ \mathbf{Z}_{yx} \\ \mathbf{Z}_{zx} \end{bmatrix} \cdot \mathbf{i}_x + \begin{bmatrix} \mathbf{Z}_{xy} \\ \mathbf{Z}_{yy} \\ \mathbf{Z}_{zy} \end{bmatrix} \cdot \mathbf{i}_y + \begin{bmatrix} \mathbf{Z}_{xz} \\ \mathbf{Z}_{yz} \\ \mathbf{Z}_{zz} \end{bmatrix} \cdot \mathbf{i}_z, \tag{2.32}$$

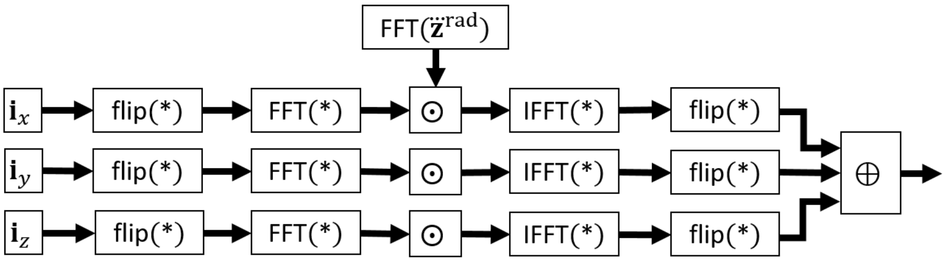

Figure 2.7: Overall procedure to calculate each row of the the matrix-vector product in (2.32)

where each of the blocks $\mathbf{Z}_{ij}$ has a block-Toeplitz structure, as described before. The multiplication of each component $\mathbf{Z}_{ij}$ of the coupling matrix with the corresponding component $\mathbf{i}_j$ of the current vector can be performed by the procedure depicted in Fig 2.6. By taking into account all possible polarizations, the overall procedure to compute each row of (2.32) is depicted schematically in Fig 2.7. Since the FFTs of $\mathbf{i}_j$ only have to be computed once per iteration, we have to compute in total 12 FFTs/IFFTs per iteration: three at the input and nine at the output. Moreover, it should be noted that the FFTs of $\dddot{\mathbf{z}}^{\mathrm{rad}}$ can be computed before entering the iterative procedure in Fig 2.4. Consequently, these FFTs do not add significantly to the total computation time.

2.5.4. Construction coupling tensor

The procedure described in the previous sections allows us to reduce the memory requirements from $9N_x^2N_y^2N_z^2$ to $9(2N_x-1)(2N_y-1)(2N_z-1)$. Moreover, the number of reaction integrals that have to be evaluated, is reduced by the same amount. However, we can further reduce both the memory requirements and the number of reaction integrals that have to be evaluated.

To understand how this can be done, let us consider again the one-dimensional grid, shown in Fig 2.5. Since the magnitude of the reaction integral only depends on the absolute distance between the basis and test function, the following relation holds

$$|Z_{-i}| = |Z_i|. \tag{2.33}$$

Consequently, the first N_x-1 entries of $\dot{\mathbf{z}}^{\mathrm{rad}}$ can be obtained from the last N_x-1 entries, by correcting the sign. The entire vector $\dot{\mathbf{z}}^{\mathrm{rad}}$ can then be obtained by only evaluating the last N_x entries. To this extent, we may fix the basis function to the first line segment, and sweep the test function over all of the line segments within the grid. In the 3-dimensional case, the entire tensor $\dddot{\mathbf{z}}^{\mathrm{rad}}$ can be obtained by only evaluating the entries $\dddot{\mathbf{z}}^{\mathrm{rad}}_{i,j,k}$ with $N_x \le i \le 2N_x-1$, $N_y \le i \le 2N_y-1$ and $N_z \le i \le 2N_z-1$. This can be done by fixing the basis function to the first voxel in the grid, and sweeping the test function over all of the voxels within the grid, as shown in Fig 2.8b. All other entries can then be obtained from these $N_xN_yN_z$ entries, by correcting the sign. This procedure reduces the memory requirements and the number of reaction integrals that have to be evaluated from $9(2N_x-1)(2N_y-1)(2N_z-1)$ to $9N_xN_yN_z$.

However, both the memory requirements and the number of reaction integrals that have to be evaluated, can be reduced even further. To understand how this can be done, let us consider the 2-dimensional grid shown in Fig. 2.8a, illustrated for x-polarized and y-polarized currents. The reaction integral between the x-polarized currents with index ① and ④ is equal to the reaction integral between the y-polarized currents with index ① and ②. A similar relation holds for the z-polarized currents. Therefore, the tensors $\dddot{\mathbf{z}}^{\mathrm{rad},yy}$ and $\dddot{\mathbf{z}}^{\mathrm{rad},zz}$, corresponding to the components $\mathbf{Z}_{yy}$ and $\mathbf{Z}_{zz}$, can be obtained from the tensor $\dddot{\mathbf{z}}^{\mathrm{rad},xx}$, corresponding to the component $\mathbf{Z}_{xx}$, by interchanging the dimensions of the tensor. Similarly, all tensors $\dddot{\mathbf{z}}^{\mathrm{rad},ij}$, corresponding to the cross-polarized components of $\mathbf{Z}^{\mathrm{rad}}$, can be obtained from the tensor $\dddot{\mathbf{z}}^{\mathrm{rad},xy}$, corresponding to $\mathbf{Z}_{xy}$, by interchanging the appropriate dimensions of the tensors. Therefore, we only have to compute $\dddot{\mathbf{z}}^{\mathrm{rad},xx}$ and $\dddot{\mathbf{z}}^{\mathrm{rad},xy}$, which reduces the memory requirements and the number of reaction integrals that have to be calculated from $9N_xN_yN_z$ to $2N_xN_yN_z$.

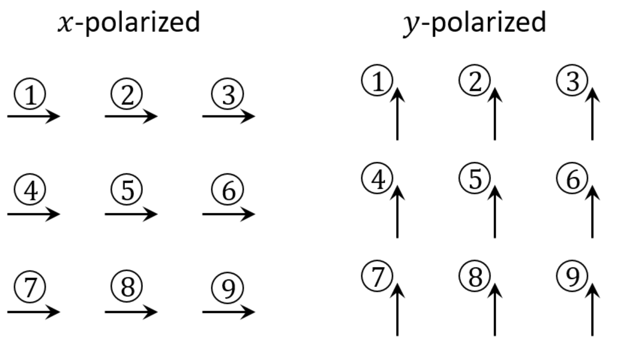

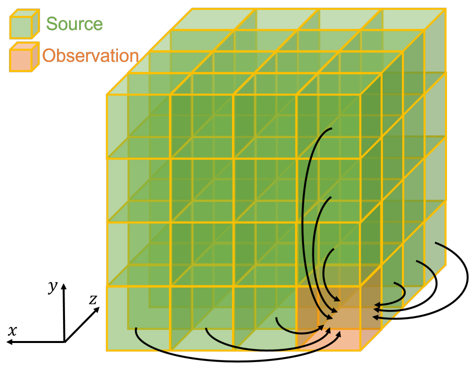

Figure 2.8: (a) Two-dimensional grid with x- and y-polarized currents and (b) construction of $\ddot{\mathbf{z}}^{\mathrm{rad}}$ by fixing the test function to the first voxel in the grid and sweeping the basis functions over all of the voxels within the grid

3

Optimization of the Volumetric Method of Moments

Chapter 2 has given an overview of the volumetric Method of Moments, developed in [14]. However, the MATLAB tool has not been optimized in terms of its computation time. Moreover, the V-MoM becomes less accurate when simulating geometries that are not well-represented by the structured grid. Finally, the numerical calculation of the reaction integrals, described in Section 2.3, is relatively inaccurate compared to alternative procedures, such as the method proposed in [23].

This chapter is structured as follows. First, Section 3.1 describes the optimization of the tool in terms of its computation time. Next, Section 3.2 introduces a procedure to enhance the accuracy of the solution, when simulating geometries that do not conform to the structured grid. Subsequently, Section 3.3 describes the implementation of an alternative numerical scheme to calculate the reaction integrals. This method is based on a reduction from volume to surface integrals, and allows us to calculate the reaction integrals up to machine precision. Finally, section 3.4 provides a validation of the optimized MATLAB tool.

3.1. Acceleration

3.1.1. Optimization of the FFT-based matrix-vector product

From the profiler in Fig 3.1, one can notice that the "flip" operations, performed before the FFTs and after the IFFTs of (2.28), take up a significant portion of the total computation time. However, these flips can be removed by taking advantage of the properties of the FFT and the IFFT. By considering the definitions of the FFT and the IFFT

$$I[k] = \mathrm{FFT}(i[n]) = \sum_{k=0}^{N-1} i[n] e^{-j\frac{2\pi k}{N}n} \tag{3.1}$$

$$i[n] = \mathrm{IFFT}(I[k]) = \frac{1}{N}\sum_{k=0}^{N-1} I[k] e^{j\frac{2\pi k}{N}n}, \tag{3.2}$$

one can notice that, apart from the scaling factor N, the two operators differ only in the sign at the exponent. Therefore, these two operators can be interchanged, if we reverse the order of the sequences. This property allows us to avoid the "flip" operations. However, since the vectors in (2.28) were extended to represent a circular convolution, one has to pay attention to the ordering of their entries. For the 1-dimensional case, the circular convolution is correctly represented if the vector of the currents is ordered as follows

$$\mathbf{i}^{\mathrm{p}} = \begin{bmatrix} i_{N_x} & 0 & \cdots & 0 & i_1 & i_2 & \cdots & i_{N_x-1} \end{bmatrix}^T, \tag{3.3}$$

where the entries from position 2 to position N_x+1 are padded with zeros. The matrix-vector product can then be calculated with the following expression

$$\mathbf{v} = \left[\mathrm{FFT}\left(\mathrm{FFT}(\dot{\boldsymbol{z}}^{\mathrm{rad}}) \odot \mathrm{IFFT}(\mathbf{i}^{\mathrm{p}})\right)\right]_{2:N_x+1}, \tag{3.4}$$

Function Name	Calls	Total Time (s)	Self Time* (s)	Total Time Plot (dark band = self time)
CGFFT_single_sphere_GlobVar_only_CG	1	33.969	0.001	
bicgstab	1	33.968	0.487	
sparfun\private\iterapp	8	33.477	0.003	
...ingle_sphere_GlobVar_only_CG>@(xx)multCG3DMask_GlobVar(xx)	8	33.475	0.006	
multCG3DMask_GlobVar	8	33.469	1.997	
multCG3DMask_GlobVar>calculateProduct3	8	10.686	8.739	
multCG3DMask_GlobVar>calculateProduct2	8	10.562	8.685	
multCG3DMask_GlobVar>calculateProduct1	8	10.224	8.238	
rot90	96	5.811	5.811	

17%

Figure 3.1: The profiler, which shows the contribution of each operation to the total computation time

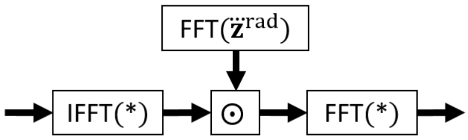

Figure 3.2: The modified procedure to calculate the matrix-vector product in (2.25)

where the entries from position 2 to position N_x+1 are retained. In the 2-dimensional case, the matrix $\mathbf{i}^{\text{p}}$ is ordered as follows

$$\mathbf{i}^{\text{p}} = \begin{bmatrix} i_{N_x,N_y} & 0 & \cdots & i_{N_x,1} & i_{N_x,2} & \cdots & i_{N_x,N_y-1} \\ 0 & 0 & \cdots & 0 & 0 & \cdots & 0 \\ \vdots & \vdots & \ddots & \vdots & \vdots & \ddots & \vdots \\ i_{1,1} & 0 & \cdots & i_{1,1} & i_{1,2} & \cdots & i_{1,N_y-1} \\ i_{1,2} & 0 & \cdots & i_{2,1} & i_{2,2} & \cdots & i_{1,N_y-1} \\ \vdots & \vdots & \ddots & \vdots & \vdots & \ddots & \vdots \\ i_{1,N_y-1} & \vdots & \ddots & i_{N_x-1,1} & i_{N_x-1,2} & \cdots & i_{N_x-1,N_y-1} \end{bmatrix}. \tag{3.5}$$

Finally, in the 3-dimensional case, the tensor $\mathbf{i}^{\text{p}}$, has "pages" defined as follows

$$\mathbf{i}^{\text{p}}_{\text{page},\text{n}_z} = \begin{bmatrix} i_{N_x,N_y,n_z} & 0 & \cdots & i_{N_x,1,n_z} & i_{N_x,2,n_z} & \cdots & i_{N_x,N_y-1,n_z} \\ 0 & 0 & \cdots & 0 & 0 & \cdots & 0 \\ \vdots & \vdots & \ddots & \vdots & \vdots & \ddots & \vdots \\ i_{1,1,n_z} & 0 & \cdots & i_{1,1,n_z} & i_{1,2,n_z} & \cdots & i_{1,N_y-1,n_z} \\ i_{1,2,n_z} & 0 & \cdots & i_{2,1,n_z} & i_{2,2,n_z} & \cdots & i_{1,N_y-1,n_z} \\ \vdots & \vdots & \ddots & \vdots & \vdots & \ddots & \vdots \\ i_{1,N_y-1,n_z} & \vdots & \ddots & i_{N_x-1,1,n_z} & i_{N_x-1,2,n_z} & \cdots & i_{N_x-1,N_y-1,n_z} \end{bmatrix}, \tag{3.6}$$

where the "pages" are ordered as in (3.3), with the "pages" being zero-padded from position 2 to position N_z+1. The modified procedure to calculate the matrix vector products in (2.25) is depicted schematically in Fig 3.2.

3.1.2. Optimization of the memory allocation

The second optimization of the developed MATLAB tool is related to the memory allocation during the simulation. As explained in Section 2.4, the V-MoM uses an iterative method, called the Conjugate Gradient (CG),

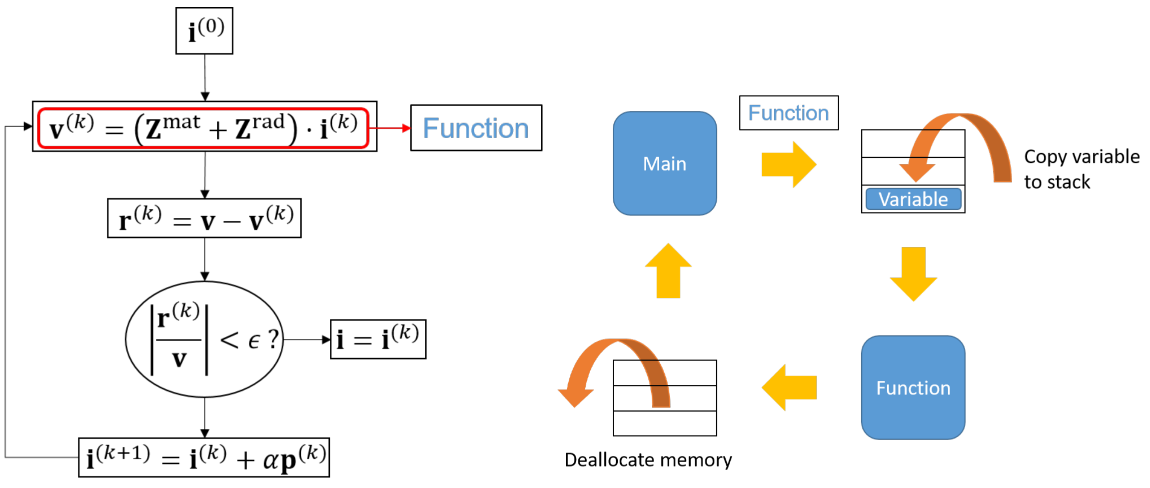

(a) (b)

Figure 3.3: (a) The iterative method, which calls a function to perform the matrix-vector products in (2.21) and (b) the process that is initiated by the function call

to find the solution of the matrix equation in (2.15). At each iteration, the CG calculates the residual error defined by (2.21). As explained in Section 2.5, the matrix-vector products in (2.21) are accelerated by utilizing FFTs/IFFTs. As shown in Fig 3.3a, this procedure requires a function call, which initiates the process illustrated in Fig 3.3b. After the function is called, a copy of its input variables is stored on the stack. Subsequently, the function executes its code, after which it returns control to the main code. Finally, the memory, used to store the input variables of the function, is de-allocated.

The input variables of the function in Fig 3.3b are the radiation tensors $\ddot{\mathbf{z}}^{\text{rad}}$, defined in Section 2.5.3. For large scale problems, these tensors may contain millions of entries. Moreover, the function is executed at every iteration of the CG. Consequently, allocation and de-allocation of memory may take a significant portion of the total computation time. Fortunately, this can be avoided by declaring the radiation tensors as global variables. Since global variables are visible throughout the entire program, both the main file and the function can operate on the same variable, which avoids unnecessary allocation and de-allocation of memory.

3.1.3. Reduction of the number of FFTs in the matrix-vector products

The third optimization is related to the specific implementation of the matrix-vector product shown in (2.32). By taking into account all possible polarizations, the overall procedure to compute each row of (2.32), is depicted schematically in Fig. 3.4a. As shown in Fig. 3.4a, this procedure starts by performing a 3-dimensional IFFT on the tensors $\mathbf{i}^{\text{p}}$, corresponding to the three components of the current vector $\mathbf{i}$. Next, element-wise multiplications are performed with the FFT of $\ddot{\mathbf{z}}^{\text{rad}}$. Subsequently, a 3-dimensional FFT is performed on each of the resulting tensors, after which the three components are added according to (2.32).

However, due to the linearity of the FFTs, we can swap the final summation with the FFTs, which reduces the total number of FFTs/IFFTs. Fig. 3.4a depicts the resulting procedure to compute each row of (2.32). Since the procedure in Fig. 3.4a is performed for each row of (2.32), the total amount of FFTs/IFFTs per iteration is reduced from 12 to six. Since the total computation time of the iterative solver is dominated by the FFTs, this reduction results in a significant acceleration of the MATLAB tool.

3.1.4. Time comparison

To assess the performance of the three optimizations described in Section 3.1.1 to 3.1.3, a cube has been simulated, having a length $L = \lambda_0/2$, constituted of a dielectric with permittivity $\varepsilon_r = 4$, excited by a plane wave propagating in the z-direction, as shown in Fig 3.5a. The cube has been discretized with voxels having a size $\Delta = L/61$ and $\Delta = L/101$. Figs 3.5b and 3.5c show the total computation time and the relative time reduction for the two discretization levels, where each row includes the optimizations of the rows above. The last row of Figs 3.5b and 3.5c show the total relative time reduction.

While the removed "flip" operations and the reduced number of FFTs result in a relative time reduction that is more or less independent of the discretization level, the finer discretization level benefits more from

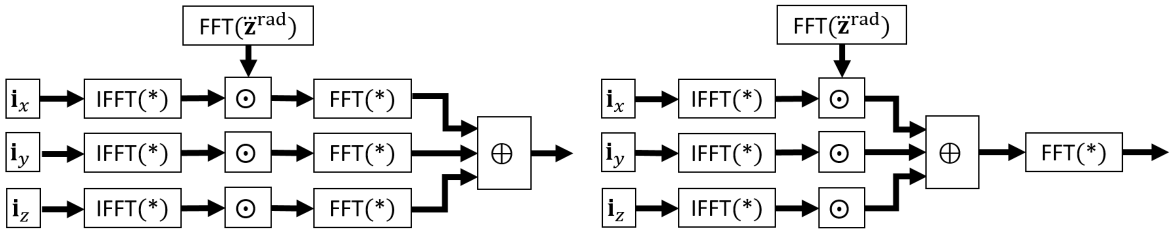

(a) (b)

Figure 3.4: Overall procedure to calculate each row of the matrix-vector product in (2.32) (a) before swapping the summation with the FFTs and (b) after swapping the summation with the FFTs

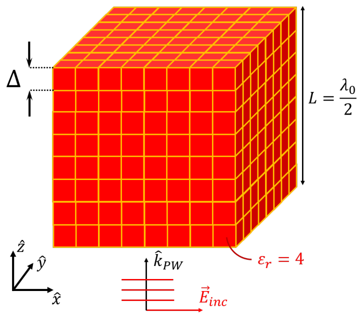

(a)

	Computation time	Relative time reduction
Original	21.15s	
Global variables	18.56s	12.2%
Removed flips	15.57s	16.1%
Reduced number FFTs	8.52s	45.2%
Total		59.7%

(b)

	Computation time	Relative time reduction
Original	132.69s	
Global variables	109.77s	17.3%
Removed flips	94.06s	14.3%
Reduced number FFTs	50.71s	46.1%
Total		61.8%

(c)

Figure 3.5: (a) Dielectric cube having a size $L = \lambda_0/2$ and permittivity $\varepsilon_r = 4$, illuminated by a plane wave propagating in the z-direction and computation time and relative time reduction for a discretization level of (b) $\Delta = L/61$ and (c) $\Delta = L/101$

the optimization of the memory allocation. This result could have been anticipated, since the tensors $\ddot{\mathbf{z}}^{\text{rad}}$ require much more memory, if the discretization level is refined. Nevertheless, the total relative time reduction is roughly 60% in both cases. Finally, it should be mentioned that the relative time reduction is independent of the simulated geometry since the optimizations described in Section 3.1.1 to 3.1.3 simply reduce the execution time of each iteration.

3.2. Tapered relative permittivities

As mentioned in Section 2.3, the V-MoM uses a structured grid to discretize the integral equation in (2.5). Despite its advantages in terms of memory requirements and computational complexity, the use of a structured grid results in a lower accuracy, when the geometry is not well-represented by the structured grid, as shown in the example of Fig 3.6a. In this case, the scatterer is approximated by the voxels whose centers are inside the scatterer, as shown in Fig 3.6b. This representation can be refined by dividing the voxels into three groups: the voxels that are entirely inside the scatterer, the voxels that are entirely outside the scatterer, and the voxels that are partially inside the scatterer, as shown in Fig 3.6c. While the voxels that are entirely outside of the scatterer receive the permitivity of the background $\varepsilon_{r,bg}$, and the voxels that are entirely inside the scatterer receive the local permittivity of the scatterer ε_r, the voxels that are partially inside the scatterer will receive a permittivity $\varepsilon_{r,av}$, defined as follows

$$\varepsilon_{r,av} = \frac{V_{\text{int}}}{V_t}\varepsilon_r + (1 - \frac{V_{\text{int}}}{V_t})\varepsilon_{r,bg} = \varepsilon_{r,bg} + \frac{V_{\text{int}}}{V_t}(\varepsilon_r - \varepsilon_{r,bg}), \tag{3.7}$$

which is an average of ε_r and ε_{bg}, where ε_r is weighted by the percentage of the voxel that is inside the scatterer and ε_{bg} is weighted by the percentage of the voxel that is outside the scatterer.

3.2.1. Validation

To compare the traditional procedure of Fig 3.6b to the refined approach of Fig 3.6c, both procedures have been used to simulate a dielectric sphere with radius $R = \lambda_0/2$ and permittivity $\varepsilon_r = 4$ and $\varepsilon_r = 8$. The sphere is illuminated by a plane wave with amplitude $\vec{E}_{\text{inc}} = 1\text{V/m}$, propagating in the z-direction, as shown in Fig 3.7a. In both cases, the sphere is discretized, using basis functions with $\Delta = \lambda_0/81$. The results have been compared

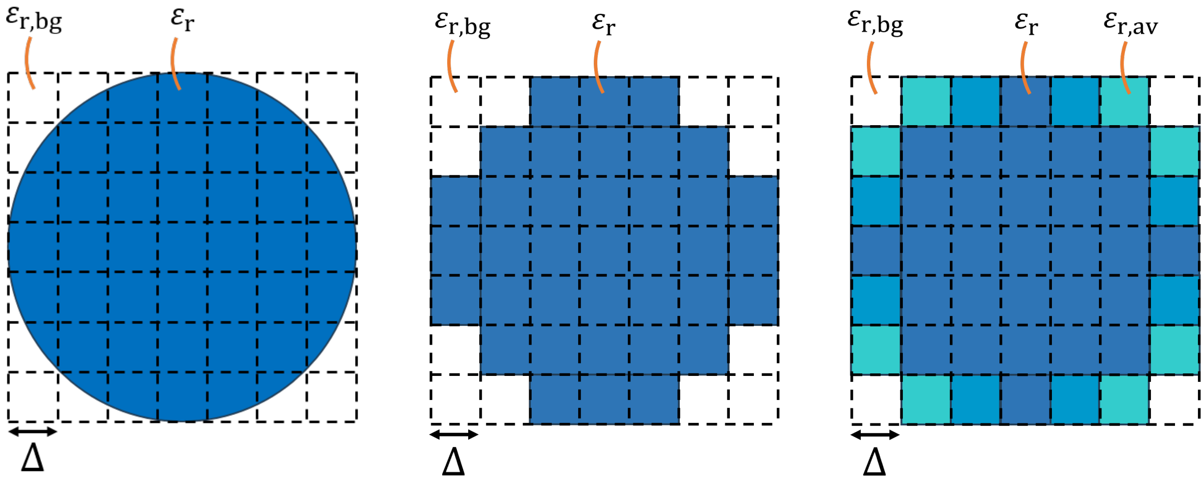

(a) (b) (c)

Figure 3.6: Grid with a non-rectangular geometry with (a) the original geometry, (b) the traditional approximation and (c) the refined approximation

to the analytical solution obtained by the Mie Series [33],[34].

Figs 3.7c and 3.7d show the magnitude of the total electric field $\vec{E}$ on the z-axis of the sphere, for $\varepsilon_r = 4$ and $\varepsilon_r = 8$, respectively. To assess the performance, the relative error with respect to the Mie series has been defined as follows

$$\epsilon_{\text{solver}} = \left\| \frac{|\vec{E}^t_{\text{solver}}| - |\vec{E}^t_{\text{Mie}}|}{|\vec{E}^t_{\text{Mie}}|} \right\|, \tag{3.8}$$

where $\|\cdot\|$ denotes the 2-norm of the vector and $|\vec{E}^t_{\text{solver}}|$ denotes the solution obtained from the V-MoM, using either of the two approaches. Fig. 3.7b shows the relative error ϵ_{solver}, obtained using both approaches. From Fig. 3.7b, it becomes clear that the geometry with $\varepsilon_r = 8$ benefits much more from the averaging. The reason is that this geometry is more resonant. Consequently, the solution is much more sensitive to changes in the geometry.

3.3. Improved evaluation of the reaction integrals

As mentioned in Section 2.3, obtaining the coupling matrix $\mathbf{Z}^{\text{rad}}$ requires the numerical evaluation of the reaction integrals in (2.14). However, the procedure, described in Section 2.3, is relatively inaccurate compared to alternative procedures. In particular, the reaction integrals can be reduced from volume integrals to surface integrals [23], which allows us to evaluate the resulting integrals up to machine precision. To this extent, we will have to slightly modify the integral equation in (2.5).

First, by multiplying (2.5) with $j\omega\varepsilon_0(\varepsilon_r(\vec{r}) - \varepsilon_{r,bg})$, we obtain the following expression

$$j\omega\varepsilon_0(\varepsilon_r(\vec{r}) - \varepsilon_{r,bg})\vec{E}^i(\vec{r}) = \vec{J}_{eq}(\vec{r}) - j\omega\varepsilon_0(\varepsilon_r(\vec{r}) - \varepsilon_{r,bg}) \iiint_V G^{EJ}_{fs}(\vec{r} - \vec{r}')\vec{J}_{eq}(\vec{r}')\, d\vec{r}'. \tag{3.9}$$

The free space Green's function $G^{EJ}_{fs}(\vec{r} - \vec{r}')$ can be expressed as follows

$$G^{EJ}_{fs}(\vec{r} - \vec{r}') = -j\omega\mu(I + \frac{1}{k_0^2}\nabla\nabla\cdot)G_0(\vec{r} - \vec{r}'), \tag{3.10}$$

where the scalar Green's function $G_0(\vec{r} - \vec{r}')$ is defined as

$$G_0(\vec{r} - \vec{r}') = \frac{e^{-jk_0|\vec{r} - \vec{r}'|}}{4\pi|\vec{r} - \vec{r}'|}. \tag{3.11}$$

By substituting (3.10) into (3.9), we obtain the following expression

$$j\omega\varepsilon_0(\varepsilon_r(\vec{r}) - \varepsilon_{r,bg})\vec{E}^i(\vec{r}) = \vec{J}_{eq}(\vec{r}) - (k_0^2 + \nabla\nabla\cdot) \iiint_V G_0(\vec{r} - \vec{r}')\vec{J}_{eq}(\vec{r}')\, d\vec{r}'. \tag{3.12}$$

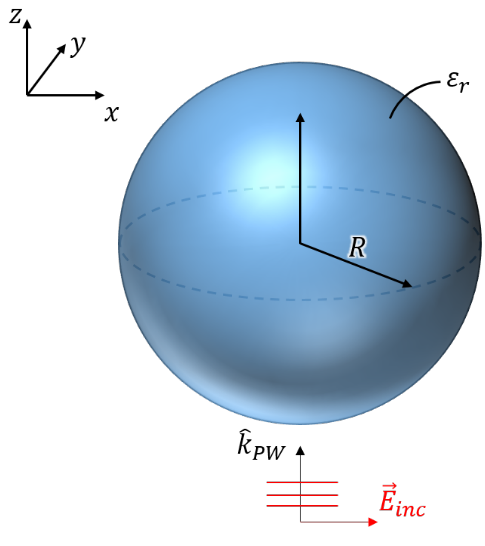

(a)

	V-MoM	V-MoM, tapered
$\varepsilon_r = 4$	1.27%	1.07%
$\varepsilon_r = 8$	16.76%	11.65%

(b)

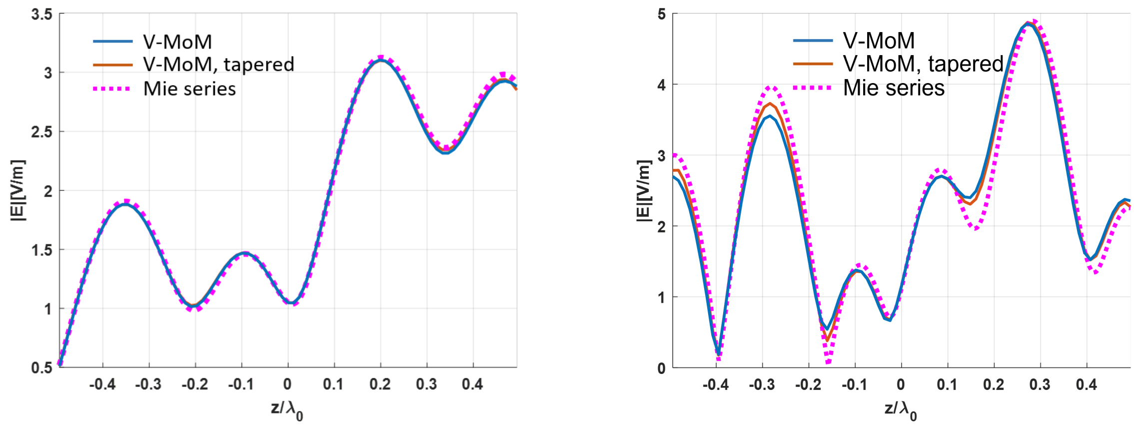

(c)

(d)

Figure 3.7: (a) Simulated geometry consisting of a dielectric sphere with radius $R = \lambda_0/2$ and permittivity $\varepsilon_r = 4$ or $\varepsilon_r = 8$, (b) comparison between the error committed by the traditional approach and the approach of averaging the permittivity, and magnitude of the electric field on the z-axis of the sphere for (c) a permittivity $\varepsilon_r = 4$, and (d) a permittivity $\varepsilon_r = 8$

(3.12) can be rewritten with the help of the following identity [35]

$$(k_0^2 + \nabla\nabla\cdot) \iiint_V G_0(\vec{r} - \vec{r}\,')\vec{J}_{\mathrm{eq}}(r')\,dr' = \nabla\times\nabla\times \iiint_V G_0(\vec{r} - \vec{r}\,')\vec{J}_{\mathrm{eq}}(r')\,dr' - \vec{J}_{\mathrm{eq}}(r). \tag{3.13}$$

By substituting (3.13) into (3.12), we obtain the following expression

$$j\omega\varepsilon_0(\varepsilon_r(\vec{r}) - \varepsilon_{r,bg})\vec{E}^i(\vec{r}) = \varepsilon_r(\vec{r})\vec{J}_{eq}(\vec{r}) - (\varepsilon_r(\vec{r}) - \varepsilon_{r,bg})\nabla\times\nabla\times \iiint_V G_0(\vec{r} - \vec{r}\,')\vec{J}_{eq}(\vec{r}\,')\,d\vec{r}\,'. \tag{3.14}$$

Finally, by dividing (3.14) by $\varepsilon_r(\vec{r})$, we obtain the following expression

$$j\omega\varepsilon_0 \frac{\varepsilon_r(\vec{r}) - \varepsilon_{r,bg}}{\varepsilon_r(\vec{r})}\vec{E}^i(\vec{r}) = \vec{J}_{eq}(\vec{r}) - \frac{\varepsilon_r(\vec{r}) - \varepsilon_{r,bg}}{\varepsilon_r(\vec{r})}\nabla\times\nabla\times \iiint_V G_0(\vec{r} - \vec{r}\,')\vec{J}_{eq}(\vec{r}\,')\,d\vec{r}\,'. \tag{3.15}$$

As shown in [23], this last step offers numerical advantages in the case of inhomogeneous scatterers. The integral equation in (3.15) has been discretized with the Galerkin method, using the following piece-wise constant basis functions

$$\vec{b}_n(\vec{r}) = \frac{1}{\sqrt{\Delta^3}}\mathrm{rect}\left(\frac{\vec{r} - \vec{r}_n\,'}{\Delta}\right)\hat{p}_n, \tag{3.16}$$

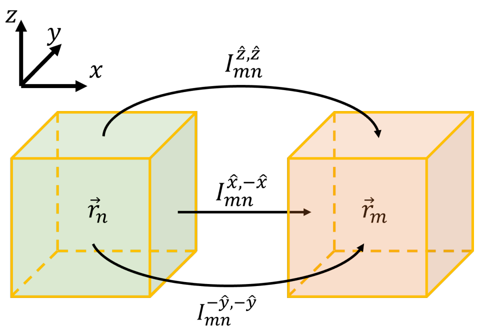

Figure 3.8: Reaction integrala between one face of basis function $\vec{b}_n(\vec{r}')$ and one face of test function $\vec{b}_m(\vec{r})$

where the normalization constant $1/\sqrt{\Delta^3}$ has been chosen such that the entries of the system matrix do not change significantly, when the discretization level is changed. By applying a Galerkin projection to (3.15), using the basis functions defined in (3.16), we obtain the following matrix equation

$$\mathbf{v} = (\mathbf{I} - \boldsymbol{Z}^{\text{mat}}\boldsymbol{Z}^{\text{rad}})\mathbf{i}, \tag{3.17}$$

where $\mathbf{I}$ denotes the identity matrix. The m^{th} entry of the excitation vector $\mathbf{v}$ is given by the following expression

$$v_m = \langle j\omega\varepsilon_0 \frac{\varepsilon_r(\vec{r}) - \varepsilon_{r,bg}}{\varepsilon_r(\vec{r})}\vec{E}^i(\vec{r}), \vec{b}_m(\vec{r})\rangle_V = j\omega\varepsilon_0 \frac{\varepsilon_r(\vec{r}) - \varepsilon_{r,bg}}{\varepsilon_r(\vec{r})}\vec{E}^i \cdot \hat{p}_m\sqrt{\Delta^3} = j\omega\varepsilon_0 \frac{\varepsilon_r(\vec{r}) - \varepsilon_{r,bg}}{\varepsilon_r(\vec{r})} v_m\sqrt{\Delta}, \tag{3.18}$$

where v_m denotes the voltage impressed on the m^{th} basis function. The diagonal matrix $\boldsymbol{Z}^{\text{mat}}$ is defined as follows

$$\boldsymbol{Z}^{\text{mat}} = \operatorname{diag}\left(\frac{\varepsilon_{r,1} - \varepsilon_{r,bg}}{\varepsilon_{r,1}}, \frac{\varepsilon_{r,2} - \varepsilon_{r,bg}}{\varepsilon_{r,2}}, \ldots, \frac{\varepsilon_{r,N_t} - \varepsilon_{r,bg}}{\varepsilon_{r,N_t}}\right), \tag{3.19}$$

and the entries of $\mathbf{Z}^{\text{rad}}$ are given by the following expression

$$Z_{mn}^{\text{rad}} = \iiint_V \left(\nabla \times \nabla \times \iiint_V G_0(\vec{r} - \vec{r}')\vec{b}_n(\vec{r}')\,d\vec{r}'\right) \cdot \vec{b}_m(\vec{r})\,d\vec{r}. \tag{3.20}$$

As shown in Appendix A, the volume integrals in (3.20) can be reduced to the following form

$$Z_{mn}^{\text{rad}} = \frac{1}{\Delta^3}\sum_k \sum_l (\hat{n}_k \times \hat{p}_m) \cdot (\hat{n}_l \times \hat{p}_n) I_{mn}^{kl}, \tag{3.21}$$

where the surface integral I_{mn}^{kl} can be expressed as follows

$$I_{mn}^{kl} = \iint_{S_k} \iint_{S_l} G_0(\vec{r} - \vec{r}')\,d\vec{r}'\,d\vec{r}, \tag{3.22}$$

which is the reaction integral between one face of basis function $\vec{b}_n(\vec{r}')$, and one face of test function $\vec{b}_m(\vec{r})$, as illustrated in (3.8), where k and l denote the indexes of the faces of the test and basis function, respectively. The summation in (3.21) is performed over each face of the basis and test function, where $\hat{n}_k$ and $\hat{n}_l$ denote the corresponding normal vectors of each of the faces, i.e. $\hat{n}_k, \hat{n}_l \in \{-\hat{x}, \hat{x}, -\hat{y}, \hat{y}, -\hat{z}, \hat{z}\}$.

The reduction from volume to surface integrals has three distinct advantages. First of all, the 6D-integrals in (2.14) have been reduced to 4D-integrals. Second, the integrand in (3.22) contains the scalar Green's function $G_0(\vec{r} - \vec{r}')$, which is numerically less expensive to evaluate than the Dyadic Green's function $G_{fs}^{EJ}(\vec{r} - \vec{r}')$. Finally, the $1/R^3$-singularity in $G_{fs}^{EJ}(\vec{r} - \vec{r}')$ has been reduced to a $1/R$-singularity, which can be evaluated efficiently by the pre-existing tool DIRECTFN, introduced in [36] and [37]. Moreover, this approach allows us to take into account the singularities on the face-, edge- and vertex-adjacent voxels, which were not taken into account, with the previous integration technique, presented in Section 2.3.

3.3.1. Construction tensor

As explained in Section 2.3, the entire coupling matrix $\mathbf{Z}^{\text{rad}}$ can be characterized by two tensors $\dddot{\boldsymbol{z}}^{\text{rad},xx}$ and $\dddot{\boldsymbol{z}}^{\text{rad},xy}$, corresponding to the $\mathbf{Z}_{xx}$ and $\mathbf{Z}_{xy}$ components of the coupling matrix. We will first explain how to construct the tensor $\dddot{\boldsymbol{z}}^{\text{rad},xx}$.

By substituting $\hat{p}_n = \hat{x}$ and $\hat{p}_m = \hat{x}$ into (3.21), we obtain the following expression

$$Z_{mn}^{\text{rad}} = \frac{1}{\Delta^3} \sum_k \sum_l (\hat{n}_k \times \hat{x}) \cdot (\hat{n}_l \times \hat{x}) I_{mn}^{kl} \tag{3.23}$$

The terms in (3.23) are only nonzero whenever $\hat{n}_k$ and $\hat{n}_l$ are both parallel to $\pm\hat{y}$ or $\pm\hat{z}$. Therefore, the summation in (3.23) has 8 nonzero terms. However, the integrals I_{mn}^{kl} contain many duplicates. To understand this observation, let us consider two adjacent voxels, as shown in Fig 3.9a. $I_{11}^{-\hat{z},\hat{z}}$ represents the reaction integral between two opposite faces of the same voxel. On the other hand, $I_{21}^{\hat{z},\hat{z}}$ represents the reaction integral between the faces of two adjacent voxels with the same normal vectors, i.e. $n_k = n_l = \hat{z}$. Since the distance between the faces are both equal to Δ and the normal vectors are oriented in the same way, the two integrals are numerically equivalent. Moreover, the reaction integrals between faces with normal vectors $\hat{n}_k = \pm\hat{y}$ and $\hat{n}_l = \pm\hat{y}$ can be constructed from the reaction integrals between faces with normal vectors $\hat{n}_k = \pm\hat{z}$ and $\hat{n}_l = \pm\hat{z}$, analogous to the way in which $\dddot{\boldsymbol{z}}^{\text{rad},yy}$ and $\dddot{\boldsymbol{z}}^{\text{rad},zz}$ could be constructed from $\dddot{\boldsymbol{z}}^{\text{rad},xx}$.

To avoid performing the same integral multiple times, we will first define $\boldsymbol{z}^{\text{surf},\hat{z},\hat{z}}$ as the tensor, obtained by fixing the observation domain to the first face with $\hat{n}_k = \hat{z}$ and sweeping the source domain over all of the faces with $\hat{n}_l = \hat{z}$ within the grid, as illustrated in Fig 3.9b. Since all of the nonzero terms in (3.23) can be constructed from the term with $\hat{n}_k = \hat{z}$ and $\hat{n}_l = \hat{z}$, the tensor $\dddot{\boldsymbol{z}}^{\text{rad},xx}$ can be constructed from $\boldsymbol{z}^{\text{surf},\hat{z},\hat{z}}$ as follows

$$\dddot{\boldsymbol{z}}_{i,j,k}^{\text{rad},xx} = 2\boldsymbol{z}_{i,j,k}^{\text{surf},\hat{z},\hat{z}} - \boldsymbol{z}_{i,j,k+1}^{\text{surf},\hat{z},\hat{z}} - \boldsymbol{z}_{i,j,k-1}^{\text{surf},\hat{z},\hat{z}} + 2\boldsymbol{z}_{i,k,j}^{\text{surf},\hat{z},\hat{z}} - \boldsymbol{z}_{i,k+1,j}^{\text{surf},\hat{z},\hat{z}} - \boldsymbol{z}_{i,k-1,j}^{\text{surf},\hat{z},\hat{z}}, \tag{3.24}$$

where the subscript $k+1$ denotes a shift along $\hat{z}$ of all the entries in the tensor and the subscript i,k,j indicates that the y- and z-dimension have been interchanged. While the first three terms on the right-hand side of (3.24) represent the interactions between all of the faces with $\hat{n}_k = \pm\hat{z}$ and $\hat{n}_l = \pm\hat{z}$, the last three terms represent the interactions between all of the faces with $\hat{n}_k = \pm\hat{y}$ and $\hat{n}_l = \pm\hat{y}$, which can be recognized from the fact that the y- and z-dimension of the tensor have been interchanged.

Let us now consider the tensor $\dddot{\boldsymbol{z}}^{\text{rad},xy}$, corresponding to the $\mathbf{Z}_{xy}$ component of the coupling matrix. By substituting $\hat{p}_m = \hat{x}$ and $\hat{p}_n = \hat{y}$ into (3.21), we obtain the following expression

$$Z_{mn}^{\text{rad}} = \sum_k \sum_l (\hat{n}_k \times \hat{x}) \cdot (\hat{n}_l \times \hat{y}) I_{mn}^{kl} \tag{3.25}$$

The terms in (3.25) are only nonzero whenever $\hat{n}_k = \pm\hat{x}$ and $\hat{n}_l = \pm\hat{y}$. Therefore, the summation in (3.25) has 4 nonzero terms. Similar to before, we will first define $\boldsymbol{z}^{\text{surf},\hat{y},\hat{x}}$, as the tensor obtained by fixing the observation domain to the first face with normal vector $\hat{n}_l = \hat{y}$ and sweeping the source domain over all of the faces with normal vector $\hat{n}_k = \hat{x}$. Since all of the nonzero terms in (3.25) can be obtained from the term with $\hat{n}_l = \hat{y}$ and $\hat{n}_k = \hat{x}$, the tensor $\dddot{\boldsymbol{z}}^{\text{rad},xy}$ can be constructed from $\boldsymbol{z}^{\text{surf},\hat{y},\hat{x}}$ as follows

$$\dddot{\boldsymbol{z}}_{i,j,k}^{\text{rad},xy} = -\boldsymbol{z}_{i,j,k}^{\text{surf},\hat{y},\hat{x}} + \boldsymbol{z}_{i,j+1,k}^{\text{surf},\hat{y},\hat{x}} + \boldsymbol{z}_{i-1,j,k}^{\text{surf},\hat{y},\hat{x}} - \boldsymbol{z}_{i-1,j+1,k}^{\text{surf},\hat{y},\hat{x}}, \tag{3.26}$$

where the subscripts $j+1$ and $i-1$ denote a shift along $\hat{y}$ and $\hat{x}$ of all the entries in the tensor.

3.3.2. Evaluation reaction integrals

To obtain the tensors $\boldsymbol{z}^{\text{surf},\hat{z},\hat{z}}$ and $\boldsymbol{z}^{\text{surf},\hat{y},\hat{x}}$, we have to evaluate the reaction integrals between the corresponding faces of the voxels. These integrals can be divided into four groups as shown in Figs 3.10a-3.10d. The first group is illustrated in Fig 3.10a and consists of non-adjacent faces. Since the faces are separated, the singularity of the scalar Green's function $G_0(\vec{r}-\vec{r}')$ is not encountered on the integration domain. The second group is illustrated in Fig 3.10b and consists of coinciding faces. In this case, the singularity of $G_0(\vec{r}-\vec{r}')$ is encountered whenever $\vec{r} = \vec{r}'$. The third group is illustrated in Fig 3.10c and consists of edge-adjacent faces. In this case the singularity of $G_0(\vec{r}-\vec{r}')$ is encountered at the coinciding edge of the two faces. The last group is illustrated in Fig 3.10d and consists of vertex-adjacent faces. In this case the singularity of $G_0(\vec{r}-\vec{r}')$ is encountered at the coinciding vertex of the two faces.

The reaction integrals corresponding to the non-adjacent faces have been evaluated numerically using the Gauss-Legendre quadrature [38], as explained in Appendix B. On the other hand, the reaction integrals between coinciding faces, edge-adjacent faces and vertex-adjacent faces can be evaluated using the pre-existing

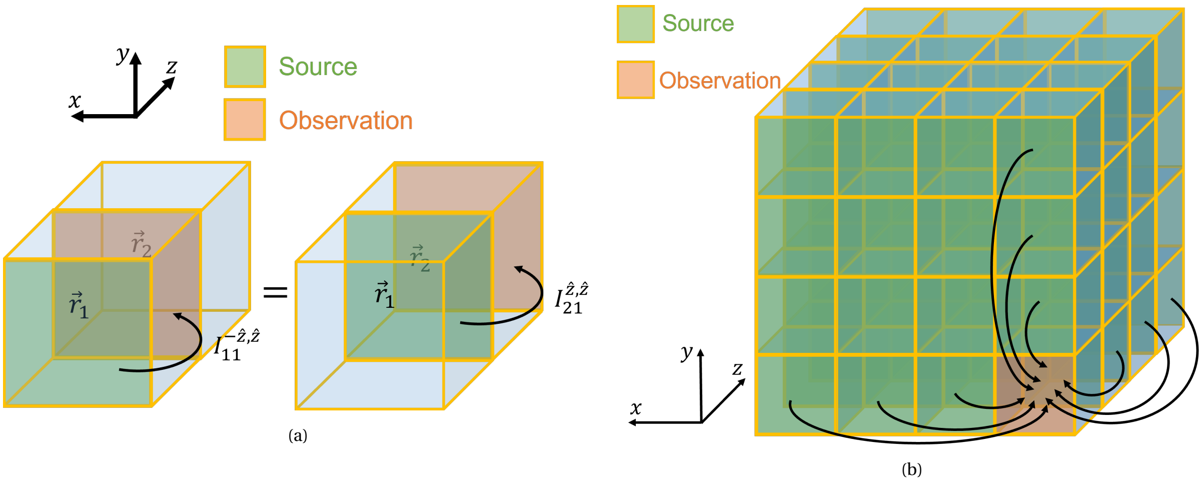

Figure 3.9: (a) The reaction integral between two opposite faces of the same voxel and the reaction integral between the faces of two adjacent voxels with the same normal vectors and (b) the construction of $z^{\text{surf},\hat{z},\hat{z}}$ by fixing the observation domain to the first face with $\hat{n}_k = \hat{z}$ and sweeping the source domain over all of the faces with $\hat{n}_l = \hat{z}$ within the grid

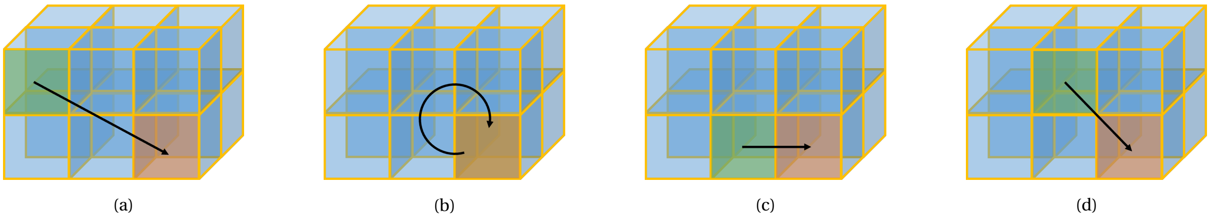

Figure 3.10: Reaction integral between (a) non-adjacent faces, (b) coinciding faces, (c) edge-adjacent faces and (d) vertex-adjacent faces

tool DIRECTFN, introduced in [36] and [37]. This tool is based on a direct integration method, in which the singularity of $G_0(\vec{r}-\vec{r}')$ is treated by a change from Cartesian to polar coordinates. With this transformation, the $1/R$-singularity is cancelled by the Jacobian.

To choose an appropriate number of integration points, we have plotted the numerical convergence of the integration in Figs. 3.11a and 3.11b. Fig. 3.11a shows the convergence in the case of non-adjacent faces versus the number of integration points for different distances between the source and observation domain. As shown in Fig. 3.11a, the reaction integrals converge faster if the distance between the source and observation domain is increased. For this reason, the number of integration points per integral has been chosen according to the staircase pattern in Fig 3.11c. This pattern has been chosen to reach machine precision with the minimal required computational effort. Fig 3.11b shows the convergence in the case of coinciding faces, edge-adjacent faces or vertex-adjacent faces. Similar to before, the number of integration points per integral has been chosen to reach machine precision with the minimal required computational effort.

3.3.3. Comparison

To compare the performance of the procedure, described in the previous sections, to the original procedure in Section 2.3, we have simulated a dielectric sphere with radius $R = \lambda_0/4$ and permittivity $\varepsilon_r = 4.3$ and $\varepsilon_r = 12.85$. The sphere is illuminated by a plane wave with amplitude $\vec{E}_{\text{inc}} = 1\text{V/m}$, propagating in the z-direction, as shown in Fig 3.7a. Moreover, the V-MoM uses a discretization level of $\Delta = \lambda_0/81$ in both cases.

To compare the accuracy of the reaction integrals, we have defined the relative error committed by the original procedure as follows

$$\epsilon_{\text{original}} = \left\| \frac{\dddot{\mathbf{z}}^{\text{rad}}_{\text{original}} - \dddot{\mathbf{z}}^{\text{rad}}_{\text{optimized}}}{\dddot{\mathbf{z}}^{\text{rad}}_{\text{optimized}}} \right\|, \tag{3.27}$$

where $\dddot{\mathbf{z}}^{\text{rad}}_{\text{original}}$ denotes the radiation tensor, obtained by the original procedure in Section 2.3 and $\dddot{\mathbf{z}}^{\text{rad}}_{\text{optimized}}$ denotes the radiation tensor, obtained by the new procedure described in the previous sections.

Fig. 3.12 shows the relative error of $\dddot{\mathbf{z}}^{\text{rad}}_{\text{original}}$ versus the distance between the basis and test function. While

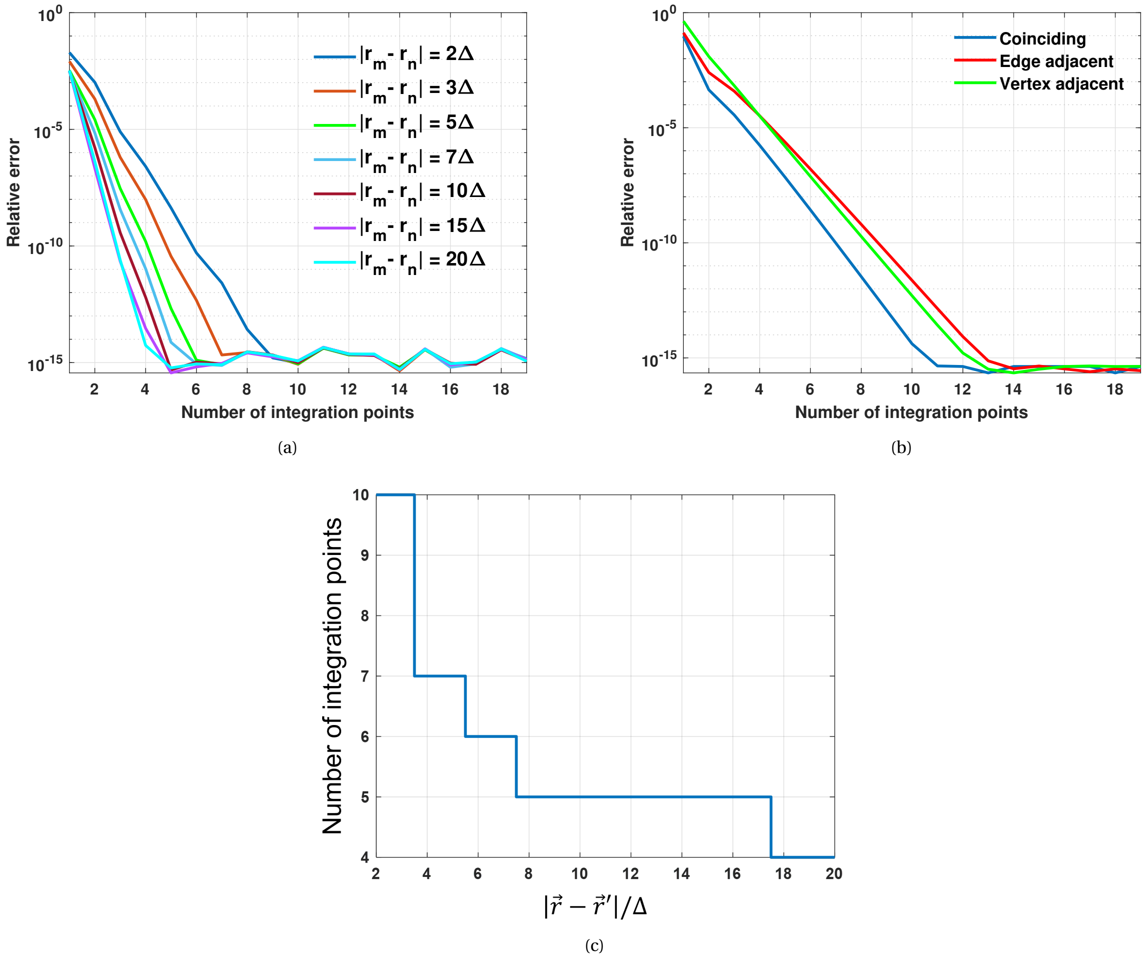

Figure 3.11: Convergence of the reaction integrals (a) between non-adjacent faces and (b) between adjacent or coinciding faces and (c) number of integration points used for the numerical integration versus distance between the source and observation domain

the first term of $\ddot{\mathbf{z}}^{\text{rad}}_{\text{original}}$ is relatively accurate, the second term commits an error of about 18%. This observation can be understood as follows. The first term of $\ddot{\mathbf{z}}^{\text{rad}}_{\text{original}}$ represents the self-reaction integral which contains a singularity whenever $\vec{r} = \vec{r}'$. In Section 2.3 this singularity has been extracted, using the procedure presented in [30] and [31], which led to the expression in (2.18). On the other hand, the second term of $\ddot{\mathbf{z}}^{\text{rad}}_{\text{original}}$ represents the reaction integral between two adjacent voxels, which contains a singularity at the coinciding face of the two voxels. Since this singularity has not been treated by the procedure, presented in Section 2.3, a significant error is committed in the evaluation of the second term of $\ddot{\mathbf{z}}^{\text{rad}}_{\text{original}}$.

Figs 3.13a and 3.13b show the magnitude of the total electric field $\vec{E}$ on the z-axis of the sphere, for $\varepsilon_r = 4.3$ and $\varepsilon_r = 12.85$, respectively. From Figs 3.13a and 3.13b it becomes apparent that the requirements on the accuracy of the integrals become much more severe, when the permittivity of the scatterer increases. Figs. 3.13a and 3.13b show the numerical convergence of the iterative solver, for $\varepsilon_r = 4.3$ and $\varepsilon_r = 12.85$, respectively. While the convergence follows a similar trend for both procedures in the case $\varepsilon_r = 4.3$, the oscillations ,introduced by the inaccuracy of the integrals, have a tremendous impact on the numerical convergence in the case $\varepsilon_r = 12.85$. Finally, it should be noted that the computation time of the reaction integrals was negligible compared to the time of the iterative solver in both cases.

3.4. Validation

In this section, we will validate the final code of the optimized V-MoM and compare its performance with CST [39]. First, the V-MoM is validated against the Mie Series [33],[34]. In the formulation of the Mie Series, the incident field and the scattered field are expanded in terms of spherical harmonics, after which the expan-

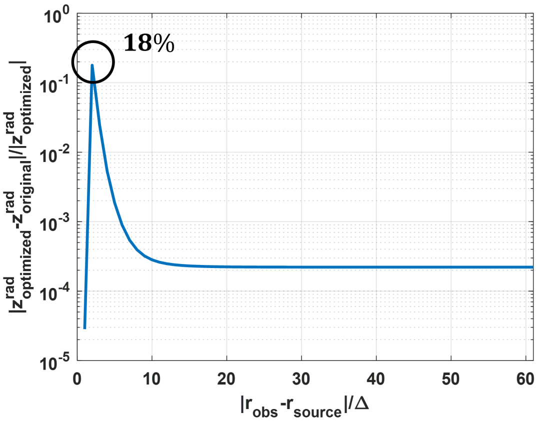

Figure 3.12: Relative error committed by the original procedure, described in Section 2.3 versus the distance between the source and observation domain

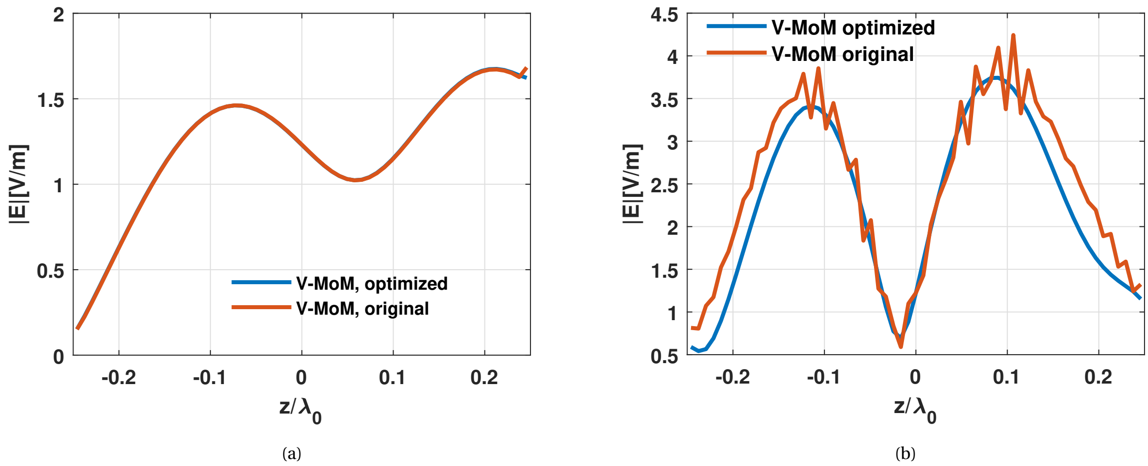

Figure 3.13: Magnitude of the total electric field $\vec{E}$ on the z-axis of the sphere, for (a) $\epsilon_r = 4.3$ and (b) $\epsilon_r = 12.85$

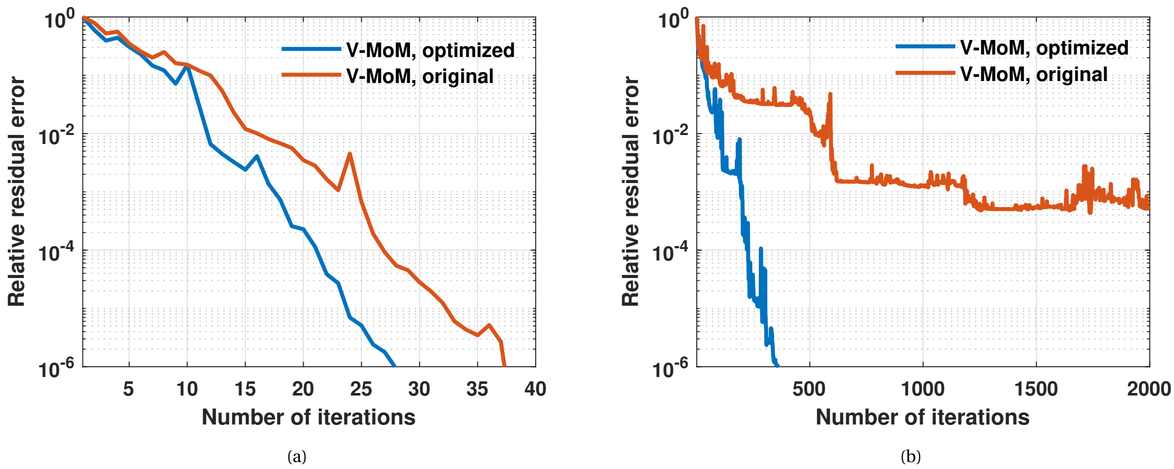

Figure 3.14: Numerical convergence of the iterative solver, for (a) $\epsilon_r = 4.3$ and (b) $\epsilon_r = 12.85$

sion coefficients are obtained by enforcing the boundary conditions on the surface of the sphere. Since this formulation provides an analytical solution it will serve as a reliable validation of the tool. Next, the perfor-

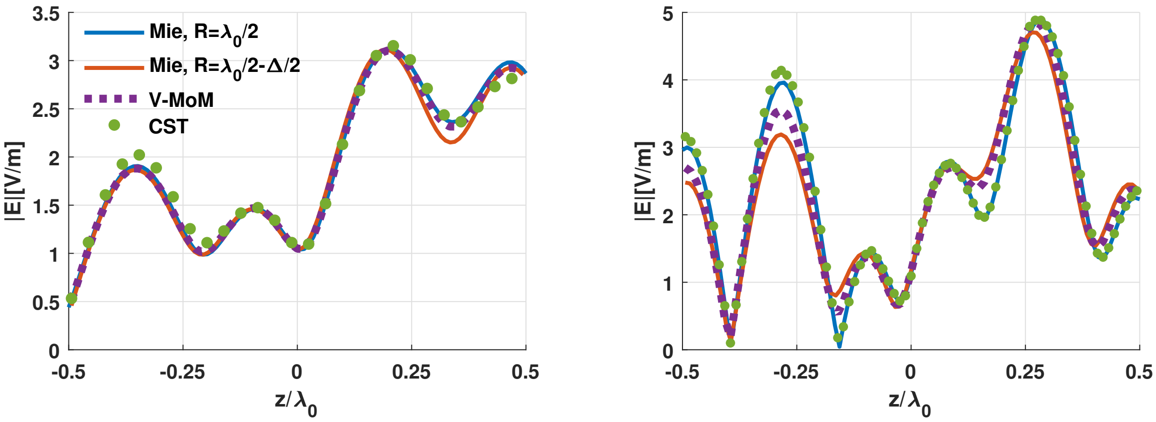

(a)

(b)

	V-MoM	CST
Relative error w.r.t. Mie Series	1.27%	4.1%
Computation time	39.4s	88s

(c)

Figure 3.15: Magnitude of the total electric field $\vec{E}$ on the z-axis of the sphere, for (a) $\varepsilon_r = 4$ and (b) $\varepsilon_r = 8$ and (c) a comparison between CST and the V-MoM in terms of accuracy and computation time

mance of the V-MoM is compared to the performance of CST, by simulating a realistic scenario consisting of a hemispherical lens, excited by a $\lambda_0/2$ dipole.

3.4.1. Mie Series

The V-MoM has been validated against the Mie Series [33],[34] by simulating a dielectric sphere with radius $R = \lambda_0/2$ and permittivity $\varepsilon_r = 4$ and $\varepsilon_r = 8$. The sphere is illuminated by a plane wave with amplitude $\vec{E}_{\text{inc}} = 1\text{V/m}$, propagating in the z-direction, as shown in Fig 3.7a. In both cases, the sphere is discretized, using basis functions with $\Delta = \lambda_0/81$. Moreover, the performance of the V-MoM has been compared to the performance of CST. To compare the accuracy of the V-MoM to the accuracy of CST, the relative error with respect to the Mie Series has been defined as in (3.8). During the CST simulation, the frequency domain solver has been used, because of the resonant nature of the problem.

Figs 3.15a and 3.15c show the magnitude of the total electric field $\vec{E}$ on the z-axis of the sphere, for $\varepsilon_r = 4$ and $\varepsilon_r = 8$, respectively. In both cases, the error committed by the V-MoM is within the discretization tolerance. Fig. 3.15c shows the comparison between the relative error committed by the V-MoM and the relative error committed by CST as well as the comparison between the computation time of both solvers. Fig. 3.15c shows that the V-MoM outperforms CST in terms of both accuracy and computation time. It should be noted that the calculation of the reaction integrals of the V-MoM took an additional $7s$. However, since these integrals can be reused, the computation time of the reaction integrals is not very relevant.

3.4.2. Lens antenna

The performance of the V-MoM has been compared to the performance of CST by simulating a realistic scenario consisting of a hemispherical dielectric lens with permittivity $\varepsilon_r = 2.34$. The lens has been simulated both for a plane wave excitation and with a $\lambda_0/2$ dipole as the feeding element. The hemispherical lens is constructed by placing a cylinder with radius $R = 1\text{mm}$ and height $H = 0.4\text{mm}$ below a hemisphere with radius $R = 1\text{mm}$. The $\lambda_0/2$ dipole has a square cross-section having a width and height $w = h = \lambda_0/20$ and a gap of length $\lambda_0/10$. In both cases, the lens has been discretized, using basis function with $\Delta = \lambda_0/20$. Both geometries are illustrated in Figs. 3.16a and 3.16b.

Figs 3.17a and 3.17b show the magnitude of the total electric field inside the lens on the XZ-plane for a plane wave excitation at a frequency $f = 294\text{GHz}$. While Fig. 3.17a shows the field, obtained using the V-MoM, Fig. 3.17b shows the field, obtained using CST. Figs. 3.17a and 3.17b show that the field obtained by the V-MoM and the field obtained by CST are in excellent agreement. Figs 3.18a and 3.18b show the magnitude of the

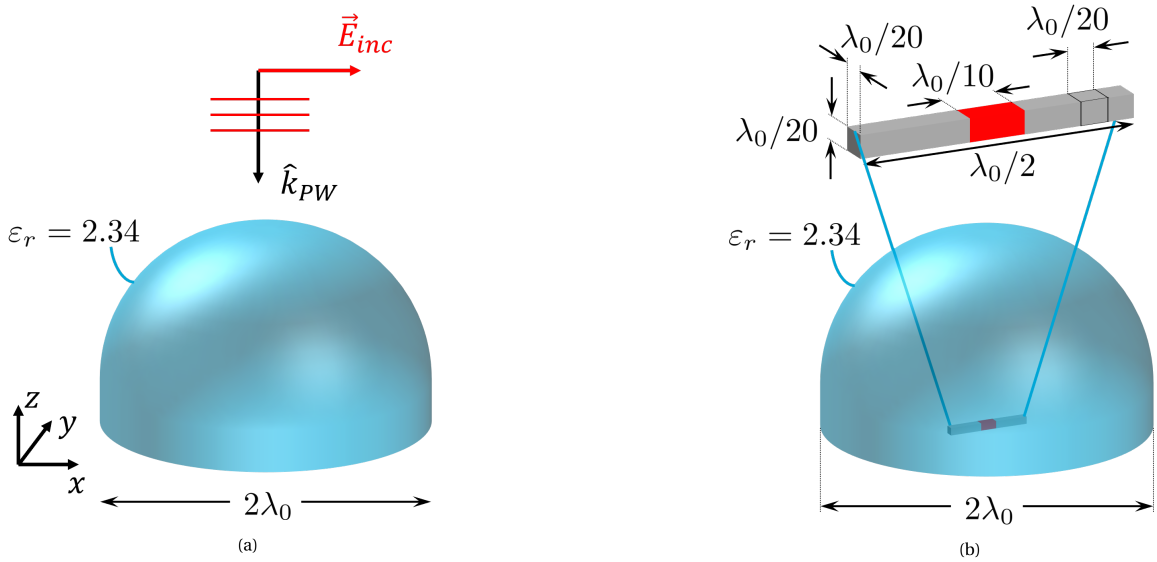

Figure 3.16: Simulated geometry consisting of a $2\lambda_0$ hemispherical lens with permittivity $\varepsilon_r = 2.34$ (a) excited by a plane wave and (b) excited by a $\lambda_0/2$ dipole

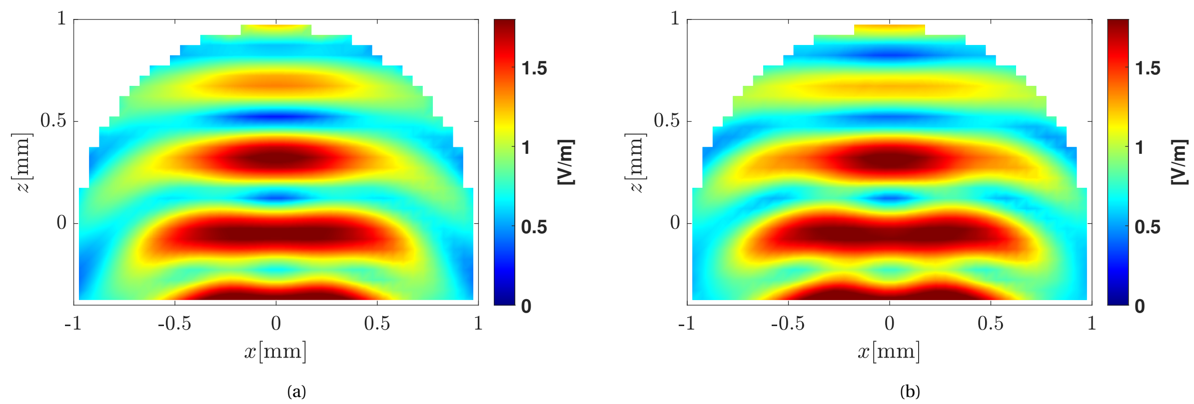

Figure 3.17: Magnitude of the total electric field $\vec{E}$ on the XZ-plane inside the lens for a plane wave excitation (a) obtained using the V-MoM and (b) obtained using CST

total electric field inside the lens on the XZ-plane with the $\lambda_0/2$ dipole as the feeding element at a frequency $f = 294$GHz. While Fig. 3.17a shows the field, obtained using the V-MoM, Fig. 3.17b shows the field, obtained using CST. Similar to before, Figs 3.18a and 3.18b show that the field obtained by the V-MoM and the field obtained by CST are in excellent agreement.

Finally, the input impedance has been calculated, for a dipole with the same dimensions as in Fig. 3.16b. The input impedance has been obtained, both for a dipole located in free space, and for the hemispherical lens in Fig. 3.16b. Fig. 3.19a shows the input impedance of the $\lambda_0/2$ dipole in free space, obtained using both the V-MoM and CST. Since CST cannot model a volumetric excitation, nine discrete ports have been placed in parallel over the gap. Fig. 3.19a shows that the real part of the input impedance, obtained from both solvers are in good agreement. However, the imaginary part shows a larger discrepancy. The difference observed in Fig. 3.19a is probably due to the different representations of the excitation, which only affects the imaginary part. Moreover, the use of a single basis function to model the cross-section of the dipole may not be enough to correctly represent the current distribution.

Fig. 3.19b shows the input impedance of the hemispherical lens with the $\lambda_0/2$ dipole as the feeding element. Similar to before, Fig. 3.19b shows that the real part of the input impedance, obtained using the two solvers, are in good agreement, while the imaginary part shows a larger discrepancy. As mentioned before, this is probably due to the different representations of the excitation and the use of a single basis function to model the cross-section of the dipole. Moreover, it becomes apparent that the V-MoM correctly reproduces the os-

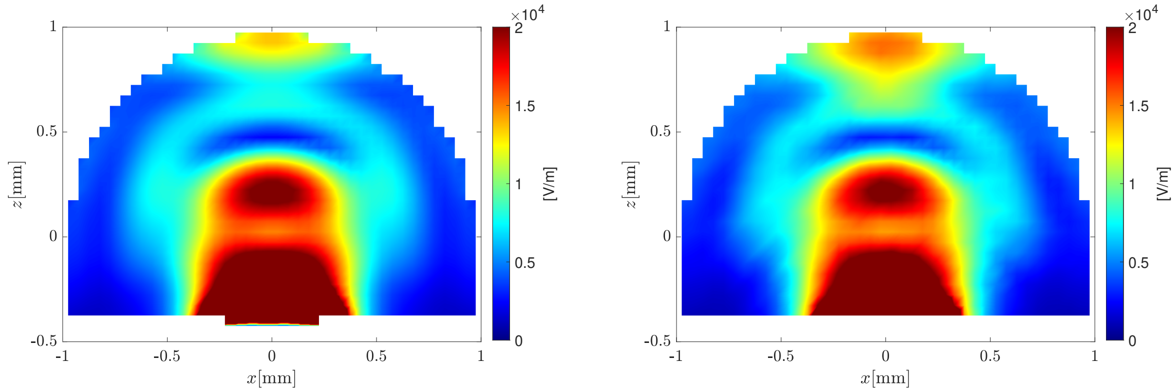

(a) (b)

Figure 3.18: Magnitude of the total electric field on the XZ-plane inside the lens excited by the $\lambda_0/2$ dipole (a) obtained using the V-MoM and (b) obtained using CST

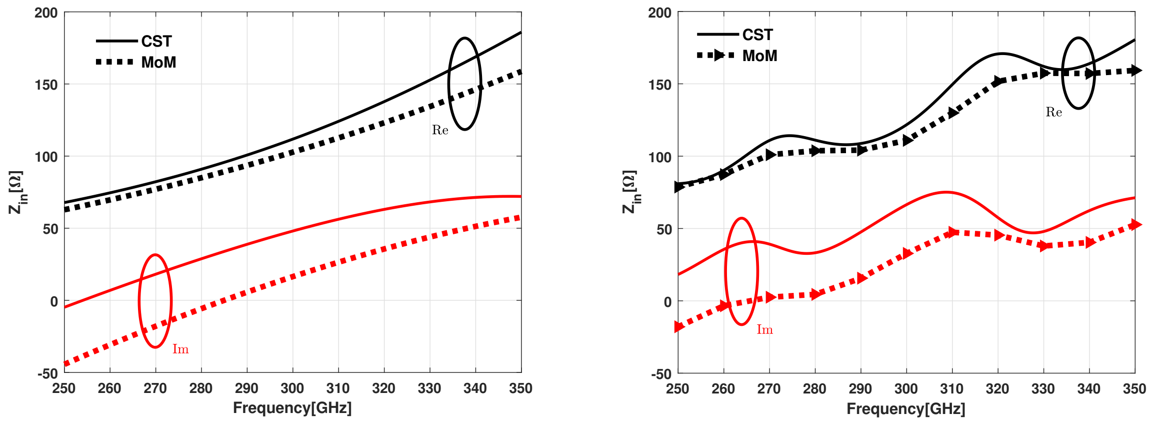

(a) (b)

	V-MoM	CST
Computation time	37s	201s

(c)

Figure 3.19: Input impedance of a $\lambda_0/2$ dipole (a) in free space and (b) as the feed of a lens antenna and (c) the comparison between the computation of CST and the V-MoM

cillations with frequency. Finally, Fig. 3.19c shows the comparison between the computation time of CST and the computation of the V-MoM. Fig. 3.19c shows that the V-MoM is roughly six times faster than CST. It should be noted that the computation of the reaction integrals of the V-MoM took an additional 21s. However, since these integrals can be reused, the computation time of the reaction integrals is not very relevant.

4

Analysis of a dipole with nonzero thickness in free space

In this Chapter, we will introduce the spectral domain formulation that allows us to study infinitely long printed transmission lines, taking into account the non-zero thickness of the conductors. In [40] a similar formulation has been presented to study infinitely long dipoles, assuming that the main conductor has infinitesimal thickness. In that formulation, the losses have been modelled by introducing an equivalent surface impedance. However, ignoring the finite thickness of the conductor has two important consequences. First of all, when considering a microstrip, the nonzero thickness of the conductor can have a major impact on the characteristic impedance, when the thickness of the conductor becomes significant, compared to the distance between the main conductor and the ground plane [20],[21]. Second, if the finite thickness of the conductor is not embedded into the formulation, the influence of the thickness of the conductor on the losses of the transmission line, has to be introduced in an alternative way. The software tool, proposed in [19], estimates the influence of the conductor thickness by using the modified surface impedance, given by [22]. However, this approach fails to take into account the asymmetric current distribution inside the main conductor of the microstrip. Consequently, we would like to develop a formulation that takes into account the non-zero thickness of the conductors.

In the subsequent sections, we will develop a spectral domain formulation, based on the local form of Ohm's law. By making a justified assumption on the transverse current distribution and by applying a Galerkin projection, we will be able to find an expression for the spectrum of the longitudinal current distribution. The longitudinal current distribution can then be converted from the spectral domain to the spatial domain by performing an inverse Fourier transform.

Moreover, the relevant parameters of the transmission line, such as the characteristic impedance, the propagation constant and the losses can be obtained from the polar singularities of the current spectrum. In particular, the propagation constant is given by the location of the pole, while the characteristic impedance can be obtained by interpreting the residue contribution of the input impedance as the contribution from two infinitely long transmission lines. To substantiate this interpretation, we will compare the resulting characteristic impedance with an alternative definition of the characteristic impedance, in which the voltage along the transmission line is defined as the line integral of the transverse electric field.

This chapter is structured as follows. In Section 4.1, we will develop the spectral domain formulation by studying an infinitely long dipole, located in free space. Next, Section 4.2 will introduce the presence of an infinitely extended perfectly conducting ground plane by applying the image theorem.

4.1. Free space dipole

In this section, we will develop the spectral domain formulation by considering an infinitely long dipole, located in free space. In Section 4.1.1, we will derive the transmission line Green's function of the geometry. Next, Section 4.1.2 will introduce one possible definition of the characteristic impedance in which the voltage along the transmission line is defined as the line integral of the transverse electric field. Subsequently, Section 4.1.3 will explain how to extract the relevant parameters of the transmission line from the spectrum of the longitudinal current distribution and provide a validation of the current, obtained from the spectral domain

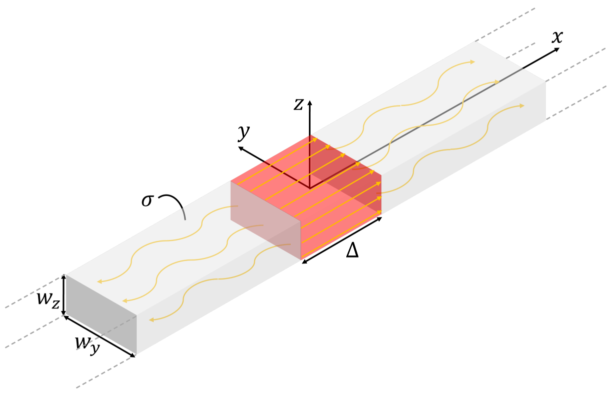

Figure 4.1: Infinitely extended dipole with height w_z and width w_y, constructed from a material with conductivity σ, oriented along the x-axis and excited by a delta-gap excitation of length Δ.

formulation. Finally, in Section 4.1.4, we will demonstrate the formulation, developed in Section 4.1.1 to 4.1.3, by performing a parametric analysis versus the relevant dimensions of the transmission line.

4.1.1. Derivation transmission-line Green's function

Let us consider an infinitely long dipole with height w_z and width w_y, constituted of a material having conductivity σ. The dipole is oriented along the x-axis, and excited by a delta-gap excitation of length Δ, as shown in Fig. 4.1. Inside the dipole, the current density $\vec{j}$ and the electric field $\vec{e}$ are related through the local form of Ohm's law

$$\vec{j} = \sigma \vec{e}. \tag{4.1}$$

By expressing the total electric field $\vec{e}$ as the superposition of the incident field $\vec{e}_{\text{inc}}$ and the scattered field $\vec{e}_{\text{scatt}}$, we obtain following expression

$$\vec{j} = \sigma(\vec{e}_{\text{inc}} + \vec{e}_{\text{scatt}}). \tag{4.2}$$

By assuming that $\vec{j}$ only has a nonzero x-component, and by applying the separation of variables, the current density can be expressed as follows

$$\vec{j} = i(x)\, j_t(y,z)\,\hat{x}, \tag{4.3}$$

where $i(x)$ represents the net longitudinal current and $j_t(y,z)$ represents the transverse distribution of the current. Similarly, $\vec{e}_{\text{inc}}$ can be expressed as follows

$$\vec{e}_{\text{inc}} = e_{\text{inc},l}(x)\, e_{\text{inc},t}(y,z)\,\hat{x}, \tag{4.4}$$

where $\vec{e}_{\text{inc,l}}(x)$ and $\vec{e}_{\text{inc,t}}(y,z)$ represent the longitudinal and transverse dependencies of the incident field, respectively. By substituting (4.3) and (4.4) into (4.2), by equating the x-components of the left- and right-hand sides of (4.2) and by introducing the resistivity $\rho = 1/\sigma$, we obtain the following expression

$$\rho\, i(x)\, j_t(y,z) = e_{\text{inc},l}(x)\, e_{\text{inc},t}(y,z) + e_{\text{scatt},x}, \tag{4.5}$$

where $e_{\text{scatt},x}$ denotes the x-component of the scattered field. By expressing $e_{\text{scatt},x}$ as the convolution between the x-component of the transverse current distribution j_x and the xx-component of the free-space Green's function $g^{ej}_{xx}(x-x', y-y', z-z')$, (4.5) becomes as follows

$$\rho\, i(x)\, j_t(y,z) = e_{\text{inc},l}(x)\, e_{\text{inc},t}(y,z) + \int_{-\infty}^{\infty}\int_{-\infty}^{\infty}\int_{-\infty}^{\infty} g^{ej}_{xx}(x-x', y-y', z-z')\, i(x')\, j_t(y',z')\, dx'\, dy'\, dz'. \tag{4.6}$$

The xx-component of the free-space Green's function $g^{ej}_{xx}(x-x', y-y', z-z')$ can be expressed in terms of its plane wave spectrum $G^{ej}_{xx}(k_x, k_y, k_z)$, as shown in the following expression

$$g^{ej}_{xx}(x-x', y-y', z-z') = \frac{1}{8\pi^3}\int_{-\infty}^{\infty}\int_{-\infty}^{\infty}\int_{-\infty}^{\infty} G^{ej}_{xx}(k_x, k_y, k_z)\, e^{-jk_x(x-x')}\, e^{-jk_y(y-y')}\, e^{-jk_z(z-z')}\, dk_x\, dk_y\, dk_z. \tag{4.7}$$

where

$$G_{xx}^{ej}(k_x,k_y,k_z) = j\frac{\zeta}{k}\frac{k^2-k_x^2}{k^2-k_x^2-k_y^2-k_z^2}. \tag{4.8}$$

By substituting (4.7) into (4.6) and by bringing all of the terms containing the current $i(x)$ to one side, we obtain the following expression

$$\begin{aligned} e_{\text{inc},l}(x)e_{\text{inc},t}(y,z) &= \rho i(x) j_t(y,z) - \\ \int_{-\infty}^{\infty}\int_{-\infty}^{\infty}\int_{-\infty}^{\infty}\left(\frac{1}{8\pi^3}\int_{-\infty}^{\infty}\int_{-\infty}^{\infty}\int_{-\infty}^{\infty} G_{xx}^{ej}(k_x,k_y,k_z)e^{-jk_x(x-x')}e^{-jk_y(y-y')}e^{-jk_z(z-z')}\,dk_x\,dk_y\,dk_z\right)& \\ i(x')j_t(y',z')\,dx'\,dy'\,dz'.& \end{aligned} \tag{4.9}$$

By changing the order of integration, (4.9) can be expressed as follows

$$\begin{aligned} e_{\text{inc},l}(x)e_{\text{inc},t}(y,z) &= \rho i(x) j_t(y,z) - \\ \frac{1}{8\pi^3}\int_{-\infty}^{\infty}\int_{-\infty}^{\infty}\int_{-\infty}^{\infty} G_{xx}^{ej}(k_x,k_y,k_z)e^{-jk_x x}e^{-jk_y y}e^{-jk_z z}& \\ \left(\int_{-\infty}^{\infty} i(x')e^{jk_x x'}\,dx'\right)\left(\int_{-\infty}^{\infty}\int_{-\infty}^{\infty} j_t(y',z')e^{jk_y y'}e^{jk_z z'}\,dy'\,dz'\right)dk_x\,dk_y\,dk_z.& \end{aligned} \tag{4.10}$$

By recognizing the Fourier transform of $i(x)$ and the Fourier transform of $j_t(y,z)$ and by expressing both $e_{\text{inc},l}(x)$ and $i(x)$ as an inverse Fourier transform, (4.10) becomes as follows

$$\begin{aligned} \frac{1}{2\pi}\int_{-\infty}^{\infty} E_{\text{inc},l}(k_x)e^{-jk_x x}\,dk_x e_{\text{inc},t}(y,z) &= \frac{1}{2\pi}\int_{-\infty}^{\infty} I(k_x)e^{-jk_x x}\,dk_x \rho j_t(y,z) - \\ \frac{1}{2\pi}\int_{-\infty}^{\infty} I(k_x)e^{-jk_x x}\,dk_x\frac{1}{4\pi^2}\int_{-\infty}^{\infty}\int_{-\infty}^{\infty} G_{xx}^{ej}(k_x,k_y,k_z)&J_t(k_y,k_z)e^{-jk_y y}e^{-jk_z z}\,dk_y\,dk_z. \end{aligned} \tag{4.11}$$

Since the dipole is assumed to be infinite, (4.11) is valid for every x. Hence, we can equate the spectra in k_x, which results in the following expression

$$E_{\text{inc},l}(k_x)e_{\text{inc},t}(y,z) = I(k_x)\left(\rho j_t(y,z) - \frac{1}{4\pi^2}\int_{-\infty}^{\infty}\int_{-\infty}^{\infty} G_{xx}^{ej}(k_x,k_y,k_z)J_t(k_y,k_z)e^{-jk_y y}e^{-jk_z z}\,dk_y\,dk_z\right). \tag{4.12}$$

By defining the following projection operator

$$\langle f(y,z), g(y,z)\rangle_A = \iint_A f(y,z)g(y,z)\,dy\,dz, \tag{4.13}$$

where A denotes the cross-section of the dipole, and by projecting (4.12) onto the transverse current distribution $j_t(y,z)$, one obtains the following expression

$$\begin{aligned} E_{\text{inc},l}(k_x)\langle e_{\text{inc},t}(y,z), j_t(y,z)\rangle_A &= I(k_x)\Big(\rho\langle j_t(y,z), j_t(y,z)\rangle_A - \\ \langle\frac{1}{4\pi^2}\int_{-\infty}^{\infty}\int_{-\infty}^{\infty} G_{xx}^{ej}(k_x,k_y,k_z)J_t(k_y,k_z)&e^{-jk_y y}e^{-jk_z z}\,dk_y\,dk_z, j_t(y,z)\rangle_A\Big). \end{aligned} \tag{4.14}$$

The projection in the space domain can be equivalently calculated as a projection in the spectral domain, as shown in the following expression

$$\begin{aligned} \langle\frac{1}{4\pi^2}\int_{-\infty}^{\infty}\int_{-\infty}^{\infty} G_{xx}^{ej}(k_x,k_y,k_z)J_t(k_y,k_z)e^{-jk_y y}e^{-jk_z z}\,dk_y\,dk_z, j_t(y,z)\rangle_A &= \\ \frac{1}{4\pi^2}\int_{-\infty}^{\infty}\int_{-\infty}^{\infty} G_{xx}^{ej}(k_x,k_y,k_z)J_t^2(k_y,k_z)\,dk_y\,dk_z.& \end{aligned} \tag{4.15}$$

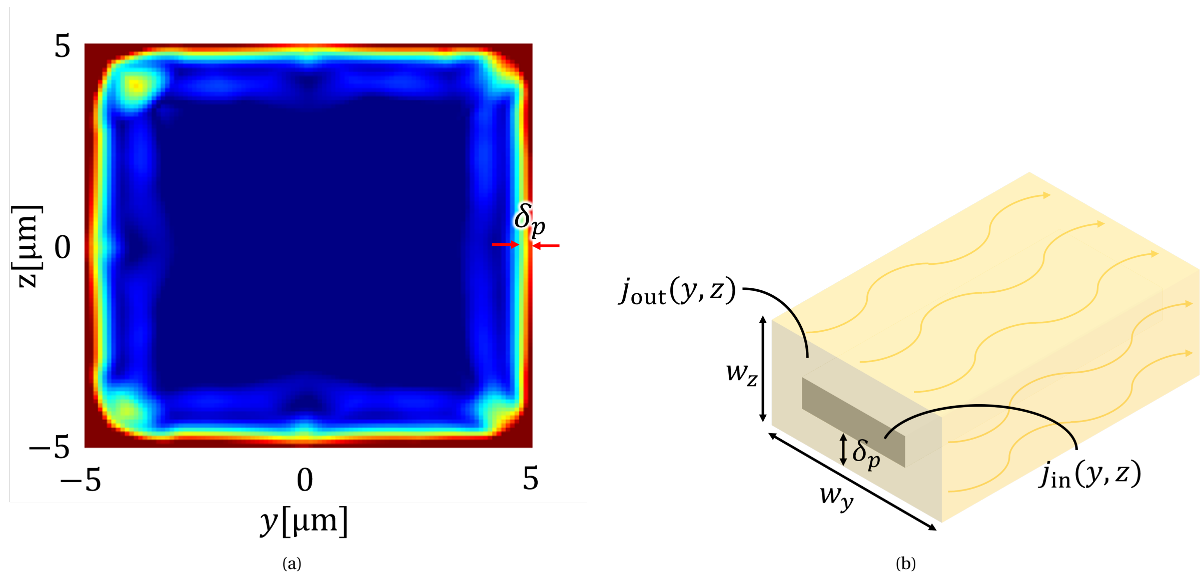

Figure 4.2: Transverse current distribution on a dipole located in free space, (a) extracted from CST, and (b) approximated using the Leontovich boundary condition

By substituting (4.15) into (4.14), we obtain the following expression

$$E_{\mathrm{inc},l}(k_x)\langle e_{\mathrm{inc},t}(y,z), j_t(y,z)\rangle_A = I(k_x)\Bigg(\rho\langle j_t(y,z), j_t(y,z)\rangle_A - \frac{1}{4\pi^2}\int_{-\infty}^{\infty}\int_{-\infty}^{\infty} G^{ej}_{xx}(k_x,k_y,k_z)J_t^2(k_y,k_z)\,dk_y\,dk_z\Bigg). \tag{4.16}$$

From (4.16) the spectrum of the current can be obtained as follows

$$I(k_x) = \frac{E_{\mathrm{inc},l}(k_x)\langle e_{\mathrm{inc},t}(y,z), j_t(y,z)\rangle_A}{\rho\langle j_t(y,z), j_t(y,z)\rangle_A - D(k_x)}, \tag{4.17}$$

where the longitudinal spectral Green's function $D(k_x)$ is given by the following expression

$$D(k_x) = \frac{1}{4\pi^2}\int_{-\infty}^{\infty}\int_{-\infty}^{\infty} G^{ej}_{xx}(k_x,k_y,k_z)J_t^2(k_y,k_z)\,dk_y\,dk_z. \tag{4.18}$$

The general expression for $I(k_x)$ is given by (4.17). However, obtaining its explicit expression requires an assumption on the transverse current distribution $j_t(y,z)$. To make a justified assumption, Fig. 4.2a shows the transverse current distribution obtained from CST for a dipole in free space, having a width and thickness $w_z = w_y = 10\mu\mathrm{m}$, constituted of a material with conductivity $\sigma = 10^7\mathrm{S/m}$. As shown in Fig. 4.2a the current is mostly localized at the outer surface of the dipole and decays exponentially inside the metal. However, by assuming an exponential decay within the metal, one obtains a rather complicated expression for $J_t(k_y,k_z)$. To simplify the expression of the transverse current distribution, we will approximate the exponential decay inside the metal, by using the Leontovich boundary condition [25]. This choice will allow us to close the integral in k_z in (4.18) analytically.

By using the Leontovich boundary condition, we may assume that the current inside the dipole is uniformly distributed on a strip, located at the outer surface of the metal, having a thickness equal to the penetration depth δ_p, and zero elsewhere, as shown in Fig. 4.2b. The transverse current distribution $j_t(y,z)$ can then be expressed as follows

$$j_t(y,z) = \frac{1}{2\delta_p(w_y + w_z - 2\delta_p)}\left(j_{\mathrm{out}}(y,z) - j_{\mathrm{in}}(y,z)\right), \tag{4.19}$$

where the outer rectangular function $j_{\mathrm{out}}(y,z)$ is given by the following expression

$$j_{out}(y,z) = \mathrm{rect}\left(\frac{y}{w_y}\right)\mathrm{rect}\left(\frac{z}{w_z}\right), \tag{4.20}$$

and the inner rectangular function $j_{\text{in}}(y,z)$ is expressed as follows

$$j_{\text{in}}(y,z) = \text{rect}\left(\frac{y}{w_y - 2\delta_p}\right)\text{rect}\left(\frac{z}{w_z - 2\delta_p}\right). \tag{4.21}$$

The constant in front of (4.19) is chosen such that the integration of $j_t(y,z)$ over the cross-section of the dipole is equal to one. Consequently, $i(x)$ represents the net current along the dipole. The Fourier transforms of $j_{\text{out}}(y,z)$ and $j_{\text{in}}(y,z)$ can then be expressed as follows

$$J_{\text{out}}(k_y,k_z) = w_y w_z \text{sinc}\left(\frac{k_y w_y}{2}\right)\text{sinc}\left(\frac{k_z w_z}{2}\right) \tag{4.22}$$

$$J_{\text{in}}(k_y,k_z) = (w_y - 2\delta_p)(w_z - 2\delta_p)\text{sinc}\left(k_y \frac{w_y - 2\delta_p}{2}\right)\text{sinc}\left(k_z \frac{w_z - 2\delta_p}{2}\right). \tag{4.23}$$

By assuming the dipole to be excited by a delta-gap generator, the longitudinal and transverse distribution of the incident field can be expressed as follows

$$e_{\text{inc},l}(x) = \frac{1}{\Delta}\text{rect}\left(\frac{x}{\Delta}\right) \tag{4.24}$$

$$e_{\text{inc},t}(y,z) = \text{rect}\left(\frac{y}{w_y}\right)\text{rect}\left(\frac{z}{w_z}\right). \tag{4.25}$$

The Fourier transform of $e_{\text{inc},l}(x)$ can then be expressed as follows

$$E_{\text{inc},l}(k_x) = \text{sinc}\left(\frac{k_x\Delta}{2}\right) \tag{4.26}$$

The chosen distributions of $j_t(y,z)$ and $e_{\text{inc},t}(y,z)$ allow for simple analytical evaluations of the two spatial projections in (4.17):

$$\langle e_{\text{inc},t}(y,z), j_t(y,z)\rangle_A = \frac{1}{2\delta_p(w_y + w_z - 2\delta_p)}\left(\int_{-w_z/2}^{w_z/2}\int_{-w_y/2}^{w_y/2} dy\,dz - \int_{-w_z/2+\delta_p}^{w_z/2-\delta_p}\int_{-w_y/2+\delta_p}^{w_y/2-\delta_p} dy\,dz\right) = 1 \tag{4.27}$$

$$\langle j_t(y,z), j_t(y,z)\rangle_A = \frac{1}{4\delta_p^2(w_y + w_z - 2\delta_p)^2}\left(\int_{-w_z/2}^{w_z/2}\int_{-w_y/2}^{w_y/2} dy\,dz - \int_{-w_z/2+\delta_p}^{w_z/2-\delta_p}\int_{-w_y/2+\delta_p}^{w_y/2-\delta_p} dy\,dz\right) = \frac{1}{2\delta_p(w_y + w_z - 2\delta_p)}. \tag{4.28}$$

Finally, by substituting (4.27) and (4.26) into (4.17), we obtain the following expression

$$I(k_x) = \frac{\text{sinc}\left((k_x\Delta)/2\right)}{\rho\langle j_t(y,z), j_t(y,z)\rangle_A - D(k_x)}. \tag{4.29}$$

The most computationally expensive part of calculating $I(k_x)$ is to evaluate the double integral of $D(k_x)$, which can be expressed as follows

$$D(k_x) = \frac{1}{4\pi^2}\int_{-\infty}^{\infty}\int_{-\infty}^{\infty} G_{xx}^{ej}(k_x,k_y,k_z) J_t^2(k_y,k_z)\,dk_y\,dk_z = \frac{1}{4\delta_p^2(w_y + w_z - 2\delta_p)^2}(I_1 + I_2 - 2I_3), \tag{4.30}$$

where I_1, I_2 and I_3 are given by the following expressions

$$I_1 = \frac{j\zeta}{k}\frac{w_y^2 w_z^2(k^2 - k_x^2)}{4\pi^2}\int_{-\infty}^{\infty}\int_{-\infty}^{\infty}\frac{\text{sinc}^2\left(k_y w_y/2\right)\text{sinc}^2(k_z w_z/2)}{k^2 - k_x^2 - k_y^2 - k_z^2}\,dk_y\,dk_z \tag{4.31}$$

$$I_2 = \frac{j\zeta}{k}\frac{(w_y - 2\delta_p)^2(w_z - 2\delta_p)^2(k^2 - k_x^2)}{4\pi^2}\int_{-\infty}^{\infty}\int_{-\infty}^{\infty}\frac{\text{sinc}^2\left(k_y(w_y - 2\delta_p)/2\right)\text{sinc}^2(k_z w_z/2)}{k^2 - k_x^2 - k_y^2 - k_z^2}\,dk_y\,dk_z \tag{4.32}$$

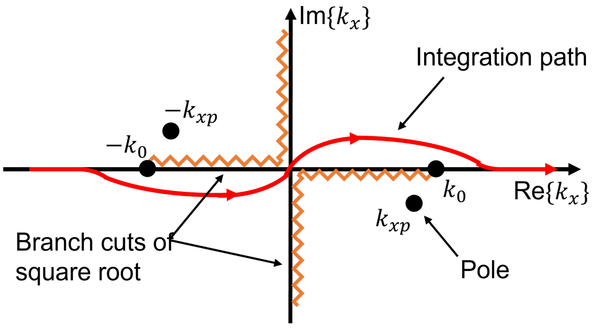

Figure 4.3: Spectral plane of $I(k_x)$ for a dipole in free space

$$
\begin{aligned}
I_3 = \frac{j\zeta}{k} \frac{w_y w_z (w_y - 2\delta_p)(w_z - 2\delta_p)(k^2 - k_x^2)}{4\pi^2} \cdot \\
\int_{-\infty}^{\infty}\int_{-\infty}^{\infty} \frac{\operatorname{sinc}\big(k_y(w_y - 2\delta_p)/2\big)\operatorname{sinc}\big(k_y w_y/2\big)\operatorname{sinc}\big(k_z(w_z - 2\delta_p)/2\big)\operatorname{sinc}(k_z w_z/2)}{k^2 - k_x^2 - k_y^2 - k_z^2} \, dk_y \, dk_z.
\end{aligned}
\tag{4.33}
$$

As shown in Appendix D, the integral in k_z can be closed analytically, which results in the following expressions for I_1, I_2, and I_3

$$
I_1 = \frac{j\zeta}{k} \frac{(k_x^2 - k^2) w_y^2}{2\pi} \int_{-\infty}^{\infty} \left[\frac{w_z \operatorname{sinc}^2\big(k_y w_y/2\big)}{k_x^2 + k_y^2 - k^2} + \frac{e^{-w_z\sqrt{k_x^2+k_y^2-k^2}} - 1}{(k_x^2 + k_y^2 - k^2)^{\frac{3}{2}}} \operatorname{sinc}^2\left(\frac{k_y w_y}{2}\right) \right] dk_y \tag{4.34}
$$

$$
\begin{aligned}
I_2 = \frac{j\zeta}{k} \frac{(k_x^2 - k^2)(w_y - 2\delta_p)^2}{2\pi} \int_{-\infty}^{\infty} \Bigg[\frac{w_z - 2\delta_p}{k_x^2 + k_y^2 - k^2} \operatorname{sinc}^2\left(k_y \frac{w_y - 2\delta_p}{2}\right) \\
+ \frac{e^{-(w_z - 2\delta_p)\sqrt{k_x^2+k_y^2-k^2}} - 1}{(k_x^2 + k_y^2 - k^2)^{\frac{3}{2}}} \operatorname{sinc}^2\left(\frac{k_y w_y}{2}\right) \Bigg] dk_y
\end{aligned}
\tag{4.35}
$$

$$
\begin{aligned}
I_3 = \frac{j\zeta}{k} \frac{(k_x^2 - k^2) w_y (w_y - 2\delta_p)}{2\pi} \int_{-\infty}^{\infty} \Bigg[\frac{w_z - 2\delta_p}{k_x^2 + k_y^2 - k^2} \operatorname{sinc}\left(\frac{k_y w_y}{2}\right) \operatorname{sinc}\left(k_y \frac{w_y - 2\delta_p}{2}\right) + \\
\frac{e^{-(w_z - \delta_p)\sqrt{k_x^2+k_y^2-k^2}} - e^{-\delta_p\sqrt{k_x^2+k_y^2-k^2}}}{(k_x^2 + k_y^2 - k^2)^{\frac{3}{2}}} \operatorname{sinc}\left(\frac{k_y w_y}{2}\right) \operatorname{sinc}\left(k_y \frac{w_y - 2\delta_p}{2}\right) \Bigg] dk_y.
\end{aligned}
\tag{4.36}
$$

In Section 4.1.4, we will demonstrate the importance of the assumption on the transverse current distribution by making a comparison between the results obtained by using the Leontovich boundary condition and the results obtained by assuming a uniform current distribution on the cross-section. If a uniform current distribution is used, only I_1 should be retained in the calculation of the longitudinal spectral Green's function, which results in the following expression

$$
D(k_x) = \frac{j\zeta}{k} \frac{(k_x^2 - k^2)}{2\pi} \int_{-\infty}^{\infty} \left[\frac{w_z \operatorname{sinc}^2\big(k_y w_y/2\big)}{k_x^2 + k_y^2 - k^2} + \frac{e^{-w_z\sqrt{k_x^2+k_y^2-k^2}} - 1}{(k_x^2 + k_y^2 - k^2)^{\frac{3}{2}}} \operatorname{sinc}^2\left(\frac{k_y w_y}{2}\right) \right] dk_y. \tag{4.37}
$$

In this case, the spatial projection becomes as follows

$$
\langle j_t(y,z), j_t(y,z) \rangle_A = \frac{1}{w_y w_z}. \tag{4.38}
$$

4.1.2. Definition of the characteristic impedance

In this section, we will give one possible definition of the characteristic impedance in which the voltage along the transmission line is defined as the line integral of the transverse electric field. In Section 4.1.3, we will give an alternative definition, by interpreting the residue contribution of the input admittance as the contribution from two infinitely long transmission lines. In Section 4.1.4, we will then support this interpretation by comparing the characteristic impedance, obtained using the two different definitions.

Let us first consider the longitudinal current distribution $i(x)$, which can be calculated as the following inverse Fourier Transform

$$i(x) = \frac{1}{2\pi}\int_{-\infty}^{\infty} I(k_x)e^{-jk_x x}dk_x, \tag{4.39}$$

where the integral can be performed numerically by integrating over the contour shown in Fig. 4.3. Note that the pole k_{xp} has been separated from the branch point k_0 due to the presence of the Ohmic losses. Therefore, it is possible to explicitly calculate the contribution due to the pole, by applying the residue theorem [41]. This results in a forward traveling current wave $i_{\text{res}}(x)$, which can be expressed as follows

$$i_{\text{res}}(x) = I^+ e^{-jk_{xp}x}, \tag{4.40}$$

where the amplitude I^+ can be expressed as follows

$$I^+ = -j\frac{\operatorname{sinc}\big((k_{xp}\Delta)/2\big)}{D'(k_{xp})}. \tag{4.41}$$

The location of the pole k_{xp} can be found through a local root-finding algorithm, such as the Newton-Raphson method, as explained in Appendix C.

To obtain the characteristic impedance of the transmission line, we have to relate the current wave to a voltage wave traveling along the dipole. If we assume that a quasi-TEM wave is propagating along the dipole, we may define the voltage as the line integral of the transverse electric field from a point located at the surface of the dipole to infinity [40], as shown in the following expression

$$v(x) = \int_{w_z/2}^{\infty} e_z(x, y=0, z)dz. \tag{4.42}$$

where $e_z(x, y = 0, z)$ denotes the z-component of the electric field, observed at $y = 0$. By expressing $e_z(x, y = 0, z)$ in terms of its plane wave spectrum $E_z(k_x, k_y, k_z)$, we obtain the following expression

$$v(x) = \int_{w_z/2}^{\infty}\left(\frac{1}{8\pi^3}\int_{-\infty}^{\infty}\int_{-\infty}^{\infty}\int_{-\infty}^{\infty} E_z(k_x, k_y, k_z)e^{-jk_x x}e^{-jk_z z}\,dk_x\,dk_y\,dk_z\right)dz. \tag{4.43}$$

$E_z(k_x, k_y, k_z)$ can be expressed as follows

$$E_z(k_x, k_y, k_z) = I(k_x)J_t(k_x, k_y, k_z)G_{zx}^{ej}(k_x, k_y, k_z), \tag{4.44}$$

where the zx-component of the free space Dyadic Green's function $G_{zx}^{ej}(k_x, k_y, k_z)$ is given by the following expression

$$G_{zx}^{ej}(k_x, k_y, k_z) = -\frac{j\zeta}{k}\frac{k_z k_x}{k^2 - k_x^2 - k_y^2}. \tag{4.45}$$

By substituting (4.44) and (4.45) into (4.43), we obtain the following expression

$$v(x) = -\frac{j\zeta}{k}\frac{1}{8\pi^3}\int_{-\infty}^{\infty}\int_{-\infty}^{\infty}\int_{-\infty}^{\infty} I(k_x)J_t(k_x, k_y, k_z)\frac{k_z k_x}{k^2 - k_x^2 - k_y^2 - k_z^2}e^{-jk_x x}\int_{w_z/2}^{\infty} e^{-jk_z z}dz\,dk_x\,dk_y\,dk_z. \tag{4.46}$$

By assuming that the radiation condition is satisfied, i.e. $\lim_{z\to\infty} e^{-jk_z z} = 0$, the integral in z can be closed analytically, which leads to the following expression

$$v(x) = \frac{\zeta}{k}\frac{1}{8\pi^3}\int_{-\infty}^{\infty}\int_{-\infty}^{\infty}\int_{-\infty}^{\infty} I(k_x)J_t(k_x, k_y, k_z)\frac{k_x}{k^2 - k_x^2 - k_y^2 - k_z^2}e^{-jk_x x}e^{-jk_z w_z/2}\,dk_x\,dk_y\,dk_z. \tag{4.47}$$

By using the Leontovich boundary condition for the transverse current distribution, the voltage can be expressed as follows

$$v(x) = \frac{v_{\text{out}}(x) - v_{\text{in}}(x)}{2\delta_p(w_y + w_z - 2\delta_p)}, \tag{4.48}$$

where the voltage due to the outer rectangular function $v_{\text{out}}(x)$ is given by the following expression

$$v_{\text{out}}(x) = \frac{\zeta}{k}\frac{w_y w_z}{8\pi^3}\int_{-\infty}^{\infty}\int_{-\infty}^{\infty}\int_{-\infty}^{\infty} I(k_x)\text{sinc}\left(\frac{k_y w_y}{2}\right)\text{sinc}\left(\frac{k_z w_z}{2}\right)\frac{k_x}{k^2 - k_x^2 - k_y^2 - k_z^2}e^{-jk_x x}e^{-jk_z w_z/2}\,dk_x\,dk_y\,dk_z, \tag{4.49}$$

and the voltage due to the inner rectangular function $v_{\text{in}}(x)$ is expressed as follows

$$\begin{aligned} v_{\text{in}}(x) = \frac{\zeta}{k}\frac{(w_y - 2\delta_p)(w_z - 2\delta_p)}{8\pi^3}\int_{-\infty}^{\infty}\int_{-\infty}^{\infty}\int_{-\infty}^{\infty} I(k_x)\text{sinc}\left(k_y\frac{w_y - 2\delta_p}{2}\right)\text{sinc}\left(k_z\frac{w_z - 2\delta_p}{2}\right)\cdot \\ \frac{k_x}{k^2 - k_x^2 - k_y^2 - k_z^2}e^{-jk_x x}e^{-jk_z w_z/2}\,dk_x\,dk_y\,dk_z. \end{aligned} \tag{4.50}$$

As shown in Appendix D, the integrals in k_z can be closed analytically, which results in the following expressions

$$v_{\text{out}}(x) = \frac{w_y}{8\pi^2}\int_{-\infty}^{\infty}\int_{-\infty}^{\infty} I(k_x)\text{sinc}\left(\frac{k_y w_y}{2}\right)\frac{\zeta k_x}{k}\frac{e^{-w_z\sqrt{k_x^2+k_y^2-k^2}} - 1}{k_x^2 + k_y^2 - k^2}e^{-jk_x x}\,dk_x\,dk_y \tag{4.51}$$

$$v_{\text{in}}(x) = \frac{w_y - 2\delta}{8\pi^2}\int_{-\infty}^{\infty}\int_{-\infty}^{\infty} I(k_x)\text{sinc}\left(k_y\frac{w_y - 2\delta_p}{2}\right)\frac{\zeta k_x}{k}\frac{e^{-(w_z-\delta_p)\sqrt{k_x^2+k_y^2-k^2}} - e^{-\delta_p\sqrt{k_x^2+k_y^2-k^2}}}{k_x^2 + k_y^2 - k^2}e^{-jk_x x}\,dk_x\,dk_y. \tag{4.52}$$

To simplify the notation, we will define the function $Z(k_x)$ as follows

$$\begin{aligned} Z(k_x) = \frac{\zeta k_x}{k}\frac{1}{8\pi\delta_p(w_y + w_z - 2\delta_p)}\int_{-\infty}^{\infty}\left[w_y\text{sinc}\left(\frac{k_y w_y}{2}\right)\frac{e^{-w_z\sqrt{k_x^2+k_y^2-k^2}} - 1}{k_x^2 + k_y^2 - k^2} - \right. \\ \left.(w_y - 2\delta_p)\text{sinc}\left(k_y\frac{w_y - 2\delta_p}{2}\right)\frac{e^{-(w_z-\delta_p)\sqrt{k_x^2+k_y^2-k^2}} - e^{-\delta_p\sqrt{k_x^2+k_y^2-k^2}}}{k_x^2 + k_y^2 - k^2}\right]dk_y. \end{aligned} \tag{4.53}$$

With this definition, $v(x)$ can be expressed as follows

$$v(x) = \frac{1}{2\pi}\int_{-\infty}^{\infty} I(k_x)Z(k_x)e^{-jk_x x}dk_x. \tag{4.54}$$

The contribution of the polar singularity to the integral in (4.54) can then be evaluated using the residue theorem [41], which results in a forward traveling voltage wave along the dipole, as shown in the following expression

$$v_{\text{res}}(x) = V^+ e^{-jk_{xp}x}, \tag{4.55}$$

where the amplitude V^+ is expressed as follows

$$V^+ = -j\frac{\text{sinc}\left((k_{xp}\Delta)/2\right)}{D'(k_{xp})}Z(k_{xp}). \tag{4.56}$$

Finally, the characteristic impedance $Z_{0,\text{TEM}}$ can be defined as the ratio between the amplitudes of the voltage and current waves, as shown in the following expression

$$Z_{0,\text{TEM}} = \frac{V^+}{I^+} = Z(k_{xp}). \tag{4.57}$$

Similar to before, the location of the pole k_{xp} can be found through a local root-finding algorithm, such as the Newton-Raphson method, as explained in Appendix C.

As mentioned in Section 4.1.1, we will investigate the influence of the assumption on the transverse current distribution, on the main parameters of the transmission line, by making a comparison between the results obtained by using the Leontovich boundary condition and the results obtained by assuming a uniform current distribution on the cross-section. If a uniform current distribution is used in the calculation of the characteristic impedance, only the outer rectangular function j_{out} should be retained. Consequently, $Z(k_x)$ becomes as follows

$$Z(k_x) = \frac{\zeta k_x}{k} \frac{1}{4\pi w_z} \int_{-\infty}^{\infty} \operatorname{sinc}\left(\frac{k_y w_y}{2}\right) \frac{e^{-w_z\sqrt{k_x^2+k_y^2-k^2}} - 1}{k_x^2 + k_y^2 - k^2} dk_y. \tag{4.58}$$

In thath case, the characteristic impedance is still defined by (4.57), where k_{xp} denotes the pole of the current spectrum $I(k_x)$ that is obtained, using (4.37) as the longitudinal spectral Green's function.

4.1.3. Transmission line characterization and validation

In this section, we will explain how to extract the relevant parameters of the transmission line, such as the characteristic impedance, the effective permittivity and the losses and provide a validation of the formulation developed in Section 4.1.1. In Section 4.1.2, we have given one possible definition of the characteristic impedance, in which the voltage is defined as the line integral of the transverse electric field. In this section, we will provide an alternative definition by interpreting the residue contribution of the input admittance as the contribution from two infinitely long transmission lines. To this extent, let us consider again the expression of the current $i(x)$, shown in (4.39). By averaging the current over the gap, the input admittance can be expressed as follows

$$Y_{\text{in}} = \frac{1}{2\pi} \int_{-\infty}^{\infty} I(k_x) \operatorname{sinc}\left(\frac{k_x \Delta}{2}\right) dk_x, \tag{4.59}$$

where the integral can be performed numerically by integrating over the same contour shown in Fig. 4.3. To characterize the transmission line in terms of its characteristic impedance, its effective dielectric permittivity and its losses, we will consider the residue contribution of (4.59), which can be expressed as follows

$$Y_{\text{res}} = -j \frac{\operatorname{sinc}^2\big((k_{xp}\Delta)/2\big)}{D'(k_{xp})}. \tag{4.60}$$

Y_{res} represents the portion of the input admittance, due to the residue contribution of the current $i_{\text{res}}(x)$, as defined in (4.40). By examining (4.40), it becomes apparent that $i_{\text{res}}(x)$ represents a forward propagating current wave with amplitude I^+ and propagation constant k_{xp}. Considering the similarity between (4.40) and the expression of a traveling current wave from transmission line theory, it is tempting to interpret $i_{\text{res}}(x)$ as the current flowing on two infinitely long transmission lines. By interpreting the term $\operatorname{sinc}^2\big((k_{xp}\Delta)/2\big)$ as a transformer with turn ratio $n = \operatorname{sinc}\big((k_{xp}\Delta)/2\big)$, we obtain the equivalent circuit, shown in Fig. 4.5a. With these interpretations, we may define the characteristic impedance of the dipole in the following alternative way

$$Z_{0,\text{res}} = j \frac{D'(k_{xp})}{2}. \tag{4.61}$$

To support the above interpretation, Fig. 4.5b shows the comparison between the characteristic impedance, obtained from the definition in (4.57), and the characteristic impedance, obtained from the definition in (4.61), for a dipole in free space having a height $w_z = 1\mu$m and width $w_y = 20\mu$m, constituted of a material with conductivity $\sigma = 4.1\cdot 10^7$S/m. The similarity between the two results indeed seem to support the interpretation, suggested above. The difference observed in Fig. 4.5b originates from two underlying differences between the definition in (4.57) and the definition in (4.61).

First of all, in the definition in (4.57), the voltage along the dipole is defined as the line integral of the transverse electric field from a point at the surface of the dipole to infinity. This definition is based on the assumption that a TEM-wave is propagating along the dipole, as shown in Fig.4.4a. If this assumption was true, the transverse electric field would satisfy the Laplace equation and the voltage could be rigorously defined as the line integral of the transverse electric field. However, the assumption of a TEM-wave is only valid at infinite distance from the source. At finite distance from the source, the field is directed from one arm of the dipole to the other, as shown in Fig. 4.4b. Therefore, the definition of the voltage in (4.42) is not entirely rigorous.

Second, in the definition of (4.61), the voltage over the gap is defined by averaging the incident field over the cross-section of the dipole. On the other hand, in the definition of (4.57), the voltage along the dipole is

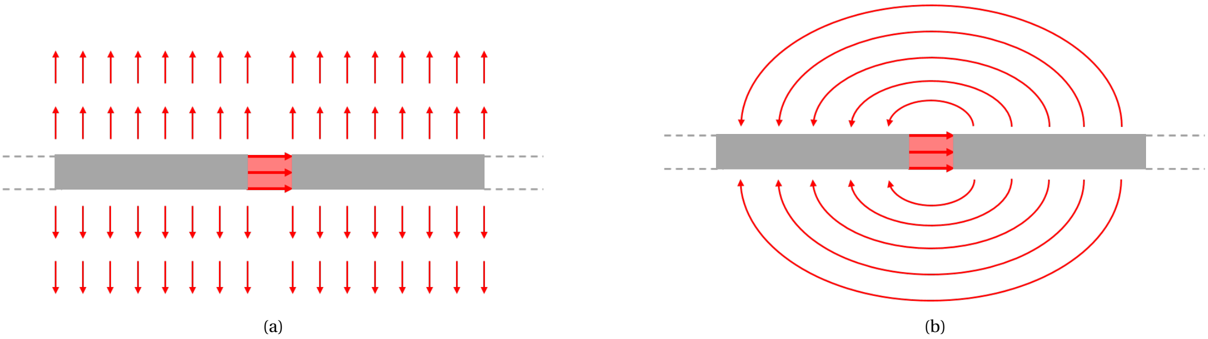

Figure 4.4: Field distribution of an infinite dipole (a) assuming a TEM wave and (b) assuming a realistic field distribution

defined as the line integral of the transverse electric field, starting from the surface of the metal. Nevertheless, we may regard the similarity, observed in Fig. 4.5b, as a justification of the interpretation, suggested before. In Chapter 6, we will develop this interpretation more rigorously for a microstrip and use it to derive an equivalent circuit representation to characterize the input impedance of the microstrip.

To extract the propagation constant, the effective permittivity and the losses of the transmission line, we will again consider the residue contribution of the current, defined in (4.40). By examining (4.40), it becomes apparent that the propagation constant of the current wave is given by the location of the pole k_{xp} in the spectral plane. As an example, Fig. 4.6a shows the dispersion diagram of a dipole in free space having a height $w_z = 1\mu$m and width $w_y = 20\mu$m, constituted of a material with conductivity $\sigma = 4.1 \cdot 10^7$S/m.

To extract the effective permittivity and the losses of the transmission line, we will express the propagation constant as $k_{xp} = \beta - j\alpha$, where β denotes the phase constant and α denotes the attenuation constant. The effective dielectric permittivity can then be obtained from the phase constant as follows

$$\varepsilon_{\text{eff}} = \left(\frac{\beta}{k_0}\right)^2. \tag{4.62}$$

The losses are characterized by the attenuation constant α and can be converted to dB$/\lambda$ as follows

$$\alpha[\text{dB}/\lambda] = 8.868\alpha[\text{Np}]\lambda. \tag{4.63}$$

Finally, the formulation developed in Section 4.1.1 has been validated by obtaining the longitudinal current $i(x)$ for a dipole, located in free space, having a thickness $w_z = 10\mu$m and width $w_y = 10\mu$m, constituted of a material with conductivity $\sigma = 10^7$S/m. Fig. 4.6b shows the current obtained from (4.39), together with the current, obtained from CST as well as the residue contribution $i_{\text{res}}(x)$. Fig. 4.6b shows that the current, obtained from CST, and the current, obtained from (4.39), are in excellent agreement. Moreover, at large distance from the gap (i.e. $x > 4\lambda_0$), the current obtained from (4.39) becomes indistinguishable from the residue contribution $i_{\text{res}}(x)$.

4.1.4. Parametric analysis

In this subsection, we will illustrate the formulation, developed in Sections 4.1.1 to 4.1.3, by performing a parametric analysis versus the relevant dimensions of the dipole. Fig. 4.7a shows the attenuation in dB$/\lambda_0$ of a dipole in free space having a thickness $w_z = 1\mu$m, constituted of a material with conductivity $\sigma = 4.1 \cdot 10^7$S/m for varying width. Moreover, Fig. 4.7a shows the comparison between the attenuation constant, obtained by assuming a uniform current distribution on the cross-section, and the attenuation constant, obtained by using the Leontovich boundary condition. Clearly, the assumption on the transverse current distribution has a major impact on the losses of the transmission line. In particular, the losses, obtained by using the Leontovich boundary condition are significantly larger, since the current is assumed to be distributed over a smaller area. For the same reason, the losses tend to decrease when the width of the dipole is increased.

Fig. 4.7b shows the attenuation in dB$/\lambda_0$ of a dipole in free space having a width $w_y = 20\mu$m, constituted of a material with conductivity $\sigma = 4.1 \cdot 10^7$S/m for varying thickness. Similar to before, the losses tend to decrease when the thickness is increased, since the area over which the current is distributed becomes larger. However, when we compare the attenuation constant, obtained by assuming a uniform distribution on the cross-section to the attenuation constant, obtained using the Leontovich boundary condition, we may notice

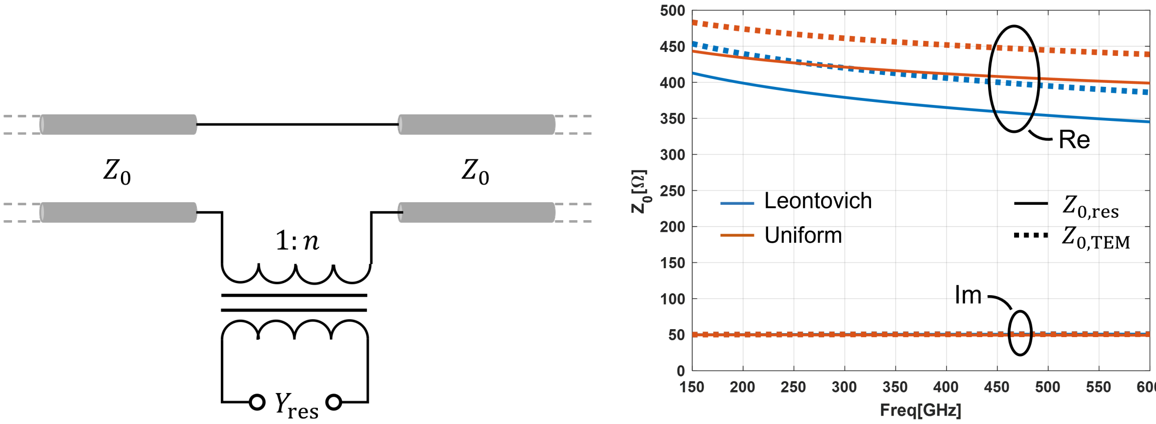

(a) (b)

Figure 4.5: (a) The equivalent circuit obtained by interpreting $Y_{\rm res}$ as the contribution from two parallel transmission lines connected to a transformer, and (b) a comparison between the characteristic impedance obtained from (4.57) and the characteristic impedance obtained from (4.61)

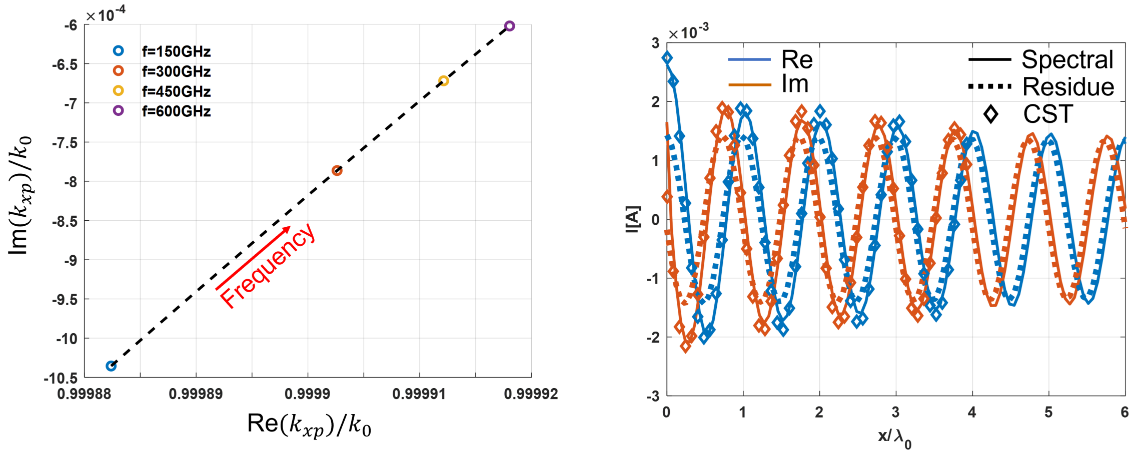

(a) (b)

Figure 4.6: (a) The dispersion diagram of a dipole in free space having a thickness $w_z = 1\mu$m and width $w_y = 20\mu$m, constituted of a material with conductivity $\sigma = 4.1 \cdot 10^7$S/m, and (b) the current on a dipole in free space having a thickness $w_z = 10\mu$m and width $w_y = 10\mu$m, constituted of a material with conductivity $\sigma = 10^7$S/m, obtained from (4.39) and CST, together with the residue contribution, given by (4.40)

that the dependence on w_z is much weaker in the latter case. This can be understood by noting that the width of the dipole is much larger than the thickness. Since the current is localized at the outer surface of the dipole, varying the thickness tends to have a small effect on the total area over which the current is distributed. Finally, Figs. 4.7a and 4.7b show that the attenuation constant tends to decrease, when the frequency is increased. This can be understood by noting that the dipole becomes electrically larger, which results in a smaller attenuation constant.

Figs. 4.7c and 4.7d show the characteristic impedance, obtained using the definition in (4.61), of a dipole with the same dimensions and material parameters as Figs. 4.7a and 4.7b, respectively. Figs. 4.7c and 4.7d show that the characteristic impedance has a very weak dependence on the dimensions of the dipole. This can be understood by considering a charge distributed on an infinitely long cylinder, as shown in Fig. 4.8. As a consequence of Gauss' law, the electric field outside the charge region does not depend on the radius. In the present case, we are of course considering a current distribution instead of a charge distribution. However, since the characteristic impedance is defined, by considering only the residue contribution $i_{\rm res}(x)$, we may assume that a quasi-TEM wave is propagating along the dipole. With this assumption, the transverse electric field satisfies the Laplace equation as in electrostatics, which results in a characteristic impedance that is independent of

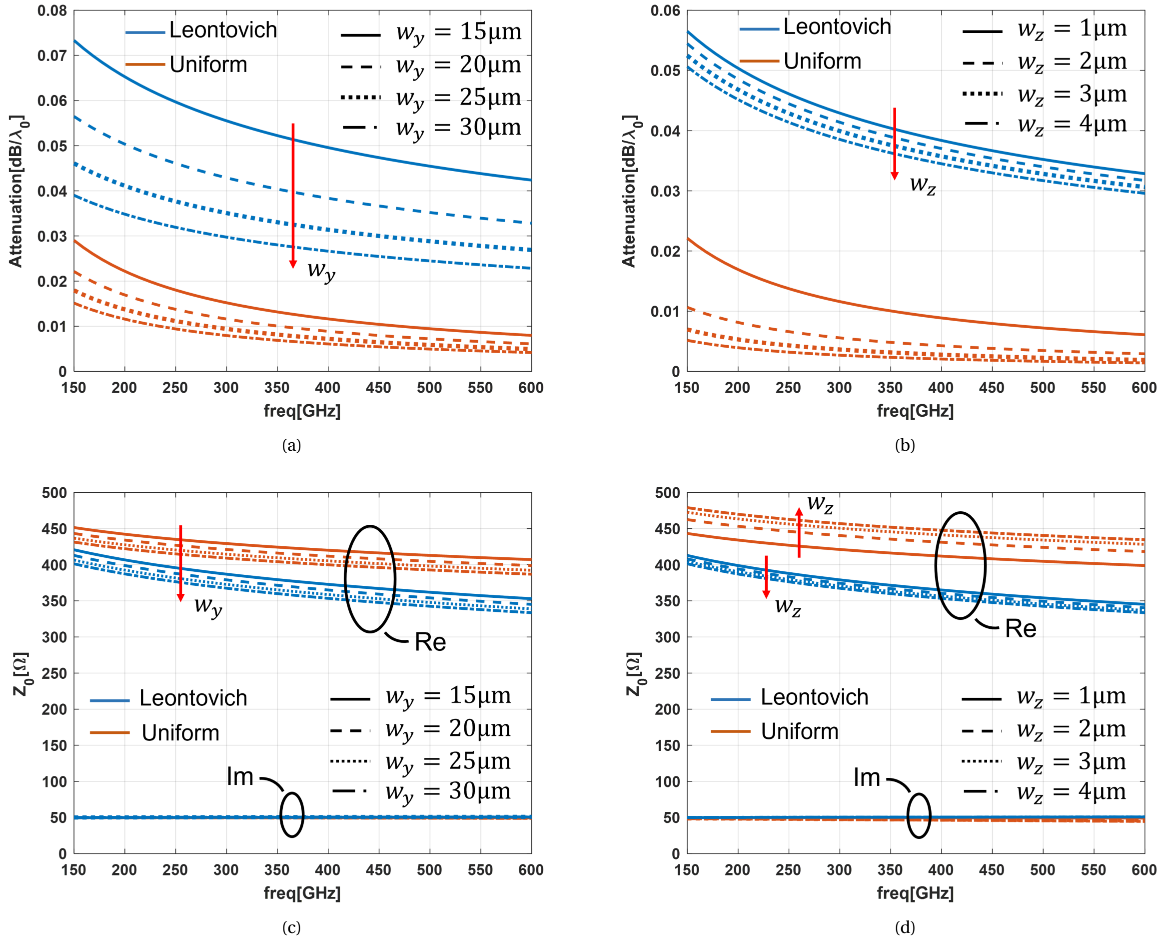

Figure 4.7: Losses of a dipole in free space, constituted of a material with conductivity $4.1 \cdot 10^7$S/m and (a) having a metal thickness $w_z = 1\mu$m for varying width w_y, and (b) having a width $w_y = 20\mu$m for varying metal thickness w_z, and characteristic impedance of a dipole in free space, constituted of a material with conductivity $4.1 \cdot 10^7$S/m and (c) having a metal thickness $w_z = 1\mu$m for varying width w_y, and (d) having a width $w_y = 20\mu$m for varying metal thickness w_z

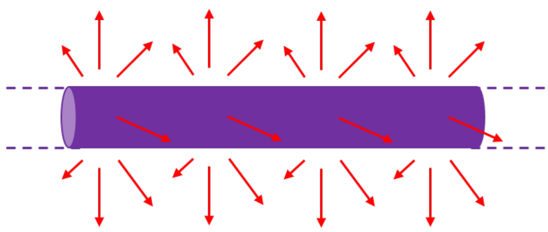

Figure 4.8: Charge distributed on an infinitely long cylinder

the transverse dimensions of the dipole. The weak dependence that can still be observed in Figs. 4.7c and 4.7d originates from the lack of a cylindrical symmetry. Additionally, Figs. 4.7c and 4.7d show that the difference between the characteristic impedance, obtained by assuming a uniform distribution on the cross-section, and the characteristic impedance, obtained by using the Leontovich boundary condition, tends to increase with frequency. This can be understood by noting that the penetration depth δ_p decreases with frequency, which increases the difference between the two distributions. As mentioned before, Figs. 4.7c and 4.7d have been obtained using the definition in (4.61). The same parametric analysis has been performed, using the definition in (4.57). For the sake of conciseness, these results have been omitted. Nevertheless, when using the definition in (4.57), the qualitative behaviour remains the same as in Figs. 4.7c and 4.7d.

4.2. Ground plane with image theorem

In Section 4.1, a spectral domain formulation has been developed to study infinitely long dipoles in free space, taking into account the non-zero thickness of the conductor. In this section, we will introduce the presence of an infinitely extended perfectly conducting ground plane by applying the image theorem.

In Section 4.2.1, we will derive the transmission line Green's function of the geometry. Next Section 4.2.2 will introduce one possible definition of the characteristic impedance in which the voltage along the transmission line is defined as the line integral of the transverse electric field. Finally, in Section 4.2.3, we will demonstrate the formulation, developed in Section 4.2.1 and 4.2.2 by performing a parametric analysis versus the relevant dimensions of the transmission line.

4.2.1. Derivation Green's function

The presence of an infinitely extended perfectly conducting ground plane can be introduced by applying the image theorem [42], illustrated in Fig. 4.9. The scattered field will then be the superposition of the field, produced by the original current distribution $j_t(y,z)$, and the field produced by the image current $j_{\text{t,image}}(y,z)$. The original current distribution is still given by (4.19). Moreover, the image current $j_{\text{t,image}}(y,z)$ can be obtained from the original current distribution by applying a shift of $-2(d+w_z/2)$ along $\hat{z}$, which results in the following expression

$$j_{\text{t,image}}(y,z) = \frac{1}{2\delta_p(w_y+w_z-2\delta_p)}\left(j_{\text{out,image}}(y,z) - j_{\text{in,image}}(y,z)\right), \tag{4.64}$$

where $j_{\text{out,image}}(y,z)$ and $j_{\text{in,image}}(y,z)$ are given by the following expressions

$$j_{\text{out,image}}(y,z) = \text{rect}\left(\frac{y}{w_y}\right)\text{rect}\left(\frac{z+2(d+w_z/2)}{w_z}\right) \tag{4.65}$$

$$j_{\text{in,image}}(y,z) = \text{rect}\left(\frac{y}{w_y-2\delta_p}\right)\text{rect}\left(\frac{z+2(d+w_z/2)}{w_z-2\delta_p}\right). \tag{4.66}$$

By Applying a Fourier transform to (4.65) and (4.66), we obtain the following expressions

$$J_{\text{out,image}}(k_y,k_z) = w_y w_z \text{sinc}\left(\frac{k_y w_y}{2}\right)\text{sinc}\left(\frac{k_z w_z}{2}\right)e^{-jk_z 2(d+w_z/2)} \tag{4.67}$$

$$J_{\text{in,image}}(k_y,k_z) = (w_y-2\delta_p)(w_z-2\delta_p)\text{sinc}\left(k_y\frac{w_y-2\delta_p}{2}\right)\text{sinc}\left(k_z\frac{w_z-2\delta_p}{2}\right)e^{-jk_z 2(d+w_z/2)}, \tag{4.68}$$

where the multiplication factor $e^{-jk_z 2(d+w_z/2)}$ represents the displacement along $\hat{z}$. The spectral current is still given by (4.17), where the spatial projections are performed with respect to the original current distribution $j_t(y,z)$, since the image current $j_{t,image}(y,z)$ is only fictitious. As a consequence of the superposition principle, $D(k_x)$ can be written as follows

$$D(k_x) = D_{\text{original}}(k_x) + D_{\text{image}}(k_x), \tag{4.69}$$

where $D_{\text{original}}(k_x)$ denotes the original longitudinal spectral Green's function, given by (4.30), and $D_{\text{image}}(k_x)$ denotes the additional term, resulting from the image current. $D_{\text{image}}(k_x)$ can be expressed as follows

$$D_{\text{image}}(k_x) = \frac{1}{4\pi^2}\int_{-\infty}^{\infty}\int_{-\infty}^{\infty} G_{xx}^{ej}(k_x,k_y,k_z)J_{t,image}(k_y,k_z)J_t(k_y,k_z)\,dk_y\,dk_z. \tag{4.70}$$

Note again that the projection is performed with respect to the original current distribution. Similar to before, $D_{\text{image}}(k_x)$ can be expressed as follows

$$D_{\text{image}}(k_x) = \frac{1}{4\delta_p^2(w_y+w_z-2\delta_p)^2}\left(I_{\text{1,image}} + I_{\text{2,image}} - 2I_{\text{3,image}}\right), \tag{4.71}$$

where $I_{\text{1,image}}$, $I_{\text{2,image}}$ and $I_{\text{3,image}}$ are given by the following expressions

$$I_{\text{1,image}} = \frac{j\zeta}{k}\frac{w_y^2 w_z^2(k^2-k_x^2)}{4\pi^2}\int_{-\infty}^{\infty}\int_{-\infty}^{\infty}\frac{\text{sinc}^2(k_y w_y/2)\,\text{sinc}^2(k_z w_z/2)}{k^2-k_x^2-k_y^2-k_z^2}e^{-jk_z 2(d+w_z/2)}\,dk_y\,dk_z \tag{4.72}$$

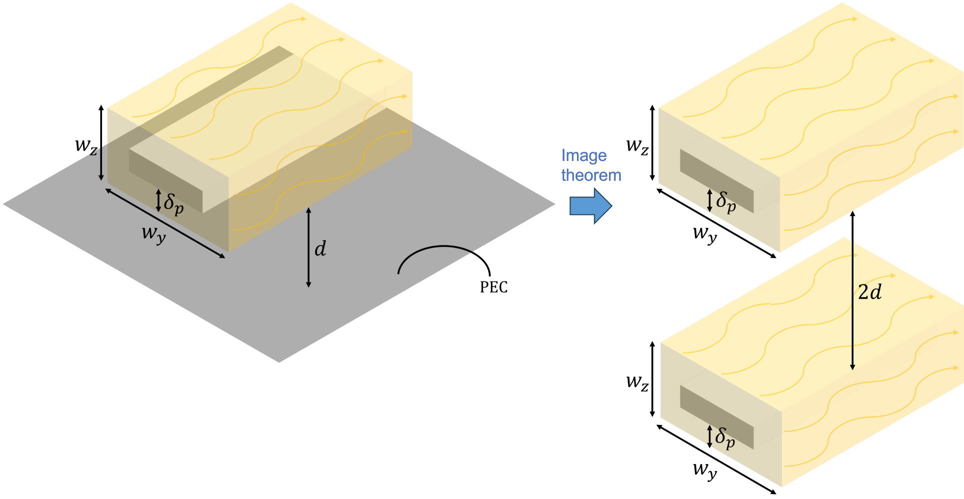

Figure 4.9: Application of the image theorem [42] to replace a perfectly conducting ground plane by an image current

$$I_{2,\mathrm{image}} = \frac{j\zeta}{k}\frac{(w_y-2\delta_p)^2(w_z-2\delta_p)^2(k^2-k_x^2)}{4\pi^2} \int_{-\infty}^{\infty}\int_{-\infty}^{\infty} \frac{\mathrm{sinc}^2\big(k_y(w_y-2\delta_p)/2\big)\,\mathrm{sinc}^2\big(k_z(w_z-2\delta_p)/2\big)}{k^2-k_x^2-k_y^2-k_z^2} e^{-jk_z 2(d+w_z/2)}\, dk_y\, dk_z \tag{4.73}$$

$$I_{3,\mathrm{image}} = \frac{j\zeta}{k}\frac{w_y w_z(w_y-2\delta_p)(w_z-2\delta_p)(k^2-k_x^2)}{4\pi^2}\cdot \int_{-\infty}^{\infty}\int_{-\infty}^{\infty} \frac{\mathrm{sinc}\big(k_y(w_y-2\delta_p)/2\big)\,\mathrm{sinc}\big(k_y w_y/2\big)\,\mathrm{sinc}\big(k_z(w_z-2\delta_p)/2\big)\,\mathrm{sinc}(k_z w_z/2)}{k^2-k_x^2-k_y^2-k_z^2} e^{-jk_z 2(d+w_z/2)}\, dk_y\, dk_z. \tag{4.74}$$

As shown in Appendix E, the integrals in k_z can be closed analytically, which results in the following expressions

$$I_{1,\mathrm{image}} = \frac{j\zeta}{k}\frac{(k_x^2-k^2)w_y^2}{4\pi}\int_{-\infty}^{\infty}\mathrm{sinc}^2\left(\frac{k_y w_y}{2}\right)\frac{e^{-2(d+w_z)\sqrt{k_x^2+k_y^2-k^2}}+e^{-2d\sqrt{k_x^2+k_y^2-k^2}}-2e^{-(2d+w_z)\sqrt{k_x^2+k_y^2-k^2}}}{(k_x^2+k_y^2-k^2)^{\frac{3}{2}}}\, dk_y \tag{4.75}$$

$$I_{2,\mathrm{image}} = \frac{j\zeta}{k}\frac{(k_x^2-k^2)(w_y-2\delta)^2}{4\pi}\cdot \int_{-\infty}^{\infty}\mathrm{sinc}^2\left(\frac{k_y w_y}{2}\right)\frac{e^{-2(d+w_z-\delta_p)\sqrt{k_x^2+k_y^2-k^2}}+e^{-2(d+\delta_p)\sqrt{k_x^2+k_y^2-k^2}}-2e^{-(2d+w_z)\sqrt{k_x^2+k_y^2-k^2}}}{(k_x^2+k_y^2-k^2)^{\frac{3}{2}}}\, dk_y \tag{4.76}$$

$$I_{3,\mathrm{image}} = \frac{j\zeta}{k}\frac{(k_x^2-k^2)w_y(w_y-2\delta_p)}{4\pi}\int_{-\infty}^{\infty}\mathrm{sinc}\left(\frac{k_y w_y}{2}\right)\mathrm{sinc}\left(k_y\frac{w_y-2\delta_p}{2}\right)\cdot \frac{e^{-(2d+2w_z-\delta_p)\sqrt{k_x^2+k_y^2-k^2}}+e^{-(2d+\delta_p)\sqrt{k_x^2+k_y^2-k^2}}-e^{-(2d+w_z+\delta)\sqrt{k_x^2+k_y^2-k^2}}-e^{-(2d+w_z-\delta)\sqrt{k_x^2+k_y^2-k^2}}}{(k_x^2+k_y^2-k^2)^{\frac{3}{2}}}\, dk_y. \tag{4.77}$$

In Section 4.2.3, we will demonstrate the importance of the assumption on the transverse current distribution by making a comparison between the results obtained by using the Leontovich boundary condition and the results obtained by assuming a uniform distribution on the cross-section. If a uniform current distribution is used in the calculation of $D(k_x)$, $D_{\mathrm{original}}(k_x)$ is given by (4.37). To obtain $D_{\mathrm{image}}(k_x)$, only (4.75), should be retained, which results in the following expression

$$D_{\mathrm{image}}(k_x) = \frac{j\zeta}{k}\frac{(k_x^2-k^2)}{4\pi w_z^2}\int_{-\infty}^{\infty}\mathrm{sinc}^2\left(\frac{k_y w_y}{2}\right)\frac{e^{-2(d+w_z)\sqrt{k_x^2+k_y^2-k^2}}+e^{-2d\sqrt{k_x^2+k_y^2-k^2}}-2e^{-(2d+w_z)\sqrt{k_x^2+k_y^2-k^2}}}{(k_x^2+k_y^2-k^2)^{\frac{3}{2}}}\, dk_y. \tag{4.78}$$

4.2.2. Characteristic impedance

In this section, we will provide one possible definition of the characteristic impedance in which the voltage along the transmission line is defined as the line integral of the transverse electric field. Similar to Section 4.1.2, the current wave $i_{\text{res}}(x)$ and its amplitude I^+ are given by (4.40) and (4.41). However, since the ground plane acts as an equipotential surface, we will now define the voltage $v(x)$ as follows

$$v(x) = -\int_{-(d+w_z/2)}^{-w_z/2} e_z(x, y=0, z)\,dz, \tag{4.79}$$

where $e_z(x, y=0, z)$ denotes the z-component of the electric field, observed at $y=0$. Note that the integral in (4.79) is defined from $-(d+w_z/2)$ to $-w_z/2$, since the origin of the reference system is defined to be at the center of the dipole. By expressing $e_z(x, y=0, z)$ in terms of its plane wave spectrum, and by separating the contribution from the original current distribution $j_t(y,z)$ and the contribution from the image current $j_{t,\text{image}}(y,z)$, one can express (4.79) as follows

$$\begin{aligned} v(x) = -\frac{j\zeta}{k}\frac{1}{8\pi^3}\int_{-\infty}^{\infty}\int_{-\infty}^{\infty}\int_{-\infty}^{\infty} I(k_x)(J_t(k_x,k_y,k_z) + J_{t,\text{image}}(k_x,k_y,k_z))\cdot \\ \frac{k_z k_x}{k^2-k_x^2-k_y^2-k_z^2} e^{-jk_x x}\int_{-(d+w_z/2)}^{-w_z/2} e^{-jk_z z}\,dz\,dk_x\,dk_y\,dk_z. \end{aligned} \tag{4.80}$$

By closing the integral in z analytically, (4.80) becomes as follows

$$\begin{aligned} v(x) = \frac{\zeta}{k}\frac{1}{8\pi^3}\int_{-\infty}^{\infty}\int_{-\infty}^{\infty}\int_{-\infty}^{\infty} I(k_x)(J_t(k_x,k_y,k_z) + J_{t,\text{image}}(k_x,k_y,k_z))\cdot \\ \frac{k_x}{k^2-k_x^2-k_y^2-k_z^2}(e^{-jk_z(d+w_z)/2} - e^{-jk_z w_z/2})e^{-jk_x x}\,dk_x\,dk_y\,dk_z. \end{aligned} \tag{4.81}$$

The voltage $v(x)$ can now be expressed as a combination of four terms,

$$v(x) = \frac{v_{\text{out}}(x) + v_{\text{out,image}}(x) - (v_{\text{in}}(x) + v_{\text{in,image}}(x))}{2\delta_p(w_y + w_z - 2\delta_p)} \tag{4.82}$$

where $v_{\text{out}}(x)$, $v_{\text{out,image}}(x)$, $v_{\text{in}}(x)$ and $v_{\text{in,image}}(x)$ are expressed as follows

$$\begin{aligned} v_{\text{out}}(x) = \frac{\zeta}{k}\frac{w_y w_z}{8\pi^3}\int_{-\infty}^{\infty}\int_{-\infty}^{\infty}\int_{-\infty}^{\infty} I(k_x)\operatorname{sinc}\left(\frac{k_y w_y}{2}\right)\operatorname{sinc}\left(\frac{k_z w_z}{2}\right)\cdot \\ \frac{k_x}{k^2-k_x^2-k_y^2-k_z^2}(e^{jk_z(d+w_z/2)} - e^{jk_z w_z/2})e^{-jk_x x}\,dk_x\,dk_y\,dk_z \end{aligned} \tag{4.83}$$

$$\begin{aligned} v_{\text{in}}(x) = \frac{\zeta}{k}\frac{w_y w_z}{8\pi^3}\int_{-\infty}^{\infty}\int_{-\infty}^{\infty}\int_{-\infty}^{\infty} I(k_x)\operatorname{sinc}\left(k_y\frac{w_y-2\delta_p}{2}\right)\operatorname{sinc}\left(k_z\frac{w_z-2\delta_p}{2}\right)\cdot \\ \frac{k_x}{k^2-k_x^2-k_y^2-k_z^2}(e^{jk_z(d+w_z/2)} - e^{jk_z w_z/2})e^{-jk_x x}\,dk_x\,dk_y\,dk_z \end{aligned} \tag{4.84}$$

$$\begin{aligned} v_{\text{out,image}}(x) = -\frac{\zeta}{k}\frac{w_y w_z}{8\pi^3}\int_{-\infty}^{\infty}\int_{-\infty}^{\infty}\int_{-\infty}^{\infty} I(k_x)\operatorname{sinc}\left(\frac{k_y w_y}{2}\right)\operatorname{sinc}\left(\frac{k_z w_z}{2}\right)e^{-jk_z 2(d+w_z/2)}\cdot \\ \frac{k_x}{k^2-k_x^2-k_y^2-k_z^2}(e^{jk_z(d+w_z/2)} - e^{jk_z w_z/2})e^{-jk_x x}\,dk_x\,dk_y\,dk_z \end{aligned} \tag{4.85}$$

$$\begin{aligned} v_{\text{in,image}}(x) = -\frac{\zeta}{k}\frac{w_y w_z}{8\pi^3}\int_{-\infty}^{\infty}\int_{-\infty}^{\infty}\int_{-\infty}^{\infty} I(k_x)\operatorname{sinc}\left(k_y\frac{w_y-2\delta_p}{2}\right)\operatorname{sinc}\left(k_y\frac{w_y-2\delta_p}{2}\right)e^{-jk_z 2(d+w_z/2)}\cdot \\ \frac{k_x}{k^2-k_x^2-k_y^2-k_z^2}(e^{jk_z(d+w_z/2)} - e^{jk_z w_z/2})e^{-jk_x x}\,dk_x\,dk_y\,dk_z. \end{aligned} \tag{4.86}$$

As shown in Appendix D, the integrals in k_z can be closed analytically, which leads to the following expressions

$$v_{\text{out}}(x) = \frac{w_y}{8\pi^2}\int_{-\infty}^{\infty}\int_{-\infty}^{\infty} I(k_x)\text{sinc}\left(\frac{k_y w_y}{2}\right)\frac{\zeta k_x}{k}\cdot \frac{1+e^{-(d+w_z)\sqrt{k_x^2+k_y^2-k^2}}-e^{-d\sqrt{k_x^2+k_y^2-k^2}}-e^{-w_z\sqrt{k_x^2+k_y^2-k^2}}}{k_x^2+k_y^2-k^2}e^{-jk_xx}\,dk_x\,dk_y \tag{4.87}$$

$$v_{\text{in}}(x) = \frac{w_y-2\delta}{8\pi^2}\int_{-\infty}^{\infty}\int_{-\infty}^{\infty} I(k_x)\text{sinc}\left(k_y\frac{w_y-2\delta_p}{2}\right)\frac{\zeta k_x}{k}\cdot \frac{e^{-\delta_p\sqrt{k_x^2+k_y^2-k^2}}+e^{-(d+w_z-\delta_p)\sqrt{k_x^2+k_y^2-k^2}}-e^{-(d+\delta_p)\sqrt{k_x^2+k_y^2-k^2}}-e^{-(w_z-\delta_p)\sqrt{k_x^2+k_y^2-k^2}}}{k_x^2+k_y^2-k^2}e^{-jk_xx}\,dk_x\,dk_y \tag{4.88}$$

$$v_{\text{out,image}}(x) = -\frac{w_y}{8\pi^2}\int_{-\infty}^{\infty}\int_{-\infty}^{\infty} I(k_x)\text{sinc}\left(\frac{k_y w_y}{2}\right)\frac{\zeta k_x}{k}\cdot \frac{e^{-(d+w_z)\sqrt{k_x^2+k_y^2-k^2}}+e^{-2d\sqrt{k_x^2+k_y^2-k^2}}-e^{-d\sqrt{k_x^2+k_y^2-k^2}}-e^{-(2d+w_z)\sqrt{k_x^2+k_y^2-k^2}}}{k_x^2+k_y^2-k^2}e^{-jk_xx}\,dk_x\,dk_y \tag{4.89}$$

$$v_{\text{in,image}}(x) = -\frac{w_y-2\delta_p}{8\pi^2}\int_{-\infty}^{\infty}\int_{-\infty}^{\infty} I(k_x)\text{sinc}\left(k_y\frac{w_y-2\delta_p}{2}\right)\frac{\zeta k_x}{k}e^{-jk_xx}\cdot \frac{e^{-(d+w_z-\delta_p)\sqrt{k_x^2+k_y^2-k^2}}+e^{-(2d+\delta_p)\sqrt{k_x^2+k_y^2-k^2}}-e^{-(d+\delta_p)\sqrt{k_x^2+k_y^2-k^2}}-e^{-(2d+w_z-\delta_p)\sqrt{k_x^2+k_y^2-k^2}}}{k_x^2+k_y^2-k^2}\,dk_x\,dk_y. \tag{4.90}$$

To simplify the notation, we will define the function $Z(k_x)$ as follows

$$Z(k_x) = Z_{\text{out}}(k_x) - Z_{\text{in}}(k_x), \tag{4.91}$$

where $Z_{\text{out}}(k_x)$ and $Z_{\text{in}}(k_x)$ are given by the following expressions

$$Z_{\text{out}}(k_x) = \frac{\zeta k_x}{k}\frac{w_y}{8\pi\delta(w_y+w_z-2\delta)}\int_{-\infty}^{\infty}\text{sinc}\left(\frac{k_y w_y}{2}\right)\cdot \frac{1+e^{-(2d+w_z)\sqrt{k_x^2+k_y^2-k^2}}-e^{-2d\sqrt{k_x^2+k_y^2-k^2}}-e^{-w_z\sqrt{k_x^2+k_y^2-k^2}}}{k_x^2+k_y^2-k^2}dk_y \tag{4.92}$$

$$Z_{\text{in}}(k_x) = \frac{\zeta k_x}{k}\frac{w_y-2\delta}{8\pi\delta(w_y+w_z-2\delta)}\int_{-\infty}^{\infty}\text{sinc}\left(k_y\frac{w_y-2\delta_p}{2}\right)\cdot \frac{e^{-\delta\sqrt{k_x^2+k_y^2-k^2}}+e^{-(2d+w_z-\delta)\sqrt{k_x^2+k_y^2-k^2}}-e^{-(2d+\delta)\sqrt{k_x^2+k_y^2-k^2}}-e^{-(w_z-\delta)\sqrt{k_x^2+k_y^2-k^2}}}{k_x^2+k_y^2-k^2}dk_y. \tag{4.93}$$

With these definitions, the voltage $v(x)$ can be expressed as in (4.54). Similar to before, the residue contribution gives rise to a traveling voltage wave $v_{\text{res}}(x)$, given by (4.55), with amplitude V^+, given by (4.56). The characteristic impedance $Z_{0,\text{TEM}}$ can then be defined as in (4.57).

In section 4.2.3, we will demonstrate the importance of the assumption on the transverse current distribution by comparing the characteristic, obtained by using the Leontovich boundary condition, with the characteristic impedance, obtained by assuming a uniform current distribution on the cross-section. If a uniform current distribution is assumed, only $v_{\text{out}}(x)$ and $v_{\text{out,image}}(x)$ should be used in the calculation of $Z(k_x)$. Consequently, $Z(k_x)$ becomes as follows

$$Z(k_x) = \frac{\zeta k_x}{w_z k}\int_{-\infty}^{\infty}\text{sinc}\left(\frac{k_y w_y}{2}\right)\frac{1+e^{-(2d+w_z)\sqrt{k_x^2+k_y^2-k^2}}-e^{-2d\sqrt{k_x^2+k_y^2-k^2}}-e^{-w_z\sqrt{k_x^2+k_y^2-k^2}}}{k_x^2+k_y^2-k^2}dk_y, \tag{4.94}$$

In this case, the characteristic impedance $Z_{0,\text{TEM}}$ is still defined by (4.57), where k_{xp} denotes the pole of the current spectrum $I(k_x)$ that is obtained, using (4.37) to calculate $D_{\text{original}}(k_x)$ and (4.78) to calculate $D_{\text{image}}(k_x)$.

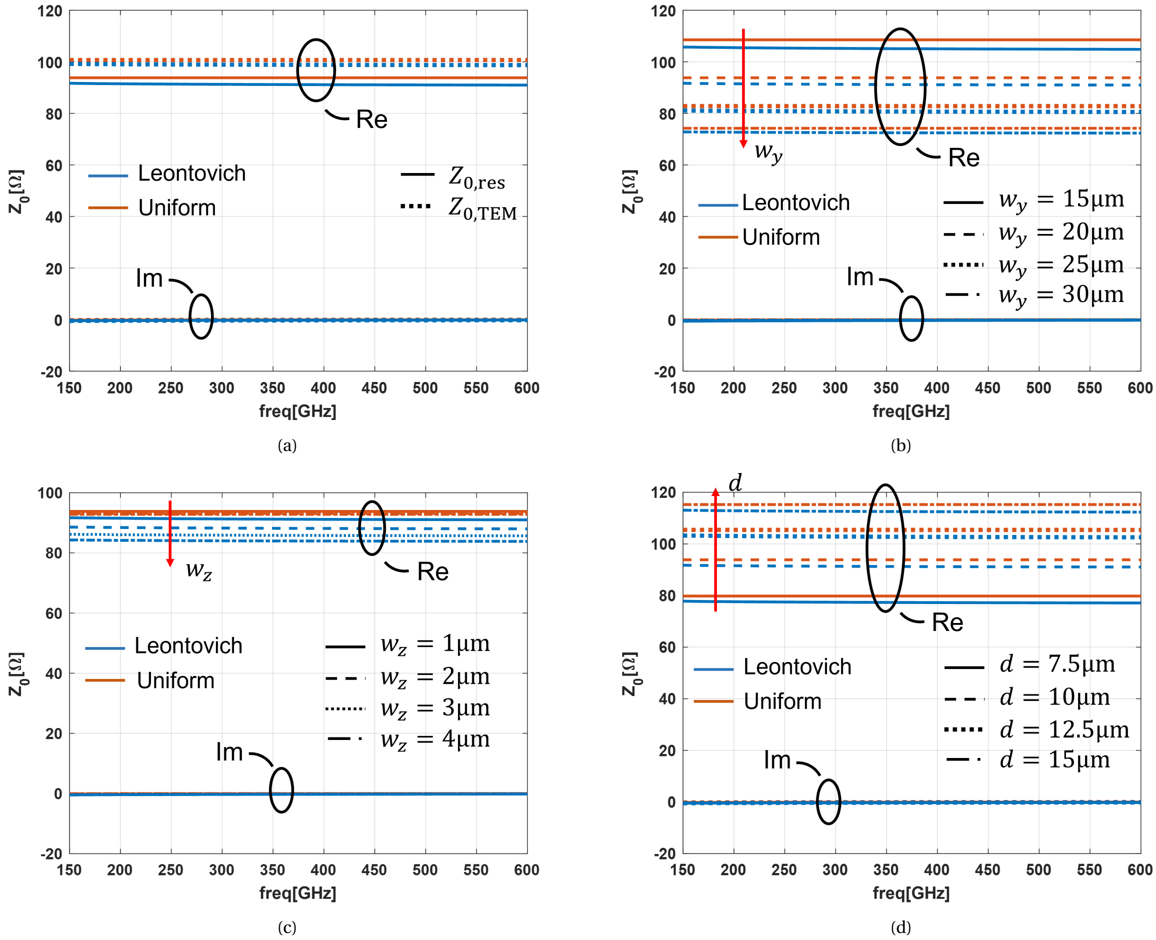

(a) (b) (c) (d)

Figure 4.10: Characteristic impedance of a dipole, constituted of a material with conductivity $\sigma = 4.1 \cdot 10^7$ S/m, in the presence of a perfectly conducting ground plane, (a) having a metal thickness $w_z = 1\mu$m and a width $w_y = 20\mu$m, located at a distance $d = 10\mu$m from the ground plane, with a comparison between the definition in (4.57) and the definition in (4.61), (b) having a metal thickness $w_z = 1\mu$m, located at a distance $d = 10\mu$m from the ground plane for varying width w_y, and (c) having a width $w_y = 20\mu$m, located at a distance $d = 10\mu$m from the ground plane for varying metal thickness w_z, and (d) having a metal thickness $w_z = 1\mu$m and width $w_y = 20\mu$m for varying distance d between the metal strip and the ground plane

4.2.3. Parametric analysis

In this section, we will first show a comparison between the characteristic impedance obtained from the definition in (4.57) and the characteristic impedance obtained from the definition in (4.61). Next, we will demonstrate the formulation, developed in Sections 4.2.1 and 4.2.2, by performing a parametric analysis versus the relevant dimensions of the transmission line.

Fig. 4.10a shows the comparison between the characteristic impedance obtained from (4.57) and the characteristic impedance obtained from (4.61), for a dipole having a height $w_z = 1\mu$m and width $w_y = 20\mu$m, constituted of a material with conductivity $\sigma = 4.1 \cdot 10^7$ S/m, located at a distance $d = 10\mu$m from an infinitely extended perfectly conducting ground plane. Similar to Section 4.1.3, the resemblance between the results obtained from the two definitions seem to support the interpretation of the residue contribution as a current wave propagating along two infinitely long transmission lines, as suggested in Section 4.1.3. The difference, observed in Fig. 4.10a, originates from an underlying difference between the two definitions of the characteristic impedance. In the definition of (4.61), the voltage over the gap is defined by averaging the incident electric field over the cross-section of the dipole. On the other hand, in the definition of (4.57), the voltage along the dipole is defined as the line integral of the transverse electric field, starting from the surface of the metal. Nevertheless, the similarity between the characteristic impedance, obtained from the two different definitions, can be regarded as a justification to interpret the residue contribution of the input admittance as the contribution from two infinitely long transmission lines.

(a) (b)

Figure 4.11: Field distribution of a microstrip (a) neglecting fringe effects and (b) assuming a realistic field distribution

Fig. 4.10b shows the characteristic impedance, obtained from the definition in (4.57), of a dipole having a thickness $w_z = 1\mu$m, constituted of a material with conductivity $\sigma = 4.1 \cdot 10^7$S/m, located at a distance $d = 10\mu$m from a perfectly conducting ground plane for varying width of the dipole. Fig. 4.10b shows that the characteristic impedance decreases when the width of the dipole is increased. This can be understood by considering a quasi-static analysis, in which the electric field is assumed to be confined between the metals, and fringe effects are ignored, as illustrated in Fig 4.11a. If the width of the dipole is increased, the current is distributed over a larger area. Consequently, the electric field between the metals is weaker, which leads to a lower voltage and therefore a smaller characteristic impedance. In reality, the field distribution is more similar to Fig 4.11b. Nevertheless, one should expect a similar qualitative behaviour.

Fig. 4.10c shows the characteristic impedance, obtained from the definition in (4.57), of a dipole having a width $w_y = 20\mu$m, constituted of a material with conductivity $\sigma = 4.1 \cdot 10^7$S/m, and located at a distance $d = 10\mu$m from a perfectly conducting ground plane for varying thickness of the dipole. Similar to before, Fig. 4.10c shows that the characteristic impedance decreases when the thickness of the dipole is increased. Fig. 4.10d shows the characteristic impedance, obtained from the definition in (4.57), of a dipole having a width $w_y = 20\mu$m and thickness $w_z = 1\mu$m, constituted of a material with conductivity $\sigma = 4.1 \cdot 10^7$S/m, for varying distance between the dipole and the ground plane. Fig. 4.10d shows that the characteristic impedance increases when the distance between the strip and the ground plane is increased. This can be understood by considering the same quasi-static analysis as before. By making the same assumption on the field distribution, the electric field strength becomes independent of d. Hence, increasing the distance, leads to a higher voltage between the metals and therefore a larger characteristic impedance. As mentioned before, Figs. 4.10b to 4.10d have been obtained using the definition in (4.61). The same parametric analysis has been performed, using the definition in (4.57). For the sake of conciseness, these results have been omitted. Nevertheless, when using the definition in (4.57), the qualitative behaviour remains the same as in Figs. 4.10b to 4.10d.

Fig. 4.12a shows the attenuation in dB/λ_0 of a dipole with the same dimensions and material parameters as in Fig. 4.10b. Fig. 4.12b shows that the attenuation constant decreases, when the width of the dipole is increased. However, the dependence on the width is much weaker compared to Fig. 4.7c, in which the characteristic impedance of a dipole in free space was shown. This can be understood by considering the perturbation method [43], which allows us to express the attenuation constant α as follows

$$\alpha = \frac{P_l}{P_0}, \tag{4.95}$$

where P_l denotes the power lost per unit length and P_0 denotes the power transmitted along the transmission line. Both for a dipole located in free space and for a dipole in the presence of a ground plane, the power lost per unit length decreases, if the width of the dipole is increased, due to the increased area over which the current is distributed. However, we may recall from Fig. 4.10b that the characteristic impedance of a dipole in the presence of a ground plane decreases, if the width of the dipole is increased. Since P_0 is proportional to the characteristic impedance, the power transmitted along the line decreases as well. For a dipole in the presence of a ground plane, these two effects compensate, which leads to a much weaker dependence of the attenuation constant on the width.

Fig. 4.12b shows the attenuation in dB/λ_0 of a dipole with the same dimensions and material parameters as in Fig. 4.10c. Similar to before, Fig. 4.12b shows that the attenuation constant decreases, when the thickness of the dipole is increased, due to the larger area over which the current is distributed. By examining Fig. 4.12b, it becomes apparent that the dependence is much weaker, if the Leontovich boundary condition is used. The explanation is similar to the one given in Section 4.2.1. Since the width of the metal strip is much larger than its

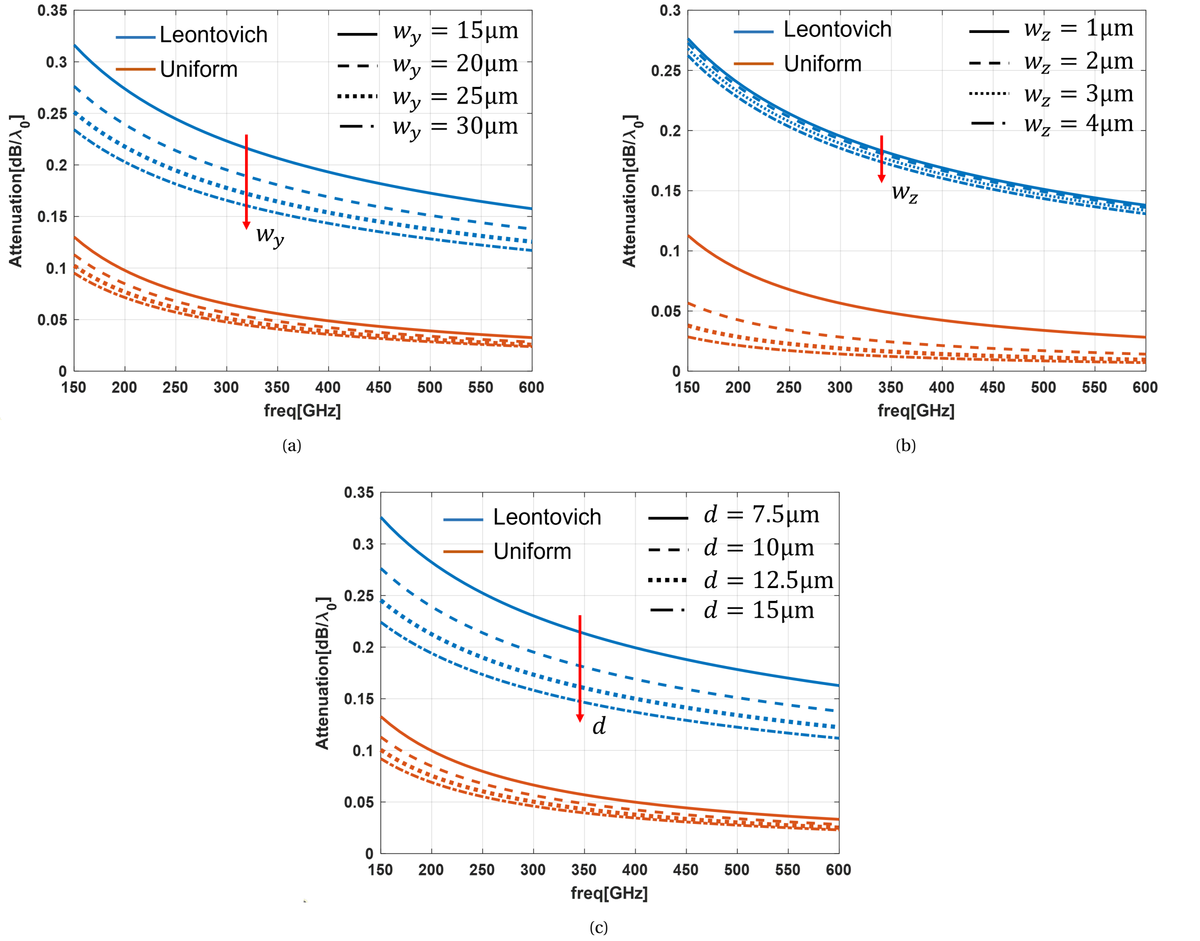

Figure 4.12: Losses of a dipole in the presence of a perfectly conducting ground plane (a) having a metal thickness $w_z = 1\mu$m, located at a distance $d = 10\mu$m from the ground plane for varying width w_y, (b) having a width $w_y = 20\mu$m, located at a distance $d = 10\mu$m from the ground plane for varying metal thickness w_z, and (c) having a metal thickness $w_z = 1\mu$m and width $w_y = 20\mu$m, for varying distance d between the metal strip and the ground plane

thickness, the area over which the current is distributed does not vary much, when the thickness of the dipole is changed.

5

Analysis of a dipole with non-zero thickness in an arbitrary stratification

In this chapter, the formulation, introduced in Chapter 4, will be extended to study the microstrip transmission line, shown in Fig. 5.1. To study this problem, the spectral domain Green's function for stratified media is used, which allows the modelling of arbitrary stratifications. The spectral domain Green's function for stratified media has a spectral dependence on k_x and k_y, i.e. wavenumbers of the directions, longitudinal with respect to the stratification, and a spatial dependence on z' and z, denoting the z-coordinate of the source and observation point, respectively. For this reason, the projection in the y-direction will be calculated in the spectral domain, while the projection in the z-direction will be calculated in the spatial domain. Consequently, evaluating the longitudinal spectral Green's function $D(k_x)$ amounts to evaluating a 3D-integral. However, since the dependence on the observation point z is only in the exponent of the voltage waves in the equivalent transmission-line model, the integral in z can be closed analytically. As we shall see, the amplitudes of the voltage waves in the equivalent transmission-line model will generally have a complicated dependence on z'. As a consequence, the integral in z' cannot be closed analytically. Therefore, the integrals in k_y and z' will have to be performed numerically.

This chapter is structured as follows. In section 5.1, we will illustrate the procedure by deriving the transmission-line Green's function of a dipole in free space, using the spectral domain Green's function for stratified media. For this geometry, the integrals in z and z' can both be closed analytically. In section 5.2, we will apply the same procedure to the more realistic geometry of a microstrip.

5.1. Free space

To illustrate the procedure and demonstrate its validity, we will derive the transmission-line Green's function of a volumetric dipole in free space, carrying a uniform current distribution, using the spectral domain Green's function for stratified media. For this geometry, the integrals in z and z' can both be closed analytically. As expected, the procedure, used in this section, results in the same equation, derived in Section 4.1.1, by starting with the 3D spectral Green's function.

Let us consider again the spectral current $I(k_x)$, given by (4.17). Since the stratified media Green's function has a spectral dependence on k_y and a spatial dependence on z and z', the longitudinal spectral Green's function $D(k_x)$ can be expressed as follows

$$D(k_x) = \frac{1}{2\pi} \int_{-\infty}^{\infty} \int_{0}^{w_z} \int_{0}^{w_z} G_{xx}^{ej}(k_x, k_y, z, z') J_t(k_y, z') J_t(k_y, z) dz dz' dk_y, \tag{5.1}$$

where the projection in the y-direction is calculated in the spectral domain, and the projection in the z-direction is calculated in the spatial domain. The equivalent transmission-line model of free space is shown in Fig. 5.2, in which both the upper and lower transmission lines represent a semi-infinite air region above and below the source, which is located at $z = z'$. Since both transmission lines are infinite, there will only be a forward propagating voltage wave along the transmission lines. Hence, the voltages inside the regions $z \in [z', \infty)$

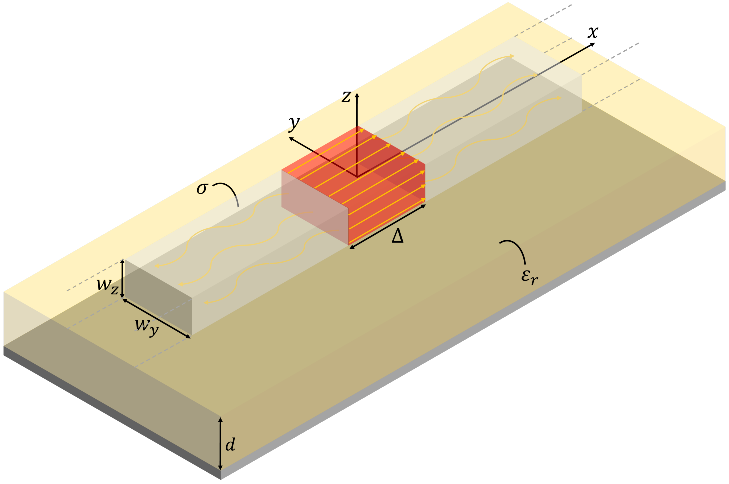

Figure 5.1: Infinite microstrip with metal thickness w_z, width w_y, dielectric thickness d and conductivity, σ oriented along the x-axis and excited by a delta-gap excitation with length Δ

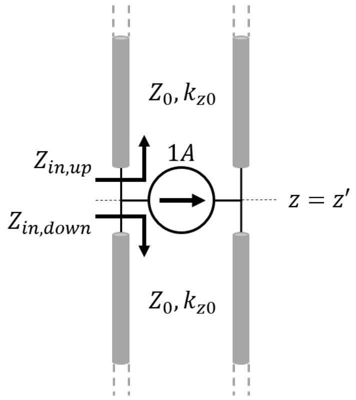

Figure 5.2: Equivalent transmission line model in free space

and $z \in (-\infty, z']$ can be expressed as follows

$$V_{TE/TM}(z > z') = \frac{Z_{TE/TM}}{2} e^{-jk_z(z-z')} \tag{5.2}$$

$$V_{TE/TM}(z < z') = \frac{Z_{TE/TM}}{2} e^{jk_z(z-z')}. \tag{5.3}$$

By substituting (5.2) and (5.3) into the xx-component of the Dyadic Green's function $G^{ej}_{xx}(k_x, k_y, z, z')$, we obtain the following expression

$$G^{ej}_{xx}(k_x, k_y, z, z') = -\frac{V_{TM}k_x^2 + V_{TE}k_y^2}{k_x^2 + k_y^2} = -\frac{Z_{TM}k_x^2 + Z_{TE}k_y^2}{2(k_x^2 + k_y^2)} e^{\mp jk_z(z-z')}, \tag{5.4}$$

where the $\mp$ depends on the observation region ($z \in [z', \infty)$ and $z \in (-\infty, z']$). Since this section serves as a demonstration of the procedure, we will consider the following transverse current distribution

$$j_t(y, z) = \frac{1}{w_y w_z} \text{rect}\left(\frac{y}{w_y}\right) \text{rect}\left(\frac{z}{w_z}\right). \tag{5.5}$$

By performing a Fourier transform in y, we obtain the following expression

$$J_t(k_y, z) = \text{sinc}\left(\frac{k_y w_y}{2}\right) \frac{1}{w_z} \text{rect}\left(\frac{z}{w_z}\right). \tag{5.6}$$

By substituting (5.4) and (5.6) into (5.1) and by taking into account the different expression for the two observation regions, the longitudinal spectral Green's function $D(k_x)$ can be expressed as follows

$$\begin{aligned} D(k_x) = \frac{1}{2\pi}\int_{-\infty}^{\infty}\Bigg(\int_0^{w_z}\int_{z'}^{w_z} -\frac{Z_{TM}k_x^2 + Z_{TE}k_y^2}{2(k_x^2+k_y^2)} e^{-jk_z(z-z')} dz dz' \\ + \int_0^{w_z}\int_0^{z'} -\frac{Z_{TM}k_x^2 + Z_{TE}k_y^2}{2(k_x^2+k_y^2)} e^{jk_z(z-z')} dz dz'\Bigg) \operatorname{sinc}^2\left(\frac{k_y w_y}{2}\right) dk_y. \end{aligned} \tag{5.7}$$

Since the dependence on z and z' is only in the exponent, both integrals can be closed analytically, which results in the following expression

$$D(k_x) = -\frac{1}{2\pi}\int_{\infty}^{\infty} \frac{Z_{TM}k_x^2 + Z_{TE}k_y^2}{k_x^2+k_y^2}\left(\frac{w_z}{jk_z} + \frac{1-e^{-jk_z w_z}}{k_z^2}\right)\operatorname{sinc}^2\left(\frac{k_y w_y}{2}\right) dk_y. \tag{5.8}$$

By substituting $Z_{TM} = \zeta_0 k_{z0}/k_0$, $Z_{TE} = \zeta_0 k_0/k_{z0}$ and $k_z = -j\sqrt{k_x^2+k_y^2-k_0^2}$ into (5.8) and by performing some algebraic manipulations (5.8) can be expressed as follows

$$D(k_x) = j\frac{\zeta}{k}\frac{k_x^2-k^2}{2\pi}\int_{-\infty}^{\infty}\left(\frac{w_z}{k_x^2+k_y^2-k^2} + \frac{e^{-w_z\sqrt{k_x^2+k_y^2-k^2}}-1}{(k_x^2+k_y^2-k^2)^{\frac{3}{2}}}\right)\operatorname{sinc}^2\left(\frac{k_y w_y}{2}\right) dk_y. \tag{5.9}$$

As anticipated, the longitudinal spectral Green's function in (5.9), derived using the spectral domain Green's function for stratified media, is congruent with (4.37), obtained using the 3D spectral Green's function of free space.

5.2. Microstrip

In Section 5.1, we have used the spectral domain Green's function for stratified media to derive the tranmsission line Green's function of a dipole located in free space. In this section, we will use the same procedure to study the more realistic geometry of the microstrip, shown in Fig. 5.1.

In Section 5.2.1, we will derive the transmission line Green's function of this geometry. Next Section 5.2.2 will introduce one possible definition of the characteristic impedance in which the voltage along the transmission line is defined as the line integral of the transverse electric field. Finally, in Section 5.2.3, we will demonstrate the formulation developed in Sections 5.2.1 and 5.2.2 by performing a parametric analysis versus the relevant dimensions of the transmission line.

5.2.1. Derivation Green's function

Let us consider the microstrip, shown in Fig. 5.1, consisting of an infinitely long metal strip, having a width w_y and thickness h, constituted of a material with conductivity σ, printed on a dielectric substrate with permittivity ε_d and thickness d, with underneath an infinitely extended ground plane, constituted of a material with conductivity σ. The ground plane is assumed to have a thickness large enough, such that the electric field entering the ground plane is entirely absorbed. Hence, the ground plane can be modeled as a semi-infinite region.

Fig. 5.3a shows the stratification of the microstrip. The corresponding equivalent transmission-line model is shown in Fig. 5.3b. In Fig. 5.3b, the transmission-lines right above and below the current source represent the air region above the dielectric. The transmission-line directly below the air region represents the dielectric substrate, while the transmission line on the bottom represents the infinitely extended ground plane. Finally, the current source represents an electric current flowing inside the metal strip at $z = z'$.

From the previous sections, it is clear that we need to project the scattered field onto the transverse current distribution. Therefore, we need to evaluate the field in the region $z \in [0, w_z]$. In the transmission-line model of Fig. 5.3b, this region corresponds to the transmission-lines right above and below the current source.

First, we will calculate the input impedance, looking from the transmission line right below the current source towards the transmission line representing the dielectric, as shown in the following expression

$$Z_{\text{in},d} = Z_d\frac{Z_\sigma + Z_d\tanh(jk_{zd}d)}{Z_d + Z_\sigma\tanh(jk_{zd}d)}. \tag{5.10}$$

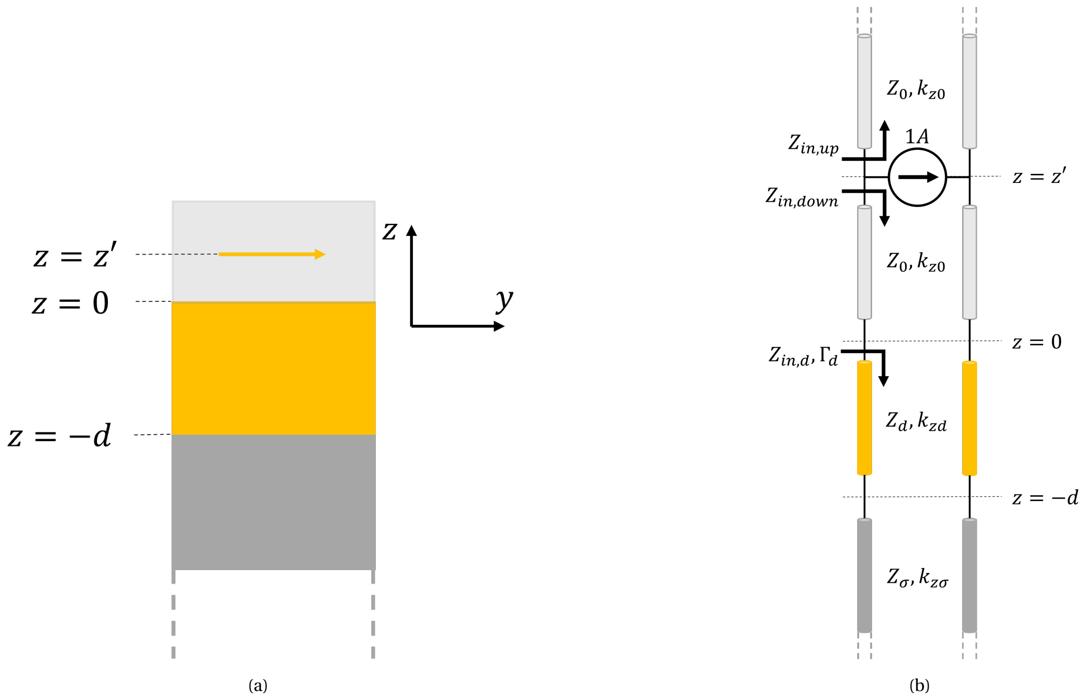

Figure 5.3: (a) The stratification and (b) the equivalent transmission line-model of the microstrip

Next, we can calculate the input impedance looking from the source towards the air region below, as shown in the following expression

$$Z_{\text{in,down}} = Z_0 \frac{Z_{\text{in},d} + Z_0 \tanh(jk_{z0}z')}{Z_0 + Z_{\text{in},d} \tanh(jk_{z0}z')}. \tag{5.11}$$

Finally, we can calculate the voltage at the current source, as follows

$$V_{\text{in}} = V(z = z') = \frac{Z_{\text{in,down}} Z_0}{Z_{\text{in,down}} + Z_0}. \tag{5.12}$$

Since the upper air region is infinite, there will only be a forward propagating wave along the transmission line, as shown in the following expression

$$V(z > z') = V_{\text{in}} e^{-jk_{z0}(z-z')}. \tag{5.13}$$

Since the air region below the source is finite, the voltage in this region will be the superposition of a forward and backward propagating wave, as shown in the following expression

$$V(0 < z < z') = V^+_{\text{lower}} e^{jk_{z0}(z-z')} + V^-_{\text{lower}} e^{-jk_{z0}(z-z')}. \tag{5.14}$$

By applying the boundary condition at $z = 0$, we obtain the following expression

$$V(0 < z < z') = V^+_{\text{lower}} (e^{jk_{z0}(z-z')} + \Gamma_d e^{-jk_{z0}(z+z')}), \tag{5.15}$$

where the reflection coefficient Γ_d can be expressed as follows

$$\Gamma_d = \frac{Z_{\text{in},d} - Z_0}{Z_{in,d} + Z_0}. \tag{5.16}$$

Finally, by applying the boundary condition at $z = z'$, we can find the amplitude V^+ of the forward propagating wave, as shown in the following expression

$$V^+ = \frac{V_{\text{in}}}{1 + \Gamma_d e^{-2jk_{z0}z'}}. \tag{5.17}$$

Once the amplitudes of the voltage waves are obtained, the xx-component of the Dyadic Green's function $G^{ej}_{xx}(k_x, k_y, z, z')$ can be constructed. In the region $z \in [z', \infty)$, $G^{ej}_{xx}(k_x, k_y, z, z')$ is given by the following expression

$$G^{ej}_{xx}(k_x, k_y, z > z') = -\frac{V_{\text{TM}} k_x^2 + V_{\text{TE}} k_y^2}{k_x^2 + k_y^2} = -\frac{V^+_{\text{TM,upper}} k_x^2 + V^+_{\text{TE,upper}} k_y^2}{(k_x^2 + k_y^2)} e^{-jk_{z0}(z-z')}, \tag{5.18}$$

while in the region $z \in [0, z']$, $G^{ej}_{xx}(k_x, k_y, z, z')$ can be expressed as follows

$$\begin{aligned} G^{ej}_{xx}(k_x, k_y, 0 < z < z') = -\frac{V_{\text{TM}} k_x^2 + V_{\text{TE}} k_y^2}{k_x^2 + k_y^2} = \\ -\frac{V^+_{\text{TM,lower}} k_x^2 + V^+_{\text{TE,lower}} k_y^2}{k_x^2 + k_y^2} e^{jk_{z0}(z-z')} - \frac{\Gamma_{\text{TM},d} V^+_{\text{TM,lower}} k_x^2 + \Gamma_{\text{TE},d} V^+_{\text{TE,lower}} k_y^2}{k_x^2 + k_y^2} e^{-jk_{z0}(z+z')}. \end{aligned} \tag{5.19}$$

Finally, by substituting (5.18) and (5.19) into (5.1) and by making an assumption on the transverse current distribution $J_t(k_y, z')$, we can obtain an expression for the longitudinal spectral Green's function $D(k_x)$. For clarity, we will first assume a uniform current distribution on the cross-section, which results in the following expression

$$\begin{aligned} D(k_x) = -\frac{1}{2\pi} \int_{-\infty}^{\infty} \int_0^{w_z} \int_{z'}^{w_z} \frac{V^+_{\text{TM,upper}} k_x^2 + V^+_{\text{TE,upper}} k_y^2}{k_x^2 + k_y^2} e^{-jk_{z0}(z-z')} \operatorname{sinc}^2\left(\frac{k_y w_y}{2}\right) dz dz' dk_y - \\ \frac{1}{2\pi} \int_{-\infty}^{\infty} \int_0^{w_z} \int_0^{z'} \frac{V^+_{\text{TM,lower}} k_x^2 + V^+_{\text{TE,lower}} k_y^2}{k_x^2 + k_y^2} e^{jk_{z0}(z-z')} \operatorname{sinc}^2\left(\frac{k_y w_y}{2}\right) dz dz' dk_y - \\ \frac{1}{2\pi} \int_{-\infty}^{\infty} \int_0^{w_z} \int_0^{z'} \frac{\Gamma_{\text{TM},d} V^+_{\text{TM,lower}} k_x^2 + \Gamma_{\text{TE},d} V^+_{\text{TE,lower}} k_y^2}{k_x^2 + k_y^2} e^{-jk_{z0}(z+z')} \operatorname{sinc}^2\left(\frac{k_y w_y}{2}\right) dz dz' dk_y. \end{aligned} \tag{5.20}$$

Note that the expression above is different for the two observation regions, where the region $z \in [z', w_z]$ only contains a forward propagating voltage wave, while the region $z \in [0, z']$ contains both a forward and backward propagating wave. By closing the integrals in z analytically, (5.20) can be expressed as follows

$$\begin{aligned} D(k_x) = -\frac{j}{2\pi} \int_{-\infty}^{\infty} \int_0^{w_z} \frac{V^+_{\text{TM,upper}} k_x^2 + V^+_{\text{TE,upper}} k_y^2}{k_x^2 + k_y^2} \frac{e^{-jk_{z0}(w_z - z')} - 1}{k_{z0}} \operatorname{sinc}^2\left(\frac{k_y w_y}{2}\right) dz' dk_y - \\ \frac{j}{2\pi} \int_{-\infty}^{\infty} \int_0^{w_z} \frac{V^+_{\text{TM,lower}} k_x^2 + V^+_{\text{TE,lower}} k_y^2}{k_x^2 + k_y^2} \frac{e^{-jk_{z0}z'} - 1}{k_{z0}} \operatorname{sinc}^2\left(\frac{k_y w_y}{2}\right) dz' dk_y - \\ \frac{j}{2\pi} \int_{-\infty}^{\infty} \int_0^{w_z} \frac{\Gamma_{\text{TM},d} V^+_{\text{TM,lower}} k_x^2 + \Gamma_{\text{TE},d} V^+_{\text{TE,lower}} k_y^2}{k_x^2 + k_y^2} \frac{e^{-2jk_{z0}z'} - e^{-jk_{z0}z'}}{k_{z0}} \operatorname{sinc}^2\left(\frac{k_y w_y}{2}\right) dz' dk_y. \end{aligned} \tag{5.21}$$

(5.21) contains an integral in k_y and z'. Unfortunately, these integrals cannot be closed analytically. To understand the reason, consider the expression for the voltage at the current source, given by (5.12). As shown in (5.12), the voltage at the current source depends on $Z_{\text{in,down}}$. As shown in (5.11), $Z_{\text{in,down}}$ has a rather complicated dependence on z'. Hence, the integral in z' cannot be closed analytically. The same argument applies to the dependence on k_y. Consequently, the integrals in k_y and z' will have to be performed numerically.

(5.21) gives the expression of the longitudinal Green's function, assuming a uniform current distribution on the cross-section. If the Leontovich boundary condition is used to model the transverse current distribution, the longitudinal Green's function $D(k_x)$ can be expressed as follows

$$D(k_x) = \frac{1}{4\delta_p^2 (w_y + w_z - 2\delta_p)^2} \left(D_1(k_x) + D_2(k_x) + D_3(k_x)\right). \tag{5.22}$$

The derivation of $D_1(k_x)$, $D_2(k_x)$ and $D_3(k_x)$ is reported in Appendix H.1 and results in the following expressions

$$
\begin{aligned}
D_1(k_x) = &-\frac{j}{2\pi}\int_{-\infty}^{\infty}\int_{0}^{\delta_p}\frac{V^+_{\text{TM,upper}}k_x^2+V^+_{\text{TE,upper}}k_y^2}{k_x^2+k_y^2}\,\frac{e^{-jk_{z0}(\delta_p-z')}-1}{k_{z0}}\,w_y^2\text{sinc}^2\left(\frac{k_y w_y}{2}\right)dz'dk_y-\\
&\frac{j}{2\pi}\int_{-\infty}^{\infty}\int_{0}^{\delta_p}\frac{V^+_{\text{TM,lower}}k_x^2+V^+_{\text{TE,lower}}k_y^2}{k_x^2+k_y^2}\,\frac{e^{-jk_{z0}z'}-1}{k_{z0}}\,w_y^2\text{sinc}^2\left(\frac{k_y w_y}{2}\right)dz'dk_y-\\
&\frac{j}{2\pi}\int_{-\infty}^{\infty}\int_{0}^{\delta_p}\frac{\Gamma_{\text{TM},d}V^+_{\text{TM,lower}}k_x^2+\Gamma_{\text{TE},d}V^+_{\text{TE,lower}}k_y^2}{k_x^2+k_y^2}\,\frac{e^{-2jk_{z0}z'}-e^{-jk_{z0}z'}}{k_{z0}}\,w_y^2\text{sinc}^2\left(\frac{k_y w_y}{2}\right)dz'dk_y-\\
&\frac{j}{\pi}\int_{-\infty}^{\infty}\int_{0}^{\delta_p}\frac{V^+_{\text{TM,upper}}k_x^2+V^+_{\text{TE,upper}}k_y^2}{k_x^2+k_y^2}\,\frac{e^{-jk_{z0}(w_z-\delta_p-z')}-e^{-jk_{z0}(\delta_p-z')}}{k_{z0}}\,w_y^2\text{sinc}^2\left(\frac{k_y w_y}{2}\right)dz'dk_y-\\
&\frac{j}{\pi}\int_{-\infty}^{\infty}\int_{0}^{\delta_p}\frac{V^+_{\text{TM,upper}}k_x^2+V^+_{\text{TE,upper}}k_y^2}{k_x^2+k_y^2}\,\frac{e^{-jk_{z0}(w_z-z')}-e^{-jk_{z0}(w_z-\delta_p-z')}}{k_{z0}}\\
&w_y\text{sinc}\left(\frac{k_y w_y}{2}\right)\left(w_y\text{sinc}\left(\frac{k_y w_y}{2}\right)-(w_y-2\delta_p)\text{sinc}\left(k_y\frac{w_y-2\delta_p}{2}\right)\right)dz'dk_y,
\end{aligned}
\tag{5.23}
$$

$$
\begin{aligned}
D_2(k_x) = &-\frac{j}{2\pi}\int_{-\infty}^{\infty}\int_{\delta_p}^{w_z-\delta_p}\frac{V^+_{\text{TM,upper}}k_x^2+V^+_{\text{TE,upper}}k_y^2}{k_x^2+k_y^2}\,\frac{e^{-jk_{z0}(w_z-\delta_p-z')}-1}{k_{z0}}\\
&\left(w_y\text{sinc}\left(\frac{k_y w_y}{2}\right)-(w_y-2\delta_p)\text{sinc}\left(k_y\frac{w_y-2\delta_p}{2}\right)\right)^2 dz'dk_y-\\
&\frac{j}{2\pi}\int_{-\infty}^{\infty}\int_{\delta_p}^{w_z-\delta_p}\frac{V^+_{\text{TM,lower}}k_x^2+V^+_{\text{TE,lower}}k_y^2}{k_x^2+k_y^2}\,\frac{e^{-jk_{z0}(z'-\delta_p)}-1}{k_{z0}}\\
&\left(w_y\text{sinc}\left(\frac{k_y w_y}{2}\right)-(w_y-2\delta_p)\text{sinc}\left(k_y\frac{w_y-2\delta_p}{2}\right)\right)^2 dz'dk_y-\\
&\frac{j}{2\pi}\int_{-\infty}^{\infty}\int_{\delta_p}^{w_z-\delta_p}\frac{\Gamma_{\text{TM},d}V^+_{\text{TM,lower}}k_x^2+\Gamma_{\text{TE},d}V^+_{\text{TE,lower}}k_y^2}{k_x^2+k_y^2}\,\frac{e^{-2jk_{z0}z'}-e^{-jk_{z0}(z'+\delta_p)}}{k_{z0}}\\
&\left(w_y\text{sinc}\left(\frac{k_y w_y}{2}\right)-(w_y-2\delta_p)\text{sinc}\left(k_y\frac{w_y-2\delta_p}{2}\right)\right)^2 dz'dk_y-\\
&\frac{j}{2\pi}\int_{-\infty}^{\infty}\int_{\delta_p}^{w_z-\delta_p}\frac{V^+_{\text{TM,upper}}k_x^2+V^+_{\text{TE,upper}}k_y^2}{k_x^2+k_y^2}\,\frac{e^{-jk_{z0}(w_z-z')}-e^{-jk_{z0}(w_z-\delta_p-z')}}{k_{z0}}\\
&w_y\text{sinc}\left(\frac{k_y w_y}{2}\right)\left(w_y\text{sinc}\left(\frac{k_y w_y}{2}\right)-(w_y-2\delta_p)\text{sinc}\left(k_y\frac{w_y-2\delta_p}{2}\right)\right)dz'dk_y,
\end{aligned}
\tag{5.24}
$$

$$
\begin{aligned}
D_3(k_x) = -\frac{j}{2\pi}\int_{-\infty}^{\infty}\int_{w_z-\delta_p}^{w_z} &\frac{V^+_{\text{TM,upper}}k_x^2 + V^+_{\text{TE,upper}}k_y^2}{k_x^2+k_y^2}\frac{e^{-jk_{z0}(w_z-z')}-1}{k_{z0}} w_y^2\text{sinc}^2\left(\frac{k_y w_y}{2}\right)dz'dk_y - \\
\frac{j}{2\pi}\int_{-\infty}^{\infty}\int_{w_z-\delta_p}^{w_z} &\frac{V^+_{\text{TM,lower}}k_x^2 + V^+_{\text{TE,lower}}k_y^2}{k_x^2+k_y^2}\frac{e^{-jk_{z0}(z'-w_z+\delta_p)}-1}{k_{z0}} w_y^2\text{sinc}^2\left(\frac{k_y w_y}{2}\right)dz'dk_y - \\
\frac{j}{2\pi}\int_{-\infty}^{\infty}\int_{w_z-\delta_p}^{w_z} &\frac{\Gamma_{\text{TM},d}V^+_{\text{TM,lower}}k_x^2 + \Gamma_{\text{TE},d}V^+_{\text{TE,lower}}k_y^2}{k_x^2+k_y^2}\frac{e^{-2jk_{z0}z'}-e^{-jk_{z0}(z'+\delta_p)}}{k_{z0}} w_y^2\text{sinc}^2\left(\frac{k_y w_y}{2}\right)dz'dk_y - \\
\frac{j}{2\pi}\int_{-\infty}^{\infty}\int_{w_z-\delta_p}^{w_z} &\frac{V^+_{\text{TM,upper}}k_x^2 + V^+_{\text{TE,upper}}k_y^2}{k_x^2+k_y^2}\frac{e^{-jk_{z0}(w_z-z')}-e^{-jk_{z0}(z'+w_z-\delta_p)}}{k_{z0}} w_y^2\text{sinc}^2\left(\frac{k_y w_y}{2}\right)dz'dk_y.
\end{aligned} \tag{5.25}
$$

In Section 4.1.1, it has been shown that the current inside a dipole decays exponentially from the surface of the metal. To simplify the expression for $J_t(k_y, k_z)$, the transverse current distribution has been approximated, using the Leontovich boundary condition. This approximation allowed the integral in k_z to be closed analytically. However, when using the transmission-line Green's function for stratified media, the projection in the y-direction is performed in the spectral domain, while the projection in the z-direction is performed in the spatial domain. In this case, only the integral in z is closed analytically, while the integrals in k_y and z' are performed numerically. Consequently, using the Leontovich boundary condition to approximate the exponential decay inside the dipole does not provide the same advantages as in the case of free space. Consequently, we may use the following alternative transverse current distribution

$$
j_t(y,z) = \frac{2}{w_y\pi}\frac{1}{\sqrt{1-(2y/w_y)^2}}\frac{e^{-z/\delta_p}+e^{(z-w_z)/\delta_p}}{2\delta_p(1-e^{-w_z/\delta_p})}. \tag{5.26}
$$

The distribution in z is chosen to model the exponential decay inside the dipole, while the distribution in y is chosen to be the edge-singular distribution to remain consistent with the commonly used planar formulations. In Appendix H.2, the same procedure is applied using (5.26) as the transverse current distribution, which results in the following expression

$$
\begin{aligned}
D(k_x) = -\frac{1}{2\pi}\int_{-\infty}^{\infty}\int_{0}^{w_z} &\frac{V^+_{\text{TM,upper}}k_x^2 + V^+_{\text{TE,upper}}k_y^2}{k_x^2+k_y^2}\frac{e^{-z'/\delta_p}-e^{-w_z/\delta_p}e^{-jk_{z0}(w_z-z')}}{jk_{z0}+1/\delta_p}\cdot \\
&\frac{e^{-(wz-z')/\delta_p}-e^{-jk_{z0}(w_z-z')}}{jk_{z0}-1/\delta_p}J_0\left(\frac{k_y w_y}{2}\right)\text{sinc}\left(\frac{k_y w_y}{2}\right)dz'dk_y - \\
\frac{1}{2\pi}\int_{-\infty}^{\infty}\int_{0}^{w_z} &\frac{V^+_{\text{TM,upper}}k_x^2 + V^+_{\text{TE,upper}}k_y^2}{k_x^2+k_y^2}\frac{e^{-z'/\delta_p}-e^{-jk_{z0}z'}}{jk_{z0}-1/\delta_p}\cdot \\
&\frac{e^{-(wz-z')/\delta_p}-e^{-w_z/\delta_p}e^{-jk_{z0}z'}}{jk_{z0}+1/\delta_p}J_0\left(\frac{k_y w_y}{2}\right)\text{sinc}\left(\frac{k_y w_y}{2}\right)dz'dk_y - \\
\frac{1}{2\pi}\int_{-\infty}^{\infty}\int_{0}^{w_z} &\frac{\Gamma_{\text{TM},d}V^+_{\text{TM,lower}}k_x^2 + \Gamma_{\text{TE},d}V^+_{\text{TE,lower}}k_y^2}{k_x^2+k_y^2}\frac{e^{-jk_{z0}z'}-e^{-z'/\delta_p}e^{-2jk_{z0}z'}}{jk_{z0}+1/\delta_p}\cdot \\
&\frac{e^{-w_z/\delta_p}e^{-jk_{z0}z'}-e^{-2jk_{z0}z'}e^{-(wz-z')/\delta_p}}{jk_{z0}-1/\delta_p}J_0\left(\frac{k_y w_y}{2}\right)\text{sinc}\left(\frac{k_y w_y}{2}\right)dz'dk_y.
\end{aligned} \tag{5.27}
$$

In this case, the spatial projection becomes as follows

$$
\langle j_t(y,z), j_t(y,z)\rangle_A = \frac{\delta_p(1-e^{-2w_z/\delta_p})+2w_z e^{-w_z/\delta_p}}{4w_y\delta_p^2(1-e^{-w_z/\delta_p})^2}. \tag{5.28}
$$

5.2.2. Characteristic impedance

In this section, we will give one possible definition of the characteristic impedance, in which the voltage along the transmission line is defined as the line integral of the transverse electric field. Similar to Section 4.1.2, the current wave $i_{\text{res}}(x)$ and its amplitude I^+ are given by (4.40) and (4.41). Since the ground plane has a finite conductivity, regarding it as an equipotential surface is only approximately true. Nevertheless, if the ground plane is constituted of a good conductor, we may define the voltage along the transmission line as follows

$$v(x) = -\int_{-d}^{0} e_z(x, y=0, z)\,dz, \tag{5.29}$$

where $e_z(x, y=0, z)$ denotes the z-component of the electric field, observed at $y=0$. Note that, in contrast to Section 4.2.2, the integral in (5.29) is defined from $-d$ to 0, since the origin of the reference system has been defined to be located at the bottom of the metal strip. By expressing $e_z(x, y=0, z)$ in terms of its plane wave spectrum, (5.29) can be expressed as follows

$$v(x) = -\frac{1}{4\pi^2}\int_{-d}^{0}\int_{0}^{w_z}\int_{-\infty}^{\infty}\int_{-\infty}^{\infty} G_{zx}(k_x, k_y, z, z') I(k_x) J_t(k_y, z')\,dk_y\,dk_z dz' dz, \tag{5.30}$$

where the zx-component of the dyadic Green's function $G_{zx}(k_x, k_y, z, z')$ is given by the following expression

$$G_{zx}(k_x, k_y, z, z') = \frac{\zeta k_x}{k} i_{TM} \tag{5.31}$$

To obtain i_{TM}, we will again use the equivalent transmission-line model of Fig 4.5a. Since the electric field in (5.29) is evaluated in the region $z \in [-d, 0]$, we will have to obtain the current on the transmission line that represents the dielectric substrate. Since the voltage in the region $z \in [0, z']$ has already been derived in Section 5.2.1, it is more convenient to first derive the voltage in the region $z \in [-d, 0]$. Since the transmission-line that represents the dielectric substrate is finite, the voltage in this region can be expressed as the superposition of a forward and backward traveling wave, as shown in the following expression

$$V(-d < z < 0) = V_d^+ e^{jk_{z0}z} + V_d^- e^{-jk_{z0}z}. \tag{5.32}$$

By applying the boundary condition at $z = -d$, we obtain the following expression

$$V(-d < z < 0) = V_d^+ (e^{jk_{z0}z} + \Gamma_\sigma e^{-2jk_{zd}d} e^{-jk_{zd}z}), \tag{5.33}$$

where the reflection coefficient Γ_σ is given by the following expression

$$\Gamma_\sigma = \frac{Z_\sigma - Z_d}{Z_\sigma + Z_d}. \tag{5.34}$$

By applying the boundary condition at $z = 0$, we obtain V_d^+, as shown in the following expression

$$V_d^+ = V^+ \frac{e^{-jk_{z0}z} + \Gamma_d e^{-jk_{z0}z}}{1 + \Gamma_\sigma e^{-2jk_{zd}d}} \tag{5.35}$$

Finally, by using the relation between the amplitudes of the voltage and current waves along the equivalent transmission-line model, the current in the region $z \in [-d, 0]$ becomes as follows

$$I(-d < z < 0) = -\frac{V_d^+}{Z_d}(e^{jk_{z0}z} - \Gamma_\sigma e^{-2jk_{zd}d} e^{-jk_{zd}z}). \tag{5.36}$$

By substituting (5.31) and (5.26) into (5.30), we obtain the following expression

$$\begin{aligned} v(x) = \frac{1}{4\pi^2}\int_{-d}^{0}\int_{0}^{w_z}\int_{-\infty}^{\infty}\int_{-\infty}^{\infty} I(k_x)\frac{\zeta k_x}{k}\frac{V_{\text{TM},d}^+}{Z_0} e^{-jk_{zd}z} J_0\left(\frac{k_y w_y}{2}\right)\frac{e^{-z'/\delta_p} + e^{(z'-w_z)/\delta_p}}{2\delta_p(1 - e^{-w_z/\delta_p})} e^{-jk_x x} e^{-jk_z z} dk_x dk_y dz' dz + \\ \frac{1}{4\pi^2}\int_{-d}^{0}\int_{0}^{w_z}\int_{-\infty}^{\infty}\int_{-\infty}^{\infty} I(k_x)\frac{\zeta k_x}{k}\frac{V_{\text{TM},d}^-}{Z_0} e^{-jk_{zd}z} J_0\left(\frac{k_y w_y}{2}\right)\frac{e^{-z'/\delta_p} + e^{(z'-w_z)/\delta_p}}{2\delta_p(1 - e^{-w_z/\delta_p})} e^{-jk_x x} e^{-jk_z z} dk_x dk_y dz' dz. \end{aligned} \tag{5.37}$$

By closing the integral in z analytically, we obtain the following expression

$$
\begin{aligned}
v(x) = \frac{j}{4\pi^2}\int_0^{w_z}\int_{-\infty}^{\infty}\int_{-\infty}^{\infty} I(k_x)\frac{\zeta k_x}{k}\frac{V_d^+}{Z_0}\frac{e^{-jk_{zd}z}-1}{k_{zd}}J_0\left(\frac{k_y w_y}{2}\right)\frac{e^{-z'/\delta_p}+e^{(z'-w_z)/\delta_p}}{2\delta_p(1-e^{-w_z/\delta_p})}e^{-jk_x x}e^{-jk_z z}dk_x dk_y dz' - \\
\frac{j}{4\pi^2}\int_0^{w_z}\int_{-\infty}^{\infty}\int_{-\infty}^{\infty} I(k_x)\frac{\zeta k_x}{k}\frac{V_d^-}{Z_0}\frac{e^{-jk_{zd}z}+1}{k_{zd}}J_0\left(\frac{k_y w_y}{2}\right)\frac{e^{-z'/\delta_p}+e^{(z'-w_z)/\delta_p}}{2\delta_p(1-e^{-w_z/\delta_p})}e^{-jk_x x}e^{-jk_z z}dk_x dk_y dz'.
\end{aligned}
\tag{5.38}
$$

To simplify the notation, we will define the function $Z(k_x)$ as follows

$$
\begin{aligned}
Z(k_x) = \frac{j}{2\pi}\int_0^{w_z}\int_{-\infty}^{\infty} I(k_x)\frac{\zeta k_x}{k}\frac{V_d^+}{Z_0}\frac{e^{-jk_{zd}z}-1}{k_{zd}}J_0\left(\frac{k_y w_y}{2}\right)\frac{e^{-z'/\delta_p}+e^{(z'-w_z)/\delta_p}}{2\delta_p(1-e^{-w_z/\delta_p})}e^{-jk_x x}e^{-jk_z z}dk_y dz' - \\
\frac{j}{2\pi}\int_0^{w_z}\int_{-\infty}^{\infty} I(k_x)\frac{\zeta k_x}{k}\frac{V_d^-}{Z_0}\frac{e^{-jk_{zd}z}+1}{k_{zd}}J_0\left(\frac{k_y w_y}{2}\right)\frac{e^{-z'/\delta_p}+e^{(z'-w_z)/\delta_p}}{2\delta_p(1-e^{-w_z/\delta_p})}e^{-jk_x x}e^{-jk_z z}dk_y dz'.
\end{aligned}
\tag{5.39}
$$

With this definition, the voltage $v(x)$ can be expressed as in (4.54). Similar to Section 4.1.2, the residue contribution gives rise to a traveling voltage wave $v_{\mathrm{res}}(x)$, given by (4.55), with amplitude V^+, given by (4.56). The characteristic impedance $Z_{0,\mathrm{TEM}}$ can then be defined as in (4.57).

In section 4.2.3, we will demonstrate the importance of the assumption on the transverse current distribution by making a comparison between the characteristic impedance obtained using the exponential distribution in (5.26), the characteristic impedance obtained using the Leontovich boundary condition and the characteristic impedance obtained by assuming a uniform current distribution on the cross-section.

If the Leontovich boundary condition is used, $Z(k_x)$ can be expressed as follows

$$
Z(k_x) = \frac{1}{2\delta_p(w_y+w_z-2\delta_p)}\left(Z_1(k_x)+Z_2(k_x)+Z_3(k_x)\right)
\tag{5.40}
$$

where $Z_1(k_x)$ is given by the following expression

$$
\begin{aligned}
Z_1(k_x) = \frac{j}{2\pi}\int_0^{\delta_p}\int_{-\infty}^{\infty} I(k_x)\frac{\zeta k_x}{k}\frac{V_d^+}{Z_0}\frac{e^{-jk_{zd}z}-1}{k_{zd}}w_y\mathrm{sinc}\left(\frac{k_y w_y}{2}\right)e^{-jk_x x}e^{-jk_z z}dk_y dz' - \\
\frac{j}{2\pi}\int_0^{\delta_p}\int_{-\infty}^{\infty} I(k_x)\frac{\zeta k_x}{k}\frac{V_d^-}{Z_0}\frac{e^{-jk_{zd}z}+1}{k_{zd}}w_y\mathrm{sinc}\left(\frac{k_y w_y}{2}\right)e^{-jk_x x}e^{-jk_z z}dk_y dz'.
\end{aligned}
\tag{5.41}
$$

where $Z_2(k_x)$ is given by the following expression

$$
\begin{aligned}
Z_2(k_x) = \frac{j}{2\pi}\int_{\delta_p}^{w_z-2\delta_p}\int_{-\infty}^{\infty} I(k_x)\frac{\zeta k_x}{k}\frac{V_d^+}{Z_0}\frac{e^{-jk_{zd}z}-1}{k_{zd}}\left(w_y\mathrm{sinc}\left(\frac{k_y w_y}{2}\right)-(w_y-2\delta_p)\mathrm{sinc}\left(k_y\frac{w_y-2\delta_p}{2}\right)\right)\cdot \\
e^{-jk_x x}e^{-jk_z z}dk_y dz' - \\
\frac{j}{2\pi}\int_{\delta_p}^{w_z-2\delta_p}\int_{-\infty}^{\infty} I(k_x)\frac{\zeta k_x}{k}\frac{V_d^-}{Z_0}\frac{e^{-jk_{zd}z}+1}{k_{zd}}\left(w_y\mathrm{sinc}\left(\frac{k_y w_y}{2}\right)-(w_y-2\delta_p)\mathrm{sinc}\left(k_y\frac{w_y-2\delta_p}{2}\right)\right)\cdot \\
e^{-jk_x x}e^{-jk_z z}dk_y dz'.
\end{aligned}
\tag{5.42}
$$

where $Z_3(k_x)$ is given by the following expression

$$
\begin{aligned}
Z_3(k_x) = \frac{j}{2\pi}\int_{w_z-2\delta_p}^{w_z}\int_{-\infty}^{\infty} I(k_x)\frac{\zeta k_x}{k}\frac{V_d^+}{Z_0}\frac{e^{-jk_{zd}z}-1}{k_{zd}}w_y\mathrm{sinc}\left(\frac{k_y w_y}{2}\right)e^{-jk_x x}e^{-jk_z z}dk_y dz' - \\
\frac{j}{2\pi}\int_{w_z-2\delta_p}^{w_z}\int_{-\infty}^{\infty} I(k_x)\frac{\zeta k_x}{k}\frac{V_d^-}{Z_0}\frac{e^{-jk_{zd}z}+1}{k_{zd}}w_y\mathrm{sinc}\left(\frac{k_y w_y}{2}\right)e^{-jk_x x}e^{-jk_z z}dk_y dz'.
\end{aligned}
\tag{5.43}
$$

The characteristic impedance $Z_{0,\mathrm{TEM}}$ is still defined by (4.57), where k_{xp} denotes the pole of the current spectrum $I(k_x)$ that is obtained, using (5.22) to calculate $D(k_x)$.

If a uniform current distribution is assumed, only $Z_1(k_x)$ should be retained. Consequently, $Z(k_x)$ becomes as follows

$$
\begin{aligned}
Z(k_x) = \frac{j}{2\pi w_z}\int_0^{w_z}\int_{-\infty}^{\infty} I(k_x)\frac{\zeta k_x}{k}\frac{V_d^+}{Z_0}\frac{e^{-jk_{zd}z}-1}{k_{zd}}\operatorname{sinc}\left(\frac{k_y w_y}{2}\right)e^{-jk_x x}e^{-jk_z z}dk_y dz' - \\
\frac{j}{2\pi w_z}\int_0^{w_z}\int_{-\infty}^{\infty} I(k_x)\frac{\zeta k_x}{k}\frac{V_d^-}{Z_0}\frac{e^{-jk_{zd}z}+1}{k_{zd}}\operatorname{sinc}\left(\frac{k_y w_y}{2}\right)e^{-jk_x x}e^{-jk_z z}dk_y dz'.
\end{aligned}
\tag{5.44}
$$

Similar to before, the characteristic impedance $Z_{0,\mathrm{TEM}}$ is still defined by (4.57), where k_{xp} denotes the pole of the current spectrum $I(k_x)$ that is obtained, using (5.21) to calculate $D(k_x)$.

5.2.3. Parametric analysis

In this section, we will first show a comparison between the characteristic impedance, obtained from the definition in (4.57), and the characteristic impedance, obtained from the definition in (4.61). Subsequently, we will demonstrate the formulation, developed in Sections 5.2.1 and 5.2.2, by performing a parametric analysis versus the relevant dimensions of the transmission line.

Fig. 5.4a shows the comparison between the characteristic impedance obtained from (4.57) and the characteristic impedance obtained from (4.61), for a microstrip having a width $w_y = 20\mu$m and a metal thickness $w_z = 1\mu$m, constituted of a material with conductivity $\sigma = 4.1\cdot 10^7$S/m, printed on a dielectric substrate, having a thickness $d = 10\mu$m and permittivity $\varepsilon_r = 4.3$. Fig. 5.4a shows that the definition in (4.61) has a stronger dependence on the transverse current distribution than the definition in (4.57). The reason is that the definition in (4.61) incorporates the transverse current distribution twice, when applying the Galerkin projection. Moreover, the resemblance between the characteristic impedance, obtained from the two different definitions supports the interpretation, suggested in Section 4.1.3, in which the residue contribution of the input admittance is interpreted as the contribution from two infinitely long transmission lines.

Fig. 5.4b shows the characteristic impedance of a microstrip having a metal thickness $w_z = 1\mu$m, constituted of a material with conductivity $\sigma = 4.1\cdot 10^7$S/m, printed on a dielectric substrate having a thickness $d = 10\mu$m and permittivity $\varepsilon_r = 4.3$, for varying width of the metal. Moreover, Fig. 5.4b shows the comparison between the characteristic impedance, obtained by assuming a uniform distribution on the cross-section, the characteristic impedance, obtained by using the Leontovich boundary condition, and the characteristic impedance, obtained by using the exponential distribution of (5.26). Fig. 5.4b shows that the characteristic impedance decreases when the width is increased. This can be understood from the quasi-static analysis, shown in Fig. 4.11a, in which the electric field is assumed to be confined between the metals and fringe effects are ignored. If the width of the metal is increased, the current is distributed over a larger area. Therefore, the electric field between the metals is weaker, which leads to a lower voltage and consequently a smaller characteristic impedance.

Fig. 5.4d shows the characteristic impedance of a microstrip having a width $w_y = 20\mu$m and metal thickness $w_z = 1\mu$m, constituted of a material with conductivity $\sigma = 4.1\cdot 10^7$S/m, printed on a dielectric substrate with permittivity $\varepsilon_r = 4.3$ for varying thickness of the substrate. Fig. 5.4d shows that the characteristic impedance increases when the thickness of the dielectric substrate is increased. This can be understood from the same quasi-static analysis as before. By making the same assumptions on the field distribution, the electric field strength becomes independent of d. Therefore, increasing d leads to a higher voltage and consequently a larger characteristic impedance.

Finally, Fig. 5.4c shows the characteristic impedance of a microstrip having a width $w_y = 20\mu$m, constituted of a material with conductivity $\sigma = 4.1\cdot 10^7$S/m, printed on a dielectric substrate having a thickness $d = 10\mu$m and permittivity $\varepsilon_r = 4.3$, for varying metal thickness. Fig. 5.4c shows that the characteristic impedance increases, when the thickness of the metal is increased. The reason is similar as in the example of Fig. 5.4d. As mentioned before, Figs. 5.4b to 5.4d have been obtained using the definition in (4.61). The same parametric analysis has been performed, using the definition in (4.57). For the sake of conciseness, these results have been omitted. Nevertheless, when using the definition in (4.57), the qualitative behaviour remains the same as in Figs. 5.4b to 5.4d.

Fig. 5.5b shows the attenuation in dB/λ_0 for a microstrip with the same dimensions as in Fig. 5.4c. Fig. 5.5b shows that the attenuation constant decreases, when the metal thickness is increased. The reason is that the current is distributed over a larger area, which leads to a smaller current density and lower losses. Additionally,

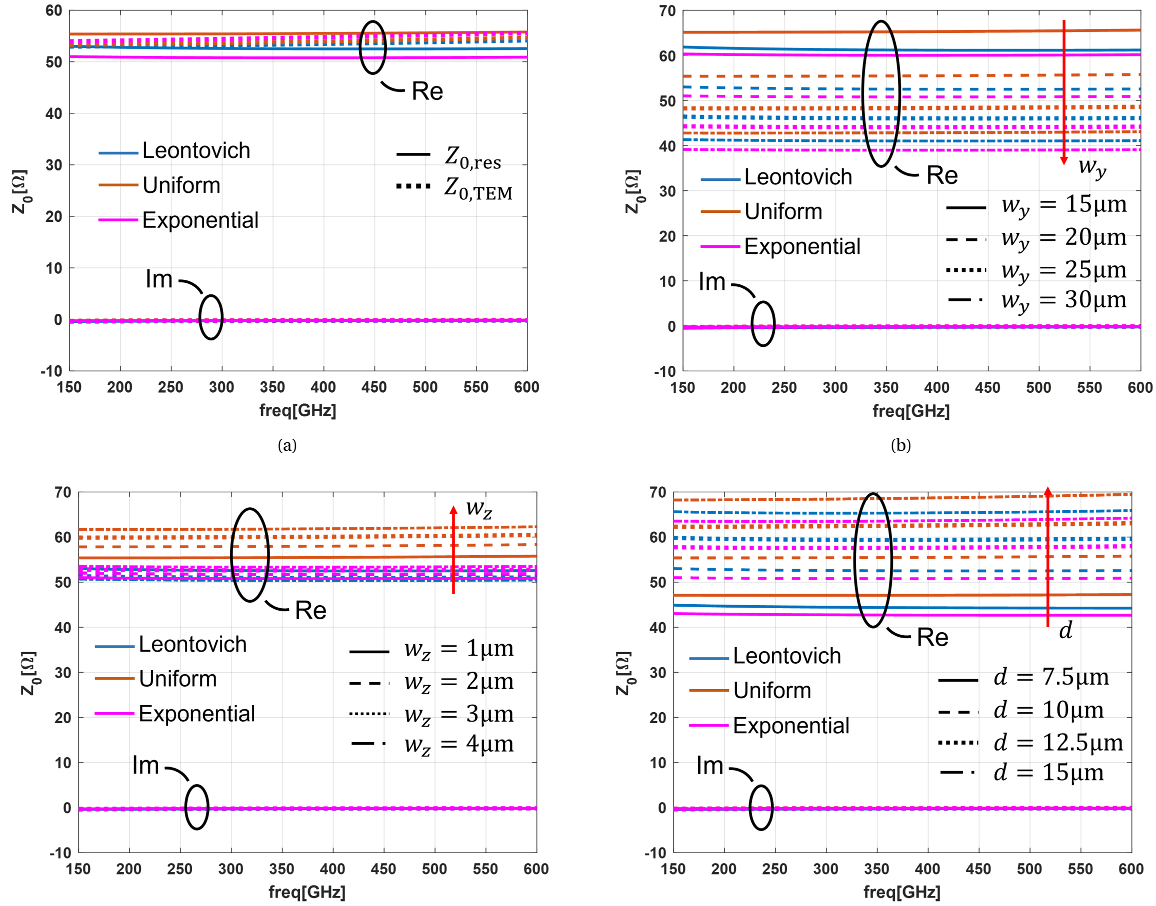

(a) (b) (c) (d)

Figure 5.4: Characteristic impedance of a microstrip constituted of a material with conductivity $\sigma = 4.1 \cdot 10^7$ S/m, printed on a dielectric substrate with permittivity $\varepsilon_r = 4.3$, (a) having a metal thickness $w_z = 1\mu m$ and dielectric thickness $d = 10\mu m$ for varying width w_y, (b) having a width $w_y = 20\mu m$ and dielectric thickness $d = 10\mu m$ for varying metal thickness w_z, and (c) having a width $w_y = 20\mu m$ and metal thickness $w_z = 1\mu m$ for varying dielectric thickness d

Fig. 5.5b shows that the attenuation constant is less sensitive to the thickness of the metal, when we use either the Leontovich boundary condition or the exponential distribution. This can be understood by noting that the width of the dipole is much larger than the thickness. Since the current is localized at the outer surface of the dipole, varying the thickness tends to have a small effect on the total area over which the current is distributed.

Fig. 5.5a shows the attenuation in dB/λ_0 for a microstrip with the same dimensions and material parameters as in Fig. 5.4b. Fig. 5.5a shows that the attenuation constant only has a weak dependence on the width of the microstrip. This can be understood by considering the perturbation method [43], which allows us to express the attenuation constant as in (4.95). Since the power lost per unit length P_l and the power transmitted along the transmission line P_0 both scale with the width of the microstrip, the two effects tend to cancel each other, which results in an attenuation constant that only has a weak dependence on the width.

Finally, Fig. 5.5c shows the attenuation constant for a microstrip with the same dimensions and material parameters as in Fig. 5.4d. Fig. 5.5c shows that the attenuation constant decreases when the thickness of the dielectric substrate is increased. This can again be understood by considering the perturbation method. Recall from Fig. 5.4d, that the characteristic impedance increases, when the thickness of the dielectric substrate is increased. Since the power transmitted along the transmission line is proportional to the characteristic impedance, the attenuation constant of the line decreases.

Fig. 5.6b shows the effective dielectric permittivity ε_{eff} for a microstrip with the same dimensions and material parameters as in Fig. 5.4c. Fig. 5.6b shows that ε_{eff} decreases significantly when the thickness of the metal is increased. This can be understood as follows. A current on the bottom of the metal strip is flowing at the interface between the dielectric substrate and the air region and will therefore have an effective permittivity

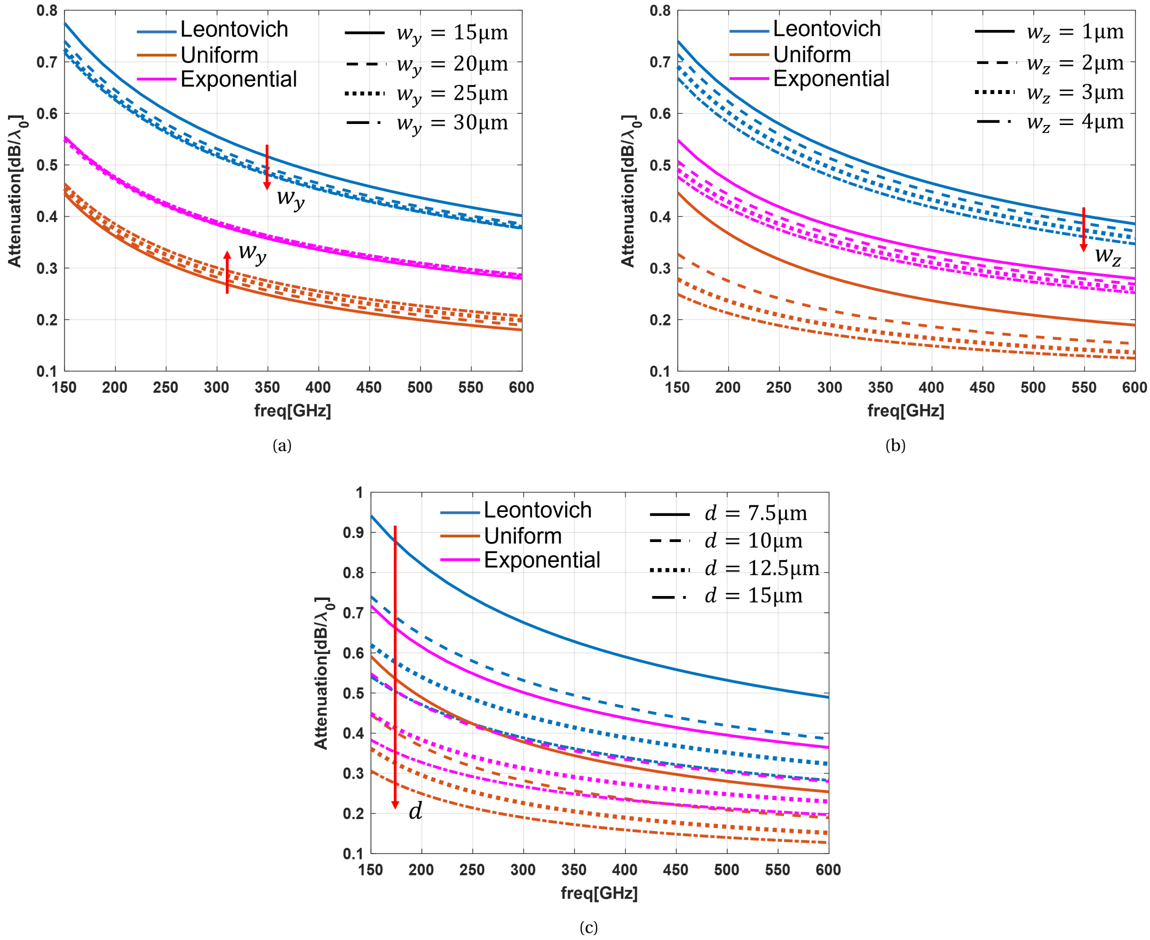

Figure 5.5: Attenuation constant of a microstrip constituted of a material with conductivity $\sigma = 4.1 \cdot 10^7$S/m, printed on a dielectric substrate with permittivity $\varepsilon_r = 4.3$ (a) having a metal thickness $w_z = 1\mu$m and dielectric thickness $d = 10\mu$m for varying width w_y, (b) having a width $w_y = 20\mu$m and dielectric thickness $d = 10\mu$m for varying metal thickness w_z, and (c) having a width $w_y = 20\mu$m and metal thickness $w_z = 1\mu$m for varying dielectric thickness d

that is close to the average of the two regions. On the other hand, a current on the top of the metal strip is located farther away from the interface and will have a lower effective permittivity. By considering both the current on the top and bottom of the metal strip, the effective permittivity becomes lower compared to a formulation in which all of the current is assumed to be at the interface between the two regions. Consequently, if the thickness of the metal is increased, the current on the top of the metal strip moves farther away from the interface of the two regions, which decreases the overall effective permittivity.

Figs. 5.6a and 5.6c show the effective dielectric permittivity for a microstrip with the same dimensions and material parameters as in Figs.5.4b and 5.4d, respectively. Figs. 5.6a and 5.6c show that the effective dielectric permittivity of the microstrip has a relatively weak dependence on the width of the metal strip and the thickness of the dielectric substrate. Finally, from Figs. 5.6a, 5.6b and 5.6c it becomes apparent that the effective permittivity, obtained by using the Leontovich boundary condition, and the effective permittivity, obtained by using the exponential distribution of (5.26), bear a close resemblance, since both distributions take into account the fact that the current is localized at the outer surface of the metal. On the other hand, the effective permittivity, obtained by assuming a uniform distribution on the cross-section, shows a larger disagreement with the other two distributions, since the uniform distribution does not take into account the skin effect.

5.3. Separation current top and bottom

Due to the presence of the dielectric substrate and the ground plane underneath, a microstrip is not symmetric in the z-direction. Therefore, it is not appropriate to assume a symmetric current distribution along this

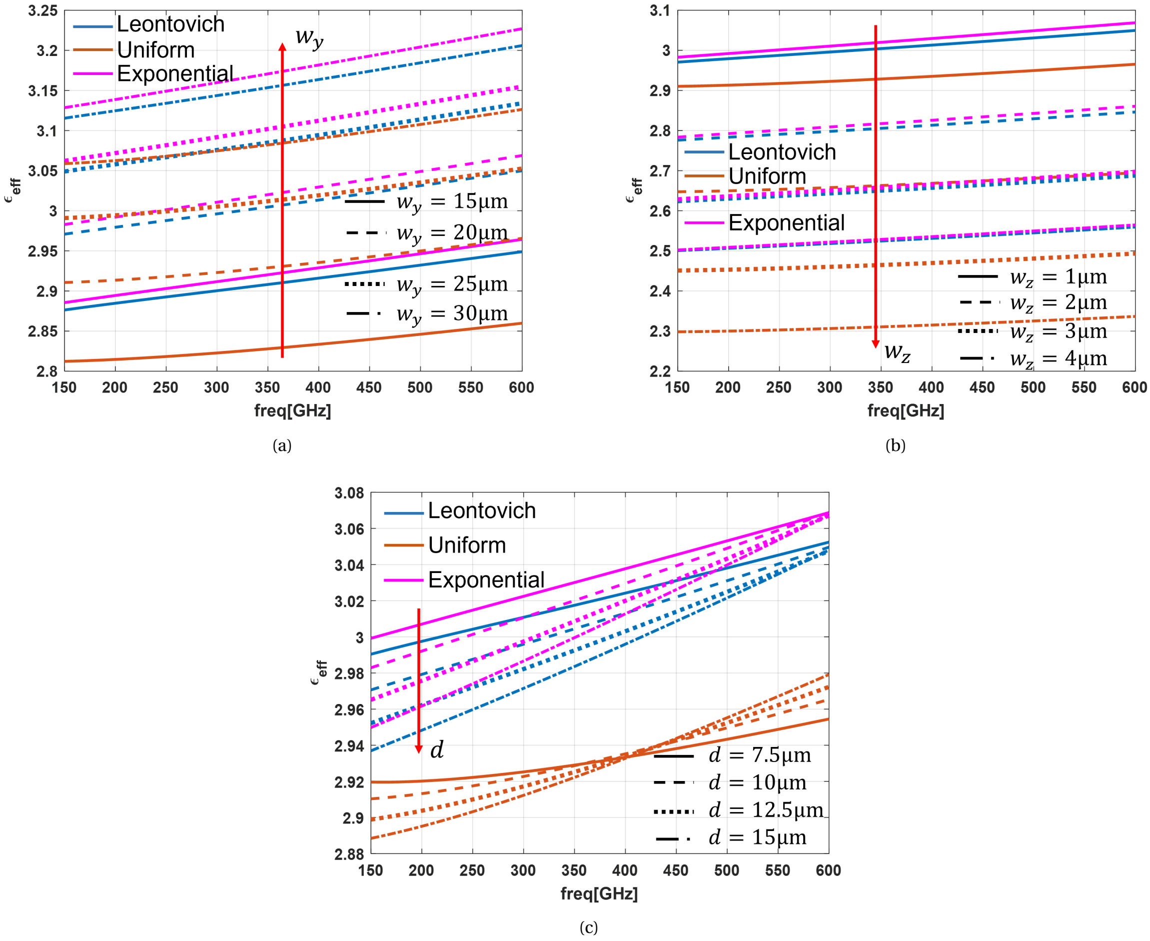

Figure 5.6: Effective dielectric permittivity of a microstrip constituted of a material having conductivity $\sigma = 4.1 \cdot 10^7$S/m, printed on a dielectric substrate with permittivity $\varepsilon_r = 4.3$ (a) having a metal thickness $w_z = 1\mu$m and dielectric thickness $d = 10\mu$m for varying width w_y, (b) having a width $w_y = 20\mu$m and dielectric thickness $d = 10\mu$m for varying metal thickness w_z, and (c) having a width $w_y = 20\mu$m and metal thickness $w_z = 1\mu$m for varying dielectric thickness d

direction. (As we shall see, the current will mainly be localized at the bottom of the strip.) To address this problem, we will define two basis functions, representing the current on the top and the bottom, allowing the current on both sides of the strip to be different.

5.3.1. Derivation Green's function

By following the same steps as in Section 4.1.1 and by expanding the transverse current distribution into two basis functions, the electric field integral equation can be expressed as follows

$$E_{\text{inc},l}(k_x)e_{\text{inc},t}(y,z) = \sum_{m=1}^{2} I_m(k_x)\rho j_{t,m}(y,z) - \sum_{m=1}^{2} I_m(k_x)\frac{1}{2\pi}\int_{-\infty}^{\infty}\int_{-\infty}^{\infty} G_{xx}^{ej}(k_x,k_y,z,z')J_{t,m}(k_y,z')e^{-jk_y y}\,dk_y\,dz', \tag{5.45}$$

where m denotes the index of the basis function. By performing a testing with the Galerkin's method, we obtain the following expression

$$
\begin{aligned}
&E_{\text{inc},l}(k_x)\langle e_{\text{inc},t}(y,z), j_{tn}(y,z)\rangle_A = \sum_{m=1}^{2} \rho I_m(k_x)\langle j_{tm}(y,z), j_{tn}(y,z)\rangle_A - \\
&\sum_{m=1}^{2} I_m(k_x)\frac{1}{2\pi}\int_{-\infty}^{\infty}\int_{-\infty}^{\infty}\int_{-\infty}^{\infty} G_{xx}^{ej}(k_x,k_y,k_z)J_{tm}(k_y,z')J_{tn}^{*}(k_y,z)\,dk_y\,dz\,dz',
\end{aligned}
\tag{5.46}
$$

where n denotes the index of the test function. The relation in (5.46) can be expressed as the following matrix equation

$$
\begin{aligned}
&\begin{bmatrix}\langle e_{\text{inc},t}(y,z), J_{t1}(y,z)\rangle_A\\ \langle e_{\text{inc},t}(y,z), J_{t2}(y,z)\rangle_A\end{bmatrix} E_{\text{inc},l}(k_x) = \\
&\left(\begin{bmatrix}\rho\langle J_{t1}(y,z), J_{t1}(y,z)\rangle_A & \rho\langle J_{t1}(y,z), J_{t2}(y,z)\rangle_A\\ \rho\langle J_{t2}(y,z), J_{t1}(y,z)\rangle_A & \rho\langle J_{t2}(y,z), J_{t2}(y,z)\rangle_A\end{bmatrix} - \begin{bmatrix}D_{11}(k_x) & D_{12}(k_x)\\ D_{21}(k_x) & D_{22}(k_x)\end{bmatrix}\right)\begin{bmatrix}I_1(k_x)\\ I_2(k_x)\end{bmatrix}.
\end{aligned}
\tag{5.47}
$$

By defining the current vector as follows

$$
\mathbf{I}(k_x) = \begin{bmatrix}I_1(k_x)\\ I_2(k_x)\end{bmatrix},
\tag{5.48}
$$

by defining the following excitation vector

$$
\mathbf{V}(k_x) = \begin{bmatrix}\langle e_{\text{inc},t}(y,z), J_{t1}(y,z)\rangle_A\\ \langle e_{\text{inc},t}(y,z), J_{t2}(y,z)\rangle_A\end{bmatrix} E_{\text{inc},l}(k_x),
\tag{5.49}
$$

by defining the coupling matrix as follows

$$
\mathbf{D}(k_x) = \begin{bmatrix}D_{11}(k_x) & D_{12}(k_x)\\ D_{21}(k_x) & D_{22}(k_x)\end{bmatrix},
\tag{5.50}
$$

and by defining the following matrix

$$
\mathbf{Z}_{\text{loss}} = \begin{bmatrix}\rho\langle J_{t1}(y,z), J_{t1}(y,z)\rangle_A & \rho\langle J_{t1}(y,z), J_{t2}(y,z)\rangle_A\\ \rho\langle J_{t2}(y,z), J_{t1}(y,z)\rangle_A & \rho\langle J_{t2}(y,z), J_{t2}(y,z)\rangle_A\end{bmatrix},
\tag{5.51}
$$

where $\mathbf{Z}_{\text{loss}}$ takes into account the Ohmic losses inside the metal strip, (5.47) can be expressed as follows

$$
\mathbf{V}(k_x) = \mathbf{Z}(k_x)\mathbf{I}(k_x),
\tag{5.52}
$$

where $\mathbf{Z}(k_x)$ is defined as follows

$$
\mathbf{Z}(k_x) = \mathbf{Z}_{\mathbf{loss}} - \mathbf{D}(k_x).
\tag{5.53}
$$

In the case of the microstrip, the entries of the matrix $\mathbf{D}(k_x)$ are calculated by evaluating the following 3D-integral

$$
D_{mn}(k_x) = \frac{1}{2\pi}\int_{-\infty}^{\infty}\int_{0}^{w_z}\int_{0}^{w_z} G_{xx}^{ej}(k_x,k_y,z,z')J_{tm}(k_y,z')J_{tn}^{*}(k_y,z)dzdz'dk_y,
\tag{5.54}
$$

The transverse current distribution will be expanded into the following two basis functions

$$
j_{t,1}(y,z) = \frac{2}{w_y\pi}\frac{1}{\sqrt{1-(2y/w_y)^2}}\frac{e^{-z/\delta_p}}{\delta_p(1-e^{-w_z/\delta_p})}
\tag{5.55}
$$

$$
j_{t,2}(y,z) = \frac{2}{w_y\pi}\frac{1}{\sqrt{1-(2y/w_y)^2}}\frac{e^{(z-w_z)/\delta_p}}{\delta_p(1-e^{-w_z/\delta_p})},
\tag{5.56}
$$

where $j_{t,1}(y,z)$ has an exponential decay starting from the bottom of the metal strip, and $j_{t,2}(y,z)$ has an exponential decay starting from the top of the metal strip. If the penetration depth δ_p, is small compared to the thickness of the metal, $j_{t,1}(y,z)$ and $j_{t,2}(y,z)$ can, for all practical purposes, be referred to as the current on the bottom and the current on the top of the metal strip. In Appendix H.3, the entries of $\mathbf{D}(k_x)$ are obtained explicitly, using the two exponential basis functions given by (5.55) and (5.56). Consequently, $D_{11}(k_x)$ can be expressed as follows

$$
\begin{aligned}
D_{11}(k_x) = &-\frac{1}{2\pi}\int_{-\infty}^{\infty}\int_{0}^{w_z}\frac{V^{+}_{\mathrm{TM,upper}}k_x^2+V^{+}_{\mathrm{TE,upper}}k_y^2}{k_x^2+k_y^2}\,\frac{e^{-z'/\delta_p}-e^{-w_z/\delta_p}e^{-jk_{z0}(w_z-z')}}{jk_{z0}+1/\delta_p}\cdot \\
&\qquad e^{-z'/\delta_p}J_0\left(\frac{k_yw_y}{2}\right)\mathrm{sinc}\left(\frac{k_yw_y}{2}\right)dz'dk_y- \\
&\frac{1}{2\pi}\int_{-\infty}^{\infty}\int_{0}^{w_z}\frac{V^{+}_{\mathrm{TM,lower}}k_x^2+V^{+}_{\mathrm{TE,lower}}k_y^2}{k_x^2+k_y^2}\,\frac{e^{-z'/\delta_p}-e^{-jk_{z0}z'}}{jk_{z0}-1/\delta_p}\cdot \\
&\qquad e^{-\frac{z'}{\delta_p}}J_0\left(\frac{k_yw_y}{2}\right)\mathrm{sinc}\left(\frac{k_yw_y}{2}\right)dz'dk_y- \\
&\frac{1}{2\pi}\int_{-\infty}^{\infty}\int_{0}^{w_z}\frac{\Gamma_{TM}V^{+}_{\mathrm{TM,lower}}k_x^2+\Gamma_{TE}V^{+}_{\mathrm{TE,lower}}k_y^2}{k_x^2+k_y^2}\,\frac{e^{-jk_{z0}z'}-e^{-z'/\delta_p}e^{-2jk_{z0}z'}}{jk_{z0}+1/\delta_p}\cdot \\
&\qquad e^{-z'/\delta_p}J_0\left(\frac{k_yw_y}{2}\right)\mathrm{sinc}\left(\frac{k_yw_y}{2}\right)dz'dk_y.
\end{aligned}
\tag{5.57}
$$

$D_{22}(k_x)$ is given by the following expression

$$
\begin{aligned}
D_{22}(k_x) = &-\frac{1}{2\pi}\int_{-\infty}^{\infty}\int_{0}^{w_z}\frac{V^{+}_{\mathrm{TM,upper}}k_x^2+V^{+}_{\mathrm{TE,upper}}k_y^2}{k_x^2+k_y^2}\,\frac{e^{-(w_z-z')/\delta_p}-e^{-jk_{z0}(w_z-z')}}{jk_{z0}-1/\delta_p}\cdot \\
&\qquad e^{-(w_z-z')/\delta_p}J_0\left(\frac{k_yw_y}{2}\right)\mathrm{sinc}\left(\frac{k_yw_y}{2}\right)dz'dk_y- \\
&\frac{1}{2\pi}\int_{-\infty}^{\infty}\int_{0}^{w_z}\frac{V^{+}_{\mathrm{TM,lower}}k_x^2+V^{+}_{\mathrm{TE,lower}}k_y^2}{k_x^2+k_y^2}\,\frac{e^{-(w_z-z')/\delta_p}-e^{-jk_{z0}z'}}{jk_{z0}-1/\delta_p}\cdot \\
&\qquad e^{-(w_z-z')/\delta_p}J_0\left(\frac{k_yw_y}{2}\right)\mathrm{sinc}\left(\frac{k_yw_y}{2}\right)dz'dk_y- \\
&\frac{1}{2\pi}\int_{-\infty}^{\infty}\int_{0}^{w_z}\frac{\Gamma_{TM}V^{+}_{\mathrm{TM,lower}}k_x^2+\Gamma_{TE}V^{+}_{\mathrm{TE,lower}}k_y^2}{k_x^2+k_y^2}\,\frac{e^{-w_z/\delta_p}e^{-jk_{z0}z'}-e^{-(w_z-z')/\delta_p}e^{-2jk_{z0}z'}}{jk_{z0}+1/\delta_p}\cdot \\
&\qquad e^{-(w_z-z')/\delta_p}J_0\left(\frac{k_yw_y}{2}\right)\mathrm{sinc}\left(\frac{k_yw_y}{2}\right)dz'dk_y.
\end{aligned}
\tag{5.58}
$$

As a consequence of the reciprocity theorem [44], $D_{12}(k_x)$ and $D_{21}(k_x)$ are equal. As shown in Appendix H.3, $D_{12}(k_x)$ and $D_{21}(k_x)$ can be expressed as follows

$$
\begin{aligned}
D_{12}(k_x) = D_{21}(k_x) = &-\frac{1}{2\pi}\int_{-\infty}^{\infty}\int_{0}^{w_z}\frac{V^{+}_{\mathrm{TM,upper}}k_x^2+V^{+}_{\mathrm{TE,upper}}k_y^2}{k_x^2+k_y^2}\,\frac{e^{-w_z-z'/\delta_p}-e^{-jk_{z0}(w_z-z')}}{jk_{z0}-1/\delta_p}\cdot \\
&\qquad e^{-z'/\delta_p}J_0\left(\frac{k_yw_y}{2}\right)\mathrm{sinc}\left(\frac{k_yw_y}{2}\right)dz'dk_y- \\
&\frac{1}{2\pi}\int_{-\infty}^{\infty}\int_{0}^{w_z}\frac{V^{+}_{\mathrm{TM,lower}}k_x^2+V^{+}_{\mathrm{TE,lower}}k_y^2}{k_x^2+k_y^2}\,\frac{e^{-(w_z-z')/\delta_p}-e^{-w_z/\delta_p}e^{-jk_{z0}z'}}{jk_{z0}+1/\delta_p}\cdot \\
&\qquad e^{-z'/\delta_p}J_0\left(\frac{k_yw_y}{2}\right)\mathrm{sinc}\left(\frac{k_yw_y}{2}\right)dz'dk_y- \\
&\frac{1}{2\pi}\int_{-\infty}^{\infty}\int_{0}^{w_z}\frac{\Gamma_{TM}V^{+}_{\mathrm{TM,lower}}k_x^2+\Gamma_{TE}V^{+}_{\mathrm{TE,lower}}k_y^2}{k_x^2+k_y^2}\,\frac{e^{-w_z/\delta_p}e^{-jk_{z0}z'}-e^{-(w_z-z')/\delta_p}e^{-2jk_{z0}z'}}{jk_{z0}-1/\delta_p}\cdot \\
&\qquad e^{-z'/\delta_p}J_0\left(\frac{k_yw_y}{2}\right)\mathrm{sinc}\left(\frac{k_yw_y}{2}\right)dz'dk_y.
\end{aligned}
\tag{5.59}
$$

By analytically inverting the matrix in (5.53), the spectral currents $I_1(k_x)$ and $I_2(k_x)$, associated with the two basis functions $j_{t,1}(y,z)$ and $j_{t,2}(y,z)$, can be calculated as follows

$$I_1(k_x) = \frac{Z_{22}(k_x)V_1(k_x) - Z_{12}(k_x)V_2(k_x)}{Z_{\text{det}}(k_x)} \tag{5.60}$$

$$I_2(k_x) = \frac{Z_{11}(k_x)V_1(k_x) - Z_{21}(k_x)V_2(k_x)}{Z_{\text{det}}(k_x)}, \tag{5.61}$$

where

$$Z_{\text{det}}(k_x) = \det(\mathbf{Z}(k_x)) = Z_{11}(k_x)Z_{22}(k_x) - Z_{12}(k_x)Z_{21}(k_x) \tag{5.62}$$

Once the spectral currents $I_1(k_x)$ and $I_2(k_x)$ are obtained, the spatial currents $i_1(x)$ and $i_2(x)$, associated to the two basis functions $j_{t,1}(y,z)$ and $j_{t,2}(y,z)$, can be calculated by performing the following inverse Fourier transform

$$i_m(x) = \frac{1}{2\pi}\int_{-\infty}^{\infty} I_m(k_x)e^{-jk_x x}dk_x. \tag{5.63}$$

Finally, the input admittance can be calculated as the superposition of the input admittance, due to $i_1(x)$ and $i_2(x)$, as shown in the following expression

$$Y_{\text{in}} = Y_1 + Y_2, \tag{5.64}$$

where

$$Y_m = \frac{1}{2\pi}\int_{-\infty}^{\infty} I_m(k_x)\text{sinc}\left(\frac{k_x\Delta}{2}\right)dk_x. \tag{5.65}$$

5.3.2. Spectral properties and validation current

To investigate the properties of the spectral currents $I_1(k_x)$ and $I_2(k_x)$, when the transverse current distribution is expanded into two basis functions, the spectral plane of $1/\det|\mathbf{Z}(k_x)|$ has been calculated for a microstrip, having a width $w_y = 1\mu$m and a metal thickness $w_z = 1\mu$m, constituted of a material with conductivity $\sigma = 1\cdot 10^8$S/m, printed on a dielectric substrate, having a thickness $d = 1\mu$m and permittivity $\varepsilon_r = 1$. Note that these dimensions and material parameters are not realistic for an actual microstrip, but have been chosen to illustrate the properties of the spectral currents $I_1(k_x)$ and $I_2(k_x)$. Fig. 5.7a shows the spectral plane of $1/Z_{\text{det}}(k_x)$. From Fig. 5.7a, it becomes apparent that the spectrum contains two poles. To understand what these poles correspond to, we will define the contribution of pole 1 and pole 2 to the currents $i_1(x)$ and $i_2(x)$ as follows

$$i_{1,\text{res},pn} = -j\frac{Z_{22}(k_{xpn})V_1(k_{xpn}) - Z_{12}(k_{xpn})V_2(k_{xpn})}{Z'_{\text{det}}(k_{xpn})}e^{-jk_{xpn}x} \tag{5.66}$$

$$i_{2,\text{res},pn} = -j\frac{Z_{11}(k_{xpn})V_1(k_{xpn}) - Z_{21}(k_{xpn})V_2(k_{xpn})}{Z'_{\text{det}}(k_{xpn})}e^{-jk_{xpn}x}, \tag{5.67}$$

where pn refers to pole 1 or pole 2.

Fig. 5.7b shows the real and imaginary part of $i_{1,\text{res},p1}$ and $i_{2,\text{res},p1}$, i.e. the contribution of pole 1 to the current flowing on the bottom of the metal strip and the contribution of pole 1 to the current flowing on the top of the metal strip. Fig. 5.7c shows the real and imaginary part of $i_{1,\text{res},p1}$ and $i_{2,\text{res},p1}$, i.e. the contribution of pole 2 to the current flowing on the bottom of the metal strip and the contribution of pole 2 to the current flowing on the top of the metal strip. Fig. 5.7b shows that pole 1 corresponds to a current distribution in which the current on the bottom of the metal strip is in phase with the current on the top, i.e. a common mode. On the other hand, Fig. 5.7c shows that pole 2 corresponds to a current distribution in which the current on the bottom of the metal strip is 180° out of phase with the current on the top, i.e. a differential mode. From Fig. 5.7a, it becomes clear that pole 1 has a much smaller attenuation constant than pole 2. Consequently, the differential mode decays much faster than the common mode, which means that the common mode is the dominant mode along the transmission line.

To validate the formulation, developed in Section 5.3.1, and to demonstrate the relevance of allowing a different current on the top and bottom of the metal strip, a microstrip has been simulated, consisting of a metal strip having a width $w_y = 10\mu$m and metal thickness $w_z = 10\mu$m, constituted of a material with conductivity $\sigma = 10^7$S/m, printed on a dielectric substrate having a thickness $d = 10\mu$m and permittivity $\varepsilon_r = 11.9$. Fig.5.8a shows $i_1(x)$, i.e. the current on the bottom of the metal strip, while Fig.5.8b shows $i_2(x)$, i.e. the current on

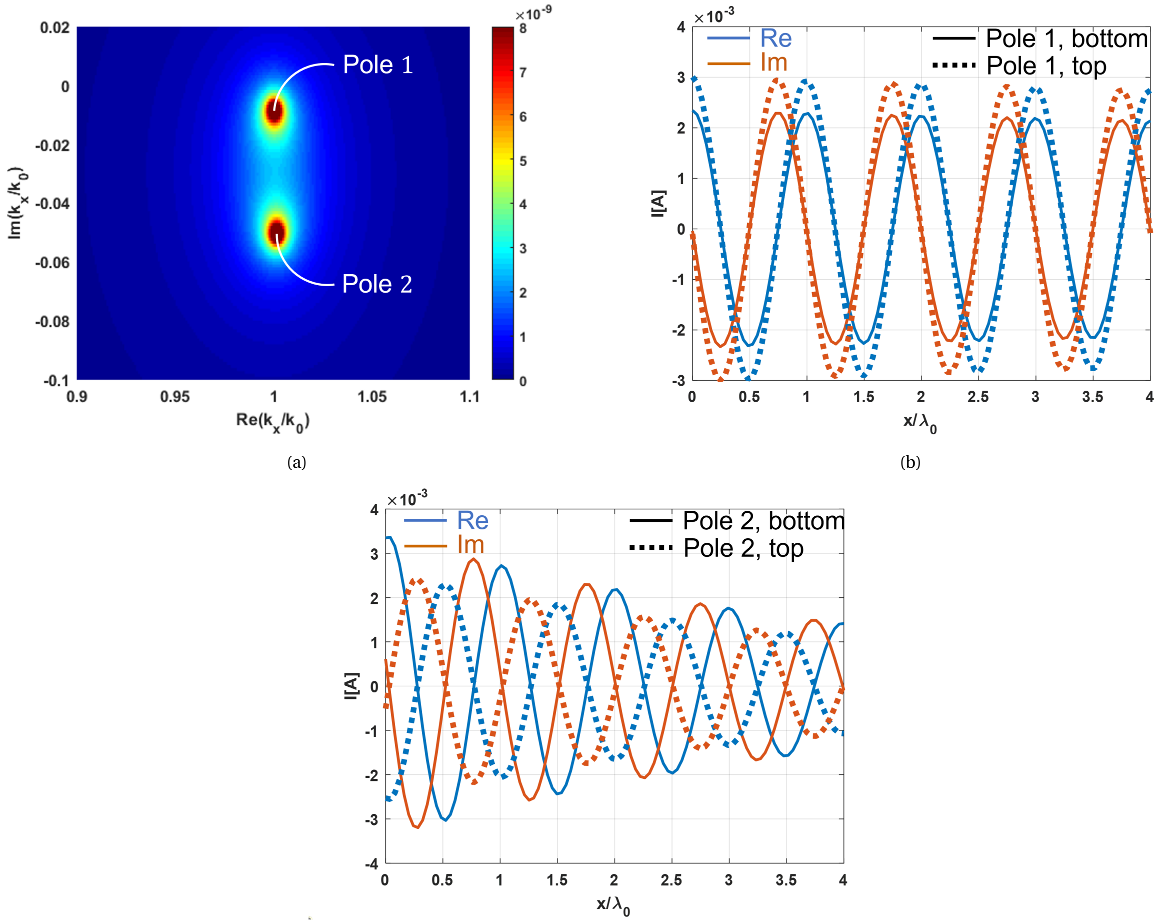

(c)

Figure 5.7: (a) The spectral plane of $1/\det|\mathbf{Z}(k_x)|$ for a microstrip, having a width $w_y = 1\mu$m and a metal thickness $w_z = 1\mu$m, constituted of a material with conductivity $\sigma = 1 \cdot 10^8$S/m, printed on a dielectric substrate, having a thickness $d = 1\mu$m and permittivity $\varepsilon_r = 1$ with the location of the two poles, (b) the current associated to pole 1 on the top and the bottom of the microstrip, and (c) the current associated to pole 2 on the top and the bottom of the microstrip

the top of the metal strip. As shown in Figs.5.8a and 5.8b, the current on the bottom is much larger than the current on the top, since the electric field is mainly focused between the metal strip and the ground plane. Therefore, the losses along the transmission line will mainly be associated with the current on the bottom of the metal strip. Moreover, for the current on the bottom of the strip, Fig.5.8a shows a good agreement between $i_1(x)$, obtained using (5.63) and the current obtained from CST. For the current on the top of the metal strip, Fig. 5.8b shows a larger discrepancy between $i_2(x)$, obtained using (5.63), and the current obtained with CST. However, since the current on the bottom is dominant, this difference is less significant, when we characterize the transmission line in terms of its characteristic impedance and its losses. Finally, it should be noted that a metal strip with equal width and thickness is not a realistic geometry. The dimensions in Figs.5.8a and 5.8b have been chosen to allow the validation with CST, which cannot simulate a realistic microstrip geometry.

5.3.3. Transmission line characterization

As discussed in Section 5.3, expanding the transverse current distribution into two basis functions leads to two polar singularities in the spectral currents $I_1(k_x)$ and $I_2(k_x)$. Therefore, it is possible to represent the microstrip by two parallel transmission lines, each with its own characteristic impedance and propagation constant. However, we would like to represent the microstrip by a single transmission line with a single characteristic impedance and propagation constant. To achieve this, we have considered two different approaches. The first approach is to define the average propagation constant k_{xp}^{av}, where each pole is weighted by its contribution to the input admittance. To this extent, we will first define the contribution of each of the poles to the

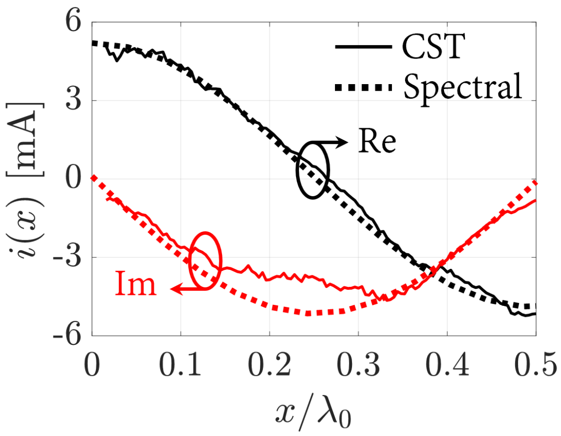

(a)

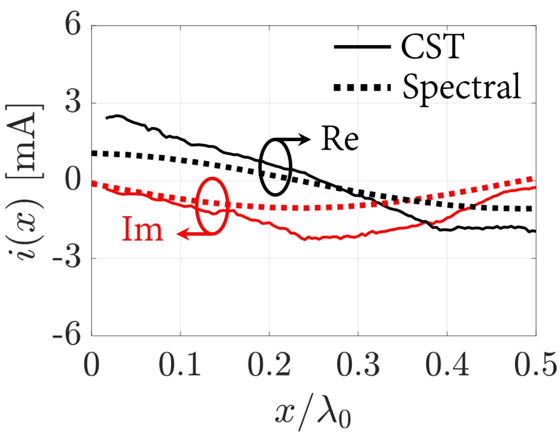

(b)

Figure 5.8: The current on a microstrip, having metal thickness $w_z = 10\mu$m, width $w_y = 10\mu$m, constituted of a material with conductivity $\sigma = 10^7$S/m and printed on a dielectric substrate having a thickness $d = 10\mu$m and permittivity $\varepsilon_r = 11.9$, (a) obtained from (5.60), i.e. the current on the bottom of the microstrip, and (b) obtained from (5.61), i.e. the current on the top of the microstrip

input admittance, as follows

$$Y_{\mathrm{res},pn} = Y_{1,\mathrm{res},pn} + Y_{2,\mathrm{res},pn}, \tag{5.68}$$

where pn refers to pole 1 or pole 2. $Y_{1,\mathrm{res},pn}$ and $Y_{2,\mathrm{res},pn}$ denote the contributions of the pole to Y_1 and Y_2 in (5.64) and are given by the following expressions

$$Y_{1,\mathrm{res},pn} = -j\frac{Z_{22}(k_{xpn})V_1(k_{xpn}) - Z_{12}(k_{xpn})V_2(k_{xpn})}{Z'_{\mathrm{det}}(k_{xpn})}\mathrm{sinc}\left(\frac{k_{xpn}\Delta}{2}\right) \tag{5.69}$$

$$Y_{2,\mathrm{res},pn} = -j\frac{Z_{11}(k_{xpn})V_1(k_{xpn}) - Z_{21}(k_{xpn})V_2(k_{xpn})}{Z'_{\mathrm{det}}(k_{xpn})}\mathrm{sinc}\left(\frac{k_{xpn}\Delta}{2}\right). \tag{5.70}$$

With these definitions we may define k_{xp}^{av} as follows

$$k_{xp}^{av} = k_{xp1}\frac{|Y_{\mathrm{res},p1}|}{|Y_{\mathrm{res},p1}| + |Y_{\mathrm{res},p2}|} + k_{xp2}\frac{|Y_{\mathrm{res},p2}|}{|Y_{\mathrm{res},p1}| + |Y_{\mathrm{res},p2}|}, \tag{5.71}$$

Note that the input admittance is practically equal the current at $x = 0$. Therefore, the poles are essentially weighted by the amplitudes of the corresponding current waves.

The second approach consists of two steps. The first step is to use the formulation developed in Section 5.3.1 to obtain the contribution of both poles to the input admittance Y_1 and Y_2, corresponding to the currents $i_1(x)$ and $i_2(x)$, as shown in the following expression

$$Y_{m,\mathrm{res}} = Y_{m,\mathrm{res},p1} + Y_{m,\mathrm{res},p2}, \tag{5.72}$$

where the contribution of each of the poles $Y_{m,\mathrm{res},pn}$, is obtained using (5.69) or (5.70). The next step is to define the following basis function

$$j_{t,z}(z) = Re^{-z/\delta_p} + e^{z-w_z/\delta_p} \tag{5.73}$$

to model the asymmetry in $\hat{z}$, where the ratio R is calculated as follows

$$R = \frac{|Y_{1,\mathrm{res}}|}{|Y_{2,\mathrm{res}}|}. \tag{5.74}$$

We will then use the formulation developed in Section 5.2.1 for a single basis function to obtain the characteristic impedance and propagation constant, in which (5.73) is used as the transverse current distribution.

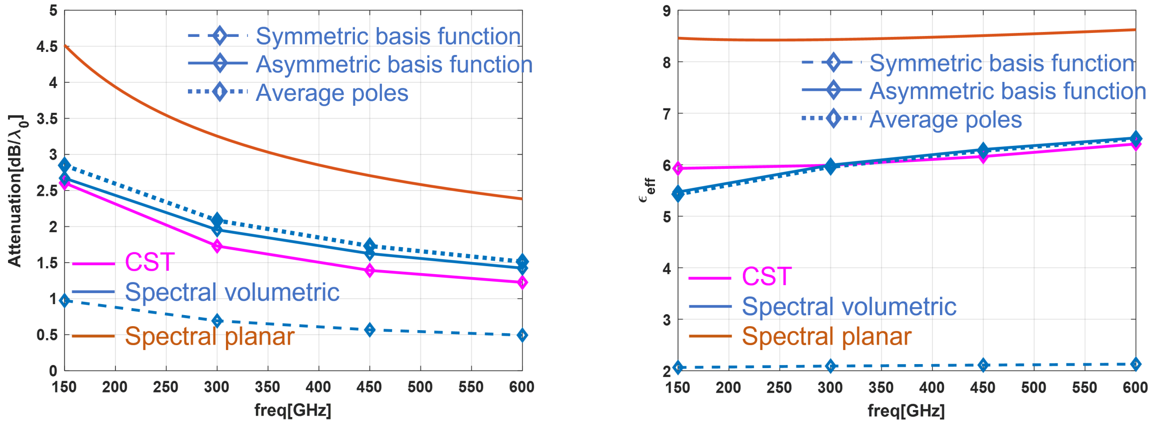

(a) (b)

Figure 5.9: Dispersion characteristics of a microstrip having metal thickness $w_z = 10\mu$m, width $w_y = 10\mu$m, constituted of a material with conductivity $\sigma = 10^7$S/m and printed on a dielectric substrate having a thickness $d = 10\mu$m and permittivity $\varepsilon_r = 11.9$, obtained from CST, using the planar formulation in [19], using the symmetric basis function in (5.26), using the asymmetric basis function in (5.73), and by averaging the poles as in (5.71), with (a) the attenuation constant, and (b) the effective dielectric permittivity

5.3.4. Validation CST

To validate both approaches, described in Section 5.3.3, a microstrip has been simulated, having a width $w_y = 10\mu$m and a metal thickness $w_z = 10\mu$m, constituted of a material with conductivity $\sigma = 10^7$S/m, printed on a dielectric substrate having a thickness $d = 10\mu$m and permittivity $\varepsilon_r = 11.9$. Fig. 5.9a shows the attenuation along the microstrip in dB/λ_0, where the dashed line denotes the attenuation constant, obtained using the single symmetric basis function defined in (5.26), the solid line denotes the attenuation constant obtained, using the asymmetric basis function, defined in (5.73) and the dotted line denotes the attenuation constant, obtained by averaging the poles as in (5.71). Moreover, the results, obtained from both CST and the planar formulation of [19], have been plotted. As shown in Fig. 5.9a, using a symmetric basis function results in a significant underestimation of the losses. The main reason is that the symmetric basis function of (5.26) overestimates the area over which the current is distributed, which leads to a smaller current density and therefore an underestimation of the losses. On the other hand, both averaging the poles as in (5.71) and using the asymmetric basis function in (5.73) results in an attenuation constant that is comparable to CST. Finally, it should be noted that the use of a planar formulation is not adequate to accurately estimate the losses for this geometry.

Fig. 5.9b shows the effective permittivity for the same geometry as in Fig. 5.9a. Similar to before, using the symmetric basis function in (5.26) results in an effective permittivity that is significantly too low. This result can be understood as follows. The current on the bottom of the dipole is practically located at the interface between the dielectric and the air region. Therefore, the effective permittivity of a current located on the bottom of the strip is close to the average between the two regions. However, the current on the top is farther away from the interface between the two regions. Therefore, the effective permittivity of a current located on the top of the strip is closer to the permittivity of the air region. By considering both the current on the top and bottom of the metal strip, the effective permittivity becomes lower compared to a formulation in which all of the current is assumed to be located at the interface. Moreover, the influence of the current on the top and bottom of the strip on the effective permittivity of the microstrip, depends on the ratio between the two currents. Therefore, an overestimation of the current on the top of the metal strip results in an underestimation of the effective permittivity of the microstrip. On the other hand, Fig. 5.9b shows that both averaging the poles as in (5.71) and using the asymmetric basis function in (5.73) results in an effective permittivity that is comparable to CST. Similar to before, the use of a planar formulation is not adequate to accurately estimate the effective permittivity for this geometry.

5.3.5. Validation Rautio

As shown in Figs. 5.9a and 5.9b, the losses and the effective permittivity, obtained by the procedures, explained in Section 5.3, correspond well with the results from CST. Nevertheless, the accuracy of the CST simulations is difficult to assess, because the discretization, used during the simulation, is relatively large with respect to

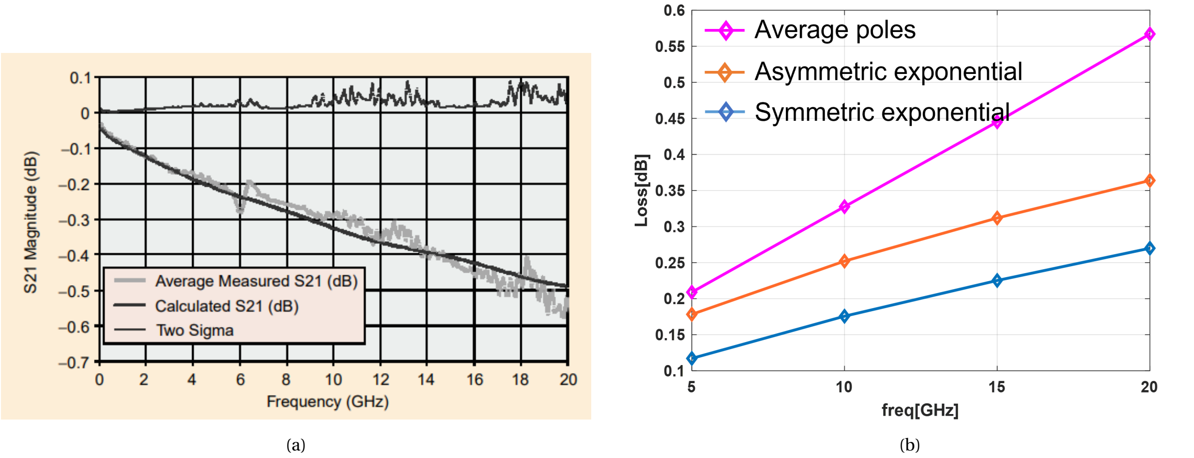

Figure 5.10: Losses in dB of a microstrip, having a length $l = 6.8$mm, a width $w_y = 51\mu$m and a metal thickness $w_z = 9\mu$m, constituted of a material with conductivity $\sigma = 3.42 \cdot 10^7$S/m, printed on a dielectric substrate having a thickness $d = 75\mu$m and permittivity $\varepsilon_r = 12.9$ with (a) the measurements from [22] and (b) the results obtained by the procedures, explained in Section 5.3.3

the penetration depth. To perform a more reliable validation, we have compared the losses, obtained by the spectral techniques, developed in this thesis, with the measurements in [22] of a microstrip, having a length $l = 6.8$mm, a width $w_y = 51\mu$m and a metal thickness $w_z = 9\mu$m, constituted of a material with conductivity $\sigma = 3.42 \cdot 10^7$S/m, printed on a dielectric substrate, having a thickness $d = 75\mu$m and permittivity $\varepsilon_r = 12.9$. While Fig. 5.10a shows the measured losses from [22], Fig.5.10b shows the losses, obtained by the spectral techniques, described in the previous sections. Fig.5.10b shows that the use of a symmetric basis function is not adequate to correctly estimate the losses along the microstrip. Using a single asymmetric basis function, on the other hand, results in a better estimation of the losses. Finally, the losses, obtained by averaging the two poles, correspond quite well with the measurements in [22]. Nevertheless, it is not entirely clear, whether this approach is fully justified. Since the procedure of using a single asymmetric basis function simply calculates the losses, associated to a current distribution with different amplitudes on both sides of the conductor, this approach should be considered the more justified procedure. Unfortunately, this procedure does not reconstruct the measurements in [22] perfectly. Hence, it may be necessary to consider alternative shapes to model the transverse current distribution.

6

Equivalent circuit characterization of a microstrip

In Chapters 4 and 5, we have developed a spectral domain formulation that allows us to characterize printed transmission lines in the presence of an arbitrary stratification, taking into account the nonzero thickness of the conductors. The relevant parameters of the transmission line can then be extracted from the polar singularities in the spectrum of the current. However, to obtain the total input admittance of the transmission line, we still have to perform the full integral in (4.59). To accelerate the convergence of the integral in (4.59), we may extract two dominant contributions of the current spectrum $I(k_x)$: the dynamic part and the asymptotic part. The dynamic part refers to the lower portion of the spectrum, which is dominated by the polar singularities. Therefore, it is possible to approximate this part of the spectrum by a Taylor expansion around the pole k_{xp}. This approximation enables an analytical evaluation of the inverse Fourier transform in (4.59).

The asymptotic part of the spectrum refers to the limit for k_x tending to infinity, and is dominated by the $k_y = 0$ component of the spectrum. The extraction of the dynamic and asymptotic part of the spectrum will enable an approximate evaluation of the input impedance through a simple equivalent circuit.

First, Section 6.1 discusses the dynamic part of the spectrum. Subsequently, Section 6.2 discusses the asymptotic part of the spectrum. Finally, Section 6.3 introduces the equivalent circuit, which enables a simple and efficient way to characterize the input admittance of the microstrip.

6.1. Dynamic part spectrum

The dynamic part of the spectrum $I(k_x)$ refers to the portion of the spectrum that is related to small values of k_x. This part of the spectrum is dominated by the polar singularities and can therefore be approximated by a Taylor expansion around the pole k_{xp}, as shown in the following expression

$$I_{\text{dyn}}(k_x) = \frac{2k_{xp}}{D'(k_{xp})(k_x^2 - k_{xp}^2)} \operatorname{sinc}\left(\frac{k_x \Delta}{2}\right). \tag{6.1}$$

The spatial current, associated with the dynamic part of the spectrum, can be calculated as the following inverse Fourier transform

$$i_{\text{dyn}}(x) = \frac{1}{2\pi} \int_{-\infty}^{\infty} \frac{2k_{xp}}{D'(k_{xp})(k_x^2 - k_{xp}^2)} \operatorname{sinc}\left(\frac{k_x \Delta}{2}\right) e^{-jk_x x} dk_x. \tag{6.2}$$

By closing the integral in (6.2) analytically, we obtain the following expressions

$$i_{\text{dyn}}(|x| > \frac{\Delta}{2}) = -\frac{j}{D'(k_{xp})} \operatorname{sinc}\left(\frac{k_{xp}\Delta}{2}\right) e^{-jk_{xp}|x|} \tag{6.3}$$

$$i_{\text{dyn}}(|x| < \frac{\Delta}{2}) = \frac{1}{\Delta} \frac{1}{D'(k_{xp})} \frac{1}{k_{xp}} (2 - 2\cos(k_{xp}) e^{-jk_{xp}\Delta/2}), \tag{6.4}$$

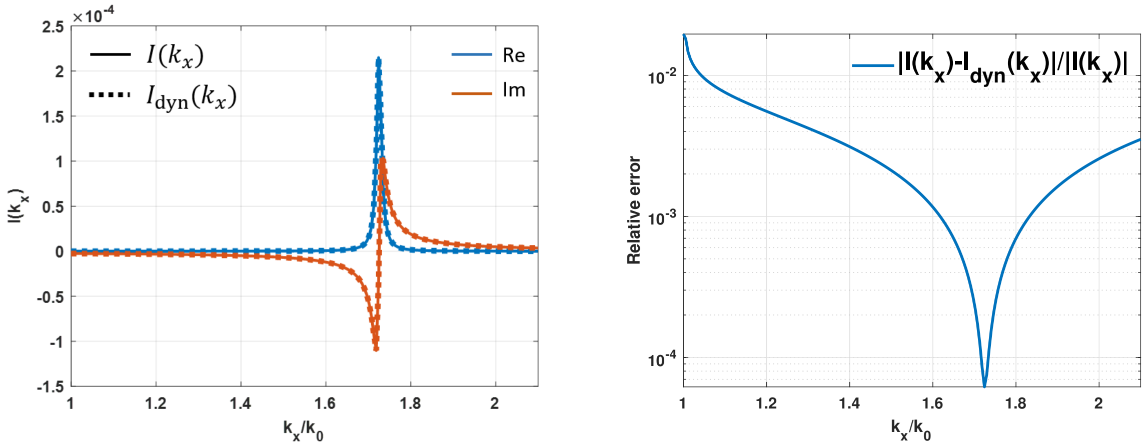

(a) (b)

Figure 6.1: (a) The current spectrum $I(k_x)$ of a microstrip, having a metal thickness $w_z = 1\mu$m and width $w_y = 20\mu$m, constituted of a material with conductivity $\sigma = 4.1 \cdot 10^7$S/m, printed on a dielectric, having a thickness $d = 10\mu$m and permittivity $\varepsilon_r = 4.3$, and its Taylor approximation defined in (6.2), and (b) the relative error of the Taylor approximation defined in (6.2) with respect to $I(k_x)$

where (6.3) is valid for observation points outside the source region, and (6.4) is valid for observation points inside the source region. From (6.3) it becomes clear that outside the source region, the dynamic part of the spectrum is associated with a quasi-TEM wave launched into the microstrip. On the other hand, inside the source region, the dynamic current $i_{\mathrm{dyn}}(x)$ contains an additional term, associated to a stationary field distribution, localized inside the source region.

To assess the accuracy of the approximation in (6.2), the dynamic part of the spectrum has been calculated for a microstrip, having a width $w_y = 20\mu$m and a metal thickness $w_z = 1\mu$m, constituted of a material with conductivity $\sigma = 4.1 \cdot 10^7$S/m, printed on a dielectric substrate having a thickness $d = 10\mu$m and permittivity $\varepsilon_r = 4.3$. Fig. 6.1a shows the comparison between the spectrum $I(k_x)$ and the Taylor approximation defined in (6.2). Moreover, Fig. 6.1b shows the error, committed when approximating $I(k_x)$ by the Taylor approximation, defined in (6.2). Clearly, for values of k_x close to the pole k_{xp}, the Taylor approximation provides an excellent reconstruction of the spectrum $I(k_x)$. On the other hand, the error increases for values of k_x that are more distant from the pole k_{xp}. However, the dynamic part of the spectrum is dominated by the polar singularity. Therefore, the error, committed for values of k_x that are more distant from k_{xp}, will have a small impact on the integral in (6.3).

6.2. Asymptotic part spectrum

As mentioned before, to obtain the input admittance of the microstrip, we have to perform the full integral in (4.59). To accelerate the evaluation of (4.59) it is convenient to extract the asymptotic part of the spectrum, which approximates $I(k_x)$ for large values of k_x. This extraction is particularly useful when the integrand in (4.59) is slowly converging at infinity, i.e. for small gap size. To find an approximation of $I(k_x)$ for large values of k_x, we will first express the sinc-function, as the following Fourier transform

$$\mathrm{sinc}\left(\frac{k_y w_y}{2}\right) = \frac{1}{w_y}\int_{-w_y/2}^{w_y/2} e^{jk_y y'}\,dy' = \frac{1}{w_y}\left(\int_{\infty}^{\infty} e^{jk_y y'}\,dy' - \int_{-\infty}^{-w_y/2} e^{jk_y y'}\,dy' - \int_{w_y/2}^{\infty} e^{jk_y y'}\,dy'\right), \tag{6.5}$$

By recognizing the first term on the right-hand side of (6.5) as the Fourier transform of a constant function, (6.5) can be expressed as follows

$$\mathrm{sinc}\left(\frac{k_y w_y}{2}\right) = \frac{1}{w_y}\left(2\pi\delta(k_y) - \int_{-\infty}^{-w_y/2} e^{jk_y y'}\,dy' - \int_{w_y/2}^{\infty} e^{jk_y y'}\,dy'\right), \tag{6.6}$$

where $\delta(k_y)$ denotes Dirac's delta. By substituting (6.6) into (5.1), the longitudinal spectral Green's function $D(k_x)$ can be expressed as the summation of three components, as shown in the following expression

$$D(k_x) = D_1(k_x) + D_2(k_x) + D_3(k_x), \tag{6.7}$$

where $D_1(k_x)$, $D_2(k_x)$ and $D_3(k_x)$ are given by the following expressions

$$D_1(k_x) = \frac{1}{w_y}\int_0^{w_z}\int_0^{w_z} G_{xx}^{ej}(k_x, k_y = 0, z, z') J_t(k_y = 0, z') J_t(z)\, dz\, dz' \tag{6.8}$$

$$D_2(k_x) = \frac{1}{w_y}\int_{-\infty}^{w_y/2}\int_{-\infty}^{\infty}\int_0^{w_z}\int_0^{w_z} G_{xx}^{ej}(k_x, k_y, z, z') J_t(k_y, z') J_t(k_y, z)\, dz\, dz'\, dk_y e^{jk_y y'}\, dy' \tag{6.9}$$

$$D_3(k_x) = \frac{1}{w_y}\int_{w_y/2}^{\infty}\int_{-\infty}^{\infty}\int_0^{w_z}\int_0^{w_z} G_{xx}^{ej}(k_x, k_y, z, z') J_t(k_y, z') J_t(k_y, z)\, dz\, dz'\, dk_y e^{jk_y y'}\, dy'. \tag{6.10}$$

The term $D_1(k_x)$ is dominant for large values of k_x. To understand the reason, we will note that the terms $D_2(k_x)$ and $D_3(k_x)$ represent the electric field at observation points $|y| > w_y/2$, radiated by a continuous superposition of current lines located in the region $y \in [-w_y/2, w_y/2]$, $z \in [0, w_z]$, that are propagating along x with a wavenumber k_x. For large values of k_x, each current line radiates only evanescent field contributions. Therefore, the contributions of $D_2(k_x)$ and $D_3(k_x)$ tend to zero in the limit $k_x \to \infty$. By using the exponential distribution, defined in (5.26), the asymptotic approximation becomes as follows

$$\begin{aligned} D_\infty(k_x) = -\frac{1}{w_y}\int_0^{w_z} V_{\text{TM,upper}}^{+} \frac{e^{-z'/\delta_p} - e^{-w_z/\delta_p} e^{-jk_{z0}(w_z - z')}}{jk_{z0} + 1/\delta_p} \frac{e^{-(wz - z')/\delta_p} - e^{-jk_{z0}(w_z - z')}}{jk_{z0} - 1/\delta_p}\, dz' - \\ \frac{1}{w_y}\int_0^{w_z} V_{\text{TM,upper}}^{+} \frac{e^{-z'/\delta_p} - e^{-jk_{z0}z'}}{jk_{z0} - 1/\delta_p} \frac{e^{-wz - z'/\delta_p} - e^{-w_z/\delta_p} e^{-jk_{z0}z'}}{jk_{z0} + 1/\delta_p}\, dz' - \\ \frac{1}{w_y}\int_0^{w_z} \Gamma_{TM} V_{\text{TM,lower}}^{+} \frac{e^{-jk_{z0}z'} - e^{-z'/\delta_p} e^{-2jk_{z0}z'}}{jk_{z0} + 1/\delta_p} \frac{e^{-w_z/\delta_p} e^{-jk_{z0}z'} - e^{-2jk_{z0}z'} e^{-(wz - z')/\delta_p}}{jk_{z0} - 1/\delta_p}\, dz'. \end{aligned} \tag{6.11}$$

To assess the accuracy of the approximation in (6.11), we have calculated the longitudinal spectral Green's function $D(k_x)$ and the asymptotic approximation $D_\infty(k_x)$ for a microstrip, having a metal thickness $w_z = 1\mu$m and width $w_y = 20\mu$m, constituted of a material with conductivity $\sigma = 4.1 \cdot 10^7$S/m, printed on a dielectric substrate, having a thickness $d = 10\mu$m and permittivity $\varepsilon_r = 4.3$. Fig. 6.2 shows the relative difference between the longitudinal spectral Green's function $D(k_x)$ and the asymptotic approximation $D_\infty(k_x)$ versus the normalized spectral wavenumber k_x. At $k_x = 500k_0$, the relative difference between $D(k_x)$ and $D_\infty(k_x)$ is roughly 1.2%. It should be noted that the integral in (4.39) needs to be extended until $k_x = 20000$ to achieve an error of about 1% if the gap size Δ is in the order of $\lambda_0/1000$.

6.3. Equivalent circuit

In this section we will introduce an equivalent circuit for characterizing the input impedance of a microstrip, printed on an electrically thin dielectric substrate. Referring to the discussion in Section 6.1, we can define the dynamic impedance, i.e. the impedance associated to the dynamic part of the spectrum, as follows

$$Y_{\text{dyn}} = -\frac{1}{2\pi}\int_{-\infty}^{\infty} \frac{2k_{xp}}{D'(k_{xp})(k_x^2 - k_{xp}^2)} \text{sinc}^2\left(\frac{k_x\Delta}{2}\right) dk_x. \tag{6.12}$$

By closing the integral in k_x analytically, we obtain the following expression

$$Y_{\text{dyn}} = Y_{\text{res}} + Y_{\text{dyn,src}}, \tag{6.13}$$

where Y_{res} is defined as follows

$$Y_{\text{res}} = -\frac{j}{D'(k_x)} \text{sinc}^2\left(\frac{k_{xp}\Delta}{2}\right), \tag{6.14}$$

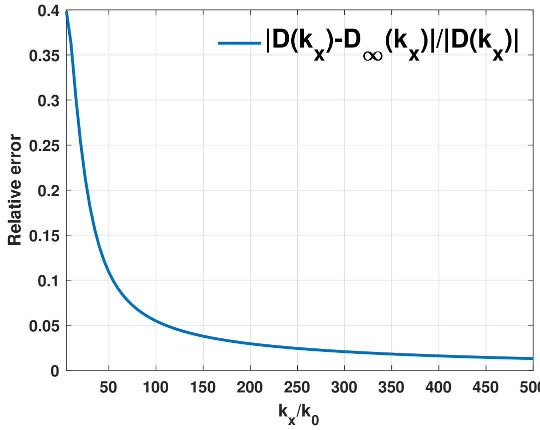

Figure 6.2: Relative error committed by approximating $D(k_x)$ by $D_\infty(k_x)$ for a microstrip, having a metal thickness $w_z = 1\mu$m and width $w_y = 20\mu$m, constituted of a material with conductivity $\sigma = 4.1 \cdot 10^7$ S/m, printed on a dielectric, having a thickness $d = 10\mu$m and permittivity $\varepsilon_r = 4.3$

and $Y_{\text{dyn,src}}$ is given by the following expression

$$Y_{\text{dyn,src}} = \frac{1}{\Delta}\frac{1}{D'(k_{xp})}\frac{2}{k_{xp}}(\text{sinc}(k_{xp}\Delta) - 1). \tag{6.15}$$

The term $Y_{\text{dyn,src}}$ is associated with the reactive current localized inside the source region. On the other hand, the term Y_{res} denotes the input admittance that is associated with the quasi-TEM wave launched into the microstrip. Referring to the discussion in Section 4.1.3, we may interpret the term $-j/D'(k_x)$ as the contribution from two parallel transmission lines, each having the characteristic impedance, defined in (4.61). The term $\text{sinc}^2(k_{xp}\Delta/2)$ can then be interpreted as a transformer with turn ratio

$$n = \text{sinc}\left(\frac{k_{xp}\Delta}{2}\right). \tag{6.16}$$

To investigate the properties of Y_{res}, we have calculated both Y_{res} and Y_{in} for a microstrip, having a metal thickness $w_z = 1\mu$m and width $w_y = 20\mu$m, constituted of a material with conductivity $\sigma = 4.1 \cdot 10^7$ S/m, printed on a dielectric substrate with permittivity $\varepsilon_r = 4.3$, for varying thickness of the substrate. Fig. 6.3a shows the comparison between the real part of Y_{in}, obtained by performing the full integral of (4.59) and the real part of Y_{res}. From Fig. 6.3a, it becomes apparent that, for electrically thin dielectric substrates, i.e. $d < \lambda_0/40$, Y_{res} dominates the real part of the input admittance. On the other hand, when the thickness of the dielectric substrate is large in terms of the wavelength, the gap directly contributes to radiation in the form of surface waves launched along the microstrip or in the form of direct free space radiation. Therefore, in this section, we will only consider microstrips, printed on electrically thin dielectric substrates. It should be noted that the influence of the metal thickness on the characteristic impedance of the microstrip mostly depends on the ratio between the metal thickness and the distance between the main conductor and the ground plane [20]. Therefore, the formulation developed in Chapters 4 and 5 is also the most relevant in the case of electrically thin dielectric substrates.

Considering the interpretation, suggested above, in which Y_{res} is interpreted as the contribution from two infinitely long transmission lines, connected to a transformer, we may define the gap admittance as follows

$$Y_{\text{gap}} = Y_{\text{in}} - Y_{\text{res}} \tag{6.17}$$

Considering the property $\text{Re}(Y_{\text{in}}) \approx \text{Re}(Y_{\text{res}})$, the gap admittance Y_{gap} will then be almost entirely imaginary.

After obtaining the location of the pole k_{xp}, the characteristic impedance Z_0 and the turn ratio n of the transformer can be calculated analytically. However, evaluating the gap admittance Y_{gap} still requires the full integral. To provide an approximation of Y_{gap}, that can be evaluated without excessive computational cost, we will resort to the asymptotic approximation, derived in Section 6.2. To this extent, we will define the quasi-static input admittance as follows

$$Y_{\text{qs}} = \frac{1}{2\pi}\int_{-\infty}^{\infty} I_\infty \left(\text{sinc}^2\left(\frac{k_x\Delta}{2}\right) - \text{sinc}^2\left(\frac{k_x\Delta_{\text{large}}}{2}\right)\right) dk_x, \tag{6.18}$$

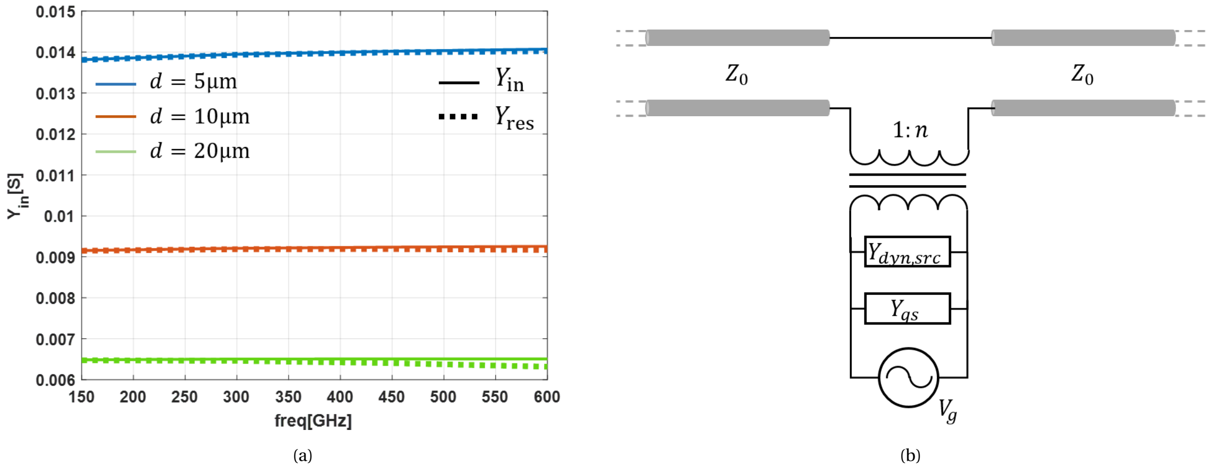

Figure 6.3: (a) The comparison between the real part of Y_{in} and Y_{res} for a microstrip, having a width $w_y = 20\mu$m and metal thickness $w_z = 1\mu$m, constituted of a material with conductivity $\sigma = 4.1 \cdot 10^7$S/m, printed on a dielectric substrate with permittivity $\varepsilon_r = 4.3$, for varying thickness of the substrate, and (b) the equivalent circuit representation of the input admittance

where I_∞ denotes the asymptotic part of the spectrum, obtained by replacing $D(k_x)$ by its asymptotic approximation $D_\infty(k_x)$, defined in (6.11). Note that the asymptotic part of the spectrum is multiplied by $\text{sinc}^2(k_x\Delta/2) - \text{sinc}^2(k_x\Delta_{\text{large}}/2)$ instead of $\text{sinc}^2(k_x\Delta/2)$, where Δ_{large} is an artificially introduced parameter. The reason is that $D_\infty(k_x)$ approximates $D(k_x)$ well for large values of k_x. Therefore, the term $\text{sinc}^2(k_x\Delta/2) - \text{sinc}^2(k_x\Delta_{\text{large}}/2)$ represents a spectral windowing function, which only selects the large values of k_x. The optimal value for Δ_{large} to reconstruct the gap admittance has been chosen to be $4d/\sqrt{\varepsilon_{\text{eff}}}$, where d denotes the thickness of the dielectric substrate and ε_{eff} denotes the effective permittivity of the microstrip.

With the definition in (6.18), the gap admittance Y_{gap} can be represented as the summation of three terms, as shown in the following expression

$$Y_{\text{gap}} = Y_{\text{qs}} + Y_{\text{dyn,src}} + Y_r, \tag{6.19}$$

where the residual admittance is expressed as follows

$$Y_r = \frac{1}{2\pi}\int\limits_{-\infty}^{\infty}\left(\left(I(k_x) - \frac{2k_{xp}}{D'(k_{xp})(k_x^2 - k_{xp}^2)}\right)\text{sinc}^2\left(\frac{k_x\Delta}{2}\right) - I_\infty\left(\text{sinc}^2\left(\frac{k_x\Delta}{2}\right) - \text{sinc}^2\left(\frac{k_x\Delta_{\text{large}}}{2}\right)\right)\right)dk_x. \tag{6.20}$$

Neglecting the residual admittance Y_r, we obtain the equivalent circuit, shown in Fig. 6.3b.

To assess the accuracy of the equivalent circuit in Fig. 6.3b, we have calculated the input admittance of a microstrip, having a width $w_y = 30\mu$m, constituted of a material with conductivity $\sigma = 4.1 \cdot 10^7$S/m, printed on a dielectric substrate, having a thickness $d = 10\mu$m and permittivity $\varepsilon_r = 4.3$, for a metal thickness $w_z = 1\mu$m or $w_z = 4\mu$m and varying gap length Δ. Figs. 6.4a and 6.4b show the imaginary part of the gap admittance Y_{gap}, obtained from the definition of (6.15), together with the imaginary part of gap admittance, obtained from the equivalent circuit in Fig. 6.3b, i.e. the summation of Y_{qs} and $Y_{\text{dyn,src}}$, for $w_z = 1\mu$m and $w_z = 4\mu$m, respectively. Moreover, to emphasize the importance of including the quasi-static, the imaginary part of $Y_{\text{dyn,src}}$ is shown as well. As shown in Figs. 6.4a and 6.4b, the gap admittance is reconstructed well by the two terms Y_{qs} and Y_{dyn}. Therefore, the integral in (6.20), will rarely have to be performed. Moreover, Fig. 6.4a shows that for small gap length, the imaginary part of the gap admittance is dominated by the quasi-static input admittance Y_{qs}. Finally, Fig. 6.4c shows the computation times of the full integral in (4.59) and the equivalent circuit in Fig. 6.3b, for the microstrips in Figs. 6.4a and 6.4b. As shown in Fig. 6.4c, the computation time of the equivalent circuit is almost two orders of magnitude smaller than the computation time of the full integral of (4.59). Moreover, it should be noted that CST cannot simulate the structures in Figs. 6.4a and 6.4b, taking into account the nonzero thickness of the conductors, due to the large aspect ratio of the metal strip.

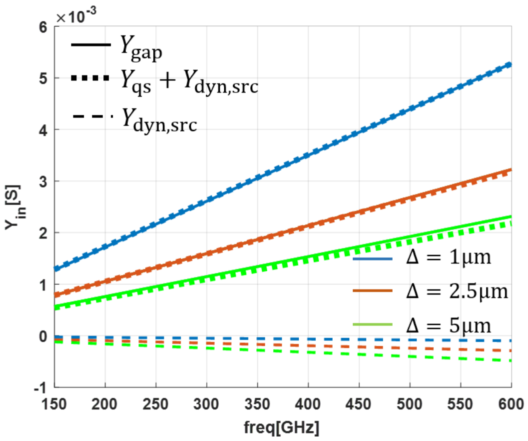

(a)

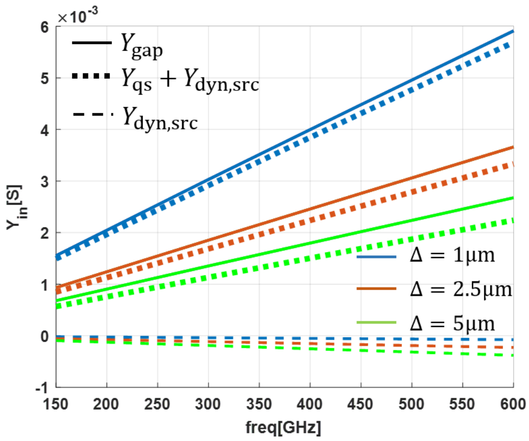

(b)

	Full integration	Equivalent circuit
Dipole 1	95s	3.1s
Dipole 2	85s	2.6s

(c)

Figure 6.4: Imaginary part of the gap admittance Y_{gap} of a microstrip, having a width $w_y = 30\mu$m, constituted of a material with conductivity $\sigma = 4.1 \cdot 10^7$S/m, printed on a dielectric substrate, having a thickness $d = 10\mu$m and permittivity $\varepsilon_r = 4.3$, obtained from the definition of (6.15), and obtained from the equivalent circuit in Fig. 6.3b, i.e. the summation of Y_{qs} and $Y_{\text{dyn,src}}$, for (a) a metal thickness $w_z = 1\mu$m, and (b) a metal thickness $w_z = 4\mu$m, and (c) the computation times of the full integral in (4.59) and the equivalent circuit in Fig. 6.3b, for the dipoles in Figs. 6.4a and 6.4b

7

Leaky structure

As mentioned in the introduction, this thesis is embedded in the main research line, carried out in the THz Sensing group, to develop a dedicated 3D MoM for the analysis of integrated lens antennas. The goal of the overall project, is to develop a strategy to separate the contribution of the metallic feed in the presence of a semi-infinite dielectric region from the contribution due to the reflections inside the dielectric lens. Within the scope of this overall project, the purpose of the spectral domain formulation, developed in Chapters 4 and 5, is to characterize the thin metallic feed of the lens antenna. To this extent, the spectral domain formulation has been extended to study an infinitely long dipole with height w_z and width w_y, located at a distance h_{gap} from a semi-infinite dielectric region, as shown in Fig.7.1.

7.1. Transverse integration path

The derivation of the longitudinal spectral Green's function $D(k_x)$, for the leaky structure in Fig. 7.1, is similar to the case of the microstrip and is reported in Appendix I. Moreover, the total current $i(x)$ and the residual current $i_{\text{res}}(x)$ can still be calculated with (4.39) and (4.40), while the characteristic impedance Z_0, the effective permittivity ε_{eff}, and the attenuation constant α can be obtained from (4.61), (4.62) (4.63). However, the dominant mode along the dipole is now associated to a leaky wave pole k_{xp}, as opposed to the bounded mode of the microstrip in Chapter 5. Since the leaky wave pole radiates into the dense medium, it is located on the bottom Riemann sheet with respect to k_2, i.e. the wavenumber of the dense medium. Moreover, as the distance between the dipole and the interface between the two regions increases, the phase constant of the leaky wave pole may decrease below k_1. In such cases, the physically significant leaky wave pole k_{xp} is also located on the bottom Riemann sheet with respect to k_1. Since the different Riemann sheets can be entered through a proper choice of the transverse integration path [18], care has to be taken, when deciding on the integration path in the transverse spectral plane.

To be more explicit, Figs.7.2a and 7.2b show the complex plane topology of the longitudinal spectral wavenumber k_x and the complex plane topology of the transverse spectral wavenumber k_y, where the branch points $k_{t,i}$ in the transverse spectral plane are given by the following expression

$$k_{t,i} = \sqrt{k_i^2 - k_x^2}. \tag{7.1}$$

The branch points in the longitudinal spectral plane are located at $k_x = \pm k_i$, and start off the branch cuts, arising from the square roots $k_{z,i} = \sqrt{k_i^2 - k_\rho^2}$. The solutions of the square root are given by the following expression

$$k_{z,i} = \sqrt{k_i^2 - k_\rho^2} = \begin{cases} -j\sqrt{k_\rho^2 - k_i^2} \\ +j\sqrt{k_\rho^2 - k_i^2}, \end{cases} \tag{7.2}$$

where the first solution is located on the top Riemann sheet with respect to k_i, and the second solution is located on the bottom Riemann sheet with respect to k_i. As mentioned before, the pole k_{xp} is a leaky wave pole and is therefore always located on the bottom Riemann Sheet with respect to k_2. Moreover, if the condition $\text{Re}(k_{xp}) \geq \text{Re}(k_1)$ is satisfied, the physically significant leaky wave pole is located in region II in the longitudinal spectral plane and is therefore located on the top Riemann sheet with respect to k_1. On the other hand, if the

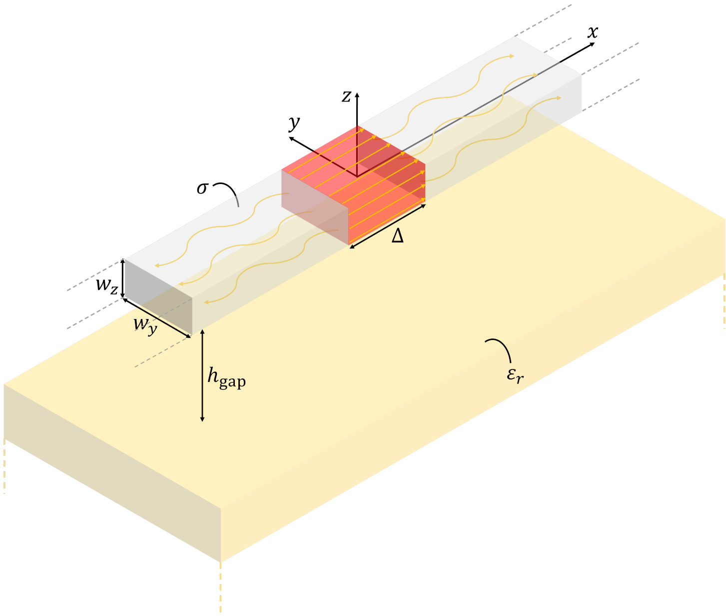

Figure 7.1: Infinite dipole with height w_z, width w_y, constituted of a material with conductivity σ, located at a distance h_{gap} from a semi-infinite dielectric region with permittivity ε_r, oriented along the x-axis and excited by a delta-gap excitation of length Δ

condition $\text{Re}(k_{xp}) \leq \text{Re}(k_1)$ is satisfied, the physically significant leaky wave pole is located in region III and is therefore located on the bottom Riemann sheet with respect to k_1. Consequently, the correct integration path in the transverse spectral plane, depends on the phase constant of the leaky wave pole. Figs.7.3a and 7.3b illustrate the correct integration paths to enter region II and region III in the longitudinal spectral plane, respectively [18], where Fig.7.4b indicates the correct Riemann sheets with respect to k_1 and k_2 to calculate each contour integral.

Although the integration paths, shown in Figs.7.3a and 7.3b allow us to enter the correct region in the longitudinal spectral plane, their implementations are inconvenient, when performing the contour integrals numerically. Fortunately, the integration paths in Figs.7.3a and 7.3b can be performed in an equivalent, but more convenient manner [18], as illustrated in Fig.7.4a. By invoking Cauchy's integral theorem [41], we obtain the following expression

$$\int_{C_1} f(k_z)\,dk_z + \int_{C_2} f(k_z)\,dk_z + \int_{C_3} f(k_z)\,dk_z = 0. \tag{7.3}$$

By rearranging the terms in (7.3), we obtain the following expression

$$\int_{C_1} f(k_z)\,dk_z = -\int_{C_2} f(k_z)\,dk_z - \int_{C_3} f(k_z)\,dk_z. \tag{7.4}$$

Consequently, the contour integral over C_1 can equivalently be calculated by performing the integral over the real axis and subtracting the contour integral over C_2. By applying, this procedure to the integration paths in Figs.7.3a and 7.3b, we obtain the equivalent integration paths, illustrated in Figs.7.5a and 7.5b.

7.2. Verification

To illustrate the procedure, and to verify the validity of the transverse integration paths, discussed in the previous section, we have calculated the total current $i(x)$ and the residual current $i_{\text{res}}(x)$ for a dipole with metal thickness $w_z = 1\mu$m and width $w_y = 30\mu$m, constituted of a material with conductivity $\sigma = 4.1 \cdot 10^7$, at a frequency $f = 300$GHz. Fig.7.6a shows the total current $i(x)$ and the residual current $i_{\text{res}}(x)$, when the dipole is printed directly on top of the dielectric medium. On the other hand, Fig.7.6b shows the total current $i(x)$ and the residual current $i_{\text{res}}(x)$, when the dipole is located at a distance $h_{\text{gap}} = 10\mu$m from the dielectric medium. Figs.7.6a and 7.6b show that the residual current $i_{\text{res}}(x)$ resembles the total current $i(x)$ well at larger distance from the source. Hence, we have indeed captured the physically significant leaky wave pole.

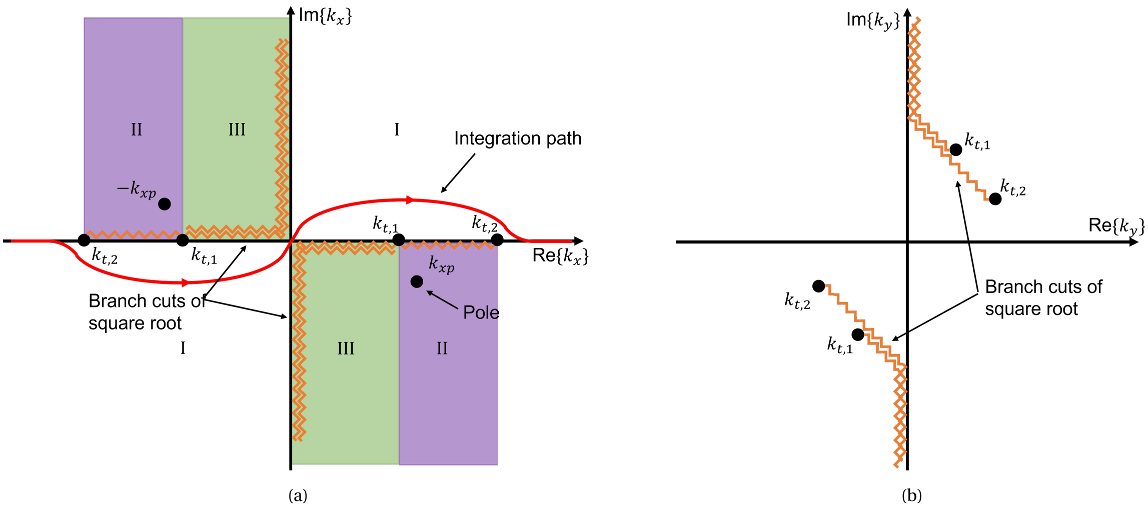

Figure 7.2: Complex plane topology of the leaky structure in Fig. 7.1 (a) for the longitudinal spectral wavenumber k_x and (b) for the transverse spectral wavenumber k_y

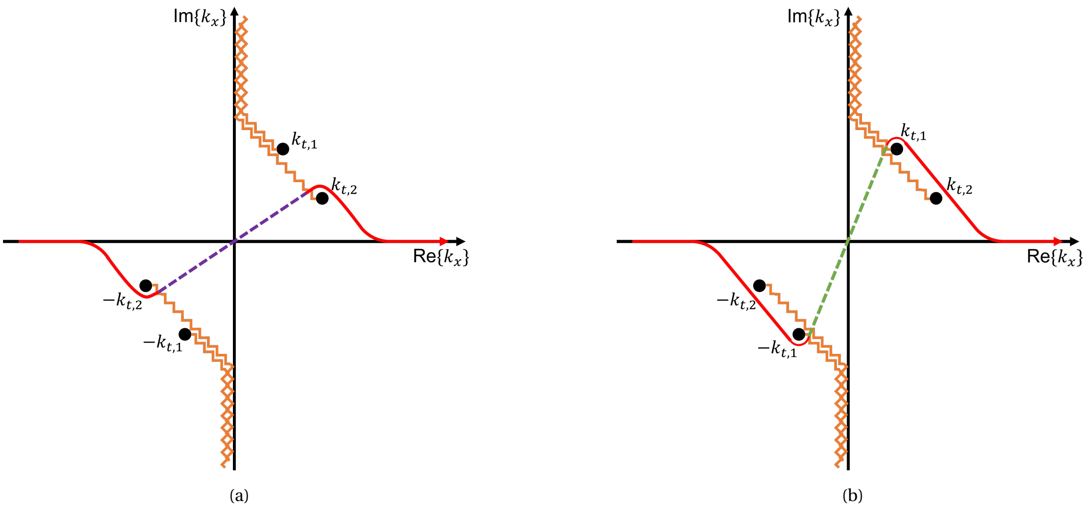

Figure 7.3: Transverse integration path to obtain a leaky wave pole (a) located in region II in the longitudinal spectral plane, and (b) located in region III in the longitudinal spectral plane

7.3. Parametric analysis

As mentioned before, the purpose of the spectral domain formulation is to characterize the thin metallic feed of the lens antenna in the presence of a semi-infinite dielectric region. To gain more insight into the dispersion properties of this structure, a parametric analysis has been performed versus the relevant dimensions of the dipole, both in the case of a dipole, printed directly on top of the dielectric region and for a dipole, located at a distance $h_{\text{gap}} = 10\mu$m from the interface between the two regions.

Fig. 7.7a shows the characteristic impedance of a dipole, having a thickness $w_z = 1\mu$m, constituted of a material with conductivity $\sigma = 4.1 \cdot 10^7$S/m, directly printed on top a semi-infinite dielectric region with permittivity $\varepsilon_r = 11.9$, for varying width of the dipole. Fig. 7.7a shows that the characteristic impedance decreases, when the width of the dipole is increased. On the other hand, Fig. 7.7b shows the characteristic impedance of a dipole, having a width $w_y = 20\mu$m, constituted of a material with conductivity $\sigma = 4.1 \cdot 10^7$S/m, printed on a semi-infinite dielectric region with permittivity $\varepsilon_r = 11.9$, for varying thickness of the dipole. Fig. 7.7b shows that the characteristic impedance increases, when the thickness of the dipole is increased. Moreover, the characteristic impedance has an almost constant imaginary part, associated to the radiative nature of the leaky wave pole.

Fig. 7.8a and 7.8b show the effective permittivity of a dipole with the same dimensions and material param-

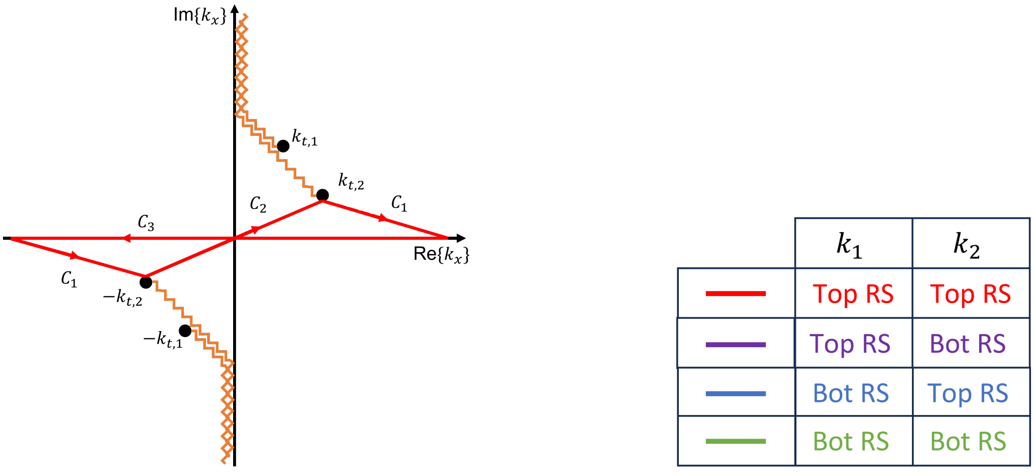

(a) (b)

Figure 7.4: (a) Application of Cauchy's integral theorem [41] in the transverse spectral plane to obtain a more convenient integration path, and (b) a legend which shows the correct Riemann sheet for each integration path

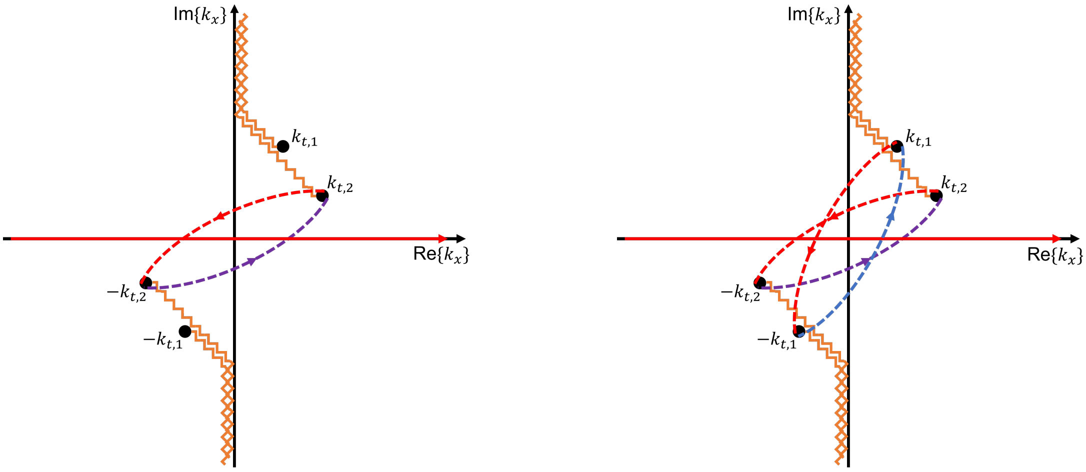

(a) (b)

Figure 7.5: Equivalent integration path to obtain a leaky wave pole (a) located in region II in the longitudinal spectral plane, and (b) located in region III in the longitudinal spectral plane

eters as in Fig. 7.7a and 7.7b, respectively. Fig. 7.8a shows that the effective permittivity increases, when the width of the dipole is increased. On the other hand, Fig. 7.8b shows that the effective permittivity decreases, when the thickness of the dipole is increased. This observation can be understood by the same argument given in Section 5.2.3. A current on the bottom of the dipole is flowing at the interface between the dielectric and the air region and will therefore have an effective permittivity that is close to the average of the two regions. On the other hand, a current on the top of the dipole is located farther away from the interface and will have a lower effective permittivity. By considering both the current on the top and the bottom of the dipole, the effective permittivity becomes larger compared to a formulation in which all of the current is assumed to be at the interface between the two regions. Consequently, if the thickness of the metal is increased, the current on the top of the dipole moves farther away from the interface of the two regions, which decreases the overall effective permittivity.

Figs. 7.9a and 7.9b show the attenuation constant of a dipole with the same dimensions and material parameters as in Figs. 7.7a and 7.7b, respectively. Fig. 7.9a shows that the attenuation constant increases, when the width of the dipole is increased. Fig. 7.9b shows that the attenuation constant increases when the thickness of the dipole is increased. This can be understood through a similar argument as before. While a current on the bottom of the dipole is flowing at the interface between the dielectric region and the air region, a current on the top of the dipole is located at a distance w_z from the interface between the two regions. This effect is

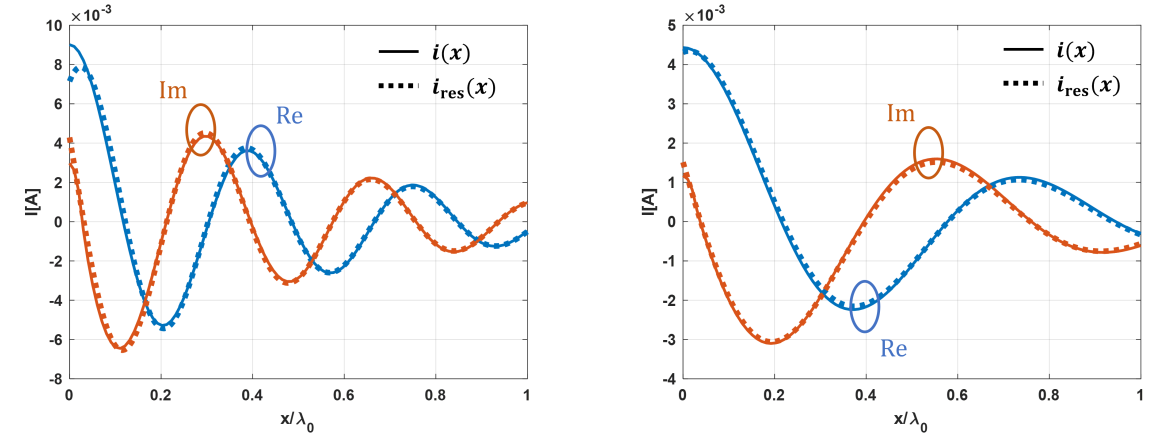

(a) (b)

Figure 7.6: Total current $i(x)$ and residual current $i_{\text{res}}(x)$ of a dipole, having a metal thickness $w_z = 1\mu$m and width $w_y = 30\mu$m, constituted of a material with conductivity $\sigma = 4.1 \cdot 10^7$, (a) directly printed on top of a semi-infinite dielectric region with permittivity $\varepsilon_r = 11.9$, and (b) located at a distance $h_{\text{gap}} = 10\mu$m from a semi-infinite dielectric region with permittivity $\varepsilon_r = 11.9$

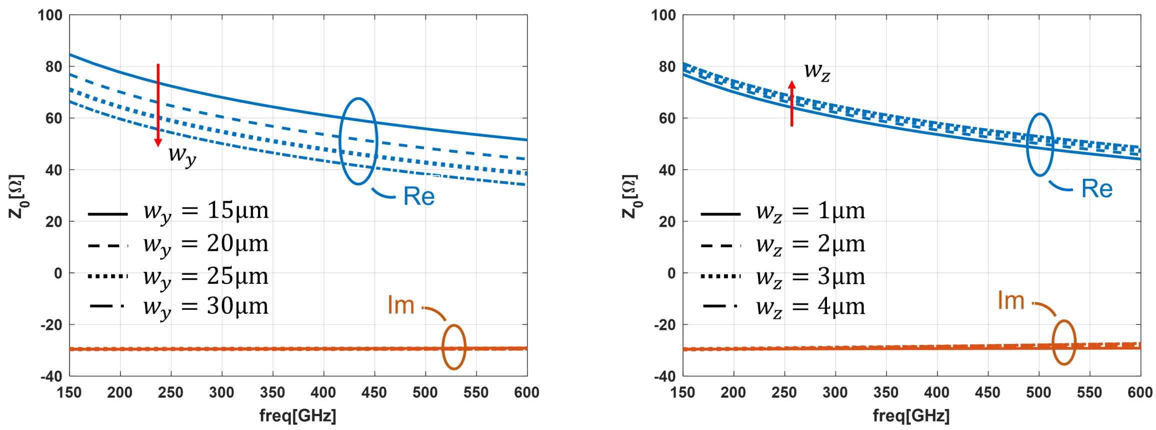

(a) (b)

Figure 7.7: Characteristic impedance of a dipole, constituted of a material with conductivity $\sigma = 4.1 \cdot 10^7$S/m, directly printed on top of a semi-infinite dielectric region with permittivity $\varepsilon_r = 11.9$, (a) for a thickness $w_z = 1\mu$m and varying width of the dipole, and (b) for a width $w_y = 20\mu$m and varying thickness of the dipole

similar to adding an extremely small air gap, which increases the leakage into the denser medium. By considering both the current on the top and the bottom of the dipole, the overall attenuation constant becomes lower compared to a formulation in which all of the current is assumed to be at the interface between the two regions. Consequently, if the thickness of the metal is increased, the current on the top of the dipole moves farther away from the interface of the two regions, which increases the overall attenuation constant. It should be noted that Fig. 7.8b is obtained, assuming a symmetric transverse current distribution. Similar to the microstrip, the actual current distribution is asymmetric in $\hat{z}$. Therefore, Fig. 7.8b might overestimate the effect of the thickness on the attenuation constant.

Figs. 7.10a and 7.10b show the characteristic impedance of a dipole with the same dimensions and material parameters as in Figs. 7.7a and 7.7b, respectively. However, the dipole is now located at a distance $h_{\text{gap}} = 10\mu$m from a semi-infinite dielectric region with permittivity $\varepsilon_r = 11.9$. Similar to before, Fig. 7.10a shows that the characteristic impedance increases, when the width of the dipole is increased. Moreover, Fig. 7.10b shows that the characteristic impedance slightly decreases, when the thickness of the dipole is increased.

Figs. 7.11a and 7.11b show the effective permittivity of a dipole with the same dimensions and material parameters as in Figs. 7.10a and 7.10b, respectively. Fig. 7.11a shows that the effective permittivity increases, when the width of the dipole is increased. On the other hand, Fig. 7.11b shows that the effective permittivity slightly decreases, when the thickness of the dipole is decreased. However, the dependence of the effective

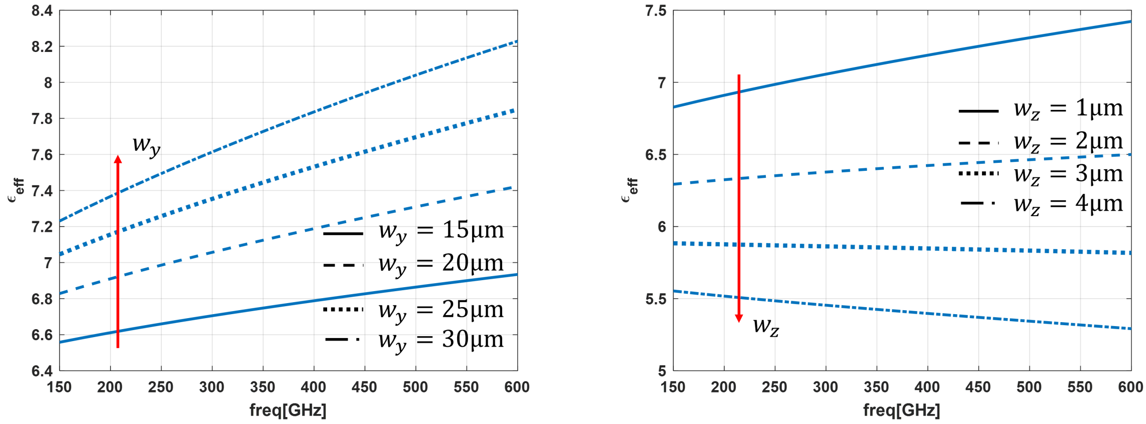

(a) (b)

Figure 7.8: Effective permittivity of a dipole, constituted of a material with conductivity $\sigma = 4.1 \cdot 10^7$ S/m, directly printed on top of a semi-infinite dielectric region with permittivity $\varepsilon_r = 11.9$, (a) for a thickness $w_z = 1\mu$m and varying width of the dipole, and (b) for a width $w_y = 20\mu$m and varying thickness of the dipole

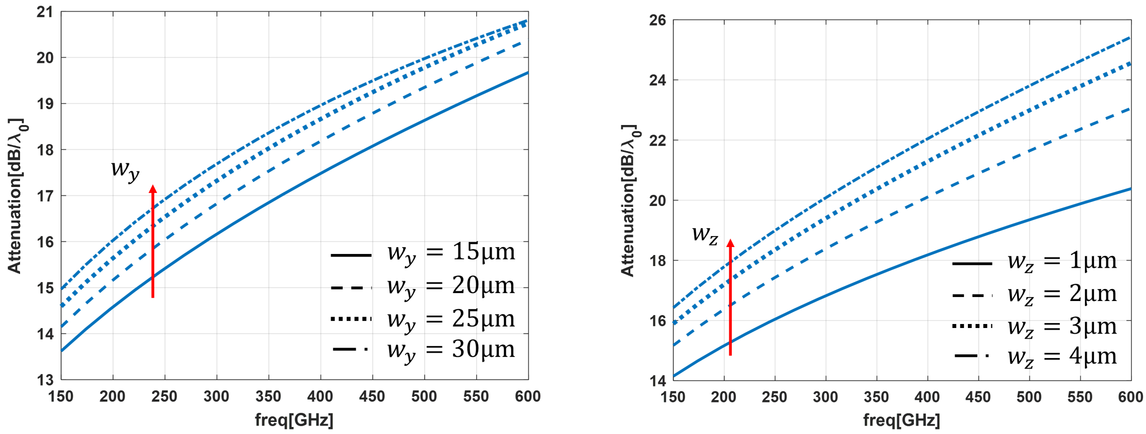

(a) (b)

Figure 7.9: Attenuation constant of a dipole, constituted of a material with conductivity $\sigma = 4.1 \cdot 10^7$ S/m, directly printed on top of a semi-infinite dielectric region with permittivity $\varepsilon_r = 11.9$ (a) for a thickness $w_z = 1\mu$m and varying width of the dipole, and (b) for a width $w_y = 20\mu$m and varying thickness of the dipole

permittivity on the thickness of the dipole is much weaker, compared to Fig. 7.8b. The reason is that the dipole is already located at a distance $h_{\text{gap}} = 10\mu$m from the interface between the two regions. Consequently, the influence of the thickness of the dipole on the effective permittivity is much smaller.

Figs. 7.12a and 7.12b show the attenuation constant of a dipole with the same dimensions and material parameters as in Fig. 7.10a and 7.10b, respectively. Fig. 7.12a shows that the attenuation constant increases, when the width of the dipole is increased. On the other hand, Fig. 7.12b shows that the attenuation constant slightly decreases, when the thickness of the dipole is decreased. However, the dependence of the attenuation constant on the thickness of the dipole is much weaker, compared to Fig. 7.9b. This observation can be understood through a similar argument as before. Since the dipole is already located at a distance $h_{\text{gap}} = 10\mu$m from the interface between the two regions, the influence of the thickness of the dipole on the leakage into the denser medium is much smaller than in Fig. 7.9b.

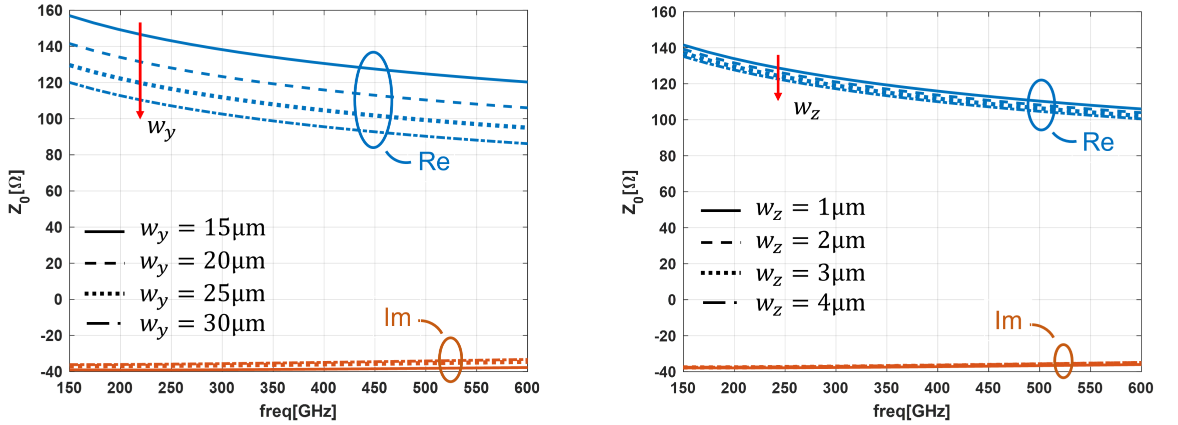

(a) (b)

Figure 7.10: Characteristic impedance of a dipole, constituted of a material with conductivity $\sigma = 4.1 \cdot 10^7$ S/m, located at a distance $h_{gap} = 10\mu m$ from a semi-infinite dielectric region with permittivity $\varepsilon_r = 11.9$, (a) for a thickness $w_z = 1\mu m$ and varying width of the dipole, and (b) for a width $w_y = 20\mu m$ and varying thickness of the dipole

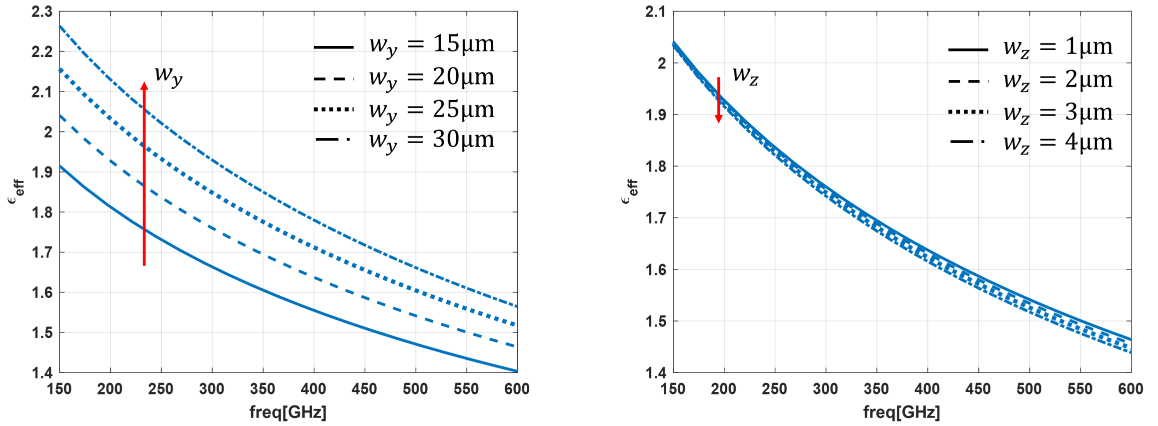

(a) (b)

Figure 7.11: Effective permittivity of a dipole, constituted of a material with conductivity $\sigma = 4.1 \cdot 10^7$ S/m, located at a distance $h_{gap} = 10\mu m$ from a semi-infinite dielectric region with permittivity $\varepsilon_r = 11.9$ (a) for a thickness $w_z = 1\mu m$ and varying width of the dipole, and (b) for a width $w_y = 20\mu m$ and varying thickness of the dipole

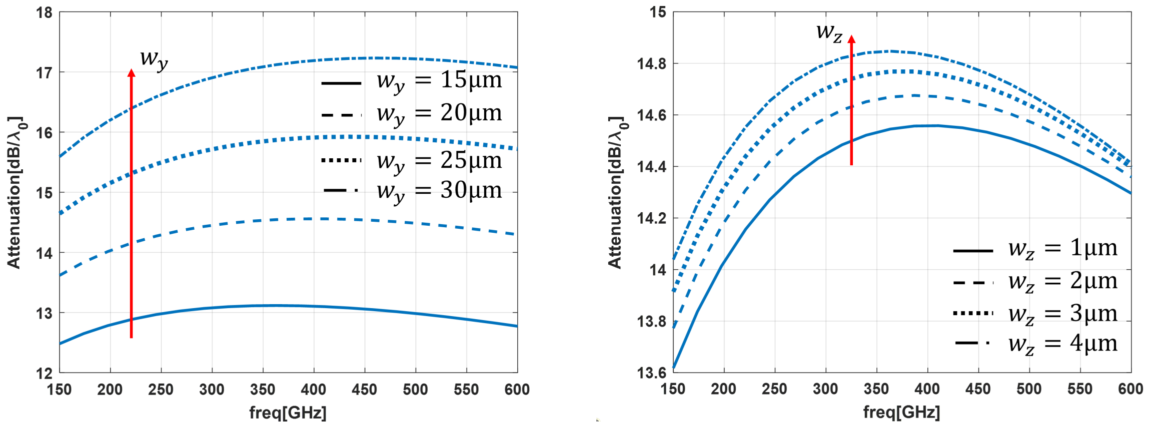

(a) (b)

Figure 7.12: Attenuation constant of a dipole, constituted of a material with conductivity $\sigma = 4.1 \cdot 10^7$ S/m, located at a distance $h_{gap} = 10\mu m$ from a semi-infinite dielectric region with permittivity $\varepsilon_r = 11.9$, (a) for a thickness $w_z = 1\mu m$ and varying width of the dipole, and (b) for a width $w_y = 20\mu m$ and varying thickness of the dipole

8
Conclusion

8.1. Summary and conclusion

The main goal of this thesis was concerned with the development of a spectral domain formulation to characterize printed transmission lines in the presence of an arbitrary stratification, taking into account the non-zero thickness of the conductors. In particular, this formulation has been demonstrated by studying one of the most common transmission line topologies: the microstrip. Since this thesis project is embedded in the main research line of the MoM development, carried out in the THz Sensing group, with the goal of developing a strategy to separate the contributions due to the feeding structure and the reflections inside the lens antennas, we have subsequently used this spectral domain formulation to gain more insight into the dynamic behaviour of dipoles in the presence of a semi-infinite dielectric region. In addition, we have continued the development of the Volumetric Method of Moments (V-MoM).

As mentioned before, the thesis work was embedded in the main research line of the THz Sensing group on the development of a MoM tool. Therefore, Chapter 2 has provided an overview of the V-MoM, developed in [14]. The V-MoM solves the Electric Field Integral Equation (EFIE), obtained by invoking the volume equivalence theorem [24]. To this extent, the EFIE is discretized using a structured grid consisting of piecewise constant basis functions. By applying the Method of Moments [26], the integral equation is converted to a matrix equation, which is solved using an iterative technique called the Conjugate Gradient Fast Fourier Transform (CG-FFT).

Next, Chapter 3 has described the optimization of the V-MoM in terms of accuracy and computation time. The computation time of the V-MoM has been reduced by removing "flip" operations, taking advantage of the properties of the FFT, by optimizing the memory allocation during the simulation, and by reducing the number of FFTs, performed by the CG-FFT. These optimizations have reduced the total computation time by roughly 60%. Moreover, we have introduced a procedure to enhance the accuracy of the solution when simulating geometries that are not well-represented by the structured grid. This procedure refines the representation of the scatterer by averaging the permittivity of the voxels that are located at the boundary of the scatterer. Finally, we have implemented a more accurate procedure to calculate the reaction integrals. This procedure is based on a reduction from volume to surface integrals [23], and allows us to calculate the resulting integrals up to machine precision.

The core of the thesis work started in Chapter 4. This chapter introduced the spectral domain formulation that allows us to study infinitely long printed transmission lines, taking into account the non-zero thickness of the conductors. This formulation is based on the local form of Ohm's law and has been introduced by studying a dipole located in free space. By approximating the exponential decay inside the dipole with the Leontovich boundary condition [25], an expression has been obtained for the spectrum of the longitudinal current distribution. Subsequently, the relevant parameters of the transmission line have been extracted from the polar singularities in the spectrum. In particular, the residue contribution of the input admittance has been interpreted as the contribution from two infinitely long transmission lines. This interpretation has been substantiated by demonstrating its resemblance with the characteristic impedance, obtained by defining the voltage along the transmission line as the line integral of the transverse electric field. Moreover, the current, obtained from this spectral domain formulation, has been shown to be in excellent agreement with CST.

In Chapter 5, the formulation, developed in Chapter 4, has been extended to allow the characterization of printed transmission lines in the presence of an arbitrary stratification. In particular, this formulation has been used to study one of the most common transmission line topologies: the microstrip. To extend the formulation, developed in Chapter 4, to arbitrary stratifications, the spectral domain Green's function for stratified media has been used. Since the spectral domain Green's function for stratified media has a spectral dependence in the transverse dimensions and a spatial dependence on z and z', the projection in the y-direction has been performed in the spectral domain, while the projection in the z-direction has been performed in the spatial domain.

Subsequently, it has been shown that the assumption of a symmetric basis function is not congruent with the asymmetric geometry of a microstrip. To represent the asymmetry of the microstrip accurately, the transverse current distribution has been expanded into two basis functions, each with an exponential decay, starting from the bottom or the top of the metal strip. It has been shown that this procedure allows us to correctly retrieve the current that is flowing on the bottom and the top of the metal strip. Moreover, the relevance of allowing a different current on the bottom and the top of the microstrip has been demonstrated through a comparison between the propagation constant, obtained by assuming a symmetric current distribution, and the propagation constant, obtained by expanding the transverse current distribution into two separate basis functions. In particular, the assumption of a symmetric transverse current distribution leads to an overestimation of the current on the top of the metal strip and consequently an underestimation of the attenuation constant and the effective permittivity. On the other hand, by expanding the transverse current distribution into two separate basis functions, we obtained an attenuation constant and effective permittivity that are in excellent agreement with CST. Nevertheless, the comparison with the measurements from [22] showed a discrepancy between the results obtained from the spectral techniques, developed in this thesis, and the measured results from [22], even when a single asymmetric basis function was used to model the transverse current distribution. Averaging the poles, however, resulted in a better reconstruction of the measurements in [22]. Nevertheless, it is not clear, whether this approach is entirely justified. Therefore, it may be necessary to consider alternative shapes to model the transverse current distribution.

Next, Chapter 6 has introduced an equivalent circuit representation to model the input impedance of a microstrip, printed on an electrically thin dielectric substrate. This circuit representation is based on the extraction of two dominant parts of the current spectrum: the dynamic part and the quasi-static part. The dynamic part of the spectrum refers to the portion of the spectrum that is related to small values of k_x. This part of the spectrum is dominated by the polar singularities and can be approximated by a Taylor approximation around the pole. An analytical evaluation of the dynamic part of the spectrum shows that it comprises both a quasi-TEM wave, launched along the microstrip, and a reactive current, associated with a stationary field distribution, localized inside the gap. On the other hand, the asymptotic part of the spectrum refers to the limit for k_x tending to infinity and can be approximated by only retaining the $k_y = 0$ component of the spectrum. By interpreting the quasi-TEM wave, launched along the microstrip, as the current along two infinitely long transmission lines, connected to a transformer, we may define a gap impedance that is almost purely imaginary. This gap impedance can then be decomposed into three parts: the impedance associated to the stationary field, resulting from the dynamic part of the spectrum, the impedance associated to the reactive currents, resulting from the asymptotic part of the spectrum, and a remaining part. The contribution of the remaining part is usually negligible, rendering the evaluation of the circuit parameters numerically efficient.

Finally, in Chapter 7, the formulation, developed in Chapters 4 and 5, has been used to study a leaky structure containing a dipole in the presence of a semi-infinite dielectric region. This geometry is particularly relevant with respect to the overall research line, carried out in the THz Sensing Group, as it allows us to obtain a better understanding of the properties of the dynamic (i.e. radiating) component of the current in an effort to isolate the contribution due to the reflections inside the lens. Since the leaky wave pole is located on the bottom Riemann Sheet, the appropriate transverse integration path has been chosen to obtain the physically significant leaky wave pole. A parametric analysis was then performed to gain insight into the properties of the dynamic (i.e. radiating) currents along the dipole.

8.2. Future work

As mentioned in the introduction, representing the thin metallic feed of the lens antenna, with the V-MoM, developed in [14], is a non-trivial task. This drawback is inherent to the V-MoM, developed in [14], and has two underlying reasons. First of all, the use of a structured grid requires the same discretization level for the entire geometry. Consequently, simultaneously simulating an electrically large lens, together with a thin metallic feed would result in a linear system with such an extreme computational complexity, that it cannot be expected to

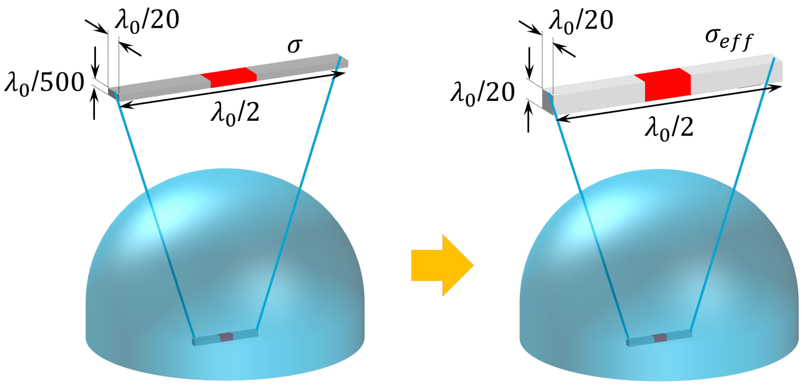

Figure 8.1: Equivalent procedure to simulate a feed with realistic dimensions by simulating a feed with convenient dimensions together with an adjusted conductivity σ_{eff}

be solved anywhere in the near future. Moreover, the system matrix, obtained by the V-MoM in [14], becomes ill-conditioned when the permittivity of the scatterer becomes large with respect to the permittivity of the background medium, a phenomenon referred to as the high-contrast (HC) breakdown [45].

To circumvent these problems, the overall goal in the THz Sensing group is to develop a strategy to separate the characterization of the feeding structure and the lens antennas. Within the scope of this overall project, the purpose of the spectral domain formulation, developed in Chapters 4, 5 and 7 is to characterize the thin metallic feed in the presence of a semi-infinite dielectric region. The V-MoM, developed in [14], will then be used to account for the reflections inside the dielectric lens [46]. This procedure will be explained in more detail in the following paragraph.

The starting point of this procedure is the parametric analysis, performed in Chapter 7, which gives insight into the dynamic behaviour of an infinitely long dipole in the presence of a semi-infinite dielectric stratification. Equipped with an understanding of the dispersion characteristics of the dynamic (i.e. radiating) components of the current, obtained from this analysis, the next step is to simulate the dielectric lens with the V-MoM, developed in [14]. However, instead of simulating a feed with realistic dimensions, and using the correct conductivity σ, we will simulate an auxiliary feed with more convenient dimensions and use an adjusted conductivity σ_{eff}, such that the propagation constant of the auxiliary feed is similar to the propagation constant of the actual feed. This procedure is illustrated in Fig. 8.1.

Since the dynamic part of the input impedance is dominated by the quasi-TEM wave launched along the dipole, this procedure will correctly reconstruct the dynamic part of the input impedance. On the other hand, the asymptotic part of the input impedance is associated to the reactive fields, localized inside the gap, and strongly depends on the dimensions of the dipole. However, since the asymptotic part of the input impedance remains unaffected by the reflections inside the dielectric lens, we may use the spectral domain formulation, developed in Chapters 4, 5 and 7, together with the extraction of the asymptotic part, described in Chapter 6, to correct the asymptotic part of the input impedance. Since the total input input impedance is well approximated by the two spectral components, this procedure should allow us to accurately reconstruct the input impedance of the original dipole.

A

Reduction volume to surface integrals

The reaction integrals are given by (3.20). By substituting the piece-wise constant basis functions, defined in (2.10), into (3.20), and by reversing the order of integration, we obtain the following expression

$$Z_{mn} = \iiint_{V_m} \left(\nabla \times \nabla \times \iiint_{V_n} G_0(\vec{r} - \vec{r}')\hat{p}_n \, d\vec{r}' \right) \cdot \hat{p}_m \, d\vec{r}, \tag{A.1}$$

where V_n and V_m denote the volume of the source and observation region, respectively, and $\hat{p}_n$ and $\hat{p}_m$ denote the corresponding polarization vectors. By using one of the vector calculus identities[1], (A.1) can be expressed as follows

$$Z_{mn} = -\iiint_{V_m} \nabla \cdot \left(\hat{p}_m \times \nabla \times \iiint_{V_n} G_0(\vec{r} - \vec{r}')\hat{p}_n \, d\vec{r}' \right) d\vec{r}, \tag{A.2}$$

where the term $\nabla \times \hat{p}_m$ vanishes, since $\hat{p}_m$ is a constant vector. By applying the divergence theorem[2], (A.2) becomes as follows

$$Z_{mn} = -\oiint_{S_m} \left(\hat{p}_m \times \nabla \times \iiint_{V_n} G_0(\vec{r} - \vec{r}')\hat{p}_n \, d\vec{r}' \right) \cdot \hat{n}_m \, d\vec{r}, \tag{A.3}$$

where S_m denotes the surface enclosing the volume V_m, and $\hat{n}_m$ denotes the outward normal vector of the surface S_m. By using one of the vector identities[3] to permute the vectors in (A.3), one obtains

$$Z_{mn} = -\oiint_{S_m} (\hat{n}_m \times \hat{p}_m) \cdot \iiint_{V_n} \nabla \times G_0(\vec{r} - \vec{r}')\hat{p}_n \, d\vec{r}' \, d\vec{r} \tag{A.4}$$

By using another vector calculus identity[4], (A.4) can be expressed as follows

$$Z_{mn} = -\oiint_{S_m} (\hat{n}_m \times \hat{p}_m) \cdot (\iiint_{V_n} \nabla G_0(\vec{r} - \vec{r}') \, d\vec{r}') \times \hat{p}_n \, d\vec{r} \tag{A.5}$$

where the term $\nabla \times \hat{p}_n$ vanishes since $\hat{p}_n$ is a constant vector. By using the relation $\nabla G_0(\vec{r} - \vec{r}') = -\nabla' G_0(\vec{r} - \vec{r}')$ [23], (A.5) can be expressed as follows

$$Z_{mn} = -\oiint_{S_m} (\hat{n}_m \times \hat{p}_m) \cdot (\hat{p}_n \times \iiint_{V_n} \nabla' G_0(\vec{r} - \vec{r}') \, d\vec{r}') \, d\vec{r} \tag{A.6}$$

1
$$\nabla \cdot (\vec{A} \times \vec{B}) = \vec{B} \cdot \nabla \times \vec{A} - \vec{A} \cdot \nabla \times \vec{B}$$

2
$$\iiint_V \nabla \cdot \vec{A} \, dV = \oiint_S \vec{A} \cdot \hat{n} \, dS$$

3
$$\vec{A} \cdot (\vec{B} \times \vec{C}) = \vec{B} \cdot (\vec{C} \times \vec{A})$$

4
$$\nabla \times (\psi A) = \psi(\nabla \times A) + (\nabla \psi) \times A$$

Finally, by using one of the corollaries of the divergence theorem[5], (A.6) can be expressed as follows

$$Z_{mn} = -\oiint_{S_m} (\hat{n}_m \times \hat{p}_m) \cdot (\hat{p}_n \times \oiint_{S_n} \nabla' G_0(\vec{r} - \vec{r}')\hat{n}_m \, d\vec{r}') \, d\vec{r}, \tag{A.7}$$

where S_n denotes the surface enclosing the volume V_n, and $\hat{n}_n$ denotes the outer normal vector of the surface S_n. Note that the term $\nabla \cdot \hat{p}_n$ vanishes, since $\hat{p}_n$ is a constant vector. Since the source and observation domains are cubes, (A.7) can be expressed as the summation in (3.22)

5

$$\iiint_V \vec{A} \nabla \psi \, dV = \oiint_S \vec{A}\psi \cdot \hat{n}_S - \iiint_V \psi \nabla \cdot \vec{A} \, dV$$

B
Gauss-Legendre

The Gauss-Legendre quadrature is a Gaussian quadrature to approximate the definite integral of a function $f(x)$. For the integration domain $x \in [-1,1]$, the Gauss-Legendre rule can be expressed as follows

$$\int_{-1}^{1} f(x)\,dx \approx \sum_{i=1}^{n} w_i f(x_i), \tag{B.1}$$

where n denotes the number of Gauss-Legendre points, x_i denotes the i^{th} root of the Legendre polynomial $P_n(x)$, and the weights w_i are given by the following expression [47]

$$w_i = \frac{2}{(1-x_i^2)(P_n'(x_i))^2}. \tag{B.2}$$

The zeros of the Legendre polynomial can be found using the Newton-Raphson method with the following initial guess [38]

$$x_{i,\text{guess}} = \cos\left(\pi\frac{2i-1}{2n}\right) + \frac{0.27}{n}\sin\left(\pi\left(\frac{2(i-1)}{N}-1\right)\frac{N-1}{N+1}\right) \tag{B.3}$$

For the integration domain $x \in [a,b]$, we can apply the change of variables

$$x = \frac{b-a}{2}u + \frac{a+b}{2} \tag{B.4}$$

In this case the integration rule becomes as follows

$$\int_{a}^{b} f(x)\,dx \approx \frac{b-a}{2}\sum_{i=1}^{n} w_i f\left(\frac{b-a}{2}u_i + \frac{a+b}{2}\right), \tag{B.5}$$

where u_i denotes the i^{th} root of the Legendre polynomial $P_n(x)$.

C
Newton-Raphson

To characterize the transmission line in terms of its characteristic impedance, attenuation constant and effective dielectric permittivity, the residue contribution has to be evaluated and the pole location of $I(k_x)$ has to be determined. The polar singularity of $I(k_x)$ corresponds to the zero of the denominator of (4.17), which can be expressed as follows

$$C(k_x) = \rho\langle j_t(y,z), j_t(y,z)\rangle_A - D(k_x). \tag{C.1}$$

The zero of (C.1) can be found through the Newton-Raphson method, which is a local root-finding algorithm. The method is an iterative technique, which calculates the zero, through successive approximations, starting with an initial guess k_{xp0}. To find the subsequent approximation, $C(k_x)$ is linearized around k_{xp0}, as shown in the following expression

$$C(k_x) \approx C(k_{xp0}) + C'(k_{xp0})(k_x - k_{xp0}). \tag{C.2}$$

The subsequent approximation k_{xp1} is obtained by finding the zero of the linear approximation,

$$C(k_{xp0}) + C'(k_{xp0})(k_{xp1} - k_{xp0}) = 0, \tag{C.3}$$

which results in

$$k_{xp1} = k_{xp0} - \frac{C(k_{xp0})}{C'(k_{xp0})}. \tag{C.4}$$

By substituting (C.1) into (C.4), we obtain the following expression

$$k_{xp1} = k_{xp0} + \frac{\rho\langle j_t(y,z), j_t(y,z)\rangle_A - D(k_{xp0})}{D'(k_{xp0})}. \tag{C.5}$$

This procedure can be applied in an iterative manner to yield the following expression

$$k_{xp,n+1} = k_{xp,n} + \frac{\rho\langle j_t(y,z), j_t(y,z)\rangle_A - D(k_{xp,n})}{D'(k_{xp,n})}. \tag{C.6}$$

where $k_{xp,n}$ denotes the approximation of the pole k_{xp} at iteration n. In general, it can be demonstrated that for a continuously differentiable function, the Newton-Raphson method converges quadratically or faster[48]. Hence, it is not necessary that the initial guess point is very accurate.

D
Integral I

D.1. Integration rule

To find the longitudinal spectral Green's functions, we have to perform the double integrals of (4.31), (4.32) and (4.33). Fortunately, the integrals in k_z can be closed analytically. To this extent, let us only consider the integral in k_z

$$I_{1,k_z} = \int_{-\infty}^{\infty} \frac{\mathrm{sinc}^2(k_z w_z/2)}{k^2 - k_x^2 - k_y^2 - k_z^2}\, dk_z \tag{D.1}$$

$$I_{2,k_z} = \int_{-\infty}^{\infty} \frac{\mathrm{sinc}^2\big(k_z(w_z - 2\delta_p)/2\big)}{k^2 - k_x^2 - k_y^2 - k_z^2}\, dk_z \tag{D.2}$$

$$I_{3,k_z} = \int_{-\infty}^{\infty} \frac{\mathrm{sinc}\big(k_z(w_z - 2\delta_p)/2\big)\,\mathrm{sinc}(k_z w_z/2)}{k^2 - k_x^2 - k_y^2 - k_z^2}\, dk_z. \tag{D.3}$$

By using the definition of the sinc, i.e. $\mathrm{sinc}\,(x) = \sin(x)/x$, and by using the trigonometric identity $\sin^2(x) = (1-\cos(2x))/2$, (D.1) and (D.2) can be expressed as follows

$$I_{1,k_z} = \frac{2}{w_z^2} \int_{-\infty}^{\infty} \frac{1-\cos(k_z w_z)}{k_z^2(k^2 - k_x^2 - k_y^2 - k_z^2)}\, dk_z \tag{D.4}$$

$$I_{2,k_z} = \frac{2}{(w_z - 2\delta_p)^2} \int_{-\infty}^{\infty} \frac{1-\cos(k_z(w_z - 2\delta_p))}{k_z^2(k^2 - k_x^2 - k_y^2 - k_z^2)}\, dk_z. \tag{D.5}$$

Similarly, by using the trigonometric identity $\sin(x)\sin(y) = (\cos(x-y) - \cos(x+y))/2$, (D.3) can be expressed as follows

$$I_{3,k_z} = \frac{2}{w_z(w_z - 2\delta_p)} \int_{-\infty}^{\infty} \frac{\cos(\delta_p) - \cos(w_z - \delta_p)}{k_z^2(k^2 - k_x^2 - k_y^2 - k_z^2)}\, dk_z. \tag{D.6}$$

Apart from the constant in front, the integrals in (D.4), (D.5) and (D.6) can all be reduced to the following integral

$$\int_{-\infty}^{\infty} \frac{\cos(ak_z) - \cos(bk_z)}{k_z^2(k_z^2 - k_{zp}^2)}\, dk_z, \tag{D.7}$$

where $k_{zp} = j\sqrt{k_x^2 + k_y^2 - k^2}$ and the constants a and b depend on the specific integral, i.e. $a = 0$ and $b = k_z w_z$ or $b = k_z(w_z - 2\delta_p)$ in case of (D.4) and (D.5), and $a = \delta_p$ and $b = w_z - \delta_p$ in case of (D.6).

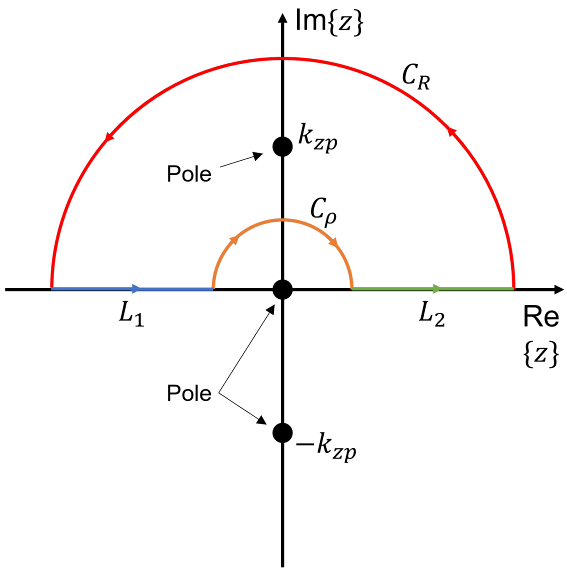

Figure D.1: Complex plane of the function $f(k_z)$, defined in (D.10), and integration contour consisting of the arcs C_R, C_ρ, L_1 and L_2

D.2. Change of variables

To close the integral in (D.7), we will first rewrite (D.7) as follows

$$\int_{-\infty}^{\infty} \frac{\cos(ak_z) - \cos(bk_z)}{k_z^2(k_z^2 - k_{zp}^2)}\, dk_z = \int_{-\infty}^{\infty} \frac{e^{jak_z} - e^{jbk_z}}{2k_z^2(k_z^2 - k_{zp}^2)}\, dk_z + \int_{-\infty}^{\infty} \frac{e^{-jak_z} - e^{-jbk_z}}{2k_z^2(k_z^2 - k_{zp}^2)}\, dk_z. \tag{D.8}$$

By making the change of variables $k_z \to -k_z$ in the second term on the right-hand side, (D.7) can be expressed as follows

$$\int_{-\infty}^{\infty} \frac{\cos(ak_z) - \cos(bk_z)}{k_z^2(k_z^2 - k_{zp}^2)}\, dk_z = \int_{-\infty}^{\infty} \frac{e^{jak_z} - e^{jbk_z}}{2k_z^2(k_z^2 - k_{zp}^2)}\, dk_z - \int_{\infty}^{-\infty} \frac{e^{jak_z} - e^{jbk_z}}{2k_z^2(k_z^2 - k_{zp}^2)}\, dk_z = \int_{-\infty}^{\infty} \frac{e^{jak_z} - e^{jbk_z}}{k_z^2(k_z^2 - k_{zp}^2)}\, dk_z. \tag{D.9}$$

Note that the minus sign of the Jacobian is cancelled by flipping the integration bounds.

D.3. Contour integral

To close the integral on the right-hand side of (D.9), let us consider its integrand

$$f(k_z) = \frac{e^{jak_z} - e^{jbk_z}}{k_z^2(k_z^2 - k_{zp}^2)}. \tag{D.10}$$

$f(k_z)$ contains three simple poles located at $k_z = \pm k_{zp}$ and $k_z = 0$. Note that the pole at $k_z = 0$ is not a double pole, since the numerator of (D.10) becomes zero at $k_z = 0$. Hence the complex plane topology is shown in Fig. D.1. Since $f(k_z)$ converges to zero in the upper-half plane, we define the contour C, shown in Fig. D.1, consisting of the four arcs C_ρ, C_R, L_1, L_2. Since $f(k_z)$ is analytic inside and on C, except for the pole at $k_z = k_{zp}$, we can apply the Cauchy residue theorem [41], which results in the following expression

$$\int_C f(k_z)\, dk_z = \int_{L_1} f(k_z)\, dk_z + \int_{L_2} f(k_z)\, dk_z + \int_{C_\rho} f(k_z)\, dk_z + \int_{C_R} f(k_z)\, dk_z = 2\pi j \operatorname*{Res}_{k_z = k_{zp}}. \tag{D.11}$$

By rearranging terms, (D.11) can be expressed as follows

$$\int_{L_1} f(k_z)\, dk_z + \int_{L_2} f(k_z)\, dk_z = 2\pi j \operatorname*{Res}_{k_z = k_{zp}} - \int_{C_\rho} f(k_z)\, dk_z - \int_{C_R} f(k_z)\, dk_z. \tag{D.12}$$

To evaluate the right-hand side of (D.12), we will first compute the contribution of the residue at $k_z = k_{zp}$, as shown in the following expression

$$2\pi j \operatorname*{Res}_{k_z = k_{zp}} = \frac{\pi(e^{jbk_{zp}} - e^{jak_{zp}})}{2jk_{zp}^3}. \tag{D.13}$$

Since the pole at $k_z = 0$ is a simple pole, we can evaluate the contribution of the arc C_ρ as follows [41]

$$\lim_{\rho\to 0}\int_{C_\rho} f(k_z)\,dk_z = -\pi j \operatorname*{Res}_{k_z=k_{zp}} f(k_z) = -\pi j \lim_{k_z\to 0} \frac{e^{jak_z}-e^{jbk_z}}{k_z(k_z^2-k_{zp}^2)} = \frac{\pi(b-a)}{k_{zp}^2}. \tag{D.14}$$

Finally, we need to consider the arc C_R. First, observe that for every point k_z on C_R, we can establish the following upper bound

$$|f(k_z)| \le M_R = \frac{2}{R^2(R^2-|k_{zp}|^2)}. \tag{D.15}$$

The length of the arc C_R is equal to $L = \pi R$. Therefore, we obtain the following upper bound on the absolute value of the integral

$$|\int_{C_R} f(k_z)\,dk_z| \le M_R L = \frac{2\pi}{R(R^2-|k_{zp}|^2)}. \tag{D.16}$$

Since this contribution goes to zero for $R\to\infty$, the integral along C_R vanishes. Consequently, we obtain the following expression

$$\int_{-\infty}^{\infty} \frac{\cos(ak_z)-\cos(bk_z)}{k_z^2(k_z^2-k_{zp}^2)}\,dk_z = \int_{L_1} f(k_z)\,dk_z + \int_{L_2} f(k_z)\,dk_z = \frac{\pi(a-b)}{k_{zp}^2} + \frac{\pi(e^{jbk_{zp}}-e^{jak_{zp}})}{jk_{zp}^3}. \tag{D.17}$$

D.4. Final substitutions

To obtain the value of the integrals of (D.1) and (D.2), we substitute $k_{zp} = j\sqrt{k_x^2+k_y^2-k^2}$, $a = 0$ and $b = w_z$ or $b = w_z - 2\delta_p$ into (D.17). To obtain the value of the integral of (D.3), we substitute $a = \delta_p$ and $b = w_z - \delta_p$. This results in the following expressions

$$I_{1,k_z} = -\frac{2\pi}{w_z(k_x^2+k_y^2-k^2)} - \frac{2\pi(e^{-w_z\sqrt{k_x^2+k_y^2-k^2}}-1)}{w_z^2(k_x^2+k_y^2-k^2)^{\frac{3}{2}}} \tag{D.18}$$

$$I_{2,k_z} = -\frac{2\pi}{(w_z-2\delta_p)(k_x^2+k_y^2-k^2)} - \frac{2\pi(e^{-(w_z-2\delta_p)\sqrt{k_x^2+k_y^2-k^2}}-1)}{(w_z-2\delta_p)^2(k_x^2+k_y^2-k^2)^{\frac{3}{2}}} \tag{D.19}$$

$$I_{3,k_z} = -\frac{2\pi}{w_z(k_x^2+k_y^2-k^2)} - \frac{2\pi(e^{-(w_z-\delta_p)\sqrt{k_x^2+k_y^2-k^2}}-e^{-\delta_p\sqrt{k_x^2+k_y^2-k^2}})}{w_z(w_z-2\delta_p)(k_x^2+k_y^2-k^2)^{\frac{3}{2}}}. \tag{D.20}$$

Finally, by substituting (D.18), (D.19) and (D.20) into the original double integrals of (4.31), (4.32) and (4.33), we obtain the final expressions given by (4.34), (4.35) and (4.36).

E

Integral II

E.1. Integration rule

To compute the voltage along the dipole, we need to perform the 3D-integrals of (4.49) and (4.50). Fortunately, the integrals in k_z can be closed analytically. To this extent, let us only consider the integral in k_z

$$v_{\mathrm{out},k_z} = \int_{-\infty}^{\infty} \frac{\mathrm{sinc}(k_z w_z/2)}{k^2 - k_x^2 - k_y^2 - k_z^2} e^{-jk_z w_z/2}\, dk_z \tag{E.1}$$

$$v_{\mathrm{in},k_z} = \int_{-\infty}^{\infty} \frac{\mathrm{sinc}\big(k_z(w_z - 2\delta_p)/2\big)}{k^2 - k_x^2 - k_y^2 - k_z^2} e^{-jk_z w_z/2}\, dk_z. \tag{E.2}$$

By using the definition $\mathrm{sinc}\,(x) = \sin(x)/x$, (E.1) and (E.2) can be reduced to the following integral

$$\int_{-\infty}^{\infty} \frac{\sin(ak_z)}{k_z(k_z^2 - k_{zp}^2)} e^{-jbk_z}\, dk_z, \tag{E.3}$$

where $k_{zp} = j\sqrt{k_x^2 + k_y^2 - k^2}$, $b = w_z/2$ and $a = w_z/2$ or $a = (w_z - 2\delta_p)/2$.

E.2. Contour integral

To close the integral in (E.3), let us consider its integrand

$$f(k_z) = \frac{\sin(ak_z)}{k_z(k_z^2 - k_{zp}^2)} e^{-jbk_z}, \tag{E.4}$$

where we assume $\mathrm{Re}(b) \geq \mathrm{Re}(a)$. The integrand on the left-hand side of (E.3) contains a simple pole at $z = \pm k_{zp}$. Note that $k_z = 0$ is not a pole, since the numerator of (E.4) becomes zero. Hence, the complex plane topology is shown in Fig. E.1. Since we are assuming $\mathrm{Re}(b) \geq \mathrm{Re}(a)$, the integrand on the left-hand side of (E.3) converges to zero in the lower half-plane. Hence, we can use the contour, shown in Fig. E.1, consisting of the arcs L and C_R. Similar to before, the integrand on the left-hand side of (E.3) is analytic inside and on C except for the pole at $k_z = -k_{zp}$. Therefore, we can apply the Cauchy residue theorem [41], which results in the following expression

$$\int_C f(k_z)\, dk_z = \int_L f(k_z)\, dk_z + \int_{C_R} f(k_z)\, dk_z = -2\pi j \operatorname*{Res}_{k_z=-k_{zp}}. \tag{E.5}$$

Note that the minus sign appears due to the clockwise direction of the contour C. It can be demonstrated that the integral $\int_{C_R} f(k_z)\, dk_z$, vanishes in the limit $R \to \infty$ in a similar fashion as in Appendix D. Hence, the integral in (E.3) can be obtained by evaluating the residue at $z = -k_{zp}$. This results in the following expression

$$\begin{aligned} &\int_{-\infty}^{\infty} \frac{\sin(ak_z)}{k_z(k_z^2 - k_{zp}^2)} e^{-jbk_z} dk_z = -2\pi j \operatorname*{Res}_{k_z=-k_{zp}} = \\ &\pi j \frac{\sin(ak_{zp})}{k_{zp}^2} e^{jbk_{zp}} = \frac{\pi(e^{j(b-a)k_{zp}} - e^{j(b+a)k_{zp}})}{2k_{zp}^2}. \end{aligned} \tag{E.6}$$

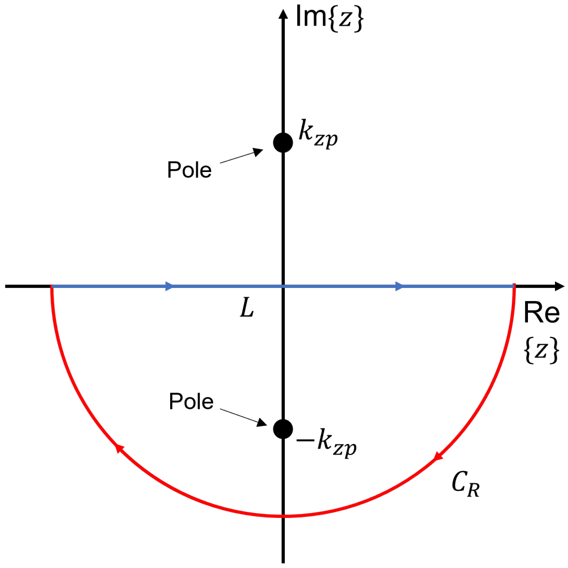

Figure E.1: Complex plane of the function $f(k_z)$, defined in (E.4), and integration contour consisting of the arcs C_R and C_ρ

E.3. Final substitutions

To obtain the value of (E.1) and (E.2), we substitute $k_{zp} = j\sqrt{k_x^2 + k_y^2 - k^2}$, $b = w_z/2$ and $a = w_z/2$ or $a = (w_z - 2\delta)/2$ into (E.6). This results in the following expressions

$$v_{\mathrm{out},k_z} = -\pi \frac{e^{-w_z\sqrt{k_x^2+k_y^2-k^2}} - 1}{w_z(k_x^2 + k_y^2 - k^2)} \tag{E.7}$$

$$v_{\mathrm{in},k_z} = -\pi \frac{e^{-(w_z-\delta_p)\sqrt{k_x^2+k_y^2-k^2}} - e^{-\delta_p\sqrt{k_x^2+k_y^2-k^2}}}{(w_z - 2\delta_p)(k_x^2 + k_y^2 - k^2)}. \tag{E.8}$$

Finally, by substituting (E.7) and (E.8) into the original 3D-integral of (4.49) and (4.50), we obtain the final expressions given by (4.51) and (4.52).

F

Integral III

F.1. Integration rule

To find the longitudinal spectral Green's functions of the geometry with the perfectly conducting ground plane, we have to perform the double integrals of (4.31), (4.32) and (4.33). Fortunately, the integrals in k_z can be closed analytically. To this extent, let us only consider the integral in k_z

$$I_{1,\text{image},k_z} = \int_{-\infty}^{\infty} \frac{\text{sinc}^2(k_z w_z/2)}{k^2 - k_x^2 - k_y^2 - k_z^2} e^{-jk_z 2(d+w_z/2)}\, dk_z \tag{F.1}$$

$$I_{2,\text{image},k_z} = \int_{-\infty}^{\infty} \frac{\text{sinc}^2\big(k_z(w_z - 2\delta_p)/2\big)}{k^2 - k_x^2 - k_y^2 - k_z^2} e^{-jk_z 2(d+w_z/2)}\, dk_z \tag{F.2}$$

$$I_{3,\text{image},k_z} = \int_{-\infty}^{\infty} \frac{\text{sinc}\big(k_z(w_z - 2\delta_p)/2\big)\,\text{sinc}(k_z w_z/2)}{k^2 - k_x^2 - k_y^2 - k_z^2} e^{-jk_z 2(d+w_z/2)}\, dk_z \tag{F.3}$$

By applying the trigonometric identity $\sin^2(x) = (1-\cos(2x))/2$ to (F.1) and (F.2), and by applying the trigonometric identity $\sin(x)\sin(y) = (\cos(x-y) - \cos(x+y))/2$ to (F.3), we obtain the following expressions

$$I_{1,image,k_z} = \frac{2}{w_z^2} \int_{-\infty}^{\infty} \frac{1-\cos(k_z w_z)}{k_z^2(k^2 - k_x^2 - k_y^2 - k_z^2)} e^{-jk_z 2(d+w_z/2)}\, dk_z \tag{F.4}$$

$$I_{2,\text{image},k_z} = \frac{2}{(w_z - 2\delta)^2} \int_{-\infty}^{\infty} \frac{1-\cos(k_z(w_z - 2\delta_p))}{k_z^2(k^2 - k_x^2 - k_y^2 - k_z^2)} e^{-jk_z 2(d+w_z/2)}\, dk_z. \tag{F.5}$$

$$I_{3,\text{image},k_z} = \frac{2}{w_z(w_z - 2\delta)} \int_{-\infty}^{\infty} \frac{\cos(\delta_p) - \cos(w_z - \delta_p)}{k_z^2(k^2 - k_x^2 - k_y^2 - k_z^2)} e^{-jk_z 2(d+w_z/2)}\, dk_z. \tag{F.6}$$

Apart from the constant in front, the integrals in (F.4), (F.5) and (F.6) can all be reduced to the following integral

$$\int_{-\infty}^{\infty} \frac{\cos(ak_z) - \cos(bk_z)}{k_z^2(k_z^2 - k_{zp}^2)} e^{jck_z}\, dk_z, \tag{F.7}$$

where $k_{zp} = j\sqrt{k_x^2 + k_y^2 - k^2}$ and $c = 2(d + w_z/2)$. The constants a and b depend on the specific integral, i.e. $a = 0$ and $b = k_z w_z$ or $b = k_z(w_z - 2\delta_p)$ in case of (F.4) and (F.5), and $a = \delta_p$ and $b = w_z - \delta_p$ in case of (F.6).

F.2. Contour integral

To close the integral in (F.7), let us consider its integrand

$$f(k_z) = \frac{\cos(ak_z) - \cos(bk_z)}{k_z^2(k_z^2 - k_{zp}^2)} e^{jck_z}, \tag{F.8}$$

where we assume $\mathrm{Re}(c) \geq \max(\mathrm{Re}(a), \mathrm{Re}(b))$. $f(k_z)$ has a simple pole at $k_z = \pm k_{zp}$. Note that $k_z = 0$ is not a pole, since the numerator of (F.8) has a double zero. Since we are assuming $\mathrm{Re}(c) \geq \max(\mathrm{Re}(a), \mathrm{Re}(b))$, $f(k_z)$ converges to zero in the lower half-plane. Hence, we can use the same contour, shown in Fig. E.1, consisting of the arcs L and C_R. Since the integrand in (F.7) is analytic inside and on C, except for the pole at $k_z = -k_{zp}$, we can apply the Cauchy residue theorem [41], which results in the following expression

$$\int_C f(k_z)\, dk_z = \int_L f(k_z)\, dk_z + \int_{C_R} f(k_z)\, dk_z = -2\pi j \operatorname*{Res}_{k_z=-k_{zp}}. \tag{F.9}$$

Note that the minus sign appears due to the clockwise direction of the contour C. It can be demonstrated that the integral $\int_{C_R} f(k_z)\, dk_z$ vanishes in the limit $R \to \infty$ in a similar fashion as in Appendix D. Hence, the integral in (E.3) can be obtained by evaluating the residue at $k_z = -k_{zp}$, as shown in the following expression

$$\begin{aligned} \int_{-\infty}^{\infty} \frac{\cos(ak_z) - \cos(bk_z)}{k_z^2(k_z^2 - k_{zp}^2)} e^{-jck_z}\, dk_z = 2\pi j \operatorname*{Res}_{k_z=-k_{zp}} = \\ 2\pi j \frac{\cos(ak_{zp}) - \cos(bk_{zp})}{k_{zp}^3} e^{-jck_{zp}} = \frac{\pi(e^{j(c+b)k_{zp}} + e^{j(c-b)k_{zp}} - (e^{j(c+a)k_{zp}} + e^{j(c-a)k_{zp}}))}{2jk_{zp}^3}. \end{aligned} \tag{F.10}$$

F.3. Final substitution

To obtain the value of (F.1) and (F.2), we substitute $k_{zp} = j\sqrt{k_x^2 + k_y^2 - k^2}$, $c = 2(d + w_z/2)$, $a = 0$ and $b = w_z$ or $b = w_z - 2\delta_p$ into (F.10). To obtain the value of (F.3), we substitute $a = \delta_p$ and $b = w_z - \delta_p$. This results in the following expressions

$$I_{1,\text{image}} = \pi \frac{e^{-2(d+w_z)\sqrt{k_x^2+k_y^2-k^2}} + e^{-2d\sqrt{k_x^2+k_y^2-k^2}} - 2e^{-(2d+w_z)\sqrt{k_x^2+k_y^2-k^2}}}{w_z^2(k_x^2+k_y^2-k^2)^{\frac{3}{2}}} \tag{F.11}$$

$$I_{2,\text{image}} = \pi \frac{e^{-2(d+w_z-\delta_p)\sqrt{k_x^2+k_y^2-k^2}} + e^{-2(d+\delta_p)\sqrt{k_x^2+k_y^2-k^2}} - 2e^{-(2d+w_z)\sqrt{k_x^2+k_y^2-k^2}}}{(w_z-2\delta)^2(k_x^2+k_y^2-k^2)^{\frac{3}{2}}} \tag{F.12}$$

$$I_{3,\text{image}} = \pi \frac{e^{-(2d+2w_z-\delta_p)\sqrt{k_x^2+k_y^2-k^2}} + e^{-(2d+\delta_p)\sqrt{k_x^2+k_y^2-k^2}} - e^{-(2d+w_z+\delta_p)\sqrt{k_x^2+k_y^2-k^2}} - e^{-(2d+w_z-\delta_p)\sqrt{k_x^2+k_y^2-k^2}}}{w_z(w_z-2\delta)(k_x^2+k_y^2-k^2)^{\frac{3}{2}}}. \tag{F.13}$$

Finally, by substituting (F.11), (F.12) and (F.13) into the original double integrals of (4.72), (4.73) and (4.74), we obtain the final expressions, given by (4.75), (4.76) and (4.77).

G

Integral IIII

G.1. Integration rule

To compute the voltage on a dipole in the presence of a perfectly conducting ground plane, we need to perform the 3D-integrals of (4.83), (4.84), (4.85) and (4.86). Fortunately, the integrals in k_z can be closed analytically. To this extent, let us only consider the integral in k_z

$$v_{\text{out},k_z}(x) = \int_{-\infty}^{\infty} \text{sinc}\left(\frac{k_z w_z}{2}\right) \frac{e^{jk_z(d+w_z/2)} - e^{jk_z w_z/2}}{k^2 - k_x^2 - k_y^2 - k_z^2} \, dk_z \tag{G.1}$$

$$v_{\text{in},k_z}(x) = \int_{-\infty}^{\infty} \text{sinc}\left(k_z \frac{w_z - 2\delta_p}{2}\right) \frac{e^{jk_z(d+w_z/2)} - e^{jk_z w_z/2}}{k^2 - k_x^2 - k_y^2 - k_z^2} \, dk_z \tag{G.2}$$

$$v_{\text{out,image},k_z}(x) = -\int_{-\infty}^{\infty} \text{sinc}\left(\frac{k_z w_z}{2}\right) \frac{e^{-jk_z(d+w_z/2)} - e^{jk_z 2d}}{k^2 - k_x^2 - k_y^2 - k_z^2} \, dk_z \tag{G.3}$$

$$v_{\text{in,image},k_z}(x) = -\int_{-\infty}^{\infty} \text{sinc}\left(k_z \frac{w_z - 2\delta_p}{2}\right) \frac{e^{-jk_z(d+w_z/2)} - e^{jk_z 2d}}{k^2 - k_x^2 - k_y^2 - k_z^2} \, dk_z.. \tag{G.4}$$

By using the substitution $k_z \to -k_z$, (G.5) to (G.8) can be expressed as follows

$$v_{\text{out},k_z}(x) = \int_{-\infty}^{\infty} \text{sinc}\left(\frac{k_z w_z}{2}\right) \frac{e^{-jk_z(d+w_z/2)} - e^{-jk_z w_z/2}}{k^2 - k_x^2 - k_y^2 - k_z^2} \, dk_z \tag{G.5}$$

$$v_{\text{in},k_z}(x) = \int_{-\infty}^{\infty} \text{sinc}\left(k_z \frac{w_z - 2\delta_p}{2}\right) \frac{-e^{-jk_z(d+w_z/2)} - e^{-jk_z w_z/2}}{k^2 - k_x^2 - k_y^2 - k_z^2} \, dk_z \tag{G.6}$$

$$v_{\text{out,image},k_z}(x) = -\int_{-\infty}^{\infty} \text{sinc}\left(\frac{k_z w_z}{2}\right) \frac{e^{-jk_z(d+w_z/2)} - e^{-jk_z 2d}}{k^2 - k_x^2 - k_y^2 - k_z^2} \, dk_z \tag{G.7}$$

$$v_{\text{in,image},k_z}(x) = -\int_{-\infty}^{\infty} \text{sinc}\left(k_z \frac{w_z - 2\delta_p}{2}\right) \frac{e^{-jk_z(d+w_z/2)} - e^{-jk_z 2d}}{k^2 - k_x^2 - k_y^2 - k_z^2} \, dk_z.. \tag{G.8}$$

By using the definition $\text{sinc}(x) = \sin(x)/x$, (G.5) to (G.8) can all be reduced to (E.6).

G.2. Final substitutions

To obtain the value of all of the terms in (G.5) to (G.8), we substitute $k_{zp} = j\sqrt{k_x^2 + k_y^2 - k^2}$, $a = w_z/2$ or $a = (w_z - 2\delta_p)/2$ and $b = d + w_z/2$, $b = w_z/2$ or $b = 2d$ into (F.10). This results in the following expressions

$$v_{\text{out},k_z}(x) = \frac{1 + e^{-(d+w_z)\sqrt{k_x^2+k_y^2-k^2}} - e^{-d\sqrt{k_x^2+k_y^2-k^2}} - e^{-w_z\sqrt{k_x^2+k_y^2-k^2}}}{k_x^2 + k_y^2 - k^2} \tag{G.9}$$

$$v_{\text{in},k_z}(x) = \frac{e^{-\delta_p\sqrt{k_x^2+k_y^2-k^2}} + e^{-(d+w_z-\delta_p)\sqrt{k_x^2+k_y^2-k^2}} - e^{-(d+\delta_p)\sqrt{k_x^2+k_y^2-k^2}} - e^{-(w_z-\delta_p)\sqrt{k_x^2+k_y^2-k^2}}}{k_x^2 + k_y^2 - k^2} \tag{G.10}$$

$$v_{\text{out,image},k_z}(x) = -\frac{e^{-(d+w_z)\sqrt{k_x^2+k_y^2-k^2}} + e^{-2d\sqrt{k_x^2+k_y^2-k^2}} - e^{-d\sqrt{k_x^2+k_y^2-k^2}} - e^{-(2d+w_z)\sqrt{k_x^2+k_y^2-k^2}}}{k_x^2 + k_y^2 - k^2} \tag{G.11}$$

$$v_{\text{in,image},k_z}(x) = -\frac{e^{-(d+w_z-\delta_p)\sqrt{k_x^2+k_y^2-k^2}} + e^{-(2d+\delta_p)\sqrt{k_x^2+k_y^2-k^2}} - e^{-(d+\delta_p)\sqrt{k_x^2+k_y^2-k^2}} - e^{-(2d+w_z-\delta_p)\sqrt{k_x^2+k_y^2-k^2}}}{k_x^2 + k_y^2 - k^2}. \tag{G.12}$$

H

Longitudinal spectral Green's function microstrip

H.1. Leontovich boundary condition

In the case of the microstrip, the longitudinal spectral Green's function $D(k_x)$ can be calculated by the 3D-integral given by (5.1). Since the integral in z' will be solved numerically, we have decided to express the transverse current distribution of the Leontovich boundary condition as a summation of three terms, as shown in the following expression

$$j_t(y,z) = \frac{1}{2\delta_p(w_y + w_z - 2\delta_p)}\left(j_{t1}(y,z) + j_{t2}(y,z) + j_{t3}(y,z)\right), \tag{H.1}$$

where $j_{t1}(y,z)$, $j_{t2}(y,z)$ and $j_{t3}(y,z)$ can be expressed as follows

$$j_{t1}(y,z) = \mathrm{rect}\left(\frac{y}{w_y}\right)\mathrm{rect}\left(\frac{z-\delta_p/2}{\delta_p}\right) \tag{H.2}$$

$$j_{t2}(y,z) = \left(\mathrm{rect}\left(\frac{y}{w_y}\right) - \mathrm{rect}\left(\frac{y}{w_y - 2\delta_p}\right)\right)\mathrm{rect}\left(\frac{z-w_z/2}{w_z - 2\delta_p}\right) \tag{H.3}$$

$$j_{t3}(y,z) = \mathrm{rect}\left(\frac{y}{w_y}\right)\mathrm{rect}\left(\frac{z-(w_z-\delta_p/2)}{\delta_p}\right). \tag{H.4}$$

By performing a Fourier transform in y, we obtain the following expressions

$$J_{t1}(k_y,z) = w_y \mathrm{sinc}\left(\frac{k_y w_y}{2}\right)\mathrm{rect}\left(\frac{z-\delta_p/2}{\delta_p}\right) \tag{H.5}$$

$$J_{t2}(k_y,z) = \left(w_y \mathrm{sinc}\left(\frac{k_y w_y}{2}\right) - (w_y - 2\delta_p)\mathrm{sinc}\left(k_y\frac{w_y - 2\delta_p}{2}\right)\right)\mathrm{rect}\left(\frac{z-w_z/2}{w_z-2\delta_p}\right) \tag{H.6}$$

$$J_{t3}(k_y,z) = w_y \mathrm{sinc}\left(\frac{k_y w_y}{2}\right)\mathrm{rect}\left(\frac{z-(w_z-\delta_p/2)}{\delta_p}\right). \tag{H.7}$$

In principle, substituting (H.1) into (5.1) results in 9 terms. However, by resorting to the reciprocity theorem [44], we can express (5.1) as a combination of 6 terms, as shown in the following expression

$$D(k_x) = D_{11}(k_x) + D_{22}(k_x) + D_{33}(k_x) + 2D_{12}(k_x) + 2D_{13}(k_x) + 2D_{23}(k_x), \tag{H.8}$$

where $D_{11}(k_x)$, $D_{22}(k_x)$ and $D_{33}(k_x)$ are given by the following expressions

$$D_{11}(k_x) = \frac{1}{2\pi}\int\limits_{-\infty}^{\infty}\int\limits_{0}^{\delta_p}\int\limits_{z'}^{\delta_p} -\frac{V^{+}_{\text{TM,upper}}k_x^2 + V^{+}_{\text{TE,upper}}k_y^2}{k_x^2+k_y^2} e^{-jk_{z0}(z-z')}\text{sinc}^2\left(\frac{k_y w_y}{2}\right)dzdz'dk_y +$$
$$\frac{1}{2\pi}\int\limits_{-\infty}^{\infty}\int\limits_{0}^{\delta_p}\int\limits_{0}^{z'} -\frac{V^{+}_{\text{TM,lower}}k_x^2 + V^{+}_{\text{TE,lower}}k_y^2}{k_x^2+k_y^2} e^{jk_{z0}(z-z')}\text{sinc}^2\left(\frac{k_y w_y}{2}\right)dzdz'dk_y + \tag{H.9}$$
$$\frac{1}{2\pi}\int\limits_{-\infty}^{\infty}\int\limits_{0}^{\delta_p}\int\limits_{0}^{z'} -\frac{\Gamma_{TM}V^{+}_{\text{TM,lower}}k_x^2 + \Gamma_{TE}V^{+}_{\text{TE,lower}}k_y^2}{k_x^2+k_y^2} e^{-jk_{z0}(z+z')}\text{sinc}^2\left(\frac{k_y w_y}{2}\right)dzdz'dk_y$$

$$D_{22}(k_x) = \frac{1}{2\pi}\int\limits_{-\infty}^{\infty}\int\limits_{\delta_p}^{w_z-\delta_p}\int\limits_{z'}^{w_z-\delta_p} -\frac{V^{+}_{\text{TM,upper}}k_x^2 + V^{+}_{\text{TE,upper}}k_y^2}{k_x^2+k_y^2} e^{-jk_{z0}(z-z')}$$
$$\left(w_y\text{sinc}\left(\frac{k_y w_y}{2}\right) - (w_y-2\delta_p)\text{sinc}\left(k_y\frac{w_y-2\delta_p}{2}\right)\right)^2 dzdz'dk_y +$$
$$\frac{1}{2\pi}\int\limits_{-\infty}^{\infty}\int\limits_{\delta_p}^{w_z-\delta_p}\int\limits_{\delta_p}^{z'} -\frac{V^{+}_{\text{TM,lower}}k_x^2 + V^{+}_{\text{TE,lower}}k_y^2}{k_x^2+k_y^2} e^{jk_{z0}(z-z')} \tag{H.10}$$
$$\left(w_y\text{sinc}\left(\frac{k_y w_y}{2}\right) - (w_y-2\delta_p)\text{sinc}\left(k_y\frac{w_y-2\delta_p}{2}\right)\right)^2 dzdz'dk_y +$$
$$\frac{1}{2\pi}\int\limits_{-\infty}^{\infty}\int\limits_{\delta_p}^{w_z-\delta_p}\int\limits_{\delta_p}^{z'} -\frac{\Gamma_{TM}V^{+}_{\text{TM,lower}}k_x^2 + \Gamma_{TE}V^{+}_{\text{TE,lower}}k_y^2}{k_x^2+k_y^2} e^{-jk_{z0}(z+z')}$$
$$\left(w_y\text{sinc}\left(\frac{k_y w_y}{2}\right) - (w_y-2\delta_p)\text{sinc}\left(k_y\frac{w_y-2\delta_p}{2}\right)\right)^2 dzdz'dk_y$$

$$D_{33}(k_x) = \frac{1}{2\pi}\int\limits_{-\infty}^{\infty}\int\limits_{w_z-\delta_p}^{w_z}\int\limits_{z'}^{w_z} -\frac{V^{+}_{\text{TM,upper}}k_x^2 + V^{+}_{\text{TE,upper}}k_y^2}{k_x^2+k_y^2} e^{-jk_{z0}(z-z')}\text{sinc}^2\left(\frac{k_y w_y}{2}\right)dzdz'dk_y +$$
$$\frac{1}{2\pi}\int\limits_{-\infty}^{\infty}\int\limits_{w_z-\delta_p}^{w_z}\int\limits_{w_z-\delta_p}^{z'} -\frac{V^{+}_{\text{TM,lower}}k_x^2 + V^{+}_{\text{TE,lower}}k_y^2}{k_x^2+k_y^2} e^{jk_{z0}(z-z')}\text{sinc}^2\left(\frac{k_y w_y}{2}\right)dzdz'dk_y + \tag{H.11}$$
$$\frac{1}{2\pi}\int\limits_{-\infty}^{\infty}\int\limits_{w_z-\delta_p}^{w_z}\int\limits_{w_z-\delta_p}^{z'} -\frac{\Gamma_{TM}V^{+}_{\text{TM,lower}}k_x^2 + \Gamma_{TE}V^{+}_{\text{TE,lower}}k_y^2}{k_x^2+k_y^2} e^{-jk_{z0}(z+z')}\text{sinc}^2\left(\frac{k_y w_y}{2}\right)dzdz'dk_y.$$

Note that the integrands in (H.15), (H.10) and (H.11) contain different expressions for the two observation regions, where the region $z \in [z', w_z]$ only contains a forward propagating wave, while the region $z \in [z', w_z]$ contains both a forward and a backward propagating wave. $D_{12}(k_x)$, $D_{13}(k_x)$ and $D_{23}(k_x)$ are expressed as follows

$$D_{12}(k_x) = \frac{1}{2\pi}\int\limits_{-\infty}^{\infty}\int\limits_{0}^{\delta_p}\int\limits_{\delta_p}^{w_z-\delta_p} -\frac{V^{+}_{\text{TM,upper}}k_x^2 + V^{+}_{\text{TE,upper}}k_y^2}{k_x^2+k_y^2} e^{-jk_{z0}(z-z')}$$
$$\text{sinc}\left(\frac{k_y w_y}{2}\right)\left(w_y\text{sinc}\left(\frac{k_y w_y}{2}\right) - (w_y-2\delta_p)\text{sinc}\left(k_y\frac{w_y-2\delta_p}{2}\right)\right)dzdz'dk_y \tag{H.12}$$

$$D_{13}(k_x) = \frac{1}{2\pi}\int\limits_{-\infty}^{\infty}\int\limits_{0}^{\delta_p}\int\limits_{w_z-\delta_p}^{w_z} -\frac{V^{+}_{\text{TM,upper}}k_x^2 + V^{+}_{\text{TE,upper}}k_y^2}{k_x^2+k_y^2} e^{-jk_{z0}(z-z')}\text{sinc}^2\left(\frac{k_y w_y}{2}\right)dzdz'dk_y \tag{H.13}$$

$$D_{23}(k_x)=\frac{1}{2\pi}\int_{-\infty}^{\infty}\int_{\delta_p}^{w_z-\delta_p}\int_{w_z-\delta_p}^{w_z}-\frac{V^+_{\text{TM,upper}}k_x^2+V^+_{\text{TE,upper}}k_y^2}{k_x^2+k_y^2}e^{-jk_{z0}(z-z')}$$
$$\text{sinc}\left(\frac{k_yw_y}{2}\right)\left(w_y\text{sinc}\left(\frac{k_yw_y}{2}\right)-(w_y-2\delta_p)\text{sinc}\left(k_y\frac{w_y-2\delta_p}{2}\right)\right)dzdz'dk_y. \tag{H.14}$$

By closing the integrals in z, we obtain the following expressions

$$D_{11}(k_x)=\frac{1}{2\pi}\int_{-\infty}^{\infty}\int_{0}^{\delta_p}-\frac{V^+_{\text{TM,upper}}k_x^2+V^+_{\text{TE,upper}}k_y^2}{k_x^2+k_y^2}\frac{e^{-jk_{z0}(\delta_p-z')}-1}{k_{z0}}\text{sinc}^2\left(\frac{k_yw_y}{2}\right)dzdz'dk_y+$$
$$\frac{1}{2\pi}\int_{-\infty}^{\infty}\int_{0}^{\delta_p}-\frac{V^+_{\text{TM,lower}}k_x^2+V^+_{\text{TE,lower}}k_y^2}{k_x^2+k_y^2}\frac{e^{-jk_{z0}z'}-1}{k_{z0}}\text{sinc}^2\left(\frac{k_yw_y}{2}\right)dzdz'dk_y+ \tag{H.15}$$
$$\frac{1}{2\pi}\int_{-\infty}^{\infty}\int_{0}^{\delta_p}-\frac{\Gamma_{TM}V^+_{\text{TM,lower}}k_x^2+\Gamma_{TE}V^+_{\text{TE,lower}}k_y^2}{k_x^2+k_y^2}\frac{e^{-2jk_{z0}z'}-e^{-jk_{z0}z'}}{k_{z0}}\text{sinc}^2\left(\frac{k_yw_y}{2}\right)dzdz'dk_y$$

$$D_{22}(k_x)=\frac{j}{2\pi}\int_{-\infty}^{\infty}\int_{\delta_p}^{w_z-\delta_p}-\frac{V^+_{\text{TM,upper}}k_x^2+V^+_{\text{TE,upper}}k_y^2}{k_x^2+k_y^2}\frac{e^{-jk_{z0}(w_z-\delta_p-z')}-1}{k_{z0}}$$
$$\left(w_y\text{sinc}\left(\frac{k_yw_y}{2}\right)-(w_y-2\delta_p)\text{sinc}\left(k_y\frac{w_y-2\delta_p}{2}\right)\right)^2dz'dk_y+$$
$$\frac{j}{2\pi}\int_{-\infty}^{\infty}\int_{\delta_p}^{w_z-\delta_p}-\frac{V^+_{\text{TM,lower}}k_x^2+V^+_{\text{TE,lower}}k_y^2}{k_x^2+k_y^2}\frac{e^{-jk_{z0}(z'-\delta_p)}-1}{k_{z0}}$$
$$\left(w_y\text{sinc}\left(\frac{k_yw_y}{2}\right)-(w_y-2\delta_p)\text{sinc}\left(k_y\frac{w_y-2\delta_p}{2}\right)\right)^2dz'dk_y+ \tag{H.16}$$
$$\frac{j}{2\pi}\int_{-\infty}^{\infty}\int_{\delta_p}^{w_z-\delta_p}-\frac{\Gamma_{TM}V^+_{\text{TM,lower}}k_x^2+\Gamma_{TE}V^+_{\text{TE,lower}}k_y^2}{k_x^2+k_y^2}\frac{e^{-2jk_{z0}z'}-e^{-jk_{z0}(z'+\delta_p)}}{k_{z0}}$$
$$\left(w_y\text{sinc}\left(\frac{k_yw_y}{2}\right)-(w_y-2\delta_p)\text{sinc}\left(k_y\frac{w_y-2\delta_p}{2}\right)\right)^2dz'dk_y$$

$$D_{33}(k_x)=\frac{j}{2\pi}\int_{-\infty}^{\infty}\int_{w_z-\delta_p}^{w_z}-\frac{V^+_{\text{TM,upper}}k_x^2+V^+_{\text{TE,upper}}k_y^2}{k_x^2+k_y^2}\frac{e^{-jk_{z0}(w_z-z')}-1}{k_{z0}}\text{sinc}^2\left(\frac{k_yw_y}{2}\right)dz'dk_y+$$
$$\frac{j}{2\pi}\int_{-\infty}^{\infty}\int_{w_z-\delta_p}^{w_z}-\frac{V^+_{\text{TM,lower}}k_x^2+V^+_{\text{TE,lower}}k_y^2}{k_x^2+k_y^2}\frac{e^{-jk_{z0}(z'-w_z+\delta_p)}-1}{k_{z0}}\text{sinc}^2\left(\frac{k_yw_y}{2}\right)dz'dk_y+ \tag{H.17}$$
$$\frac{j}{2\pi}\int_{-\infty}^{\infty}\int_{w_z-\delta_p}^{w_z}-\frac{\Gamma_{TM}V^+_{\text{TM,lower}}k_x^2+\Gamma_{TE}V^+_{\text{TE,lower}}k_y^2}{k_x^2+k_y^2}\frac{e^{-2jk_{z0}z'}-e^{-jk_{z0}(z'+w_z-\delta_p)}}{k_{z0}}\text{sinc}^2\left(\frac{k_yw_y}{2}\right)dz'dk_y$$

$$D_{12}(k_x)=\frac{j}{\pi}\int_{-\infty}^{\infty}\int_{0}^{\delta_p}-\frac{V^+_{\text{TM,upper}}k_x^2+V^+_{\text{TE,upper}}k_y^2}{k_x^2+k_y^2}\frac{e^{-jk_{z0}(w_z-\delta_p-z')}-e^{-jk_{z0}(\delta_p-z')}}{k_{z0}}$$
$$w_y\text{sinc}\left(\frac{k_yw_y}{2}\right)\left(w_y\text{sinc}\left(\frac{k_yw_y}{2}\right)-(w_y-2\delta_p)\text{sinc}\left(k_y\frac{w_y-2\delta_p}{2}\right)\right)dz'dk_y \tag{H.18}$$

$$D_{13}(k_x)=\frac{j}{2\pi}\int_{-\infty}^{\infty}\int_{0}^{\delta_p}-\frac{V^+_{\text{TM,upper}}k_x^2+V^+_{\text{TE,upper}}k_y^2}{k_x^2+k_y^2}\frac{e^{-jk_{z0}(w_z-z')}-e^{-jk_{z0}(w_z-\delta_p-z')}}{k_{z0}}w_y^2\text{sinc}^2\left(\frac{k_yw_y}{2}\right)dz'dk_y \tag{H.19}$$

$$D_{23}(k_x) = \frac{j}{2\pi} \int_{-\infty}^{\infty} \int_{\delta_p}^{w_z-\delta_p} -\frac{V^+_{\text{TM,upper}} k_x^2 + V^+_{\text{TE,upper}} k_y^2}{k_x^2+k_y^2} \frac{e^{-jk_{z0}(w_z-z')} - e^{-jk_{z0}(w_z-\delta_p-z')}}{k_{z0}}$$
$$w_y \text{sinc}\left(\frac{k_y w_y}{2}\right)\left(w_y \text{sinc}\left(\frac{k_y w_y}{2}\right) - (w_y - 2\delta_p)\text{sinc}\left(k_y \frac{w_y - 2\delta_p}{2}\right)\right) dz' dk_y \tag{H.20}$$

By collecting all of the terms with the same integration bounds, we obtain the three integrals given by (5.23), (5.24) and (5.25).

H.2. Exponential distribution

The longitudinal spectral Green's function $D(k_x)$ is still given by the 3D-integral of (5.1). However, the transverse current distribution is given by (5.26). By performing a Fourier transform in y, we obtain the following expression

$$J_t(k_y, z) = J_0\left(\frac{k_y w_y}{2}\right) \frac{e^{-z/\delta_p} - e^{(z-w_z)/\delta_p}}{2\delta_p(1-e^{-w_z/\delta_p})} \tag{H.21}$$

By substituting (H.21) into (5.1), we obtain the following expression

$$\begin{aligned} D(k_x) = \frac{1}{2\pi} \int_{-\infty}^{\infty} \int_{0}^{w_z} \int_{z'}^{w_z} -\frac{V^+_{\text{TM,upper}} k_x^2 + V^+_{\text{TE,upper}} k_y^2}{k_x^2+k_y^2} e^{-jk_{z0}(z-z')} \\ J_0\left(\frac{k_y w_y}{2}\right) \text{sinc}\left(\frac{k_y w_y}{2}\right) (e^{-z/\delta_p} + e^{(z-w_z)/\delta_p})(e^{-z'/\delta_p} + e^{(z'-w_z)/\delta_p}) dz dz' dk_y + \\ \frac{1}{2\pi} \int_{-\infty}^{\infty} \int_{0}^{w_z} \int_{0}^{z'} -\frac{V^+_{\text{TM,lower}} k_x^2 + V^+_{\text{TE,lower}} k_y^2}{k_x^2+k_y^2} e^{jk_{z0}(z-z')} \\ J_0\left(\frac{k_y w_y}{2}\right) \text{sinc}\left(\frac{k_y w_y}{2}\right) (e^{-z/\delta_p} + e^{(z-w_z)/\delta_p})(e^{-z'/\delta_p} + e^{(z'-w_z)/\delta_p}) dz dz' dk_y + \\ \frac{1}{2\pi} \int_{-\infty}^{\infty} \int_{0}^{w_z} \int_{0}^{z'} -\frac{\Gamma_{TM} V^+_{\text{TM,lower}} k_x^2 + \Gamma_{TE} V^+_{\text{TE,lower}} k_y^2}{k_x^2+k_y^2} e^{-jk_{z0}(z+z')} \\ J_0\left(\frac{k_y w_y}{2}\right) \text{sinc}\left(\frac{k_y w_y}{2}\right) (e^{-z/\delta_p} + e^{(z-w_z)/\delta_p})(e^{-z'/\delta_p} + e^{(z'-w_z)/\delta_p}) dz dz' dk_y. \end{aligned} \tag{H.22}$$

By closing the integral in z, we obtain (5.27).

H.3. Exponential distribution split

To obtain the entries of the matrix $\mathbf{D}(k_x)$, we have to evaluate the 3D-integral of (5.54). To this extent, we will use the two exponentially decaying basis functions, given by (5.55) and (5.56). By performing a Fourier transform in y, we obtain the following expressions

$$J_{t,1}(k_y, z) = J_0\left(\frac{k_y w_y}{2}\right) \frac{e^{-z/\delta_p}}{\delta_p(1-e^{-w_z/\delta_p})} \tag{H.23}$$

$$J_{t,2}(k_y, z) = J_0\left(\frac{k_y w_y}{2}\right) \frac{e^{(z-w_z)/\delta_p}}{\delta_p(1-e^{-w_z/\delta_p})}. \tag{H.24}$$

By substituting (H.23) and (H.24) into (5.54), we obtain the following expressions

$$D_{11}(k_x) = \frac{1}{2\pi}\int_{-\infty}^{\infty}\int_{0}^{w_z}\int_{z'}^{w_z} -\frac{V^+_{\text{TM,upper}}k_x^2 + V^+_{\text{TE,upper}}k_y^2}{k_x^2+k_y^2} e^{jk_{z0}(z-z')} J_0\left(\frac{k_y w_y}{2}\right)\text{sinc}\left(\frac{k_y w_y}{2}\right) e^{-z/\delta_p} e^{-z'/\delta_p} dz dz' dk_y +$$
$$\frac{1}{2\pi}\int_{-\infty}^{\infty}\int_{0}^{w_z}\int_{0}^{z'} -\frac{V^+_{\text{TM,lower}}k_x^2 + V^+_{\text{TE,lower}}k_y^2}{k_x^2+k_y^2} e^{jk_{z0}(z-z')} J_0\left(\frac{k_y w_y}{2}\right)\text{sinc}\left(\frac{k_y w_y}{2}\right) e^{-z/\delta_p} e^{-z'/\delta_p} dz dz' dk_y +$$
$$\frac{1}{2\pi}\int_{-\infty}^{\infty}\int_{0}^{w_z}\int_{0}^{z'} -\frac{\Gamma_{TM}V^+_{\text{TM,lower}}k_x^2 + \Gamma_{TE}V^+_{\text{TE,lower}}k_y^2}{k_x^2+k_y^2} e^{-jk_{z0}(z+z')} J_0\left(\frac{k_y w_y}{2}\right)\text{sinc}\left(\frac{k_y w_y}{2}\right) e^{-z/\delta_p} e^{-z'/\delta_p} dz dz' dk_y \tag{H.25}$$

$$D_{22}(k_x) = \frac{1}{2\pi}\int_{-\infty}^{\infty}\int_{0}^{w_z}\int_{z'}^{w_z} -\frac{V^+_{\text{TM,upper}}k_x^2 + V^+_{\text{TE,upper}}k_y^2}{k_x^2+k_y^2} e^{jk_{z0}(z-z')} J_0\left(\frac{k_y w_y}{2}\right)\text{sinc}\left(\frac{k_y w_y}{2}\right) e^{(z-w_z)/\delta_p} e^{(z'-w_z)/\delta_p} dz dz' dk_y +$$
$$\frac{1}{2\pi}\int_{-\infty}^{\infty}\int_{0}^{w_z}\int_{0}^{z'} -\frac{V^+_{\text{TM,lower}}k_x^2 + V^+_{\text{TE,lower}}k_y^2}{k_x^2+k_y^2} e^{jk_{z0}(z-z')} J_0\left(\frac{k_y w_y}{2}\right)\text{sinc}\left(\frac{k_y w_y}{2}\right) e^{(z-w_z)/\delta_p} e^{(z'-w_z)/\delta_p} dz dz' dk_y +$$
$$\frac{1}{2\pi}\int_{-\infty}^{\infty}\int_{0}^{w_z}\int_{0}^{z'} -\frac{\Gamma_{TM}V^+_{\text{TM,lower}}k_x^2 + \Gamma_{TE}V^+_{\text{TE,lower}}k_y^2}{k_x^2+k_y^2} e^{-jk_{z0}(z+z')} J_0\left(\frac{k_y w_y}{2}\right)\text{sinc}\left(\frac{k_y w_y}{2}\right) e^{(z-w_z)/\delta_p} e^{(z'-w_z)/\delta_p} dz dz' dk_y \tag{H.26}$$

$$D_{12}(k_x) = \frac{1}{2\pi}\int_{-\infty}^{\infty}\int_{0}^{w_z}\int_{z'}^{w_z} -\frac{V^+_{\text{TM,upper}}k_x^2 + V^+_{\text{TE,upper}}k_y^2}{k_x^2+k_y^2} e^{jk_{z0}(z-z')} J_0\left(\frac{k_y w_y}{2}\right)\text{sinc}\left(\frac{k_y w_y}{2}\right) e^{-z'/\delta_p} e^{(z-w_z)/\delta_p} dz dz' dk_y +$$
$$\frac{1}{2\pi}\int_{-\infty}^{\infty}\int_{0}^{w_z}\int_{0}^{z'} -\frac{V^+_{\text{TM,lower}}k_x^2 + V^+_{\text{TE,lower}}k_y^2}{k_x^2+k_y^2} e^{jk_{z0}(z-z')} J_0\left(\frac{k_y w_y}{2}\right)\text{sinc}\left(\frac{k_y w_y}{2}\right) e^{-z'/\delta_p} e^{(z-w_z)/\delta_p} dz dz' dk_y +$$
$$\frac{1}{2\pi}\int_{-\infty}^{\infty}\int_{0}^{w_z}\int_{0}^{z'} -\frac{\Gamma_{TM}V^+_{\text{TM,lower}}k_x^2 + \Gamma_{TE}V^+_{\text{TE,lower}}k_y^2}{k_x^2+k_y^2} e^{-jk_{z0}(z+z')} J_0\left(\frac{k_y w_y}{2}\right)\text{sinc}\left(\frac{k_y w_y}{2}\right) e^{-z'/\delta_p} e^{(z-w_z)/\delta_p} dz dz' dk_y \tag{H.27}$$

By closing the integrals in z, we obtain (5.57), (5.58) and (5.59).

I Green's function leaky structure

Fig.I.1a shows the stratification of the leaky structure in Fig.7.1. The corresponding equivalent transmission-line model is shown in Fig.I.1b. The transmission-line model in Fig.I.1b is similar to the one in Fig.5.3b, except for the omission of the bottom transmission line in Fig.5.3b. Consequently, the xx-component of the spectral domain Green's function $G^{ej}_{xx}(k_x, k_y, z, z')$, in the regions $z \in [z', \infty)$ and $z \in [0, z']$, is given by (5.18) and (5.19), in which $Z_{\text{in},d}$ is replaced by Z_d.

Since the metal is located in the region $z \in [h_{\text{gap}}, h_{\text{gap}} + w_z]$, the longitudinal spectral Green's function $D(k_x)$ is given by the following expression

$$D(k_x) = \frac{1}{2\pi} \int_{-\infty}^{\infty} \int_{h_{\text{gap}}}^{h_{\text{gap}}+w_z} \int_{h_{\text{gap}}}^{h_{\text{gap}}+w_z} G^{ej}_{xx}(k_x, k_y, z, z') J_t(k_y, z') J^*_t(k_y, z) dz dz' dk_y, \tag{I.1}$$

To model the transverse current distribution, we have decided to use the exponential distribution of (5.26). By applying a shift of h_{gap} along $\hat{z}$, (5.26) becomes as follows

$$j_t(y, z) = \frac{2}{w_y \pi} \frac{1}{\sqrt{1 - (2y/w_y)^2}} \frac{e^{-(z-h_{\text{gap}})/\delta_p} + e^{(z-h_{\text{gap}}-w_z)/\delta_p}}{2\delta_p (1 - e^{-w_z/\delta_p})}. \tag{I.2}$$

By performing a Fourier transform in y, we obtain the following expression

$$J_t(k_y, z) = J_0\left(\frac{k_y w_y}{2}\right) \frac{e^{-(z-h_{\text{gap}})/\delta_p} - e^{(z-h_{\text{gap}}-w_z)/\delta_p}}{2\delta_p (1 - e^{-w_z/\delta_p})}. \tag{I.3}$$

By substituting (5.18), (5.19) and (I.3) into (I.1), we obtain the following expression

$$\begin{aligned}
D(k_x) = \frac{1}{2\pi} \int_{-\infty}^{\infty} \int_{0}^{w_z} \int_{z'}^{w_z} -\frac{V^+_{\text{TM,upper}} k_x^2 + V^+_{\text{TE,upper}} k_y^2}{k_x^2 + k_y^2} e^{-jk_{z0}(z-z')} \\
J_0\left(\frac{k_y w_y}{2}\right) \text{sinc}\left(\frac{k_y w_y}{2}\right) (e^{-(z-h_{\text{gap}})/\delta_p} + e^{(z-h_{\text{gap}}-w_z)/\delta_p})(e^{-(z'-h_{\text{gap}})/\delta_p} + e^{(z'-h_{\text{gap}}-w_z)/\delta_p}) dz dz' dk_y + \\
\frac{1}{2\pi} \int_{-\infty}^{\infty} \int_{0}^{w_z} \int_{0}^{z'} -\frac{V^+_{\text{TM,lower}} k_x^2 + V^+_{\text{TE,lower}} k_y^2}{k_x^2 + k_y^2} e^{jk_{z0}(z-z')} \\
J_0\left(\frac{k_y w_y}{2}\right) \text{sinc}\left(\frac{k_y w_y}{2}\right) (e^{-(z-h_{\text{gap}})/\delta_p} + e^{(z-h_{\text{gap}}-w_z)/\delta_p})(e^{-(z'-h_{\text{gap}})/\delta_p} + e^{(z'-h_{\text{gap}}-w_z)/\delta_p}) dz dz' dk_y + \\
\frac{1}{2\pi} \int_{-\infty}^{\infty} \int_{0}^{w_z} \int_{0}^{z'} -\frac{\Gamma_{TM} V^+_{\text{TM,lower}} k_x^2 + \Gamma_{TE} V^+_{\text{TE,lower}} k_y^2}{k_x^2 + k_y^2} e^{-jk_{z0}(z+z')} \\
J_0\left(\frac{k_y w_y}{2}\right) \text{sinc}\left(\frac{k_y w_y}{2}\right) (e^{-(z-h_{\text{gap}})/\delta_p} + e^{(z-h_{\text{gap}}-w_z)/\delta_p})(e^{-(z'-h_{\text{gap}})/\delta_p} + e^{(z'-h_{\text{gap}}-w_z)/\delta_p}) dz dz' dk_y.
\end{aligned} \tag{I.4}$$

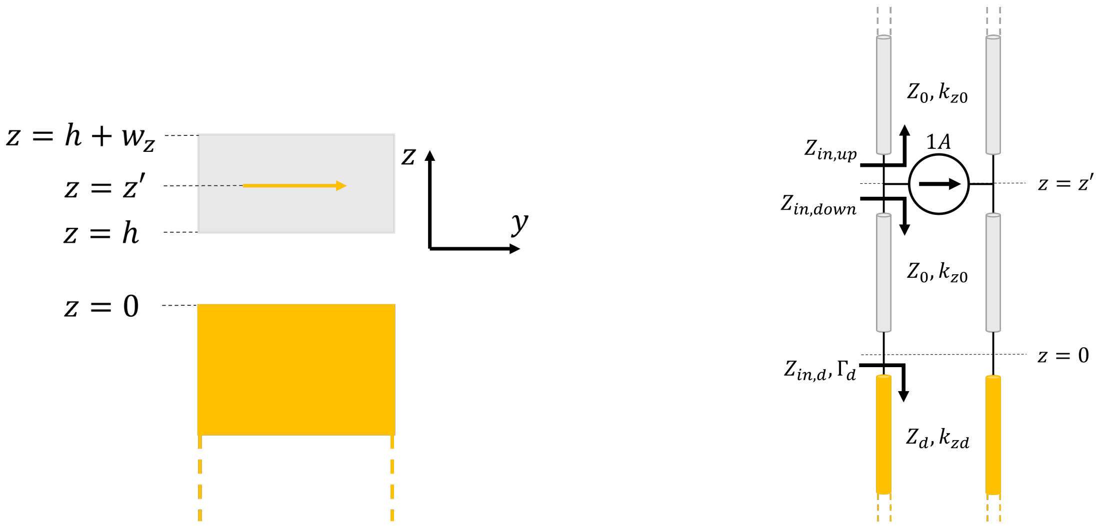

(a) (b) Equivalent transmission line model leaky structure

Figure I.1: (a) The stratification and (b) the equivalent transmission line-model of a dipole, located at a distance h_{gap} from a semi-infinite dielectric region

By closing the integral in z, we obtain the following expression

$$\begin{aligned}
D(k_x) = &-\frac{1}{2\pi}\int_{-\infty}^{\infty}\int_{0}^{w_z}\frac{V^+_{\text{TM,upper}}k_x^2 + V^+_{\text{TE,upper}}k_y^2}{k_x^2+k_y^2}\,\frac{e^{-(z'-h_{\text{gap}})/\delta_p} - e^{-w_z/\delta_p}e^{-jk_{z0}(h_{\text{gap}}+w_z-z')}}{jk_{z0}+1/\delta_p}\cdot \\
&\frac{e^{-(h_{\text{gap}}+wz-z')/\delta_p} - e^{-jk_{z0}(h_{\text{gap}}+w_z-z')}}{jk_{z0}-1/\delta_p}J_0\left(\frac{k_y w_y}{2}\right)\text{sinc}\left(\frac{k_y w_y}{2}\right)dz'dk_y - \\
&\frac{1}{2\pi}\int_{-\infty}^{\infty}\int_{0}^{w_z}\frac{V^+_{\text{TM,upper}}k_x^2 + V^+_{\text{TE,upper}}k_y^2}{k_x^2+k_y^2}\,\frac{e^{-(z'-h_{\text{gap}})/\delta_p} - e^{-jk_{z0}(z'-h_{\text{gap}})}}{jk_{z0}-1/\delta_p}\cdot \\
&\frac{e^{-(h_{\text{gap}}+wz-z')/\delta_p} - e^{-w_z/\delta_p}e^{-jk_{z0}(z'-h_{\text{gap}})}}{jk_{z0}+1/\delta_p}J_0\left(\frac{k_y w_y}{2}\right)\text{sinc}\left(\frac{k_y w_y}{2}\right)dz'dk_y - \\
&\frac{1}{2\pi}\int_{-\infty}^{\infty}\int_{0}^{w_z}\frac{\Gamma_{\text{TM},d}V^+_{\text{TM,lower}}k_x^2 + \Gamma_{\text{TE},d}V^+_{\text{TE,lower}}k_y^2}{k_x^2+k_y^2}\,\frac{e^{-jk_{z0}(z'+h_{\text{gap}})} - e^{-(z'-h_{\text{gap}})/\delta_p}e^{-2jk_{z0}z'}}{jk_{z0}+1/\delta_p}\cdot \\
&\frac{e^{-w_z/\delta_p}e^{-jk_{z0}(z'+h_{\text{gap}})} - e^{-2jk_{z0}z'}e^{-(h_{\text{gap}}+wz-z')/\delta_p}}{jk_{z0}-1/\delta_p}J_0\left(\frac{k_y w_y}{2}\right)\text{sinc}\left(\frac{k_y w_y}{2}\right)dz'dk_y.
\end{aligned} \tag{I.5}$$

Bibliography

[1] T. S. Rappaport, S. Sun, R. Mayzus, et al., "Millimeter wave mobile communications for 5g cellular: It will work!" IEEE Access, vol. 1, pp. 335–349, 2013. DOI: 10.1109/ACCESS.2013.2260813.

[2] H. Zhang, S. Bosma, A. Neto, and N. Llombart, "A dual-polarized 27 dbi scanning lens phased array antenna for 5g point-to-point communications," IEEE Transactions on Antennas and Propagation, vol. 69, no. 9, pp. 5640–5652, 2021.

[3] N. van Rooijen, M. Alonso delPino, M. Spirito, and N. Llombart, "Core-shell leaky-wave lens antenna for 150ghz fly's eye communication systems," in 2022 47th International Conference on Infrared, Millimeter and Terahertz Waves (IRMMW-THz), IEEE, 2022, pp. 1–2.

[4] L. Ferrari, O. Yurduseven, N. Llombart, et al., "Antenna coupled mkid performance verification at 850 ghz for large format astrophysics arrays," IEEE Transactions on Terahertz Science and Technology, vol. 8, no. 1, pp. 127–139, 2017.

[5] S. Hähnle, O. Yurduseven, S. van Berkel, et al., "An ultrawideband leaky lens antenna for broadband spectroscopic imaging applications," IEEE Transactions on Antennas and Propagation, vol. 68, no. 7, pp. 5675–5679, 2020.

[6] A. D. Semenov, H. Richter, H.-W. Hubers, et al., "Terahertz performance of integrated lens antennas with a hot-electron bolometer," IEEE transactions on microwave theory and techniques, vol. 55, no. 2, pp. 239–247, 2007.

[7] E. Gandini, J. Svedin, T. Bryllert, and N. Llombart, "Optomechanical system design for dual-mode stand-off submillimeter wavelength imagers," IEEE Transactions on Terahertz Science and Technology, vol. 7, no. 4, pp. 393–403, 2017.

[8] B. Cheng, Z. Cui, B. Lu, et al., "340-ghz 3-d imaging radar with 4tx-16rx mimo array," IEEE Transactions on Terahertz Science and Technology, vol. 8, no. 5, pp. 509–519, 2018.

[9] S. van Berkel, O. Yurduseven, A. Freni, A. Neto, and N. Llombart, "Thz imaging using uncooled wideband direct detection focal plane arrays," IEEE Transactions on Terahertz Science and Technology, vol. 7, no. 5, pp. 481–492, 2017.

[10] D. F. Filipovic, S. S. Gearhart, and G. M. Rebeiz, "Double-slot antennas on extended hemispherical and elliptical silicon dielectric lenses," IEEE Transactions on microwave theory and techniques, vol. 41, no. 10, pp. 1738–1749, 1993.

[11] E. Lima, J. R. Costa, M. G. Silveirinha, and C. A. Fernandes, "Ilash - software tool for the design of integrated lens antennas," in 2008 IEEE Antennas and Propagation Society International Symposium, 2008, pp. 1–4. DOI: 10.1109/APS.2008.4619133.

[12] J. Budhu and Y. Rahmat-Samii, "A novel and systematic approach to inhomogeneous dielectric lens design based on curved ray geometrical optics and particle swarm optimization," IEEE Transactions on Antennas and Propagation, vol. 67, no. 6, pp. 3657–3669, 2019.

[13] J. Geng, "Volumetric method of moments: A numerical tool for high frequency problems analysis," 2022.

[14] R. Ozzola, J. Geng, N. Llombart, A. Freni, D. Cavallo, and A. Neto, "A volumetric method of moments for integrated lens antennas," in 2022 47th International Conference on Infrared, Millimeter and Terahertz Waves (IRMMW-THz), IEEE, 2022, pp. 1–2.

[15] A. Neto and S. Maci, "Green's function for an infinite slot printed between two homogeneous dielectrics. i. magnetic currents," IEEE Transactions on Antennas and Propagation, vol. 51, no. 7, pp. 1572–1581, 2003.

[16] H. T. SHIVAMURTHY, "On the design and analysis of micro-metric resolution arrays in integrated technology for near-field dielectric spectroscopy," 2020.

[17] C. Di Nallo, F. Mesa, and D. R. Jackson, "Excitation of leaky modes on multilayer stripline structures," IEEE Transactions on Microwave Theory and Techniques, vol. 46, no. 8, pp. 1062–1071, 1998.

[18] F. Mesa, C. Di Nallo, and D. R. Jackson, “The theory of surface-wave and space-wave leaky-mode excitation on microstrip lines,” IEEE Transactions on Microwave Theory and Techniques, vol. 47, no. 2, pp. 207–215, 1999.

[19] S. L. van Berkel, A. Garufo, N. Llombart, and A. Neto, “A quasi-analytical tool for the characterization of transmission lines at high frequencies [em programmer’s notebook],” IEEE Antennas and Propagation Magazine, vol. 58, no. 3, pp. 82–90, 2016. DOI: 10.1109/MAP.2016.2541617.

[20] R. Garg, I. Bahl, and M. Bozzi, Microstrip lines and slotlines. Artech house, 2013.

[21] J.-S. G. Hong and M. J. Lancaster, Microstrip filters for RF/microwave applications. John Wiley & Sons, 2004.

[22] J. C. Rautio, “An investigation of microstrip conductor loss,” IEEE Microwave Magazine, vol. 1, no. 4, pp. 60–67, 2000.

[23] A. G. Polimeridis, J. F. Villena, L. Daniel, and J. K. White, “Stable fft-jvie solvers for fast analysis of highly inhomogeneous dielectric objects,” Journal of Computational Physics, vol. 269, pp. 280–296, 2014.

[24] D. E. Livesay and K.-M. Chen, “Electromagnetic fields induced inside arbitrarily shaped biological bodies,” IEEE Transactions on Microwave Theory and Techniques, vol. 22, no. 12, pp. 1273–1280, 1974.

[25] M. Leontovich, “Investigation of propagation of radio waves, part ii,” USSR Acad. Sci., Moscow, 1948.

[26] R. F. Harrington and J. L. Harrington, Field computation by moment methods. Oxford University Press, Inc., 1996.

[27] M. Van Beurden and S. Van Eijndhoven, “Gaps in present discretization schemes for domain integral equations,” in 2007 International Conference on Electromagnetics in Advanced Applications, IEEE, 2007, pp. 673–675.

[28] M. Van Beurden and S. Van Eijndhoven, “Well-posedness of domain integral equations for a dielectric object in homogeneous background,” Journal of Engineering Mathematics, vol. 62, pp. 289–302, 2008.

[29] J. Markkanen, P. Yla-Oijala, and A. Sihvola, “Discretization of volume integral equation formulations for extremely anisotropic materials,” IEEE Transactions on Antennas and Propagation, vol. 60, no. 11, pp. 5195–5202, 2012.

[30] A. D. Yaghjian, “Electric dyadic green’s functions in the source region,” Proceedings of the IEEE, vol. 68, no. 2, pp. 248–263, 1980.

[31] J. Van Bladel, “Singular electromagnetic fields and sources,” (No Title), 1991.

[32] J.-M. Jin, The finite element method in electromagnetics. John Wiley & Sons, 2015.

[33] G. Mie, “Beiträge zur optik trüber medien, speziell kolloidaler metallösungen,” Annalen der physik, vol. 330, no. 3, pp. 377–445, 1908.

[34] J.-P. Schäfer, “Implementierung und anwendung analytischer und numerischer verfahren zur lösung der maxwellgleichungen für die untersuchung der lichtausbreitung in biologischem gewebe,” Ph.D. dissertation, Universität Ulm, 2011.

[35] L. Sun and W. C. Chew, “A novel formulation of the volume integral equation for electromagnetic scattering,” Waves in Random and Complex Media, vol. 19, no. 1, pp. 162–180, 2009.

[36] A. G. Polimeridis, F. Vipiana, J. R. Mosig, and D. R. Wilton, “Directfn: Fully numerical algorithms for high precision computation of singular integrals in galerkin sie methods,” IEEE Transactions on Antennas and Propagation, vol. 61, no. 6, pp. 3112–3122, 2013.

[37] A. A. Tambova, M. S. Litsarev, G. Guryev, and A. G. Polimeridis, “On the generalization of directfn for singular integrals over quadrilateral patches,” IEEE Transactions on Antennas and Propagation, vol. 66, no. 1, pp. 304–314, 2017.

[38] G. von Winckel, Legendre-gauss quadrature weights and nodes, May 2004. [Online]. Available: https://nl.mathworks.com/matlabcentral/fileexchange/4540-legendre-gauss-quadrature-weights-and-nodes.

[39] C. M. Studio, “Cst microwave studio,” CST Studio Suite, 2008.

[40] D. Cavallo, W. H. Syed, and A. Neto, “Equivalent transmission line models for the analysis of edge effects in finite connected and tightly coupled arrays,” IEEE Transactions on Antennas and Propagation, vol. 65, no. 4, pp. 1788–1796, 2017.

[41] J. W. Brown and R. V. Churchill, Complex variables and applications. McGraw-Hill, 2009.

[42] D. J. Griffiths, Introduction to electrodynamics, 2005.

[43] D. M. Pozar, Microwave engineering. John wiley & sons, 2011.

[44] H. A. Lorentz, "The theorem of poynting concerning the energy in the electromagnetic field and two general propositions concerning the propagation of light," Amsterdammer Akademie der Wetenschappen, vol. 4, p. 176, 1896.

[45] A. F. Peterson, "Analysis of heterogeneous electromagnetic scatterers: Research progress of the past decade," Proceedings of the IEEE, vol. 79, no. 10, pp. 1431–1441, 1991.

[46] A. Neto, S. Maci, and P. De Maagt, "Reflections inside an elliptical dielectric lens antenna," IEE Proceedings-Microwaves, Antennas and Propagation, vol. 145, no. 3, pp. 243–247, 1998.

[47] M. Abramowitz, I. A. Stegun, and R. H. Romer, Handbook of mathematical functions with formulas, graphs, and mathematical tables, 1988.

[48] V. S. Ryaben'kii and S. V. Tsynkov, A theoretical introduction to numerical analysis. CRC press, 2006.